

---

# **A study on the extraction of negative ions from a multicusp ion source**

Anand Mathai George

A thesis submitted in fulfilment of the requirements  
for the degree of Doctor of Philosophy in Physics,  
the University of Auckland,  
2021

---

# Abstract

A beam of charged particles can perform wonders in the field of science and technology. One of the methods of producing charged particle beams is its extraction from gaseous plasma created inside ion sources. The thesis deals with a collection of studies on the extraction of negative ion beams from a multicusp ion source, where multicusp refers to the type of magnetic field used for plasma confinement inside the ion source. The study revolves around improving the  $H^-$  and  $D^-$  beam extraction from the ion source.

Two kinds of ion sources are considered in the study. One of them, the filament ion source, generates plasma through thermionic emission, while the other, the RF ion source, generates plasma through RF energy coupling. The characteristics of the extracted ion beam depend on a multitude of factors in the ion source and extraction system, and some of them are analysed in the thesis. Both ion sources produce negative ions in the plasma primarily through volume production methods. The thesis presents evidence for the negative ion production through plasma-wall surface interactions also. Results indicate that an optimum magnetic filter field is needed to increase the efficiency of volume production and a lower surface temperature is needed to enhance the surface interactions. Design upgrades of the RF ion source were also performed and improvements in  $H^-$  and  $D^-$  beam currents were achieved. The thesis also presents the results of an experimental campaign for analysing the validity of IBSimu, an ion beam extraction simulation code. Results indicate that IBSimu is capable of reproducing the ion beam emittance trends obtained in the experiments. Results of plasma analysis performed using Langmuir probe and laser photodetachment tools, and thermal analysis conducted using Solidworks simulations, are also presented in the thesis.



# Acknowledgements

Foremost, I would like to express my deep gratitude towards my supervisors, Dr. Neil Broderick and Dr. Morgan Dehnel. Neil, thank you very much for agreeing to be my supervisor in a crucial situation. I am grateful for all the support and guidance you have provided throughout my doctoral studies. Morgan, thank you for believing in me and providing all the guidance and collaboration opportunities throughout my study. Thank you for spending your time and effort in helping me achieve my dream. I would also like to place my mark of gratitude to Late Prof. Peter Derrick, whom I have never seen, but who worked very hard to ensure that I was accepted by the university as a student.

I would like to thank Dr. Motoi Wada and his students, Yuji and Maeshiro, for allowing me to perform laser photodetachment experiments at Doshisha University. Gen, thank you very much for all the discussions and support you have provided for my thesis.

I also express my gratitude towards Dr. Taneli Kalvas, University of Jyväskylä, for all the support provided for conducting the IBSimu experimental campaign and publication of the work.

I would like to thank all the staff at D-Pace for their support throughout my studies. Stephane, thank you for all your help and support and teaching me how to extract ion beams. Dave, thank you for all the guidance and support. Thomas, thank you for helping me with the mechanical designs and trusting me with the experiments. Meghan, thank you for your efforts in supporting me. I would also like to thank Morgan, Kurt, Kent, Dave and Thomas for all the financial support I received during my studies.

All the experiments presented in the thesis were conducted at Buckley systems. I would like to thank the board of directors, HR staff and other staff at Buckley systems for providing all the help needed for my work. Craig, thank you for helping me with all the fee payments and scholarship reports. I would like to especially thank Dr. Chris Philpott for all the friendly discussions and guidance. Chris, thank you for all your help, even though I spoiled most of

your Sundays with my experiments. Paul, thank you for helping me happily whenever I was stuck with my experiments. Steve, thank you for all the magnetic field measurements. Roger, thank you for always asking about my progress and experiments. Nicolas, thank you very much for those joint experiments, questions, discussions and lots of fun. I would also like to thank Tobin, Hamish and Alex for all their help during my experiments.

I would also like to thank Callaghan Innovation, New Zealand, for the funding I received during my doctoral studies.

Finally, I gratefully thank the support, encouragement and love from my family - my mother, my brother and family, during this journey. I thank my daughter Arlyn for making it so special. Especially thanking my beloved wife Rinkoo for trusting and encouraging me through these years.

Anand Mathai George  
Auckland, New Zealand  
February 2021

# Contents

<b>Abstract</b>	<b>i</b>
<b>Acknowledgements</b>	<b>ii</b>
<b>1 Introduction</b>	<b>1</b>
<b>2 Fundamental plasma properties</b>	<b>5</b>
2.1 Particle distributions in an equilibrium plasma . . . . .	5
2.2 Debye shielding . . . . .	7
2.3 Plasma frequency . . . . .	9
2.4 Plasma boundary . . . . .	10
2.4.1 <i>The Bohm criterion</i> . . . . .	10
2.4.2 <i>Floating wall potential</i> . . . . .	15
2.5 Collisions in a plasma . . . . .	16
2.5.1 <i>Weakly ionised plasma</i> . . . . .	17
2.5.2 <i>Fully ionised plasma</i> . . . . .	17
2.6 Effect of external fields in plasma . . . . .	18
2.6.1 <i>Uniform magnetic field</i> . . . . .	18
2.6.2 <i>Uniform magnetic and electric field</i> . . . . .	20
2.6.3 <i>Non uniform magnetic fields, <math>\vec{\nabla} B</math></i> . . . . .	21
2.6.4 <i>Magnetic mirror effect</i> . . . . .	24
2.7 Diffusion in plasma . . . . .	24
2.7.1 <i>Diffusion in a weakly ionised plasma</i> . . . . .	25
2.7.2 <i>Diffusion in a fully ionised plasma</i> . . . . .	26
2.8 Ionisation . . . . .	27
2.9 Negative ion formation processes . . . . .	29
2.9.1 <i>Charge exchange processes</i> . . . . .	29
2.9.2 <i>Volume production processes</i> . . . . .	30

2.9.3	<i>Surface production processes</i>	32
<b>3</b>	<b>Ion sources and beam extraction</b>	<b>33</b>
3.1	Ion extraction from plasma	33
3.1.1	<i>The plasma "meniscus"</i>	35
3.1.2	<i>Limitation due to space charge</i>	36
3.2	Liouville's theorem	39
3.3	Equations of motion of charged particle beams	41
3.4	Particle motion in transverse planes	43
3.5	Features of the Twiss ellipse	47
3.5.1	<i>Ellipse propagation in beam line</i>	48
3.5.2	<i>Orientation of ellipse</i>	49
3.5.3	<i>Location of the beam waist</i>	49
3.6	RMS Emittance	51
3.7	Normalized emittance	52
3.8	Space charge	53
3.8.1	<i>Effect of space charge in beam transport</i>	53
3.8.2	<i>Space charge compensation</i>	55
3.9	External focusing forces	57
3.10	Space charge, emittance and focusing forces	57
<b>4</b>	<b>Filament ion source experiments</b>	<b>59</b>
4.1	Filament ion source overview	60
4.2	Effect of magnetic dipole filters	62
4.2.1	<i>Influence of filter fields on negative ion current</i>	65
4.2.2	<i>Plasma parameters in <math>H_2</math> and <math>D_2</math> plasma</i>	69
4.2.3	<i>Experimental results at 30 keV beam energy</i>	71
4.3	Role of surface interactions in $H^-$ generation	74
4.4	Effect of different plasma electrode materials	77
4.5	Influence of plasma electrode aperture size	83
4.6	Conclusions	86
<b>5</b>	<b>RF ion source upgrades</b>	<b>87</b>
5.1	RF ion source overview	87
5.1.1	<i>Power absorption in ICP</i>	89
5.1.2	<i>Capacitive coupling</i>	92
5.1.3	<i>Impedance matching</i>	92

5.2	Challenges in the RF ion source operation . . . . .	93
5.3	Simulation studies of AlN window . . . . .	94
5.4	Design changes - 'PEEK design' . . . . .	100
5.5	Experimental results . . . . .	102
5.5.1	<i>Coupling efficiency and mode transitions</i> . . . . .	104
5.5.2	<i>Copper deposition on AlN window</i> . . . . .	106
5.6	Water immersed RF antenna . . . . .	109
5.7	Effect of a ceramic plasma chamber . . . . .	110
5.8	Conclusions . . . . .	112
<b>6</b>	<b>Simulations using IBSimu code</b>	<b>114</b>
6.1	Overview of IBSimu code . . . . .	114
6.2	Ion source and simulations . . . . .	117
6.3	The optical effect of plasma sheath . . . . .	119
6.4	Simulation methods . . . . .	120
6.5	Filament ion source experiments and simulations . . . . .	121
6.5.1	<i>Effect of gas flow on beam emittance</i> . . . . .	124
6.5.2	<i>Effect of plasma electrode voltage on beam emittance</i> . . . . .	128
6.5.3	<i>Charge density correction factor in simulations</i> . . . . .	129
6.6	RF ion source experiments and simulations . . . . .	130
6.7	Effect of extraction voltage on beam emittance . . . . .	132
6.8	Emittance comparisons between the ion sources . . . . .	133
6.9	Conclusions . . . . .	135
<b>7</b>	<b>Conclusions</b>	<b>137</b>
<b>A</b>	<b>Laser Photodetachment</b>	<b>140</b>
A.1	Experiments and results . . . . .	141
<b>B</b>	<b>Experiment venue - ISTF</b>	<b>146</b>
B.1	Ion source and extraction . . . . .	147
B.1.1	<i>Magnetic fields</i> . . . . .	149
B.1.2	<i>Extraction control parameters</i> . . . . .	150
B.2	Vacuum system . . . . .	152
B.3	Beam diagnostics . . . . .	154
B.3.1	<i>Faraday cup</i> . . . . .	154
B.3.2	<i>Emittance scanner</i> . . . . .	155

---

B.4	Beam tuning methods . . . . .	156
<b>C</b>	<b>Neutron radiation</b>	<b>158</b>
	<b>Bibliography</b>	<b>161</b>

# Chapter 1

---

## Introduction

Energetic charged particle beams have been present at the forefront of scientific explorations into the secret world of subatomic particles, since the introduction of particle accelerators in the early 1930s. Remarkable progress has been achieved in this field from Ernest Lawrence's 1 MeV proton beam in 1932 [1] to CERN's 6.5 TeV proton beam that discovered the Higgs boson in 2012 [2, 3]. The applications of the charged particle beams have also diversified from the fundamental particle research into the fields of medicine, manufacturing, fusion energy, national security and so on [4]. About 30000 particle accelerators are operating around the world in various fields and less than 1% operate in the field of fundamental research, as per the report in 2017 [5]. The majority of the accelerators are used in health care and industries. Beams with the required energy and quality are used for treating cancer [6], production of medical radioisotopes [7], polymer material modifications, pollutant treatments [8], ion implantation in materials [9], etc.

One of the critical parts of a particle accelerator is the *ion source*, that supplies the ions for acceleration. There is a long list of different types of ion sources in operation worldwide. Some of them are "high current gaseous ion sources, RF (Radio Frequency)-driven ion sources, microwave driven ion source, ECR (Electron Cyclotron Resonance) ion sources, laser ion sources, vacuum arc ion sources, negative ion sources, ion sources for heavy ion fusion and giant ion sources for neutral beams" [10]. The choice depends on the requirements of the type of particle (positive or negative ions), amount of beam currents, pulsed or DC beams, ion source life time etc.

The production of negative ion beams is more challenging than positive ion beams [11]. This is because the negative ions are less stable as the additional electrons are bound by very small energy. For example, the extra electron in the  $\text{H}^-$  ion is bound by an energy of only 0.75 eV [11], whereas the last electron in an H atom is bound by 13.6 eV [12]. Another

challenge in negative ion beam generation is the extraction of electrons along with negative ions from the plasma. In such cases, the extraction systems need additional magnetic fields for removing the electrons from the extracted beam [13].

Even though challenging, the production of negative ions offer some excellent advantages in the field of particle accelerators. One of them is its application in *tandem* accelerators. Tandem accelerators are electrostatic accelerators in which the negative ions injected at a ground potential accelerate towards a positive high voltage terminal. After reaching the positive terminal the negative ions are stripped off two or more electrons by a stripper system and thus get converted into positive ions [14]. These positive ions are further repelled by the high voltage positive terminal into the ground potential. Thus the ions gain twice the amount of energy compared to the case when only positive ions are used. Another advantage of negative ions is that they facilitate the easier extraction of positive ions from cyclotrons. The negative ions are fed into the cyclotrons for acceleration and they hit a stripping foil towards the end of their path and gets converted to positive ions. This reverses the Lorentz force direction on the positive ions to the opposite direction and they are extracted from the cyclotrons. Such cyclotrons are often used in medical isotope production [15]. The negative ions also find its usefulness in multi-turn charge-exchange injection process, which is used for proton charge accumulation in storage rings. This enables the production of high intensity proton beams [16, 17].

The current thesis is a collection of studies related to  $H^-$  and  $D^-$  beam generation, performed by the author in collaboration with D-Pace [18], Canada. The experiments were conducted at the Ion Source Test Facility (ISTF), Buckley Systems [19], Auckland. Details of the test facility, components and experimental set up are described in Appendix B. A picture of the basic ion source configuration, used for the experiments, is shown in Fig. 1.1. This is D-Pace's TRIUMF [13] licensed filament ion source system. D-Pace has supplied around 20 ion sources worldwide. The negative ions from the ion source are used in different tandem accelerators and cyclotrons for a variety of applications. The studies conducted by the author was targeted at improving the ion source performance and better understanding of the scientific processes involved in its operation, which is beneficial to D-Pace's business interests.

One of the goals of the thesis is the study of factors affecting the beam current extraction from the D-Pace ion source. D-Pace is looking to achieve more beam currents from its source, especially  $D^-$  beam current of at least 10 mA, due to the demand for such beams in Boron Neutron Capture Therapy (BNCT) [6]. BNCT technology is used for the treatment of malignant tumours [6]. The tumour cells containing a  $^{10}B$  drug can react with thermal neutrons and the subsequent reactions can destroy the tumour cells, without damaging the



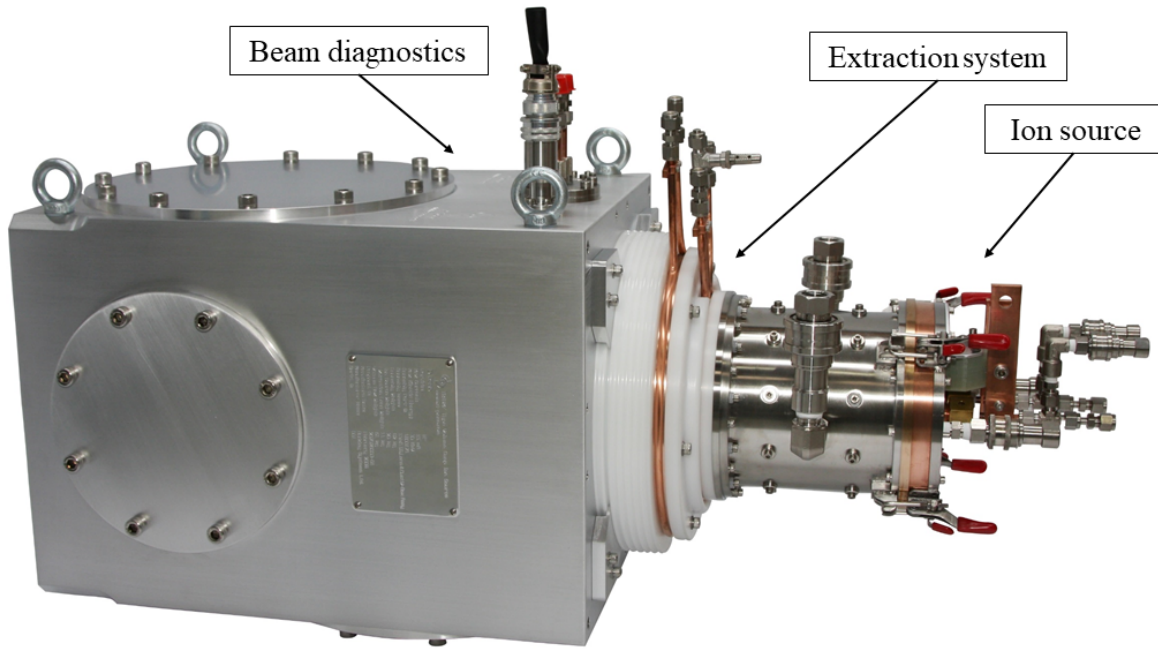


**Figure 1.1:** A picture of D-Pace's TRIUMF licensed ion source and extraction assembly [13]. This is the basic configuration used for performing the experiments outlined in the thesis. Details of the system are presented in Appendix B.

healthy tissues. The neutrons required for this process can be produced in accelerator-based facilities through the bombardment of energetic deuterium beams with Be and C target [6]. The target amount of  $D^-$  beam currents needed for a single session of the treatment is about 10-15 mA [20].

Another goal of the thesis is the improvement of D-Pace's Radio Frequency (RF) powered ion source. RF ion source offers some excellent advantages in terms of maintenance free operation and an ion source plasma free from metallic filaments. Currently, there are challenges related to the operation of the RF ion source. The study aims at solving some of these challenges and improving the RF ion source performance.

The thesis also aims to contribute to the scientific understanding of the ion source community by conducting an experimental campaign for the development of the plasma extraction code, IBSimu [21]. The study includes the development of a simulation model using IBSimu code for ion beam extraction from D-Pace's ion sources. The goal of the study is a comparison of experimentally determined beam properties for different plasma densities, electric fields, gas flows, etc. to that predicted by the simulation model. This also provides an extensive data set of experiments and simulations for D-Pace that helps in future design work involving the ion sources.

The thesis is arranged as follows:

**Chapter 2, Chapter 3** deals with the background theory related to the study. Chapter 2 deals with the basic plasma theory in the ion source and describes the reactions leading to the formation of negative ions inside the plasma. The method of extraction of ions from the plasma into a beam and different aspects related to the quality of the beam are described in chapter 3.

**Chapter 4** deals with experiments related to the study of different factors influencing the extraction of  $H^-$  and  $D^-$  beam from D-Pace's filament ion source.

**Chapter 5** describes the design upgrades performed in D-Pace's RF ion source. The reasons for the upgrades, the improvements achieved and existing challenges are outlined in this chapter.

**Chapter 6** discusses the results of the experimental campaign for the development of plasma extraction code, IBSimu.

**Appendix A** describes the laser photodetachment studies performed in a filament ion source at Doshisha University, Japan.

**Appendix B** outlines the details of the experimental venue, ISTF and the ion source and extraction system used in the experiments. It also describes the ion beam tuning methods used for the study.

**Appendix C** shows the details of the neutron radiation observed at the ISTF during the  $D^-$  beam experiments.

# Chapter 2

---

## Fundamental plasma properties

*Plasma* is considered as the fourth state of matter, where the temperature is high enough to cause particle collisions resulting in ionisations [22]. Plasma is composed of neutral particles and charged particles like electrons and ions. The name ‘plasma’ was introduced by Irving Langmuir [23]. Natural plasmas are seen, for example, in the Northern Lights phenomenon, lightning strikes and inside stars. Human-made plasmas can be seen in different scales ranging from light sources to space propulsion [10]. In the context of the current thesis, plasma is the parent medium from which a charged particle beam is extracted and accelerated. The characteristics of the extracted beam depend heavily on the properties of the plasma. This chapter deals with the features of an equilibrium plasma and its physical boundaries, collisions inside the plasma, transport of particles inside the plasma due to external fields and processes leading to the formation of positive and negative ions inside the plasma. The discussions in this chapter are based on texts from references [10, 22, 24–26].

### 2.1 Particle distributions in an equilibrium plasma

Particles inside the plasma move randomly with different energies and velocities. Ions, neutrals and electrons inside the plasma can be treated as separate plasma species. The amount of different species can be described by the *plasma density* of the corresponding species (ions, electrons or neutrals).

The positions ( $\vec{r}$ ) and velocities ( $\vec{v}$ ) of the particles inside the plasma can be represented as points in *phase space* and described using *distribution functions* [10]. The distribution function for a plasma species can be derived by considering it as an ensemble of particles in thermal equilibrium at temperature  $T$ . Such an ensemble can be considered as a distinguishable microsystem in terms of equilibrium statistical mechanics [26]. Hence the average number

of particles ( $N$ ) of the plasma species in a state of energy  $\mathcal{E}$ , is proportional to the Boltzmann factor,  $k_b T$  [25],

$$N \propto \exp\left(-\frac{\mathcal{E}}{k_b T}\right) \quad (2.1)$$

Ignoring any potential energy associated with the particle positions and assuming plasma species to be homogeneous and isotropic, the Maxwell-Boltzmann distribution function for velocities can be derived as

$$f(\vec{v}) = n_0 \left[ \frac{m}{2\pi k_b T} \right]^{3/2} \exp\left[-\frac{m(v_x^2 + v_y^2 + v_z^2)}{2k_b T}\right] \quad (2.2)$$

such that  $f(\vec{v})d\vec{r}d\vec{v}$  gives the number of particles in the elemental volume  $d\vec{r}d\vec{v} = dv_x dv_y dv_z dx dy dz$  in phase space [22, 26].  $m$  is the mass of the plasma species under consideration. The constant factor shown in the above equation is obtained by considering that the integration of the distribution function along all the velocities in phase space, gives the density,  $n_0$  in physical space.

$$\int_{-\infty}^{\infty} f(\vec{v}) dv_x dv_y dv_z = n_0 \quad (2.3)$$

The distribution of speeds,  $f(v)$ , is obtained by considering the velocity space in spherical coordinates,  $dv_x dv_y dv_z = v^2 dv \sin \theta d\theta d\phi$  and integrating over the solid angle. This gives

$$f(v) = n_0 \left[ \frac{m}{2\pi k_b T} \right]^{3/2} 4\pi v^2 \exp\left[-\frac{mv^2}{2k_b T}\right] \quad (2.4)$$

The variation in the value of the above distribution function equation as a function of particle speeds, at different thermal equilibrium temperatures, is shown in Fig. 2.1(A). Temperature is represented in units of eV ( $T \Rightarrow k_b T/e$ ,  $1 \text{ eV} \approx 11,600 \text{ K}$ ). As found in the figure and also in the above equations, when the equilibrium temperature increases, the distribution broadens and the number of particles possessing high speed values also increases. This can cause more collisions and ionisations. The mean value of speed can be obtained from equation 2.4 as

$$\langle v \rangle = \frac{1}{n_0} \int_0^{\infty} v f(v) dv = \sqrt{\frac{8k_b T}{\pi m}} \quad (2.5)$$

The distribution function of energy,  $f(\mathcal{E})$ , can be derived using the relations  $\mathcal{E} = \frac{1}{2}mv^2$  and  $d\mathcal{E} = mvdv$

$$f(\mathcal{E}) = \frac{2\pi n_0}{(\pi k_b T)^{3/2}} \mathcal{E}^{1/2} \exp\left[-\frac{\mathcal{E}}{k_b T}\right] \quad (2.6)$$

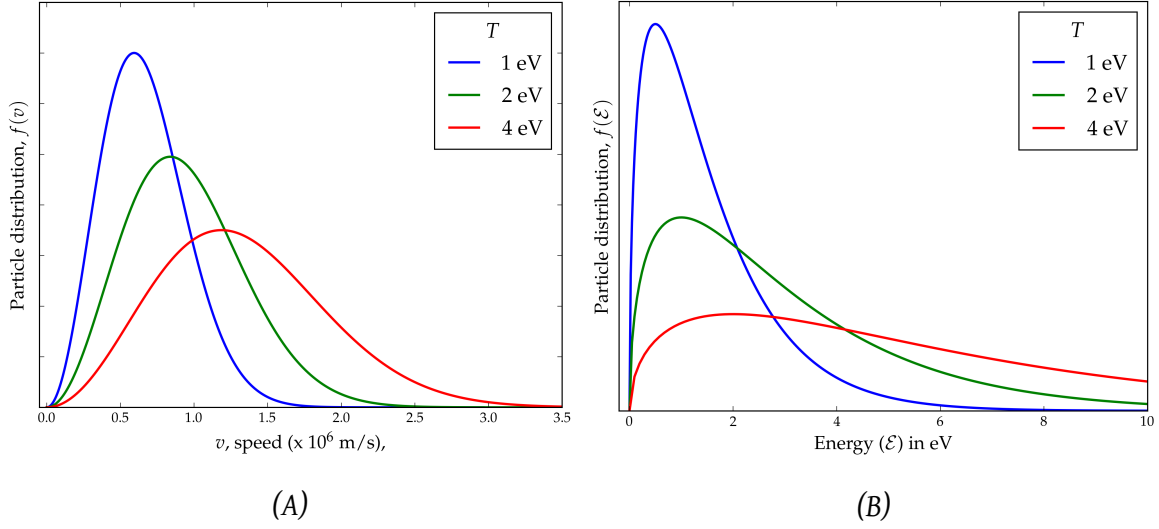


**Figure 2.1:** Maxwell-Boltzmann distribution of (A) speeds and (B) energies at different thermal equilibrium temperatures.

The variation in the particle distribution for different energies is shown in Fig. 2.1 (B). The mean kinetic energy of the plasma species at the equilibrium temperature  $T$  can be calculated as

$$\langle \mathcal{E} \rangle = \frac{1}{n_0} \int_0^\infty f(\mathcal{E}) \mathcal{E} d\mathcal{E} = \frac{3}{2} k_b T \quad (2.7)$$

Equating the above to the kinetic energy term,  $\frac{1}{2} m v^2$ , the RMS speed of a particle of mass  $m$ , inside the plasma, can be obtained as

$$v_{RMS} = \sqrt{\frac{3k_b T}{m}} \quad (2.8)$$

The concept of temperature of a plasma species is valid only if the energy distribution of the species is Maxwellian. There are kinds of plasma where the distribution deviate from Maxwellian behaviour [27]. Inside a plasma, the electrons and ions can have dissimilar Maxwellian distributions with different temperatures,  $T_e$  and  $T_i$  [26]. This is because the collision rate among the same species is higher than between different species. If the plasma is anisotropic due to external fields, then there will also be different values of temperatures, parallel and perpendicular to the fields.

## 2.2 Debye shielding

One of the properties of a plasma is its capability to protect itself from any electric potentials applied to it [24]. When a positive charge is introduced into the plasma, the total energy of

the particles locally around it in the plasma will get modified by the potential generated ( $\phi$ ) by the charge,  $\mathcal{E} \rightarrow \mathcal{E} + q\phi$ . Using equation 2.1, it can be seen that the number of particles gets altered by

$$N \propto \exp\left[-\frac{q\phi}{k_b T}\right] \quad (2.9)$$

In the case of electrons, ( $q = -e$ ), this means that the number of electrons increases near the positive charge. On the other hand, the number of positive ions decreases. The electrons will form a cloud (sheath) near the positive charge, shielding it from the rest of the plasma. The distance over which the positive charge is shielded from the rest of the plasma is an important parameter that defines one of the basic properties of the plasma. This shielding length is called the *Debye length* of the plasma [22, 24].

For deriving a mathematical expression for the Debye length, let us consider a perturbation in the energy levels of the particles by a potential,  $\phi = \phi(0)$ , at location  $r = 0$ .  $r$  represents the radial coordinate and the potential created along  $r$  is represented by  $\phi(r)$ . Considering symmetry of the potential distribution and no angular dependence, the *Poisson equation* can be obtained as

$$\nabla^2 \phi = \frac{1}{r^2} \frac{\partial}{\partial r} \left[ r^2 \frac{\partial \phi}{\partial r} \right] = -\frac{\rho}{\epsilon_0} \quad (2.10)$$

where  $\rho$  is the net charge density. Assuming that the positive ions are all having a singly ionised charge state,  $\rho = e(n_i - n_e)$ , where  $n_i$  and  $n_e$  are the densities of positive ions and electrons after  $\phi(0)$  is introduced in the plasma. At locations far away from the potential, such that  $\phi(r) \rightarrow 0$ ,  $n_i = n_e = n_0$ . Using equation 2.9 and since  $\phi(r)$  is not a function of velocities, equations 2.2 and 2.3 gets multiplied by the factor  $\exp(-q\phi/k_b T)$ . Hence the positive ion and electron densities become

$$n_e = n_0 \exp\left[\frac{e\phi}{k_b T_e}\right] ; \quad n_i = n_0 \exp\left[-\frac{e\phi}{k_b T_i}\right] \quad (2.11)$$

For simplification, we assume a condition of thermal equilibrium between ions and electrons,  $T_e = T_i = T$ . Equation 2.11 values can be substituted in equation 2.10 for  $\rho$ . The exponential terms can be expanded using Taylor series in the limit  $e\phi \ll k_b T$ , such that only linear terms in the series is considered.

$$\frac{1}{r^2} \frac{\partial}{\partial r} \left[ r^2 \frac{\partial \phi}{\partial r} \right] = \frac{2n_0 e^2 \phi}{\epsilon_0 k_b T} = \frac{2\phi}{\lambda_D^2} \quad (2.12)$$

where  $\lambda_D = (\epsilon_0 k_b T / e^2 n_0)^{1/2}$ , is defined as the Debye length of the plasma. From the properties of general electrostatic potential of a point charge, it is known that potential varies as

$1/r$ . Hence we can assume a solution for equation 2.12 as  $\phi = F(r)/r$  and obtain

$$\frac{\partial^2 F(r)}{\partial r^2} = \frac{1}{(\lambda_D/\sqrt{2})^2} F(r) \quad (2.13)$$

As evident from the above equation,  $F(r)$  should be an exponential function and decaying, since  $\phi(\infty) = 0$ . Also, considering  $\phi(0) = \phi_0$ , the final solution for the potential can be obtained as

$$\phi(r) = \phi_0 \exp\left[-\frac{\sqrt{2}r}{\lambda_D}\right] \quad (2.14)$$

Hence the applied potential is screened by the plasma by a factor  $\propto \exp(-r/\lambda_D)$  and particles in the region outside a length of  $\sim \lambda_D$  from the potential, are not affected by the potential  $\phi_0$ . The net density of positive charges equals the density of negative charges in this outside region. For regions less than  $\lambda_D$ , an imbalance in the density of charges is present and the plasma cannot be considered as neutral. This is the condition when a surface like a metallic probe is inserted into a plasma. The perturbation can only extend to the order of Debye lengths from the probe surface and beyond that the plasma is electrically neutral. This property is known as the ‘quasineutrality’ of plasma. For a typical laboratory plasma with  $T = 1 \text{ eV}$  and  $n_0 = 10^{16} \text{ m}^{-3}$ ,  $\lambda_D = 0.1 \text{ mm}$ . It should be noted that Debye length is  $\propto 1/n_0$ . For interstellar plasma,  $\lambda_D$  is several metres long [22].

## 2.3 Plasma frequency

Any local deviation from charge neutrality due to the separation of charges inside the plasma, leads to the generation of an electric field. The charges inside the plasma experience a restoring force due to this electric field. Since the ions are much heavier than electrons, they can be considered stationary with respect to the faster electrons. The generated one-dimensional electric field, for a charge separation of  $x$  distance and electron density  $n_e$ , can be estimated using Gauss’ law [22].

$$F_x = -eE_x = -\frac{e^2 n_e}{\epsilon_0} x \quad (2.15)$$

As seen here, the force is proportional to displacement  $x$ . Using Newton’s second law and the above equation, we can derive,

$$\frac{d^2 x}{dt^2} + \left[ \frac{n_e e^2}{m_e \epsilon_0} \right] x = 0 \quad (2.16)$$

The equation is of the form of a harmonic oscillator and describes the oscillation of electrons around the local deviation. The angular frequency of this oscillation is represented by  $\omega_{pe}$  and is called the *electron plasma frequency* (or simply as *plasma frequency*) [22, 24]

$$\omega_{pe} = \sqrt{\frac{n_e e^2}{m_e \epsilon_0}} \quad (2.17)$$

The frequency ( $\nu_{pe} = \omega_{pe}/2\pi$ ) corresponding to the above equation, for a plasma with  $n_e = 10^{16} \text{ m}^{-3}$  is about 1 GHz and is in the microwave band.

## 2.4 Plasma boundary

When a plasma is first ignited, there occurs a flow of charges to the plasma chamber walls [22]. Since electrons are highly mobile, they escape from the plasma faster than the ions, resulting in a net negative charge at the chamber walls relative to the plasma. This forms an electric potential barrier to the further flow of electrons from the plasma, but accelerates the movement of positive ions to the walls. In the course of time, an equilibrium potential drop will be formed between the bulk plasma and walls, which equalizes the flux of ions and electrons to the walls. This leads to the formation of a sheath, the *plasma sheath*, around the plasma boundary, which shields the bulk plasma from the wall potential. The extension of this shielding is comparable to the Debye length derived in equation 2.12 [22].

### 2.4.1 The Bohm criterion

Let us now examine the variation in potential and charge particle densities in the plasma boundary region by considering a non-magnetized plasma. This plasma is enclosed in a chamber having absorbing walls where no particles are reflected back to the plasma. A representation of such a situation is shown in Fig. 2.2. For simplicity, let all the positive ions be singly ionised with mass  $m_i$  and reach the plasma sheath from the bulk plasma at the same initial velocity  $v_0$ . Only one-dimensional motion is considered here. These ions enter the plasma sheath and start experiencing the potential  $\phi(x)$  and the velocity changes to  $v(x) = v_x$ . The total energy of ions at the beginning of the plasma sheath is purely kinetic. Then from conservation of energy,

$$\frac{1}{2} m_i v_0^2 = \frac{1}{2} m_i v_x^2 + e\phi(x) \quad (2.18)$$

where  $\phi(x) < 0$  for negative wall potential. Due to the net negative charge at the wall, we can assume that the number of electrons having enough energy to overcome the potential



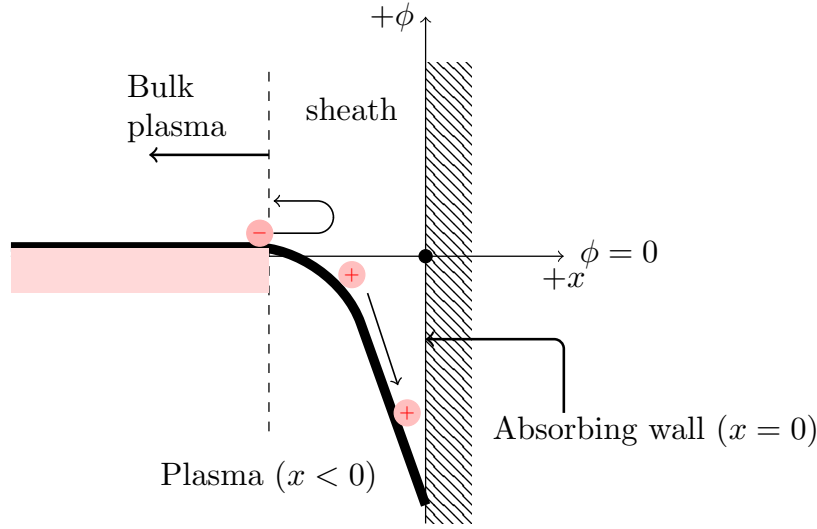


**Figure 2.2:** A representation of the variation in potential at the plasma boundary. The chamber wall is located at  $x = 0$ . The electrons from the bulk plasma experiences a potential barrier towards the wall under equilibrium conditions.

hill in the sheath is very less [26]. Hence, the density of electrons inside the sheath can be found from the same conditions as equation 2.11.

$$n_e = n_0 \exp \left[ \frac{e\phi}{k_b T_e} \right] \quad (2.19)$$

The equation is the Boltzmann relation for electrons. Note that the density of electrons is exponentially decreasing in this case, since the electric potential has negative values here. In the case of positive ions, they are accelerated and depleted at the walls. Hence the ion density needs to be determined from other means. We can consider that the positive ion mean free path is higher than the length of the sheath, such that it does not make any collisions on its way across the sheath. Then, from the equation of continuity, we can derive the following

$$n_0 v_0 = n_i(x) v_x \quad (2.20)$$

where  $n_i(x)$  is the density of ions inside the plasma sheath. Using equations 2.18 and 2.20, an expression for the ion density inside the sheath can be derived as

$$n_i = n_0 \left[ 1 - \frac{2e\phi}{m_i v_0^2} \right]^{-1/2} \quad (2.21)$$

By substituting this value and equation 2.19 in the Poisson equation, we can derive

$$\frac{d^2 \phi}{dx^2} = \frac{en_0}{\epsilon_0} \left[ \exp \left( \frac{e\phi}{k_b T_e} \right) - \left( 1 - \frac{2e\phi}{m_i v_0^2} \right)^{-1/2} \right] \quad (2.22)$$

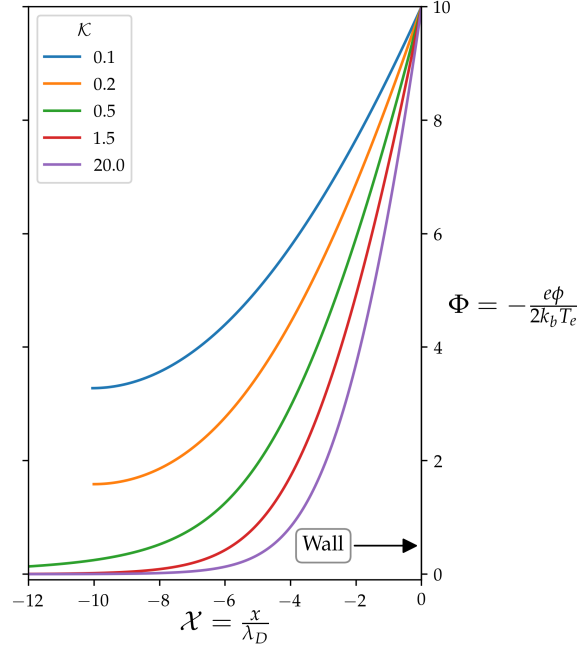


**Figure 2.3:** Variation in the normalised plasma sheath potential for different normalised ion energy values and normalised distances from the wall. The curves are the numerical solutions to equation 2.23 [28].

Following the conventions in [28], the behaviour can be better understood by defining the normalised dimensionless quantities,

$$\Phi = -\frac{e\phi}{k_b T_e}; \mathcal{K} = \frac{m_i v_0^2}{2k_b T_e}; \mathcal{X} = \frac{x}{\lambda_D}$$

where  $\Phi$  is related to the potential,  $\mathcal{K}$  is related to the ion energy and  $\mathcal{X}$  is related to the distance from the wall. Equation 2.22 can be converted into first order by multiplying both sides by  $d\Phi/d\mathcal{X}$  and then integrating with respect to  $\mathcal{X}$ . The value of constant of integration can be determined by the condition,  $\mathcal{X} \rightarrow -\infty$ ,  $\Phi$  and  $d\Phi/d\mathcal{X} \rightarrow 0$ . The equation 2.22 changes to

$$\left[\frac{d\Phi}{d\mathcal{X}}\right]^2 = 4\mathcal{K} \left[\left(1 + \frac{\Phi}{\mathcal{K}}\right)^{1/2} - 1\right] + 2(e^{-\Phi} - 1) \quad (2.23)$$

This is a non-linear equation and can be solved numerically. The solutions are shown in Fig. 2.3, for an arbitrary value of  $\Phi(0) = 10$ . As seen from the plot, the sheath successfully shields the bulk plasma from the negative wall potential for values of  $\mathcal{K} \geq 0.5$ . For values  $\mathcal{K} < 0.5$ , the sheath ceases to exist beyond a certain location, as there are no real solutions. This limit can also be derived by expanding the right side of the equation in terms of  $\Phi$  using series expansions by assuming  $|e\phi| \ll |k_b T_e|$ . Equation 2.23 becomes

$$\left[\frac{d\Phi}{d\mathcal{X}}\right]^2 = \Phi^2 \left[1 - \frac{1}{2\mathcal{K}}\right] + \mathcal{O}(\Phi^3) \approx \Phi^2 \left[1 - \frac{1}{2\mathcal{K}}\right] \quad (2.24)$$

From the above equation also, it can be seen that for  $\mathcal{K} < 0.5$ , there are no real solutions. This leads to the condition that, for a sheath to exist at the plasma boundary,

$$\mathcal{K} \geq \frac{1}{2} \implies m_i v_0^2 \geq k_b T_e \quad (2.25)$$

and is called the *Bohm-criterion* [22, 28]. We can also define a minimum velocity for positive ions corresponding to this limit,

$$v_0 \geq v_B = \sqrt{\frac{k_b T_e}{m_i}} \quad (2.26)$$

where  $v_B$  is defined as the *Bohm velocity*. The reason for this lower limit of ion energy can be understood from Fig. 2.4, where the variation in the density of ions and electrons from the arbitrary sheath edge to the plasma wall is shown. The densities are estimated using equations 2.19 and 2.21 and the dimensionless factors. It can be seen that both ion and electron densities deplete towards the wall. But for low ion energies such that  $\mathcal{K} < 0.5$ , the rate of fall of the density of ions is higher than the electrons in regions close to the bulk plasma. Hence a positive space charge cannot be set up to shield the negative wall potential.

As seen in equation 2.26, the Bohm velocity depends on the electron temperature  $T_e$  and  $T_e \gg T_i$  in the general plasma conditions [28]. If the ions had only the energy from the thermal equilibrium ( $\approx k_b T_i$ ), then none of the ions could attain the Bohm velocity. Hence there should be an additional electric field prior to the plasma sheath edge that enables the positive ions to achieve the minimum velocity for sheath formation,  $v_B$ . Defining this potential difference as  $\phi_p$ , the value can be found from the Bohm velocity condition,

$$\frac{1}{2} m_i v_B^2 = e \phi_p \implies \phi_p = \frac{k_b T_e}{2e}, \quad \Phi = 0.5 \quad (2.27)$$

The region where this potential drop exists, prior to the plasma sheath, is termed as *presheath*. The boundary between the presheath and sheath is not well defined [29]. We can find the variation in potential in the presheath region. The extension of the presheath into the plasma is assumed to be of the length scale  $L$ , where  $L \gg \lambda_D = \xi L$  [28]. By using this relation and defining normalized length in the presheath scale,  $\mathcal{X}' = x/L$ , the Poisson equation in the presheath region can be derived as

$$\xi^2 \frac{d^2 \Phi}{d\mathcal{X}'^2} = \frac{1}{n_0} (n_i - n_e) \quad (2.28)$$

A very simple picture of the expansion  $L$ , can be obtained using the above equation by considering a small finite value for  $\xi$ . The same ion and electron density relations obtained from equations 2.19 and 2.21 can be assumed. Since the value of potentials in the presheath

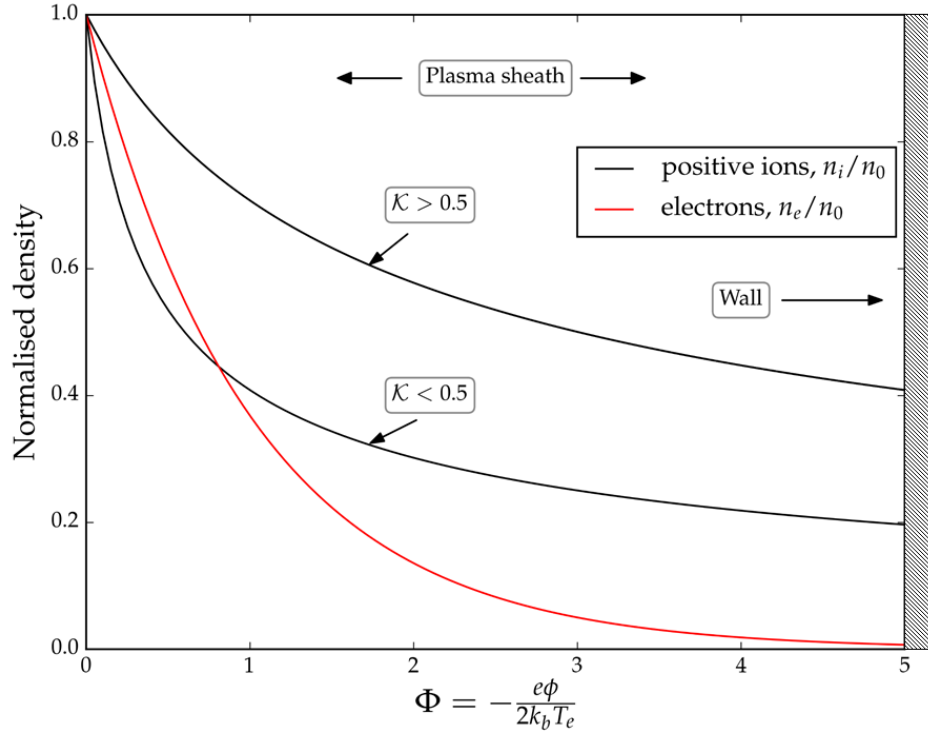


**Figure 2.4:** Normalised ion and electron densities in the plasma sheath [24].  $\Phi = 0$  represents the bulk plasma. The positive ion density falls faster than the electron density for  $\mathcal{K} < 0.5$ , in the regions close to the bulk plasma.

is expected to be equal to bulk plasma potentials ( $\approx 0$ ), the terms can be expanded in first order terms alone and we can derive [28]

$$\xi^2 \frac{d^2 \Phi}{d\mathcal{X}'^2} = \left[1 - \frac{1}{2\mathcal{K}}\right] \Phi \quad (2.29)$$

An analytical solution for  $\Phi$  in the presheath region can be obtained for the above differential equation as [30]

$$\Phi = C e^{-\mathcal{X}'/h}, \text{ where } h = \xi \left(1 - \frac{1}{2\mathcal{K}}\right)^{-1/2} \quad (2.30)$$

where  $C$  is a constant. This gives the variation in the potential in the pre sheath and it can be seen as exponentially decreasing in a length scale of the order of  $\lambda_D (1 - 1/2\mathcal{K})^{-1/2}$  which is larger than  $\lambda_D$ , for  $\mathcal{K} > 0.5$ . On the other hand, the potential varies in a length scale of  $\lambda_D$  in the sheath as in equation 2.14. Thus the change in potential across the presheath is slower than that in the sheath. This is illustrated in Fig. 2.5. Approximate location of the sheath and presheath regions, assuming Bohm velocity for ions ( $\Phi = 0.5$ ), is also shown in the figure.

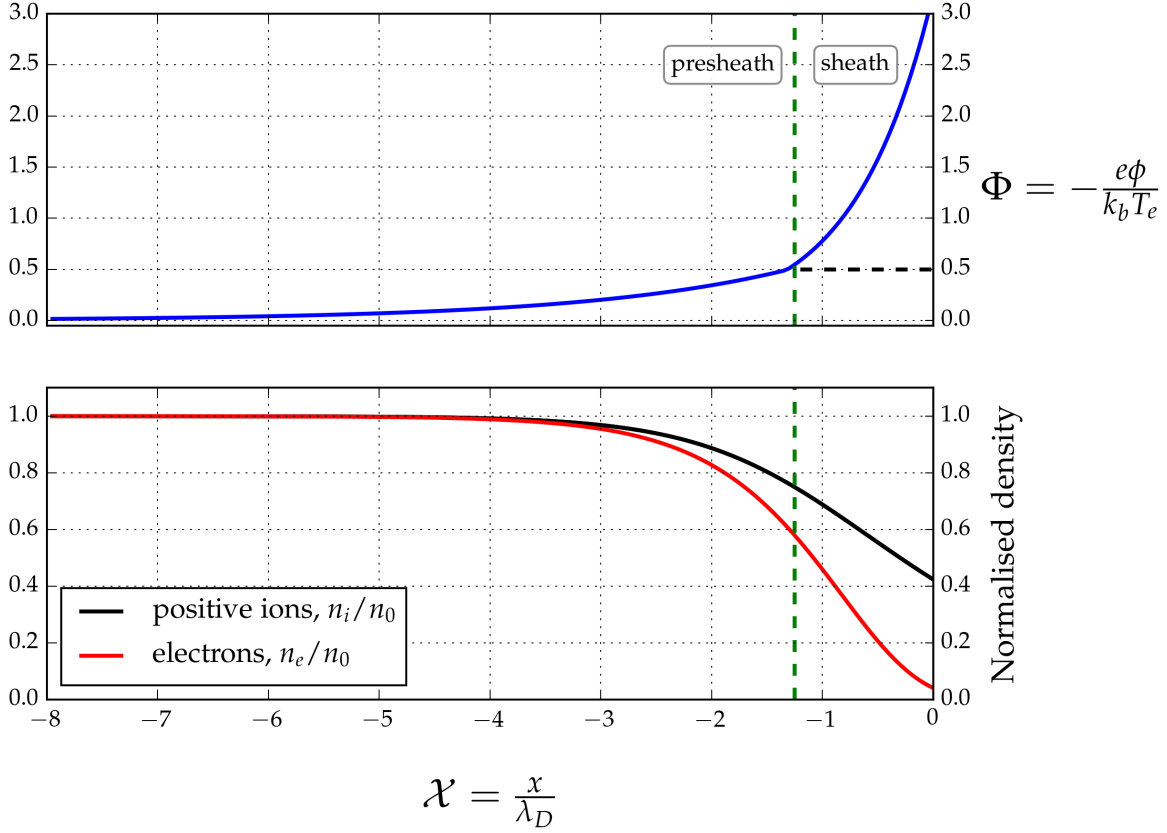


**Figure 2.5:** A representation of the expected variation in the normalized potential (top) and ion-electron densities (bottom) inside a proton-electron plasma. The wall is at  $\mathcal{X} = 0$ . The dashed green lines show the location where  $\Phi = 0.5$  (or  $\phi = -k_b T_e / 2e$ ), which corresponds to the potential drop between pre sheath and bulk plasma, when ion velocity is equal to Bohm velocity (Eq 2.27). The locations and general behaviour are only approximate.

### 2.4.2 Floating wall potential

Under equilibrium conditions, the negative potential developed at the walls ( $\phi_w$ ) will be in such a way that the net particle flux to the walls is zero [22]. It is possible to estimate this *floating potential* at the plasma walls. The flux of positive ions entering the plasma sheath, with Bohm velocity, can be obtained by

$$\Gamma_i = n_0 v_B \quad (2.31)$$

Since the ion mean free path is higher than the plasma sheath length, the flux is assumed to remain constant inside the sheath. An expression for electron flux to the wall, in one-dimension, can be derived from the distribution functions in equation 2.2. The distribution along the velocity direction  $v_x$  can be obtained by integrating the equation along the other

two directions,  $v_y, v_z$ . Then for energy,  $\mathcal{E} \rightarrow \mathcal{E} + (-e)(\phi_w)$ , distribution becomes

$$f(v_x) = n_0 \left[ \frac{m}{2\pi k_b T} \right]^{1/2} \exp \left[ - \frac{mv_x^2 - e\phi_w}{2k_b T} \right] \quad (2.32)$$

The electron flux along the  $x$ -direction can now be determined from the distribution function,

$$\Gamma_e = n_e \langle v_x \rangle = \int_0^\infty dv_x v_x f(v_x) = \frac{1}{4} n_0 \exp \left[ \frac{e\phi_w}{k_b T} \right] \left[ \frac{8k_b T_e}{m_e} \right]^{1/2} \quad (2.33)$$

Equating the ion and electron flux, the floating wall potential can be obtained as

$$\phi_w = - \frac{k_b T_e}{e} \ln \left[ \frac{m_i}{2\pi m_e} \right]^{1/2} \quad (2.34)$$

For an electron-proton plasma, the value of the floating wall potential will be  $\approx -3k_b T_e/e$  or  $\Phi = 3$ . A general representation of the variation of potentials and ion-electron densities in such a plasma, from the bulk plasma to the wall, was shown in Fig. 2.5. Since in most of the ion sources, the plasma chamber walls are usually at ground potential, the above situation can be considered as plasma acquiring a positive potential ( $\phi_w$ ) with respect to the walls.

## 2.5 Collisions in a plasma

Some of the properties observed in a plasma, for example the particle diffusion, can be explained mathematically only by considering collisions inside the plasma. Collisions can be broadly divided into *elastic* and *inelastic* [26]. Elastic collisions are those which conserve the kinetic energy and the colliding particles do not lose their identity. Inelastic collisions are those in which the kinetic energy is not conserved. The colliding particles might lose their identity and particles can be created or destroyed. These collisions lead to removal of electrons from neutral atoms leading to *ionisation*, change in internal energy state leading to *excitation* etc. Other kinds of inelastic collisions involve reactions in which the charged particles *recombine* to form neutrals or *attach* with other neutral particles.

Collisions can be between charged particles (Coulomb forces) or between charged particles and neutral atoms or molecules. The *fractional ionisation* parameter, which is the ratio of ion density to total density of ions and neutral particles,  $n_i/(n_i + n_n)$ , can be used to specify the percentage of ions in a plasma [10]. When the fractional ionisation is low, the collisions between charged particles and neutrals dominate and the plasma is said to be *weakly ionised*. On the other hand, when the fractional ionisation is high the interactions between the charged particles dominate. In such a case, the plasma can be considered as *fully ionised* [10, 22].

### 2.5.1 Weakly ionised plasma

Ionospheric plasma and low current discharge plasma are some examples of a weakly ionised plasma. The collisions inside a weakly ionised plasma can be explained by binary collisions. Electrons are the dominating species and hence electron-neutral collisions are important. An expression for the average collision frequency,  $\nu_{en}$ , can be obtained as [24].

$$\langle \nu_{en} \rangle = \langle \tau_{en}^{-1} \rangle = n_n \langle \sigma_{en} v_e \rangle \quad (2.35)$$

where  $\tau_{en} = \lambda_m / v_e$  is the collision time,  $n_n$  is the neutral particle density,  $\sigma_{en}$  is the cross section area for collisions,  $v_e$  is the electron velocity.  $\lambda_m$  is the mean free path between collisions and is obtained as  $\lambda_m = 1 / \sigma_{en} v_e$ . The value obtained in the above equation is an average over all values of  $v_e$  in the Maxwellian distribution. The mass of electrons is lower and hence its average thermal speed is higher compared to ions. Hence, assuming similar cross sections and temperatures, it is evident from the above equation that the electron-neutral collision frequency is higher than the ion-neutral collision frequency [22].

### 2.5.2 Fully ionised plasma

In the case of fully ionised plasma, the Coulomb interactions between charged particles are dominant. In contrast to the collisions in weakly ionised plasma, these interactions can happen over long distances, where one particle interacts with several other particles at the same time. The average electron-ion collision frequency over a Maxwellian distribution is estimated as [24, 26]

$$\langle \nu_{ei} \rangle = \frac{\sqrt{2} n_i Z^2 e^4 \ln \Lambda}{12 \pi^{3/2} \epsilon_0^2 m_e^{1/2} (k_b T_e)^{3/2}} \quad (2.36)$$

where  $Z$  represents the multiplicity of ionisation,  $\ln \Lambda$  factor represents the cumulative effects of small angle collisions and  $\Lambda$  is the ratio between the maximum and minimum interaction distance for the electron-ion collision. Since the Coulomb interactions are screened out outside the Debye length,  $\lambda_D$ ,

$$\Lambda = \frac{\lambda_D}{r_0} \quad (2.37)$$

where  $r_0$  is the impact parameter or distance of closest approach in the absence of Coulomb forces. From the equation for  $\langle \nu_{ei} \rangle$  it can be seen that electrons with lower velocities suffer more collisions than those with higher velocities. The electron-electron and ion-ion particle collisions are obtained as [22, 26]

$$\langle \nu_{ee} \rangle = \frac{\nu_{ei}}{n_i Z^2 / n_e} \quad (2.38)$$

$$\langle \nu_{ii} \rangle = \frac{\sqrt{2} n_i Z^4 e^4 \ln \Lambda}{12 \pi^{3/2} \epsilon_0^2 M^{1/2} (k_b T_i)^{3/2}} \quad (2.39)$$

where  $M$  is the reduced mass  $m_1 m_2 / (m_1 + m_2)$  for ions, with mass  $m_1$  and  $m_2$ .

The value of the various collision frequencies discussed above varies in a wide range depending on the plasma. These can be roughly estimated for a hydrogen plasma. Let the neutral particle density be  $n_n = 10^{20} \text{ m}^{-3}$  with 1% ionisation such that  $n_i = n_e = 10^{18} \text{ m}^{-3}$ . For simplicity, we assume  $T_i = T_e = 2 \text{ eV}$ . Then  $\langle \nu_{ei} \rangle = \langle \nu_{ee} \rangle \approx 17 \text{ MHz}$ ,  $\langle \nu_{ii} \rangle \approx 400 \text{ KHz}$ . Assuming the elastic scattering cross section corresponding to the radius of a hydrogen atom, ( $\sigma \approx 10^{-20} \text{ m}^{-3}$ ) and using eq 2.35,  $\langle \nu_{en} \rangle \approx 1 \text{ MHz}$ . This shows that even 1% ionisation is sufficient enough for the Coulomb interactions to be dominant over the charged particle-neutral interactions. On the other hand, all these collisions are found to be extremely slow compared to the plasma oscillation frequency (eq 2.17) which is of the order of GHz. This is the reason why plasmas are sometimes considered to be ‘collisionless’ [30].

## 2.6 Effect of external fields in plasma

External magnetic fields are applied to plasma for modifying the motion of particles inside the plasma. This can yield results ranging from plasma confinement to filtering the high energy electrons inside a region in plasma. The explanations in this section is based mainly on [22, 24].

### 2.6.1 Uniform magnetic field

The equation of motion for a plasma species of charge  $q$ , velocity  $\vec{v}$  and mass  $m$ , in the presence of an external magnetic field  $\vec{B}$  is given by

$$m \frac{d\vec{v}}{dt} = q(\vec{v} \times \vec{B}) \quad (2.40)$$

For simplicity, we assume that the magnetic field is in the  $z$ -direction,  $\vec{B} = B_z \hat{z}$ . In cartesian coordinates this becomes,

$$\frac{d\vec{v}}{dt} = \pm \frac{|q| B_z}{m} (v_y \hat{x} - v_x \hat{y}) \quad (2.41)$$

The  $\pm$  sign depends on the charge of the particle under consideration. Sign located on the top is used for a positive charge and the sign at the bottom is for a negative charge (for example, consider equation 2.45). Second derivatives of the  $x, y$  components in the above



equation leads to differential equation of a harmonic oscillator. Solutions for the velocity components in different directions can then be obtained as

$$v_x(t) = v_{\perp} \sin(\omega_c t + \theta_0); v_y(t) = \pm v_{\perp} \cos(\omega_c t + \theta_0); v_z(t) = v_{zi} \quad (2.42)$$

, where  $v_{\perp} = \sqrt{v_{xi}^2 + v_{yi}^2}$ , is the speed of particle in the plane perpendicular to  $\vec{B}$ . Here  $v_{xi}, v_{yi}, v_{zi}$  represent the initial velocities in the three directions. The equations represent oscillations of angular frequency, the *cyclotron frequency* or *gyro frequency*,

$$\omega_c = \frac{|q|B}{m} \quad (2.43)$$

Integration of equations 2.42 with respect to time, gives the location of the particle at different times.

$$x(t) - X_0 = -\frac{v_{\perp}}{\omega_c} \cos(\omega_c t + \theta_0); y(t) - Y_0 = \pm \frac{v_{\perp}}{\omega_c} \sin(\omega_c t + \theta_0); z - z_0 = v_{zi}t \quad (2.44)$$

$$\text{, where } X_0 = x_0 + \frac{v_{\perp}}{\omega_c} \cos \theta_0; Y_0 = y_0 \mp \frac{v_{\perp}}{\omega_c} \sin \theta_0 \quad (2.45)$$

The initial location of the particle is given by  $\vec{r} = x_0\hat{x} + y_0\hat{y} + z_0\hat{z}$ . The trajectory of the particle in the  $x - y$  plane can be identified from rearranging the equation as  $[x(t) - X_0]^2 + [y(t) - Y_0]^2 = (v_{\perp}/\omega_c)^2$ , which represents *circular motion* about a *guiding centre*,  $(X_0, Y_0)$ . This also leads to the characteristic radius in the plane of circular motion, the *Larmor radius* or *gyro radius*,

$$r_L = \frac{v_{\perp}}{\omega_c} = \frac{v_{\perp}m}{|q|B} \approx \frac{\sqrt{mk_bT}}{|q|B} \quad (2.46)$$

The phase of the circular motion about the guiding centre can be found as

$$\phi(t) = \tan^{-1} \left[ \frac{y(t) - Y_0}{x(t) - X_0} \right] = \mp(\omega_c t + \theta_0) \quad (2.47)$$

This represents a decreasing value for a positively charged particle and an increasing value for a negatively charged particle. This suggests a clockwise (anti-clockwise) circular motion for a positive (negative) charge when the magnetic field is pointing towards the observer.

The net motion will be a combination of circular motion in the  $x - y$  plane and an undisturbed motion in the  $\hat{z}$ -direction, leading to a helical trajectory in 3D space as shown in Fig. 2.6(A). In this case, the location of the guiding centre remains constant in the plane perpendicular to the magnetic field and moves with the undisturbed velocity in the magnetic field direction. The guiding centre velocity is given by

$$\vec{v}_{gc} = v_z\hat{z} = v_{\parallel}\hat{z} \quad (2.48)$$

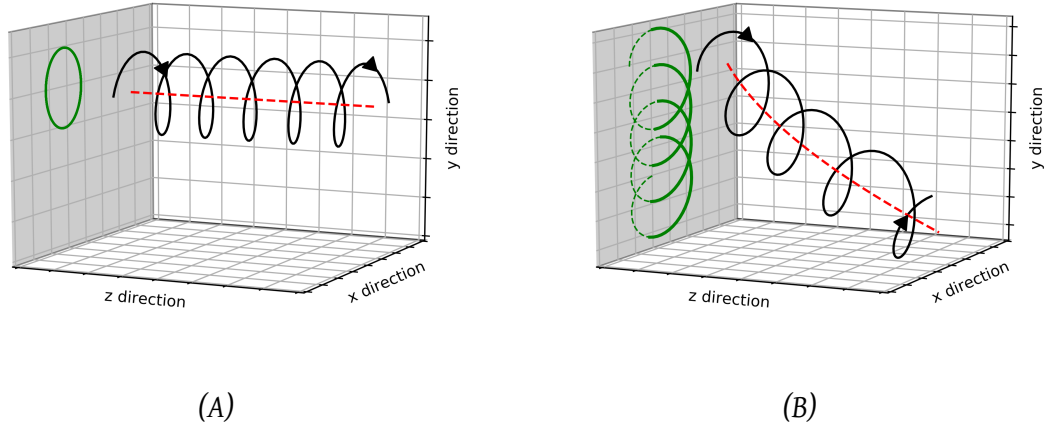


**Figure 2.6:** Path of a positively charged particle in the presence of (A) a uniform magnetic field  $\vec{B}$  in the  $z$ -direction (left to right) and (B) a combination of uniform magnetic field and uniform electric field  $\vec{E} = E_x \hat{x} + E_z \hat{z}$ . The red path represents the motion of the guiding centre. The projection of motion in the  $x - y$  plane is shown by green lines.

For a plasma temperature of 1 eV and external magnetic field of 1 T, the different parameters discussed in the above sections can be calculated as below.

Species	Velocity ( $v_{\perp}$ )	Frequency ( $\omega_c/2\pi$ )	Larmor radius ( $r_L$ )
Proton	$1.5 \times 10^4$ m/sec	15.9 MHz	0.15 mm
Electron	$6.7 \times 10^5$ m/sec	28.6 GHz	$3.8 \mu\text{m}$

**Table 2.1:** Plasma species in magnetic field.

The cyclotron motion enables the coupling of external electromagnetic power into a plasma. As shown in Table 2.1, the electron cyclotron frequency lies in the GHz range. An external microwave power coupled at this frequency helps in creating highly energetic plasmas called ECR plasma [10], when gas pressure is low enough. This also forms the basis of ECR ion sources.

### 2.6.2 Uniform magnetic and electric field

The motion of the particles get altered when a finite electric field,  $\vec{E}$ , is added to the previous situation. In that case, equation 2.40 changes to

$$m \frac{d\vec{v}}{dt} = q(\vec{E} + (\vec{v} \times \vec{B})) \quad (2.49)$$

The velocities in different directions can be derived similar to section 2.6.1.

$$v_x(t) = v'_\perp \sin(\omega_c t + \theta_0) + \frac{E_y}{B_z}; v_y(t) = \pm v'_\perp \cos(\omega_c t + \theta_0) - \frac{E_x}{B_z}; v_z(t) = v_{zi} + \frac{qE_z t}{m} \quad (2.50)$$

where  $v'_\perp$  and  $\theta_0$  are integration constants. Integrating the above equations with respect to time gives the location of the particle

$$x(t) - X_0 = -\frac{v'_\perp}{\omega_c} \cos(\omega_c t + \theta_0); y(t) - Y_0 = \pm \frac{v'_\perp}{\omega_c} \sin(\omega_c t + \theta_0); z - z_0 = v_{zi} t + \frac{qE_z t^2}{2m} \quad (2.51)$$

$$\text{,where } X_0 = x_0 + \frac{v'_\perp}{\omega_c} \cos \theta_0 + \frac{E_y}{B_z} t; Y_0 = y_0 - \frac{v'_\perp}{\omega_c} \sin \theta_0 - \frac{E_x}{B_z} t \quad (2.52)$$

It is evident from the above equations that the guiding centre coordinates in the plane of rotation are no longer constants. The velocity of the guiding centre can be obtained as

$$\vec{v}_{gc} = \frac{E_y}{B} \hat{x} - \frac{E_x}{B} \hat{y} + \left[ v_{zi} + \frac{qE_z t}{m} \right] \hat{z} \quad (2.53)$$

$$\implies \vec{v}_{gc} = \frac{\vec{E} \times \vec{B}}{B^2} + v_\parallel \hat{z} = \vec{v}_E + v_\parallel \hat{z} \quad (2.54)$$

$\vec{v}_E$ , which is independent of the charge, mass and velocity of the plasma particle, is called the ' $\vec{E} \times \vec{B}$  drift' and represents the drift of the entire plasma in electromagnetic fields [22, 24]. This happens in a direction perpendicular to both electric and magnetic fields. The motion is represented in Fig. 2.6(B). The  $E_x$  ( $E_y$ ) component of the field causes drift in the  $-\hat{y}$  ( $\hat{x}$ )-direction. Variation in the pitch of the helix is due to the  $E_z$  component. A physical understanding of the drift can be seen from the  $x - y$  projection of motion in the figure. The radius between alternate half cycles (thick and broken green lines in the figure) are different due to gain and loss of energy due to electric field in  $x$ -direction (into the page). This difference in radius causes the drift  $\vec{v}_E$

The drift discussed here is not restricted only to electric fields acting along with magnetic fields. Such drifts can occur for any *general force*,  $\vec{F}$ , when applied in combination with a magnetic field,  $\vec{B}$  and leads to a drift, evaluated similar to the  $\vec{E} \times \vec{B}$  drift,

$$\vec{v}_F = \frac{1}{q} \frac{\vec{F} \times \vec{B}}{B^2} \quad (2.55)$$

### 2.6.3 Non uniform magnetic fields, $\vec{\nabla} B$

The analysis of motion of charged particles in the presence of non uniform fields is generally simplified using the small Larmor radius approximation. As seen from table 2.1, the value

of the gyroradius is very small compared to the usual plasma chamber dimensions or inhomogeneity of magnetic fields ( $\approx L$  cm). This smallness can be represented as  $r_L/L \ll 1$  [22]. In other words the particles see an approximately constant magnetic field during the gyro motion. This assumption will help in representing the local magnetic field, at a location in plasma ( $\vec{r}$ ), in a Taylor series expansion of first order, about the guiding centre [30]. The magnetic field, at a momentary location represented by  $\vec{r}$ , in a *guiding centre coordinate system* can be obtained as

$$\vec{B}(\vec{r}) = \vec{B}_0 + \vec{r} \cdot (\vec{\nabla} \vec{B}) \quad (2.56)$$

$\vec{B}_0 \equiv B_0 \hat{z}$  is the magnetic field at the guiding centre and the *tensor*,  $\vec{\nabla} \vec{B}$ , is evaluated at the guiding centre. The terms inside the tensor represent different types of magnetic field structures (diverging /converging, gradient, curvature and shear or twisted field lines) [22]. Substituting the above equation in 2.40, we obtain

$$m \frac{d\vec{v}}{dt} = q(\vec{v} \times \vec{B}_0) + q(\vec{v} \times \vec{r} \cdot \vec{\nabla} \vec{B}) = q(\vec{v} \times \vec{B}_0) + \vec{F} \quad (2.57)$$

where  $\vec{F}$  represents the additional force due to non-uniformity of the magnetic field. A local cylindrical coordinate system can be considered with  $\hat{z}$  in  $\vec{B}_0$  direction at origin. Then, the additional force becomes [22],

$$\vec{F} = q \left( \vec{v} \times r \frac{\partial \vec{B}}{\partial r} \right) \quad (2.58)$$

In the local coordinate system,  $\vec{B} = B_r \hat{r} + B_\theta \hat{\theta} + B_z \hat{z}$ . We assume that the change in velocity in this case, compared to the uniform magnetic field, is very small and  $\vec{v}$  in the above equation is approximately equal to that found in equation 2.42. In cylindrical coordinates,  $\vec{v} = v_\theta \hat{\theta} = \mp v_\perp \hat{\theta}$  where the sign is as mentioned in equation 2.47.  $B_\theta \hat{\theta}$  is parallel to  $\vec{v}$  and therefore does not contribute to the force. The  $\hat{z}$  term contributes to the parallel component ( $\vec{F}_\parallel$ ) and  $\hat{r}$  term contributes to the perpendicular component ( $\vec{F}_\perp$ ) of the force.

$$\vec{F}_\perp = q \left( \vec{v} \times \hat{z} r \frac{\partial B_z}{\partial r} \right) = \mp q v_\perp r_L \frac{\partial B_z}{\partial r} \hat{r} \quad (2.59)$$

$$\vec{F}_\parallel = q \left( \vec{v} \times \hat{r} r \right) = \pm q v_\perp r_L \frac{\partial B_r}{\partial r} \hat{z} \quad (2.60)$$

$r_L$  is the cyclotron radius corresponding to  $\vec{B}_0$ , such that  $r_L = |q|m/B_0$ . An average value of these forces can be found out by averaging over one gyromotion [22]. The average value of the perpendicular force can be derived as

$$\langle \vec{F}_\perp \rangle = \mp q v_\perp r_L \left[ \frac{1}{2\pi} \oint \frac{\partial B_z}{\partial r} \hat{r} d\theta \right] = \mp \frac{1}{2} q v_\perp r_L (\vec{\nabla} B)_\perp \quad (2.61)$$

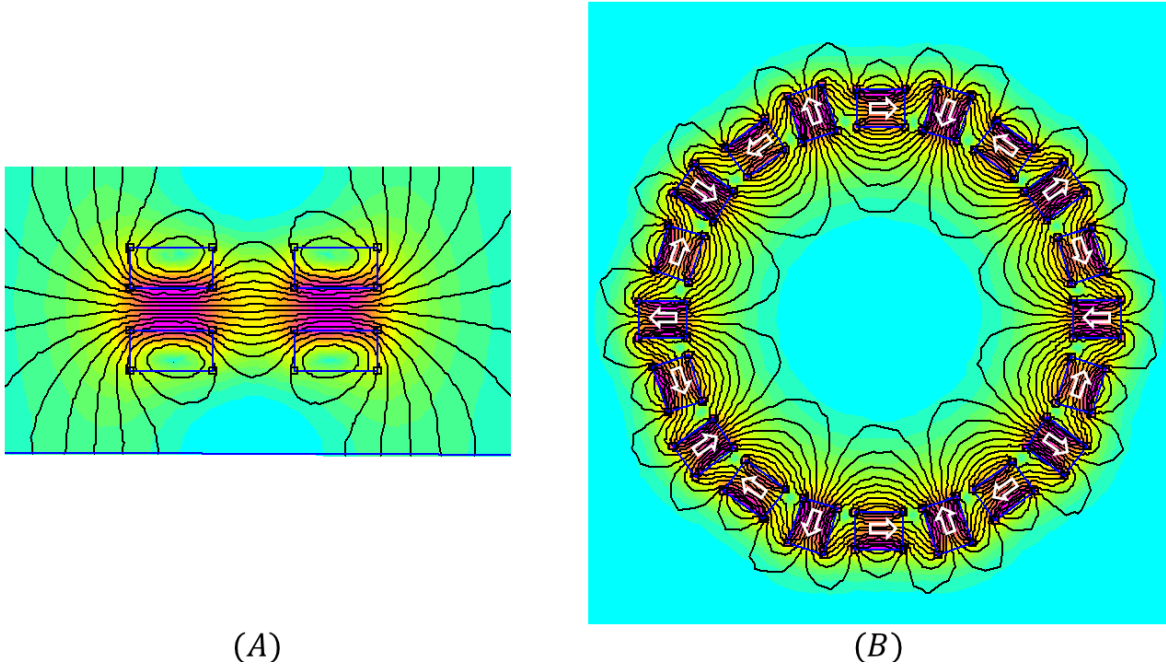


**Figure 2.7:** (A) Magnetic field generated by two solenoidal coils to form a trap for charged particles utilizing the magnetic mirror effect. The location of the cross section of the coils are represented by the rectangular boxes. (B) Multicusp magnetic field generated by permanent magnets around a plasma chamber. Arrows represent the direction of north pole of the magnet. The results are generated using FEMM magnetic simulations [31, 32].

As seen from 2.55, such a force can lead to particle drifts perpendicular to the gradient of magnetic fields and the drift velocity of the guiding centre can be estimated as

$$\vec{v}_{\nabla B} = \pm \frac{1}{2} v_{\perp} r_L \frac{\vec{B} \times \vec{\nabla} B}{B^2} \quad (2.62)$$

Unlike the  $\vec{E} \times \vec{B}$  drift, the above drift depends on the sign of the charge and leads to separation of electrons and positive ions leading to electric current flow. On the other hand, the average value of the parallel force can be similarly estimated as

$$\langle \vec{F}_{\parallel} \rangle = -\frac{mv_{\perp}^2}{2B} (\vec{\nabla} B)_{\parallel} \quad (2.63)$$

As seen from the above equation, when there is a variation in the magnetic field (converging/diverging) along a direction parallel to the magnetic field, all charged plasma particles experience a force. Also, this force is directed towards the decreasing magnetic field. Such a force can be used for directing the plasma particles away from a converging magnetic field, as discussed in the next section.

### 2.6.4 Magnetic mirror effect

The equation of the parallel force derived above can be written in terms of the magnitude of the magnetic moment of a gyrating particle [22],  $\mu = IA = mv_{\perp}^2/2B$

$$\langle \vec{F}_{\parallel} \rangle = -\mu(\vec{\nabla}B)_{\parallel} \quad (2.64)$$

When the variation in the magnetic field experienced by a particle propagating in a path is low compared to  $\vec{B}$ , then the magnetic moment can be considered an invariant, the first adiabatic invariant [22, 24]. Since  $\mu \propto v_{\perp}^2/B$ , this means that the transverse velocity should be increasing when the particle is moving towards higher magnetic field values. This leads to an increase in the transverse kinetic energy,  $(1/2)mv_{\perp}^2$ . In a magnetostatic plasma, the total kinetic energy ( $E_K$ ) of a charged particle will be a conserved quantity,

$$E_K = \frac{1}{2}mv_{\perp}^2 + \frac{1}{2}mv_{\parallel}^2 \quad (2.65)$$

and hence the  $v_{\parallel}$  component should decrease to maintain the total kinetic energy. By further increasing the  $B$  value, it can reach a situation that  $v_{\parallel}$  becomes zero and then be reversed such that the particle moves away from the converging field. This is referred to as the *magnetic mirror effect* [22].

Some of the configurations which utilize this principle in ion sources are shown in Fig. 2.7. The first picture shows the field generated by two solenoid coils, which acts as a particle trap in some ECR ion sources [33]. This creates a converging field longitudinally in both directions towards the coils, mirroring the charged particles between the high field regions. The next picture shows a magnetic multipole confinement [10] arrangement, where permanent magnets are arranged around a plasma chamber to produce very high fields at the walls and very less fields towards the interior. This reduces the anode (chamber) area, which helps in increasing the containment time of primary electrons [34, 35].

## 2.7 Diffusion in plasma

In the previous section, the transport of plasma particles in a spatially homogeneous plasma was considered in the presence of external fields. Transport of plasma particles can occur in a spatially inhomogeneous plasma, even without any external fields. Here, the inhomogeneity appears in the form of density or temperature gradients or both inside the plasma. This creates pressure gradients in the plasma and particles move from high to low pressure regions, through collisions [22]. This process is termed as *diffusion*.

### 2.7.1 Diffusion in a weakly ionised plasma

At first, we can consider diffusion in a weakly ionised, inhomogeneous plasma in the absence of any external magnetic fields. The deviations from equilibrium state due to the spatial inhomogeneity of the plasma are assumed to be very small. From the fluid consideration of the plasma, the general momentum transport equation for a hydrogen plasma can be written as [26]

$$mn \frac{d\vec{u}}{dt} = qn\vec{E} - \vec{\nabla}p - mn\nu\vec{u} \quad (2.66)$$

where  $\vec{u}$  is the fluid velocity,  $\nu$  is the charged particle-neutral collision frequency averaged over velocities,  $p$  is the pressure and  $n$  is the density of the plasma species. For the case of steady state, the L.H.S becomes zero and then the flow due to a density gradient and electric field can be obtained. Considering an isothermal plasma [26],  $p = nk_bT$

$$\vec{u} = \mu\vec{E} - D \frac{\vec{\nabla}n}{n}; \text{ where } \mu = \frac{q}{m\nu} \text{ and } D = \frac{k_bT}{m\nu} \quad (2.67)$$

$\mu$  is the mobility, which relates the movement of the plasma fluid in response to an electric field and  $D$  is the diffusion coefficient that relates the movement due to a normalised density gradient. Substituting the above in the continuity equation, in the absence of  $\vec{E}$ ,

$$\frac{\partial n}{\partial t} = \frac{k_bT}{m\nu} \nabla^2 n = D \nabla^2 n \quad (2.68)$$

As evident from the above equation, as the collision frequency increases, the diffusion decreases. It can be seen from equation 2.35 that the electron-neutral collision frequency is higher than the ion-neutral collision frequency in a weakly ionised plasma. Then, assuming the same particle temperatures and collision cross sections, the ratio of diffusion coefficient of electrons to ions can be obtained from the above equation as [26]

$$\frac{D_e}{D_i} = \left( \frac{m_i}{m_e} \right)^{1/2} \gg 1 \quad (2.69)$$

, which suggests a rapid diffusion of electrons compared to ions. Such motion results in a space charge electric field,  $\vec{E}$ , which creates a barrier for the further diffusion of electrons, but enhances the positive ion diffusion [22]. This leads to an intermediate diffusion rate value, such that the flux of ions and electrons are the equal. Such a diffusion is called *ambipolar diffusion*. Equating the electron and ion fluxes and using equation 2.68,

$$\frac{\partial n}{\partial t} = D_a \nabla^2 n, \text{ where } D_a = \frac{k_b(T_i + T_e)}{m_i\nu_{in} + m_e\nu_{en}} \approx \frac{k_b(T_i + T_e)}{m_i\nu_{in}} \quad (2.70)$$

is the *ambipolar diffusion coefficient*. We have also assumed that  $n_e = n_i = n$  in the above equation. In the case when  $T_i = T_e$  and comparing with equation 2.68, it can be seen that the ambipolar electric field leads to doubling of the diffusion coefficient of ions.

Now let us consider the situation when a transverse magnetic field is applied in the  $\hat{z}$ -direction,  $\vec{B} = B_0 \hat{z}$  in the plasma. We consider that the cyclotron frequency due to magnetic field is very much higher than the collision frequency. In that case, when the density gradient is in  $x$ -direction, the velocity in the  $x$ -direction perpendicular to the magnetic field, can be obtained as [26]

$$u_x = \frac{\nu}{m\omega_c^2} \left( qE_x - \frac{k_b T}{n} \frac{dn}{dx} \right) \quad (2.71)$$

Compared to equation 2.68, where collisions reduce diffusion, it can be seen from the above equation that collisions increase the diffusion perpendicular to the magnetic field. In other words, collisions are required for cross field diffusion. Also the ions tend to diffuse faster in the perpendicular direction (solving equations 2.35, 2.43, 2.71 gives  $u_x \propto m^{1/2}$ ) than electrons which is contrary to the situation parallel to the magnetic field. This will again lead to ambipolar diffusion where the ion and electron flux will be equal. The ambipolar diffusion coefficient can be separated into  $D_{\alpha\perp}$ , perpendicular to the magnetic field and  $D_{\alpha\parallel}$ , parallel to magnetic field. Evidently,  $D_{\alpha\parallel} = D_\alpha$  in equation 2.70. The temporal variation in the density of electron species can now be derived as [22]

$$\frac{\partial n_e}{\partial t} = D_{\alpha\perp} \left[ \frac{\partial^2 n_e}{\partial x^2} + \frac{\partial^2 n_e}{\partial y^2} \right] + D_\alpha \frac{\partial^2 n_e}{\partial z^2} \quad (2.72)$$

$$, \text{ where } D_{\alpha\perp} = \frac{\nu_{en}^2}{\nu_{en}^2 + \omega_{ce}^2} D_\alpha \quad (2.73)$$

It can be seen from the above equation that the perpendicular diffusion is less than the diffusion parallel to the magnetic field.

### 2.7.2 Diffusion in a fully ionised plasma

An interesting result can be seen in the case of *fully ionised plasma* in the presence of external magnetic fields. The perpendicular diffusion coefficient in this case is called *classical diffusion coefficient*, which is given by [26]

$$D_\perp \approx \nu_{ei} \langle r_{Le}^2 \rangle \left[ 1 + \frac{T_i}{T_e} \right] \quad (2.74)$$

where  $\nu_{ei}$  is the electron-ion collision frequency and  $r_{Le}$  is the electron Larmor radius. Since  $r_{Le}^2$  is proportional to  $T_e$  (from equation 2.46,  $r_{Le}^2 = v^2/\omega_c^2 \approx k_b T_e/m_e \omega_c^2$ ) and  $\nu_{ei}$  is



<div>H</div> <div>13.5984</div> <div>0.7542</div>																		<div>2</div> <div>He</div> <div>24.5874</div> <div>0.078*</div>																													
<div>3</div> <div>Li</div> <div>5.3917</div> <div>0.620</div>		<div>4</div> <div>Be</div> <div>9.3227</div> <div>0.19</div>																		<div>5</div> <div>B</div> <div>8.298</div> <div>0.28</div>		<div>6</div> <div>C</div> <div>11.2603</div> <div>1.268</div>		<div>7</div> <div>N</div> <div>14.5341</div> <div>j0</div>		<div>8</div> <div>O</div> <div>13.6181</div> <div>1.462</div>		<div>9</div> <div>F</div> <div>17.4228</div> <div>3.399</div>		<div>10</div> <div>Ne</div> <div>21.5645</div> <div>&lt; 0</div>																	
<div>11</div> <div>Na</div> <div>5.1391</div> <div>0.548</div>		<div>12</div> <div>Mg</div> <div>7.6462</div> <div>&lt;0</div>																		<div>13</div> <div>Al</div> <div>5.9858</div> <div>0.46</div>		<div>14</div> <div>Si</div> <div>8.1517</div> <div>1.385</div>		<div>15</div> <div>P</div> <div>10.4867</div> <div>0.743</div>		<div>16</div> <div>S</div> <div>10.36</div> <div>2.0772</div>		<div>17</div> <div>Cl</div> <div>12.9676</div> <div>3.615</div>		<div>18</div> <div>Ar</div> <div>15.7596</div> <div>&lt; 0</div>																	
<div>19</div> <div>K</div> <div>4.3407</div> <div>0.5012</div>		<div>20</div> <div>Ca</div> <div>6.1132</div> <div>0.043</div>		<div>21</div> <div>Sc</div> <div>6.5615</div> <div>&lt; 0</div>		<div>22</div> <div>Ti</div> <div>6.8281</div> <div>0.2</div>		<div>23</div> <div>V</div> <div>6.7462</div> <div>0.5</div>		<div>24</div> <div>Cr</div> <div>6.7665</div> <div>0.66</div>		<div>25</div> <div>Mn</div> <div>7.434</div> <div>&lt; 0</div>		<div>26</div> <div>Fe</div> <div>7.9024</div> <div>0.25</div>		<div>27</div> <div>Co</div> <div>7.881</div> <div>0.7</div>		<div>28</div> <div>Ni</div> <div>7.6398</div> <div>1.15</div>		<div>29</div> <div>Cu</div> <div>7.7264</div> <div>1.226</div>		<div>30</div> <div>Zn</div> <div>9.3942</div> <div>&lt; 0</div>		<div>31</div> <div>Ga</div> <div>5.9993</div> <div>0.3</div>		<div>32</div> <div>Ge</div> <div>7.8994</div> <div>1.2</div>		<div>33</div> <div>As</div> <div>9.7886</div> <div>0.80</div>		<div>34</div> <div>Se</div> <div>9.7524</div> <div>2.0206</div>		<div>35</div> <div>Br</div> <div>11.8138</div> <div>3.364</div>		<div>36</div> <div>Kr</div> <div>15.7596</div> <div>&lt; 0</div>													
<div>37</div> <div>Rb</div> <div>4.1771</div> <div>0.4860</div>		<div>38</div> <div>Sr</div> <div>5.6949</div> <div>&gt; 0</div>		<div>39</div> <div>Y</div> <div>6.2173</div> <div>= 0</div>		<div>40</div> <div>Zr</div> <div>6.6339</div> <div>0.5</div>		<div>41</div> <div>Nb</div> <div>6.7589</div> <div>1.0</div>		<div>42</div> <div>Mo</div> <div>7.092</div> <div>1.0</div>		<div>43</div> <div>Tc</div> <div>7.28</div> <div>0.7</div>		<div>44</div> <div>Ru</div> <div>7.3605</div> <div>1.1</div>		<div>45</div> <div>Rh</div> <div>7.4589</div> <div>1.2</div>		<div>46</div> <div>Pd</div> <div>8.3369</div> <div>0.6</div>		<div>47</div> <div>Ag</div> <div>7.5762</div> <div>1.303</div>		<div>48</div> <div>Cd</div> <div>8.9938</div> <div>&lt; 0</div>		<div>49</div> <div>In</div> <div>5.7864</div> <div>0.3</div>		<div>50</div> <div>Sn</div> <div>7.3439</div> <div>1.25</div>		<div>51</div> <div>Sb</div> <div>8.6084</div> <div>1.05</div>		<div>52</div> <div>Te</div> <div>9.0096</div> <div>1.9708</div>		<div>53</div> <div>I</div> <div>10.4513</div> <div>3.061</div>		<div>54</div> <div>Xe</div> <div>12.1298</div> <div>&lt; 0</div>													
<div>55</div> <div>Cs</div> <div>3.8939</div> <div>0.4715</div>		<div>56</div> <div>Ba</div> <div>5.2117</div> <div>&gt; 0</div>		<div>57,71</div> <div>La-Lu</div> <div>Actinide</div>		<div>72</div> <div>Hf</div> <div>6.8251</div> <div>&lt; 0</div>		<div>73</div> <div>Ta</div> <div>7.5496</div> <div>0.6</div>		<div>74</div> <div>W</div> <div>7.864</div> <div>0.6</div>		<div>75</div> <div>Re</div> <div>7.8335</div> <div>0.15</div>		<div>76</div> <div>Os</div> <div>8.4382</div> <div>1.1</div>		<div>77</div> <div>Ir</div> <div>8.967</div> <div>1.6</div>		<div>78</div> <div>Pt</div> <div>8.9587</div> <div>2.128</div>		<div>79</div> <div>Au</div> <div>9.2255</div> <div>2.3086</div>		<div>80</div> <div>Hg</div> <div>10.4375</div> <div>&lt; 0</div>		<div>81</div> <div>Tl</div> <div>6.1082</div> <div>0.3</div>		<div>82</div> <div>Pb</div> <div>7.4167</div> <div>0.36</div>		<div>83</div> <div>Bi</div> <div>7.2856</div> <div>1.1</div>		<div>84</div> <div>Po</div> <div>8.417</div> <div>1.9</div>		<div>85</div> <div>At</div> <div>9.3</div> <div>2.8</div>		<div>86</div> <div>Rn</div> <div>10.7485</div> <div>&lt; 0</div>													
<div>87</div> <div>Fr</div> <div>4.0727</div>		<div>88</div> <div>Ra</div> <div>5.2784</div>		<div>89,103</div> <div>Ac-Lr</div>		<div>104</div> <div>Rf</div>		<div>105</div> <div>Db</div>		<div>106</div> <div>Sg</div>		<div>107</div> <div>Bh</div>		<div>108</div> <div>Hs</div>		<div>109</div> <div>Mt</div>		<div>110</div> <div>Ds</div>		<div>111</div> <div>Rg</div>		<div>112</div> <div>Cn</div>		<div>113</div> <div>Nh</div>		<div>114</div> <div>Fl</div>		<div>115</div> <div>Mc</div>		<div>116</div> <div>Lv</div>		<div>117</div> <div>Ts</div>		<div>118</div> <div>Og</div>													
																		<div>57</div> <div>La</div> <div>5.5769</div>		<div>58</div> <div>Ce</div> <div>5.5387</div>		<div>59</div> <div>Pr</div> <div>5.473</div>		<div>60</div> <div>Nd</div> <div>5.525</div>		<div>61</div> <div>Pm</div> <div>5.582</div>		<div>62</div> <div>Sm</div> <div>5.6437</div>		<div>63</div> <div>Eu</div> <div>5.6704</div>		<div>64</div> <div>Gd</div> <div>6.1501</div>		<div>65</div> <div>Tb</div> <div>5.8638</div>		<div>66</div> <div>Dy</div> <div>5.9389</div>		<div>67</div> <div>Ho</div> <div>6.0215</div>		<div>68</div> <div>Er</div> <div>6.1077</div>		<div>69</div> <div>Tm</div> <div>6.1843</div>		<div>70</div> <div>Yb</div> <div>6.2542</div>		<div>71</div> <div>Lu</div> <div>5.4259</div>	
																		<div>89</div> <div>Ac</div> <div>5.17</div>		<div>90</div> <div>Th</div> <div>6.3067</div>		<div>91</div> <div>Pa</div> <div>5.89</div>		<div>92</div> <div>U</div> <div>6.1941</div>		<div>93</div> <div>Np</div> <div>6.2657</div>		<div>94</div> <div>Pu</div> <div>6.0262</div>		<div>95</div> <div>Am</div> <div>5.9738</div>		<div>96</div> <div>Cm</div> <div>5.9915</div>		<div>97</div> <div>Bk</div> <div>6.1979</div>		<div>98</div> <div>Cf</div> <div>6.2817</div>		<div>99</div> <div>Es</div> <div>6.42</div>		<div>100</div> <div>Fm</div> <div>6.5</div>		<div>101</div> <div>Md</div> <div>6.58</div>		<div>102</div> <div>No</div> <div>6.65</div>		<div>103</div> <div>Lr</div> <div>4.9</div>	

**Figure 2.8:** Ionisation energy and electron affinity values of elements from references [38] and [12].

proportional to  $T_e^{-3/2}$  (equation 2.36),

$$D_{\perp} \propto \frac{1}{\sqrt{T_e}} \quad (2.75)$$

Thus, the cross-field diffusion decreases as the electron temperature increases. This is in contradiction to the situation in a weakly ionised plasma. This result indicates the possibility of confining energetic electrons inside a plasma using a transverse magnetic field. Such perpendicular magnetic fields are used in negative ion sources to prevent the flow of energetic electrons into the negative ion extraction region and are regarded as *magnetic filters* [36]. But, the transport across the magnetic filters in such ion sources cannot be completely described by *classical diffusion*. Some plasma models attribute the magnetic filter action to additional diamagnetic currents and drifts [37].

## 2.8 Ionisation

A variety of ionisation processes can take place inside a plasma. This can be of electron impact ionisation, surface ionisation, photoionisation, field ionisation etc. [10]. The explanations in this section are based on [10]. Only positive ion formation is treated in this section.

**Electron impact ionisation** is a fundamental ionisation mechanism caused by the collision between an electron with sufficient energy and a neutral species. The electron energy must

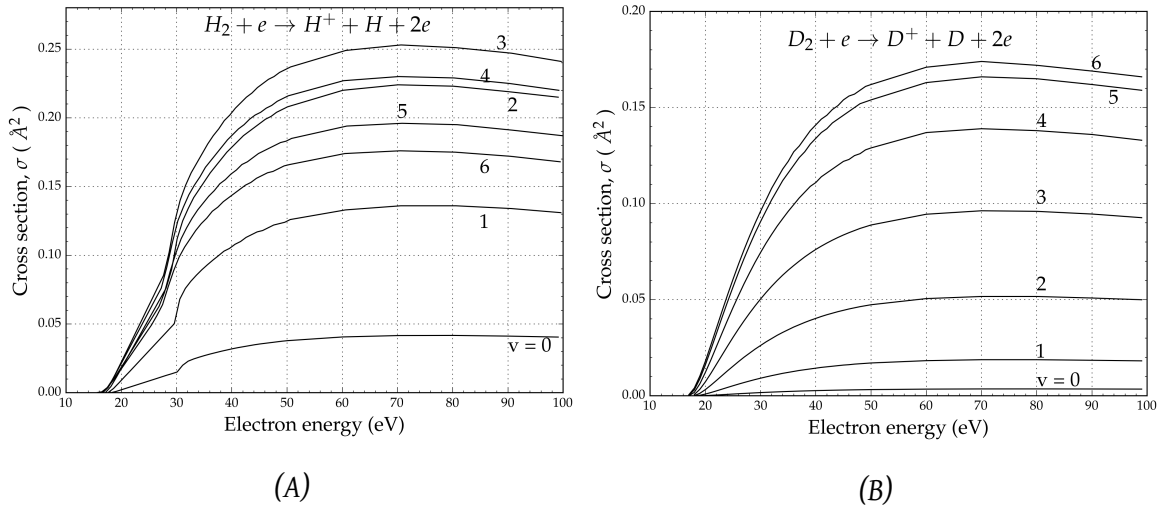
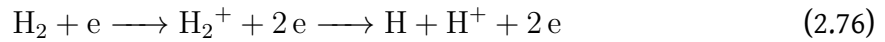


**Figure 2.9:** Cross sections of electron impact ionisation resulting in dissociative ionisation in  $H_2$  and  $D_2$  plasmas, for various vibrational energy states. Data is reproduced from graph XVI in [39].

exceed the ionisation potential of the species. The ionisation potentials of different elements are shown in Fig. 2.8. The electrons responsible for the ionisation belong to the tail of the Maxwell-Boltzmann (MB) distribution and are called the *primary* electrons. The ionisation further results in the generation of lower energy electrons called *secondary* electrons [10]. An important example of electron impact ionisation in  $H_2$  and  $D_2$  plasmas is the *dissociative ionisation* shown below.



Corresponding cross sections of the above reactions are shown in Fig. 2.9. Electron impact collision process can also result in processes other than ionisation, like *non dissociative electronic excitation*, *radiative decay dissociation* etc [39].

Electron impacts can also lead to *multiple ionisations*, which result in high charge state ions,  $Ar^{17+}$ ,  $Ta^{49+}$ ,  $Xe^{49+}$ , etc [40]. The ionisation potentials in such plasmas are in the order of keV. In general, these can be a one step process where the high charge state is created in a single interaction with an electron or a multiple step process where the ion interacts with multiple electrons, losing one electron in each step. Electron temperature needs to be high for such processes and hence the multiple ionisation is observed in high temperature plasmas, like ECR plasmas [40]. Another requirement is that the ion confinement time should be sufficiently large such that the step by step stripping of electrons can take place.

**Photoionisation** can also result in the formation of ions when the incident energy of the photon is higher than the ionisation energy. For example, the wavelength of photon needed

for photoionisation of a species with ionisation potential of 10 eV lies in the vacuum ultra violet range ( $\approx 120\text{nm}$ ).

***Ion impact ionisation*** is another method of producing ions. In this case, an energetic ion interacts with a neutral atom of low energy, resulting in a low energy ion and a fast neutral. An exchange of electron also occurs during this process and is called charge transfer or charge exchange interactions [10]. This is not a prominent method of ion generation in ion sources, but significant in high temperature plasmas like that in fusion reactors.

## 2.9 Negative ion formation processes

The ease of negative ion formation and destruction is measured by the *electron affinity*, which is the difference in energy between the neutral atom and negative ion state [12]. Electron affinity of various elements are shown in Fig. 2.8. Electron affinity should be positive for stable or metastable negative ion formation. Reaction rates for negative ion destruction are higher than its formation rate and hence offer challenges. The three widely used methods of producing negative ions are discussed below.

### 2.9.1 Charge exchange processes

One of the methods of forming negative ions is the indirect production by *double charge exchange of positive ions* [10]. Here, a beam of positive ions pass through a medium of neutral atoms of low ionisation potential, resulting in the formation of negative ions. The medium usually is a vapour of alkaline earth elements like Mg, Ca, Sr, Ba, etc. or alkali vapours of Na, K, Rb, Cs etc [10]. The positive ions capture electrons from the vapour in a single step process or two step process. The conversion efficiency is determined by the conversion factor, which is the ratio between negative ion current at the output of the medium to the positive ion beam current at the input. The conversion factor depends on the cross sections of formation and destruction of negative ions, between the positive ion beam and the particular medium, scattering of the beam, incident positive ion beam energy, etc. For example, passage of  $\text{He}^+$  beams over a Na cell, reported about 70 mA of  $\text{He}^-$  beam current at a conversion efficiency of 1.4% -2% [41]. In another experiment,  $\text{D}^+$  ions are converted into  $\text{D}^-$  with a cesium vapour cell at an efficiency of 25% [17].

Another method of negative ion generation is through direct formation in a plasma discharge. This can further be classified into *volume production methods*, which deals with processes in the volume of the plasma and *surface production methods*, which deals with the

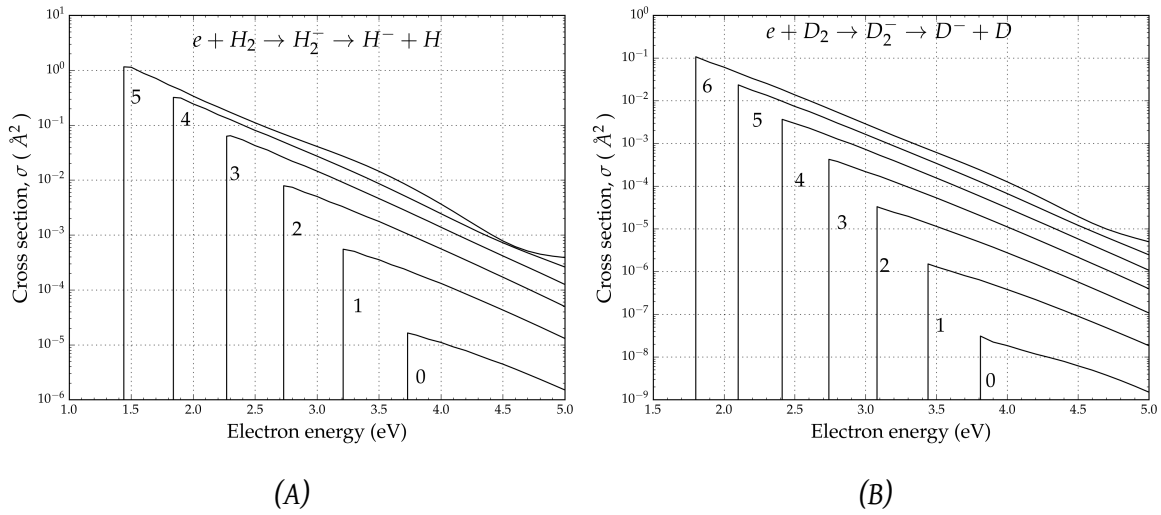


**Figure 2.10:** Dissociative attachment cross sections for different vibrational levels of (A)  $H_2$  and (B)  $D_2$  molecules. Data is reproduced from graph XXI in [39].

interaction of plasma with metallic surfaces. Further analysis of these processes is done in the context of  $H_2/D_2$  plasmas, since the scope of the thesis is limited to those.

### 2.9.2 Volume production processes

A major milestone in volume production methods happened in 1977 at Ecole Polytechnique, France, when a high fraction of  $H^-$  ions was identified in a low pressure hydrogen plasma by Bacal *et al* [42]. The major reaction responsible for the formation of such a high proportion of  $H^-$  ions were identified to be *dissociative attachment* (DA) of electrons to molecules, as shown below [42].



$v$  represents the vibrational state of the molecule. The reaction proceeds through a short-lived state of the molecule,  $H_2^-$ , which dissociates in  $\approx 10^{-15}$  sec [43]. Similar behaviour was observed in  $D_2$  plasmas also. Experimental [44] and theoretical [45] studies showed that the cross section of the above reaction increases by several orders of magnitude, compared to the ground state, when the molecules are at high vibrational-rotational levels. The cross sections for different vibrational levels are shown in Fig. 2.10. Also, the cross sections are higher for lower electron energies. It was also reported that the cross section enhancement was mainly through vibrational excitation than rotational [42].

The reactions leading to the formation of molecules with excited vibrational energy levels, which further leads to DA in the plasma, are the electron-molecule collisions shown

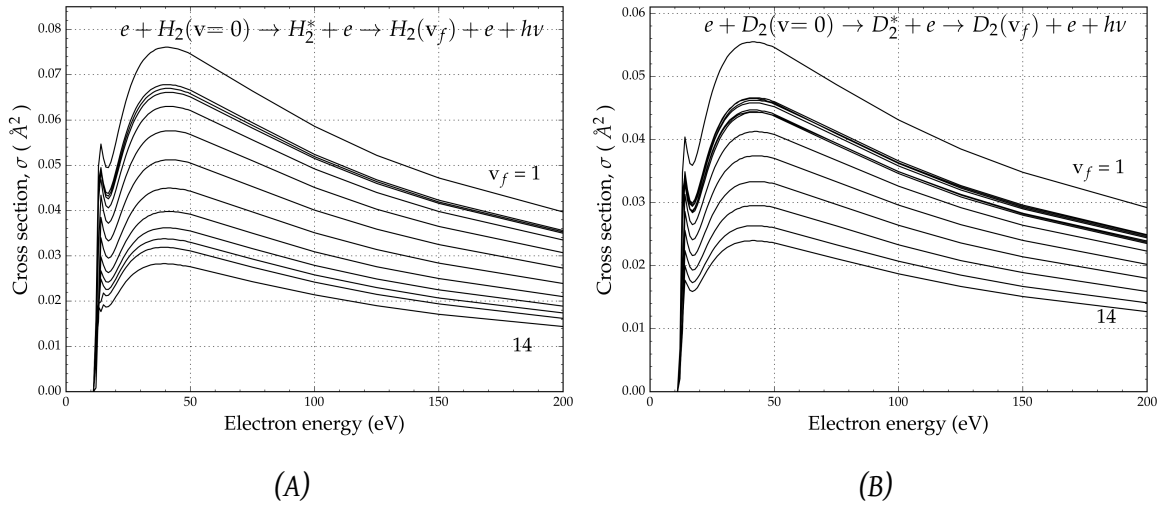
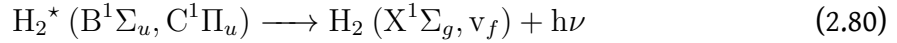
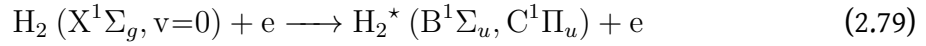


**Figure 2.11:** Cross sections of excitation–radiative decay–vibrational excitation reactions of (A)  $H_2$  and (B)  $D_2$  molecules from initial ground state vibrational level ( $v=0$ ) to different final vibrational energy states. Data is reproduced from graph XIX in [39].

below. The collisions lead to excitation–radiative decay–vibrational excitation reactions [42]



X, B, C represent the electronic energy levels,  $\Sigma$ ,  $\Pi$  correspond to the projection of total orbital angular momentum along internuclear axis, the superscript represents the spin multiplicity (singlet, triplet, etc.) and the subscript refers to the symmetry of molecular orbitals [46]. The electron-molecule collisions lead to molecular excitation from the ground state ( $X^1\Sigma_g, v = 0$ ) to excited states ( $B^1\Sigma_u, C^1\Pi_u$ ). This further decays back to the ground state through radiative decays, resulting in a higher population of molecules at high vibrational energy levels.  $v_f$  denotes the final vibrational energy level of the molecule. The cross sections for these reactions are shown in Fig. 2.11. Only singlet states are considered here, since the triplet states of  $H_2$  molecule decays by forming atomic fragments [42].

From Fig. 2.10 and 2.11 it can be seen that electrons of low energy are needed for the formation of negative ions from vibrationally excited molecules through DA. At the same time, electrons of high energy,  $\approx 50$  eV are needed for creating the vibrationally excited molecules. This points to the scenario of creating two different energy distributions within the same plasma. Ion sources, like those studied in this thesis, overcome this challenge by using additional perpendicular magnetic fields that results in the magnetic filter effects mentioned in section 2.7.2. More about this will be discussed in section 4.2.

In addition to the above DA reaction, there are several other reactions that lead to negative ion formation. Some of them are *polar dissociation*, *dissociative recombination* and *radiative capture* [43]. But the cross sections of these reactions are not sufficient enough to explain the observed negative ion densities [47].

### 2.9.3 Surface production processes

The production of negative ions due to interaction between surfaces and particles incident on it was reported as early as 1931 by Woodcock [48][42]. Later it was found that the flux of negative ions increased when the surface has adsorbed alkali metal films [11]. By 1971, the group in Russia found that the addition of cesium to the plasma enhances the negative ion production significantly [11].

The physical mechanism leading to negative ion generation, due to the interaction between surface and plasma, is termed as Surface Plasma Generation. The presence of a surface modifies the ionisation energy and electron affinity levels of the nearby atom, due to image potential formation [49]. In the case where the modified electron affinity falls below the Fermi level of the metal surface, the electron can tunnel from the Fermi level to the electron affinity level of the interacting atom [10]. This is a single step process involving the direct transfer of electrons, forming a negative ion. The interaction can be enhanced by covering the metal surface with a material of low work function. Cesium vapours are widely used in such processes due to the low work function (1.8 eV) and have achieved significant improvements in negative ion generation [11].

# Chapter 3

---

## Ion sources and beam extraction

Out of the different kinds of charged particles formed inside a plasma, the species of interest need to be extracted and formed into a beam for further applications. This is the task of an *ion source*, which is basically a combination of a *plasma source* and an *extractor* [10]. This chapter deals with the basic mechanisms involved in the formation of an ion beam from a plasma and the basic features of the beam propagation in a *beam line*. The explanations are mainly based on the texts from references [10, 50–53].

### 3.1 Ion extraction from plasma

Charged particles can be extracted from a plasma by subjecting them to electric fields. Those particles that experience the electric fields are accelerated into a beam line. These fields are established by means of electrostatic potentials on electrodes placed at the exit of the plasma chamber. A very simplified schematic of an ion extraction system is shown in Fig. 3.1. Most of the ion sources have (a) *plasma electrode*, which forms the boundary of the plasma and (b) *extraction* or *puller electrode*, which provides the electric field for extraction of ions from the plasma. The potentials on the electrodes in the extraction system determine the energy of the extracted beam,

$$E = q(V_E - V_P) \quad (3.1)$$

where  $q$  is the charge of the ion extracted,  $V_P$  and  $V_E$  are the electrostatic potentials on the plasma electrode and extraction electrode. In most cases, there will be additional electrodes present for further acceleration and focusing.

The magnitude of the electric fields needed for beam extraction depends upon the properties of the plasma. The dependence on the plasma density can be easily seen by

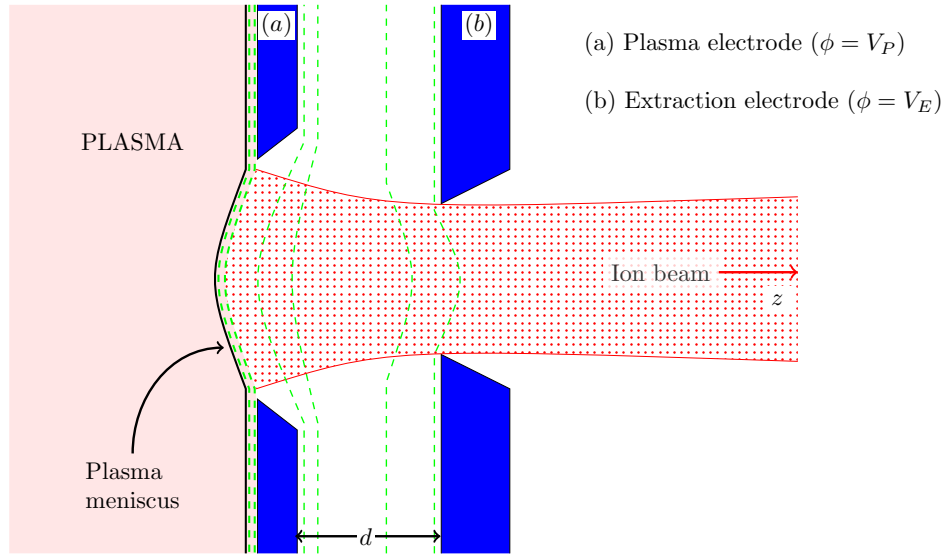


**Figure 3.1:** Schematic of ion beam extraction from plasma. Electrodes are shown in blue. Equipotential lines are denoted by dashed green lines.

considering the penetration depth of electromagnetic field in a collisionless plasma, given by  $\delta = c/\omega_p$ , where  $c$  is the velocity of light and  $\omega_{pe}$  is the plasma frequency [54]. Since  $\omega_{pe} = (n_e e^2 / \epsilon_0 m_e)^{1/2}$ ,

$$\delta = c \sqrt{\frac{\epsilon_0 m_e}{n_e e^2}} \quad (3.2)$$

where  $n_e$  is the plasma density,  $m_e$  is the electron mass,  $\epsilon_0$  is vacuum permittivity and  $e$  is the electronic charge. As can be seen from the above equation, as the plasma density increases, the penetration depth decreases and the electric field ends more abruptly in the plasma [55]. So a higher potential on the extraction electrodes is required to extract more ions.

The polarity of the electrostatic potentials on the electrodes depends on the type of ions that need to be extracted. In the case of extraction of positive (negative) ions, the extraction electrode should have a negative (positive) potential. The potentials experienced by the positive and negative ions are shown in Fig.3.2 [21]. In general, the plasma inside the ion sources will have a positive plasma potential  $\phi_p$ . In the case of positive ion extraction systems, the potential experienced by the positive ions will fall off exponentially and the ions get accelerated from the bulk plasma into the extraction region. Electrons experience a repelling potential and hence their density will decrease exponentially along the beam. Energetic electrons can also backstream into the plasma, creating the requirement for additional electron dumping [56].

In the case of negative ion extraction system, a potential well exists between the bulk plasma and positively biased extraction electrode due to repelling electric fields. The negative



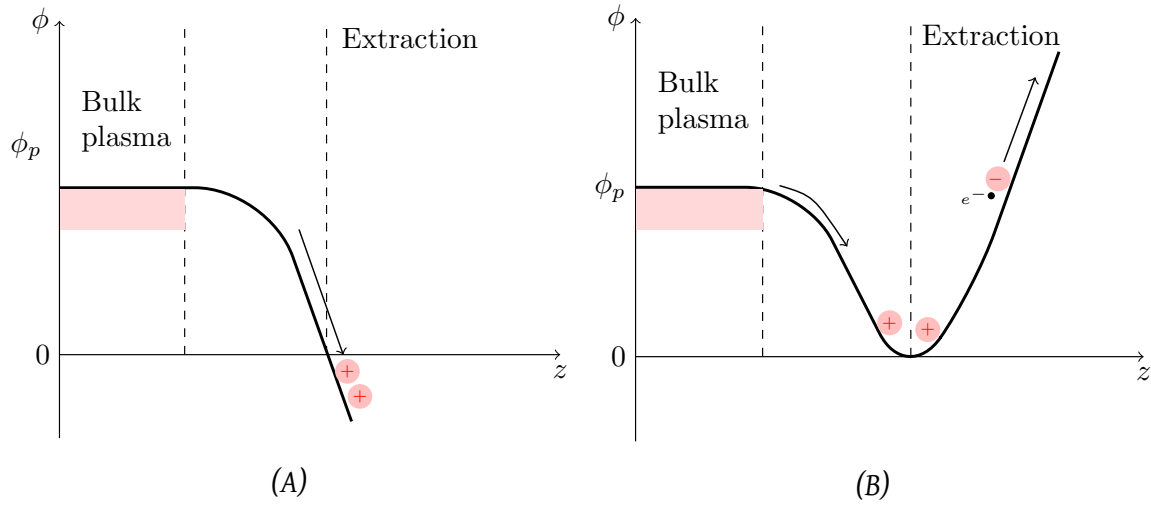


**Figure 3.2:** Variation in the potential along the beam axis for (A) positive ion extraction system and (B) negative ion extraction system [32].

ions having enough energy to overcome this potential barrier will be extracted. Unlike the positive ion extraction case, electrons having enough energy to overcome the initial potential barrier will also get extracted. Additional magnetic fields are created in the extraction region for deflecting the extracted electrons to dumping electrodes, such that they are removed from the negative ion beam. Low energy positive ions from the plasma can get trapped in the potential well. Positive ions with higher energy will get reflected back into the plasma by the positive extraction potentials.

### 3.1.1 The plasma "meniscus"

As seen in section 2.4.1 a plasma sheath exists between the plasma and the walls of the plasma chamber. Similarly, a plasma sheath interface exists between the plasma and the beam of charged particles somewhere near the plasma electrode. The amount of compensating charge particles declines from the plasma sheath towards the extraction, leading to ion beam formation. A boundary layer called *plasma meniscus* is imagined to be present between the bulk plasma and extraction, at a potential  $\approx 0$  V. Charged particles that cross the meniscus experience the electric fields and are accelerated out of the ion source. Since the shape and position of the plasma meniscus depend on the plasma parameters and extraction fields, it plays a very significant role in the optics of ion beam extraction and even in the quality of beam propagation [57]. More details on the meniscus and its influence on the beam properties can be found in the next section.

### 3.1.2 Limitation due to space charge

In the extraction of ion beam from the quasi-neutral plasma, one of the challenges to encounter is the field produced by the charges itself. This field counteracts the electric field at the beam starting surface (*plasma meniscus*). This establishes a limit for the maximum current that can be extracted from the plasma for a fixed plasma density, electrode potential and geometry. This upper limit can be established mathematically. Historically, the ion optics in the extraction system is treated in the same way as the mathematical treatment of electron guns [58]. This approach is followed here.

Let us consider a beam of negative ions flowing between the plasma electrode and extraction electrode, separated by a distance  $d$ . The plasma electrode is at  $z = 0$  and at ground potential ( $\phi(0) = 0$  V). The extraction electrode is at  $z = d$  and at a positive potential  $\phi(d) = V_0$ . The flow of charges along the  $z$ -direction only is considered with velocity  $v = v(z)$ . The extracted current density is represented as  $J$ . In this case, we assume that the *emission surface at the plasma electrode is planar*. The initial energy of the beam at the plasma electrode is assumed to be zero. An expression for the velocity of particles along the  $z$ -axis can be determined from energy conservation equations. The energy gained by the particle during the motion along the  $z$ -direction is given by

$$\frac{1}{2}mv^2 = q\phi \implies v = \sqrt{\frac{2q\phi}{m}} \quad (3.3)$$

where  $\phi = \phi(z)$ . With the continuity equation, an expression for the charge density,  $\rho$ , can be derived for a one dimensional steady state condition ( $\partial/\partial t = 0$ ).

$$\frac{\partial \rho}{\partial t} + \frac{\partial J}{\partial z} = 0 \implies J = \rho v, \text{ a constant; } \rho = J \sqrt{\frac{m}{2q\phi}} \quad (3.4)$$

The combined electrical effects of the charges can be considered as a field, *space charge*, assuming a continuous distribution of charges in space. The electric potential generated by the charges in the ion beam can be found from the Poisson equation.

$$\frac{\partial^2 \phi}{\partial z^2} = -\frac{\rho}{\epsilon_0} = -\frac{J}{\epsilon_0} \sqrt{\frac{m}{2q\phi}} \quad (3.5)$$

Multiplying both sides by  $\partial\phi/\partial z$  and integrating by parts we obtain,

$$\left[ \frac{\partial \phi}{\partial z} \right]_{\phi(z)}^2 = -\frac{4J}{\epsilon_0} \sqrt{\frac{m\phi}{2q}} + \left[ \frac{\partial \phi}{\partial z} \right]_{\phi=\phi(0)}^2 \quad (3.6)$$

where the last term is the constant of integration. It is the square of the value of the electric field at  $z = 0$ , the emission surface, for a constant value of  $J$  and is obtained by setting the condition  $\phi(0) = 0$ .

As evident from equation 3.5, when  $J = 0$ , the electric field is constant. The response of the electric field at the emission surface is of particular interest here. As  $J$  increases, the electric field at the emission surface decreases due to space charges. The maximum value of current density,  $J_{CL}$ , is obtained when the electric field at the emission surface vanishes and hence further increase in extraction of ions from the plasma is not possible. This condition is called *space charge limited emission*.  $J_{CL}$  can be obtained by equating the electric field at emission surface as zero in equation 3.6, i.e.  $(\partial\phi/\partial z)_{\phi=\phi(0)} = 0$ . Further integration and setting  $\phi = V_0$  and  $z = d$ , the maximum current density that can be extracted can be obtained as

$$J_{CL} = \frac{4}{9} \epsilon_0 \sqrt{\frac{2q}{m}} \frac{V_0^{3/2}}{d^2} \quad (3.7)$$

This equation is called the *Child-Langmuir law* initially derived by Child [59] for the flow of positive ions between conducting plates. Langmuir used this in the study of electron flow between conducting plates [60]. In the current study, it gives the maximum current density that can be achieved between the electrodes by increasing the plasma density, for a fixed potential  $V_0$  and distance  $d$ . The curve is shown in 3.3(A). It is also interesting to note that  $J_{CL} \propto (q/m)^{1/2}$  and hence it is possible to extract  $\approx 42$  times more electron current density than proton current density.

In the case when the electric field at the emission surface is non-zero, it gives the condition for  $J$ ,  $0 < J < J_{CL}$ , and this condition is called *emission limited* or *partial space charge limited*. For such a case,  $(\partial\phi/\partial z)_{\phi=\phi(0)} \neq 0$  and the following quadratic equation can be derived [61] by integrating equation 3.6.

$$j^2 - j + \frac{27}{16} f^2 (1 - f) = 0 \quad (3.8)$$

$$\text{where } j = \frac{J}{J_{CL}}, \quad E_0 = \left[ \frac{\partial\phi}{\partial z} \right]_{\phi=\phi(0)} \quad \text{and} \quad f = \frac{E_0 d}{V_0} \quad (3.9)$$

$j$  represents the normalised extracted current density and  $f$  represent the normalised electric field density at the emission surface.  $j = 1$  is the space charge limited condition.  $j = 0$  is the condition where there is no current flow and the electric field at the emission surface is  $V_0/d$ , which gives  $f = 1$ . A graph of variation of  $f$  at different values of  $j$  is shown in Fig. 3.3 [61] [62]. As can be seen, the electric field at the emission surface decreases faster as the current density approaches the space charge limit.

Space charge effects can be characterized by *perveance*, a quantity dependant only on the geometry of the extraction system and type of extracted species [52]. It gives a measure

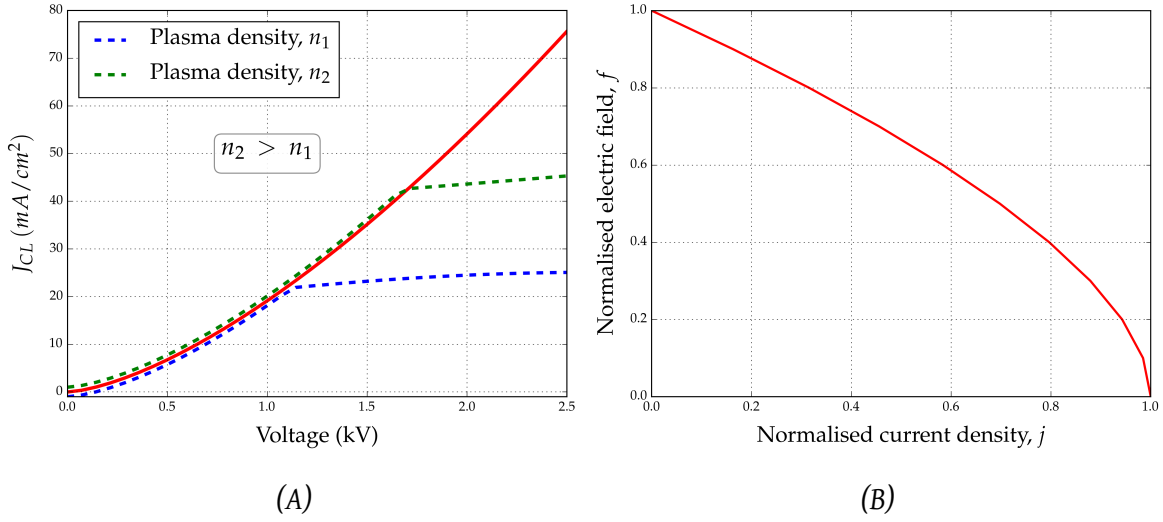


**Figure 3.3:** (A) Red curve is the space charge limited current (eq 3.7) for hydrogen ion extraction with  $d = 3.0$  mm. Other curves represent the situation for constant plasma densities. (B) Variation in the normalised electric field at the emission surface for different values of normalised current density.

of the extent of space charge limited emission from the ion source and can be defined as

$$P = \frac{I}{V_0^{3/2}} = \frac{4}{9} \epsilon_0 \sqrt{\frac{2q}{m}} \frac{\pi a^2}{d^2} \quad (3.10)$$

where  $a$  is the radius of emission surface and  $I$  is the extracted current. The experimentally determined perveance value starts to decrease when the plasma is unable to provide any more ions for extraction [63]. Hence the  $I$  value and perveance decreases. Optimal parameters that lead to a low divergence beam can be theoretically evaluated by determining the perveance of the extraction system [64].

In the derivations so far, we have assumed a planar emission surface, which is not the real case in ion sources. The Child-Langmuir law was extended to the study of electron flow between spherical and cylindrical surfaces by Langmuir and Blodgett [65]. This analysis was applied to the case of ion extraction from a curved emission surface [58], such as shown in Fig. 3.1. In the case of curved emission surface, the perveance becomes

$$P_c = \frac{I}{V_0^{3/2}} = \frac{4}{9} \epsilon_0 \sqrt{\frac{2q}{m}} \frac{\pi a^2}{d^2} \left(1 - 1.6 \frac{d}{r_c}\right) = P \left(1 - 1.6 \frac{d}{r_c}\right) \quad (3.11)$$

where  $r_c$  is the radius of curvature of the emission surface. The curvature of the emission surface is positive (negative) when the centre of curvature is in the plasma (extraction) side. Hence, if the emission surface is concave, the beam is converging and  $P_c < P$ . If the emission surface is convex, the beam is diverging and  $P_c > P$ . The convergence or divergence of

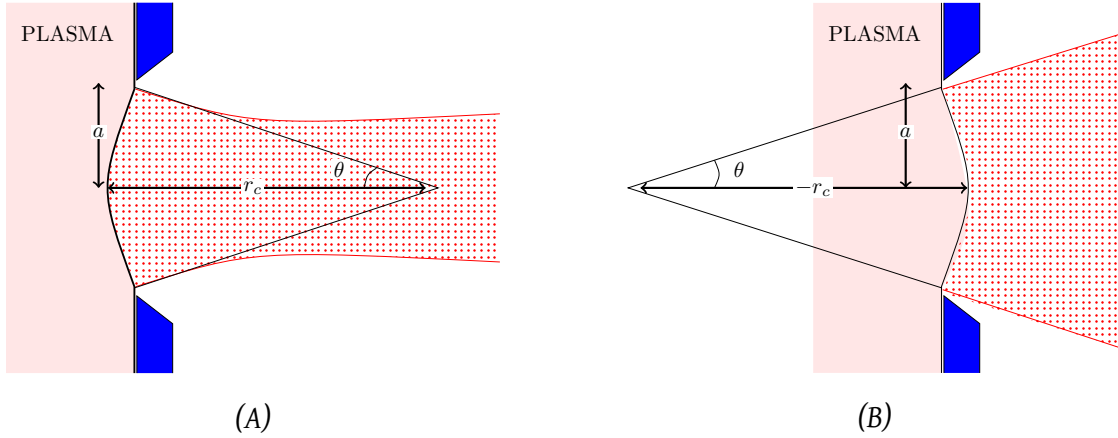


**Figure 3.4:** Location of emission surface for (A) a converging beam and (B) a diverging beam. The radius of curvature,  $r_c$  and angle  $\theta$  are also shown.

the extracted beam is represented by  $\theta \approx a/r_c$ , with  $\theta$  becoming negative for a diverging beam. The influence of the plasma parameters on  $r_c$  can be seen by equating the saturated ion current density that can be extracted from the plasma [58] to the space charge limited current for a curved emission surface. It can be obtained using Bohm velocity,  $v_B$  (in section 2.4.1), that

$$J = n_i e \sqrt{\frac{k_b T_e}{m_i}} = J_{CL} = \frac{4}{9} \epsilon_0 \sqrt{\frac{2q}{m}} \frac{V_0^{3/2}}{d^2} \left(1 - 1.6 \frac{d}{r_c}\right) \quad (3.12)$$

As can be seen from the above equation, an increase of the plasma density,  $n_i$  or the electron temperature  $T_e$  can cause an increase in the radius of curvature, moving the emission surface closer to extraction electrode and vice versa. Thus it can be seen that the plasma parameters also influence the beam optics.

## 3.2 Liouville's theorem

A particle in a beam can be completely specified if we know the information about its location  $(x, y, z)$  and momentum  $(p_x, p_y, p_z)$  in a coordinate system at a given point of time  $t$ . This information about a particle can be specified by a single point in a 6-dimensional space called *phase space*, whose axes are composed of 3 axes of location and 3 axes of momentum [22]. The number of points in the phase space corresponds to the number of particles in the beam. We can consider a *distribution function* in the 6D phase space,  $f_{6D}$ , which can be defined in the following manner [52].

$$\int f_{6D} \, dx \, dy \, dz \, dp_x \, dp_y \, dp_z = N \quad (3.13)$$

,where  $N$  is the total number of particles inside the beam. Thus the distribution function is the number of particles inside an elementary volume in phase space defined by the product of  $dx dy dz dp_x dp_y dp_z$ . The particles are considered to be non-interacting here. The motion of particles in the physical space is represented by an equivalent motion of points in the phase space. The motion in phase space can be denoted by velocity vector,  $\mathbf{v}_{ph} \equiv \{\dot{q}_j, \dot{p}_j\}$ . Since the total number of particles remain constant, this motion in phase space should satisfy the *continuity equation* [52],

$$\frac{\partial f_{6D}}{\partial t} + \nabla \cdot f_{6D} \mathbf{v}_{ph} = 0 \quad (3.14)$$

$$\frac{\partial f_{6D}}{\partial t} + f_{6D} \nabla \cdot \mathbf{v}_{ph} + \mathbf{v}_{ph} \cdot \nabla f_{6D} = 0 \quad (3.15)$$

$$\frac{\partial f_{6D}}{\partial t} + f_{6D} \sum_{j=3} \left[ \frac{\partial \dot{q}_j}{\partial q_j} + \frac{\partial \dot{p}_j}{\partial p_j} \right] + \sum_{j=3} \left[ \frac{\partial f_{6D}}{\partial q_j} \dot{q}_j + \frac{\partial f_{6D}}{\partial p_j} \dot{p}_j \right] = 0 \quad (3.16)$$

Suppose that we can define a Hamiltonian for the system,  $H(q_j, p_j, t)$ . Since  $\partial \dot{q}_j / \partial q_j = \partial^2 H / \partial q_j \partial p_j$  and  $\partial \dot{p}_j / \partial p_j = -\partial^2 H / \partial p_j \partial q_j$ , the second term vanishes and the equation becomes

$$\frac{\partial f_{6D}}{\partial t} + \sum_{j=3} \left[ \frac{\partial f_{6D}}{\partial q_j} \dot{q}_j + \frac{\partial f_{6D}}{\partial p_j} \dot{p}_j \right] = 0 \quad (3.17)$$

$$\implies \frac{df_{6D}}{dt} = 0 \quad (3.18)$$

The above equation is a statement of Liouville's theorem which establishes that the density of phase space is a conserved quantity for a Hamiltonian system [52]. This also implies that the volume occupied by a given number of representative points in phase space remains invariant. This is true in the presence of electric and magnetic fields also, as long as the forces are conservative [53]. Non-conservative fields, collisions etc can break the theorem.

It is also convenient to represent the particle trajectory of a beam, propagating in  $z$ -direction, in a 2-dimensional space called *trace space*. The coordinate pairs used are  $x - x'$  or  $y - y'$ , where  $x, y$  are the positions and  $x', y'$  are the slopes,  $x' = dx/dz$  and  $y' = dy/dz$ . The  $x - x'$  trace space area,  $A_x$  is related to the phase space volume projection onto  $x - p_x$  plane as [52]

$$A_x = \int_{trace} dx dx' = \frac{1}{p} \int dx dp_x = \frac{1}{\gamma \beta m c} \int dx dp_x \quad (3.19)$$

,where  $\gamma, \beta$  are the relativistic factors and  $\int dx dp_x$  is the projected area of the 6D phase space volume onto  $x - p_x$  plane. If the motion in  $x$ -direction can be completely decoupled from the other directions ( $y$  and  $z$ ), then  $\int dx dp_x$  will remain a constant. This implies that the

Applied field	Self field
$\nabla \cdot \vec{E}^a = \frac{\rho^a}{\epsilon_0}$	$\nabla \cdot \vec{E}^s = \frac{\rho^s}{\epsilon_0}$
$\nabla \times \vec{E}^a = -\frac{\partial \vec{B}^a}{\partial t}$	$\nabla \times \vec{E}^s = 0$
$\nabla \cdot \vec{B}^a = 0$	$\nabla \cdot \vec{B}^s = 0$
$\nabla \times \vec{B}^a = \mu_0 J^a + \mu_0 \epsilon_0 \frac{\partial \vec{E}^a}{\partial t}$	$\nabla \times \vec{B}^s = \mu_0 J^s$

**Table 3.1:** Maxwell's equations for a particle in a beam [50].

trace space area,  $A_x$ , will also be an invariant of motion if there is no change in momentum (no acceleration or deceleration,  $\gamma\beta = \text{constant}$ ). This representation helps in a direct determination of the beam trajectories and also determines the particle losses to walls or apertures in the beam line.

### 3.3 Equations of motion of charged particle beams

As shown in section 3.1, charged particles are extracted from the plasma into a beam, with the help of electric fields. Magnetic and electric fields need to be present for further beam propagation through a beam line. In addition to that, the particles in the beam experience fields due to the neighbouring space charge. The motion of particles in the presence of these fields, in the direction of beam propagation and the transverse planes, are examined in this section. The explanations are based on [50, 52].

The beam is considered to be propagating in a Cartesian frame in the longitudinal  $\hat{z}$ -direction.  $\hat{x}$  and  $\hat{y}$  are the transverse directions. The electric and magnetic fields experienced by the particles inside the beam can be divided into applied fields from external sources outside the beam ( $\vec{E}^a, \vec{B}^a$ ) and self fields from particle distribution within the beam ( $\vec{E}^s, \vec{B}^s$ ) [50]. The resultant fields can be written as

$$\vec{E} = \vec{E}^a + \vec{E}^s, \quad \vec{B} = \vec{B}^a + \vec{B}^s \quad (3.20)$$

The Lorentz force due to these fields can be obtained as

$$\vec{F}^a = q[\vec{E}^a + \vec{v} \times \vec{B}^a], \quad \vec{F}^s = q[\vec{E}^s + \vec{v} \times \vec{B}^s] \quad (3.21)$$

With *paraxial* approximation, where the longitudinal velocity is very much higher than the transverse velocities, i.e.  $v_z \gg v_x, v_y$ , particle velocity  $\vec{v}$  can be written as

$$\vec{v} = \hat{z}\beta c + \delta\vec{v} \approx \hat{z}\beta c \quad (3.22)$$

Maxwell's equations for external applied fields and self fields are shown in the Table 3.1. In the self fields, the evolution of beam is considered sufficiently slow that the time-varying terms can be neglected [50]. The self electric field,  $\vec{E}^s$  can be written in terms of a scalar potential,  $\phi$  and the self magnetic field  $\vec{B}^s$  can be written in terms of a vector potential,  $\vec{A}$  [50].

$$\vec{E}^s = -\nabla\phi \quad (3.23)$$

$$\vec{B}^s = \nabla \times \vec{A} \quad (3.24)$$

From equation 3.24 we can derive  $\nabla \times \vec{B}^s = -\nabla^2 \vec{A} = \mu_0 \vec{J}$  (Table 3.1). Since  $\vec{J} = \rho \vec{v} \approx \hat{z} \rho v_z$ , we can approximate  $\vec{A} = \hat{z} A_z$ , due to paraxial approximation. The potentials  $\phi$  and  $c\vec{A}$  form a relativistic 4-vector that transforms as a Lorentz vector for covariance,  $\mathbf{A}_\mu = (\phi, c\vec{A})$ . So we can apply the Lorentz transformation equations for finding the potentials in the moving frame, which is the rest frame of the beam (\*). The flow of charges can be considered slow enough in the beam rest frame and so the magnetic fields can be ignored. This results in potentials that are purely electrostatic in the rest frame i.e  $\mathbf{A}_\mu^* = (\phi^*, 0)$ . Then, using the inverse Lorentz transformations the magnetic potential in the ground frame of reference,  $A_z$ , can be found [50].

$$A_z = \frac{\beta}{c} \phi \quad (3.25)$$

Substituting equations (3.22) to (3.25) in (3.21), the self field force becomes

$$\vec{F}^s = q \left[ -\nabla\phi + \hat{z}\beta c \times (\nabla \times \hat{z}\frac{\beta}{c}\phi) \right] \quad (3.26)$$

This can be further written in the form [50]

$$\vec{F}^s = \frac{-q}{\gamma^2} \frac{\partial\phi}{\partial\mathbf{x}_\perp} - \hat{z}q \frac{\partial\phi}{\partial z} \quad (3.27)$$

where  $\partial\phi/\partial\mathbf{x}_\perp = \hat{x}\partial/\partial x + \hat{y}\partial/\partial y$ . The first term represents the transverse component of the self field force and the second term represents the longitudinal component. It can also be inferred that as the longitudinal velocity increases, value of  $\gamma$  increases and the transverse component of the self field force  $[\mathbf{F}^s_\perp = (-q/\gamma^2)(\partial\phi/\partial\mathbf{x}_\perp)]$  decreases, i.e. *space charge force decreases*.

Let us now consider the static applied field from equation 3.21. Separated into transverse and longitudinal components,  $\vec{v}^a = \mathbf{v}_\perp^a + \hat{z}\beta c$ ,  $\vec{B}^a = \mathbf{B}_\perp^a + \hat{z}B_z^a$ ,  $\vec{E}^a = \mathbf{E}_\perp^a + \hat{z}E_z^a$  the equation becomes

$$\vec{F}^a = q[(\mathbf{E}_\perp^a + \hat{z}E_z^a) + (\mathbf{v}_\perp^a + \hat{z}\beta c) \times (\mathbf{B}_\perp^a + \hat{z}B_z^a)] \quad (3.28)$$

$$\vec{F}^a = q[(\mathbf{E}_\perp^a + \hat{z}E_z^a) + \hat{z}(v_x^a B_y^a - v_y^a B_x^a) + (\mathbf{v}_\perp^a \times \hat{z}B_z^a) + (\hat{z}\beta c \times \mathbf{B}_\perp^a)] \quad (3.29)$$



The total *Lorentz* force on the particles can be obtained by adding equations 3.27 and 3.29. Separating them further, the forces experienced by particles in the beam in transverse and longitudinal directions can be derived as [50]

$$\mathbf{F}_\perp = q \left[ (\mathbf{E}_\perp^a) + (\mathbf{v}_\perp^a \times \hat{z} B_z^a) + (\hat{z} \beta c \times \mathbf{B}_\perp^a) - \frac{1}{\gamma^2} \frac{\partial \phi}{\partial \mathbf{x}_\perp} \right] \quad (3.30)$$

$$F_z = q \left[ E_z^a + (v_x^a B_y^a - v_y^a B_x^a) - \frac{\partial \phi}{\partial z} \right] \quad (3.31)$$

### 3.4 Particle motion in transverse planes

The transverse equation of motion in 3.30 can be expressed in terms of an independent variable  $s$ , where  $s$  is the axial coordinate (beam line location) of a reference particle travelling through the beam line. The reference particle has no momentum spread. The axial velocity can be expressed in terms of  $s$ ,  $v_z = ds/dt$

$$v_x = \frac{dx}{dt} = \frac{dx}{ds} \frac{ds}{dt} = v_z \frac{dx}{ds} = \beta c x' \quad (3.32)$$

$$v_y = \frac{dy}{dt} = \frac{dy}{ds} \frac{ds}{dt} = v_z \frac{dy}{ds} = \beta c y' \quad (3.33)$$

where  $' \equiv d/ds$ . In the paraxial approximation,  $x'$  and  $y'$  can be interpreted as the angles the particle makes with the longitudinal axis. The transverse *Lorentz* force in equation 3.30 can be written as  $\mathbf{F}_\perp = (d/dt)(m\gamma\mathbf{v}_\perp)$ . With  $\mathbf{v}_\perp = d\mathbf{x}_\perp/dt$ ,  $\mathbf{F}_\perp = (d/dt)[m\gamma(d/dt)\mathbf{x}_\perp]$ . This can be converted in terms of axial coordinate  $s$

$$\mathbf{F}_\perp = \beta c \frac{d}{ds} \left( m\gamma \frac{d}{dt} \mathbf{x}_\perp \right) \quad (3.34)$$

$$\mathbf{F}_\perp = m\gamma\beta^2 c^2 \mathbf{x}_\perp'' + m\beta c^2 (\gamma\beta)' \mathbf{x}_\perp' \quad (3.35)$$

Equation 3.35 can be substituted in the L.H.S of equation 3.30. With  $\mathbf{v}_\perp^a \times \hat{z} B_z^a$  becoming  $B_z^a v_z \mathbf{x}_\perp' \times \hat{z}$ , the equation of motion in the transverse plane can be derived as [50]

$$\mathbf{x}_\perp'' + \frac{(\gamma\beta)'}{\gamma\beta} \mathbf{x}_\perp' = \frac{q\mathbf{E}_\perp^a}{m\gamma\beta^2 c^2} + \frac{qB_z^a \mathbf{x}_\perp' \times \hat{z}}{m\gamma\beta c} + \frac{q\hat{z} \times \mathbf{B}_\perp^a}{m\gamma\beta c} - \frac{q}{m\gamma^3 \beta^2 c^2} \frac{\partial \phi}{\partial \mathbf{x}_\perp} \quad (3.36)$$

The above equation can be applied to particle motion inside different kinds of beam lines. The transverse components of the external applied electric and magnetic fields ( $\vec{E}_\perp^a$ ,  $\vec{B}_\perp^a$ ) should be substituted in the above equation to find out the particle trajectory in the transverse plane. The equations of motion for a linear focusing beam line (electric quadrupole, magnetic quadrupole, solenoid, etc.) can be obtained in the following general form [50]

$$x'' + \frac{(\gamma\beta)'}{\gamma\beta} x' + \kappa_x(s)x = -\frac{q}{m\gamma^3 \beta^2 c^2} \frac{\partial \phi}{\partial x} \quad (3.37)$$

$$y'' + \frac{(\gamma\beta)'}{\gamma\beta} y' + \kappa_y(s)y = -\frac{q}{m\gamma^3\beta^2c^2} \frac{\partial\phi}{\partial y} \quad (3.38)$$

where  $\kappa(s)$  is the focusing function which takes different forms in different beam line structures. If we consider that the beam has no acceleration ( $\gamma\beta = \text{constant}$ ) and the electric fields due to space charge are negligible ( $\partial\phi/\partial x, \partial\phi/\partial y \approx 0$ ) then the equations (3.37, 3.38) change to the *Mathieu-Hill's* equations[52].

$$x'' + \kappa_x(s)x = 0 \quad (3.39)$$

$$y'' + \kappa_y(s)y = 0 \quad (3.40)$$

The solutions of the second order linear differential equations of the above form are uniquely determined by initial values of the dependant variables ( $x$  or  $y$ ) and the first derivatives ( $x'$  or  $y'$ ) [66]. For the solution in  $x-x'$ , for equation 3.39, this is represented by the matrix below [50].

$$\begin{bmatrix} x(s) \\ x'(s) \end{bmatrix} = \begin{bmatrix} C(s) & S(s) \\ C'(s) & S'(s) \end{bmatrix} \begin{bmatrix} x(s_0) \\ x'(s_0) \end{bmatrix} \quad (3.41)$$

where  $C$  ('cosine' like) and  $S$  ('sine' like) are the solutions of equation 3.39, such that  $C'' + \kappa_x(s)C = 0$  and  $S'' + \kappa_x(s)S = 0$  and  $x(s_0), x'(s_0)$  are initial values. The eigenvalue equation of the solution matrix can be obtained in the form of the quadratic equation,  $\lambda^2 - \lambda(C + S') + 1 = 0$ . A solution to this equation leads to the eigenvalues  $\lambda_1 = \exp(i\sigma_0)$  and  $\lambda_2 = \exp(-i\sigma_0)$  with  $\cos \sigma_0 = (1/2)(C + S')$ . Such properties of the solution matrix are typical of the characteristics of differential equations outlined in *Floquet's* theorem [50, 52]. As per this theorem, two independent solutions can be obtained for equation 3.39 as below [52],

$$u(s) = \omega(s)e^{i\psi(s)}; \quad v(s) = \omega(s)e^{-i\psi(s)} \quad (3.42)$$

where  $\omega(s)$  represents the focusing action of the beam line and  $\psi(s)$  represents the phase of oscillation around the equilibrium orbit of the beam line. Substitution of  $u(s)$  or  $v(s)$  in equation 3.39 leads to the differential equation in the amplitude function,  $\omega(s)$

$$\omega''(s) + \kappa_x(s) - \frac{1}{\omega^3} = 0 \quad (3.43)$$

The general solution of equation 3.39 can be expressed as the linear combination of the independent solutions in equation 3.42. This leads to the phase-amplitude form of the solution of particle trajectory as

$$x(s) = A_i \omega(s) \cos \psi(s) \quad (3.44)$$

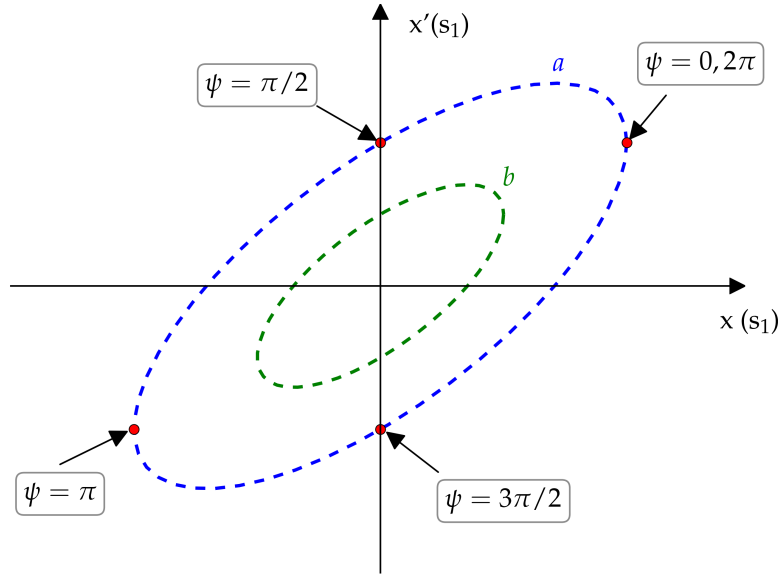


**Figure 3.5:** Trajectory traced out in  $x - x'$  trace space for different values of  $\psi(s)$  at a fixed beam line location  $s_1$ . Initial condition,  $A_i = a, b$ , where  $b < a$ .

and the derivative

$$x'(s) = A_i \left[ \omega'(s) \cos \psi(s) - \frac{1}{\omega(s)} \sin \psi(s) \right] \quad (3.45)$$

where  $A_i$  is a constant of motion, dependant only on the initial conditions and not affected by the beam line. A general graph of  $(x, x')$  using the above equations, at a fixed beam line location  $s = s_1$ , generates an ellipse as shown in Fig. 3.5. As shown in the graph, different values of  $\psi(s)$  give different particle locations on the *same* ellipse. Particles with a smaller amplitude,  $A_i$  will follow the trajectory of a smaller ellipse [67]. The equations are valid for  $y - y'$  variables also.

By combining equations 3.44 and 3.45, we can derive an *invariant* of motion in  $x - x'$  variables as below.

$$\left[ \frac{\omega^2 \omega'^2 + 1}{\omega^2} \right] x^2 + 2[-\omega \omega'] x x' + [\omega^2] x'^2 = A_i^2 \quad (3.46)$$

Equation 3.46 represents the *Courant-Snyder invariant* which is very important in the transverse beam dynamics [52]. It can also be inferred that the motion in the  $x - x'$  space, the trace space (section 3.2), can be represented by a rotated ellipse due to the quadratic form of the equation. Thus it can be rewritten as

$$\hat{\gamma} x^2 + 2\hat{\alpha} x x' + \hat{\beta} x'^2 = A_i^2 \quad (3.47)$$

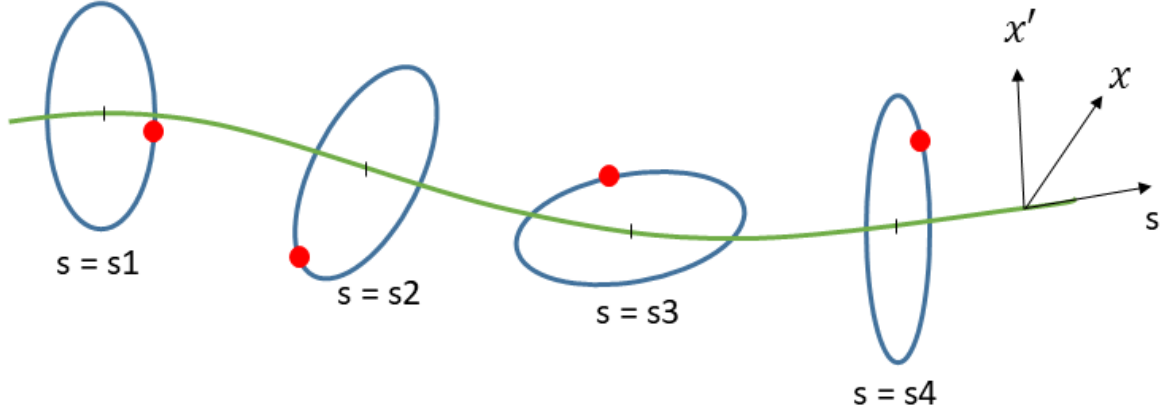


**Figure 3.6:** Trace space ellipse at different beam line locations with different arbitrary  $\hat{\beta}(s)$  values. Area of the ellipse remains the same, but the shape of the ellipse changes depending on the  $\hat{\beta}(s)$ . Location of the particle on the ellipse is dependent on  $\psi(s)$ , as shown in Fig. 3.5.

where  $\hat{\beta}(s) = \omega^2$ ,  $\hat{\alpha}(s) = (-1/2)(d\hat{\beta}/ds)$  and  $\hat{\gamma}(s) = (\hat{\alpha}^2 + 1)/\hat{\beta}$  are functions dependant only on the beam line,  $\omega(s)$  and are called the *Twiss parameters*.  $\hat{\beta}(s)$ , called the *betatron function* or *amplitude function*, reflects the exterior forces in the beam line and it affects the shape of the trace space ellipse as shown in Fig. 3.6. The area of the ellipse, represented by equation 3.47, can be obtained as  $\pi A_i^2 / (\hat{\gamma}\hat{\beta} - \hat{\alpha}^2)^{1/2} = \pi A_i^2$ , since  $\hat{\gamma}\hat{\beta} - \hat{\alpha}^2 = 1$ . Hence the area of the elliptical trajectory of a particle in the  $x - x'$  trace space is given by

$$\int_{\text{ellipse}} dx dx' = \pi A_i^2 \quad (3.48)$$

which represents an invariant in the motion through the beam line, since  $A_i$  depends only on the initial conditions of motion. In section 3.2, it was shown that 6D phase space volume and 2D trace space area (for decoupled case) are invariants in the beam propagation through a beam line. This can be compared with equation 3.48 and can be said that we can associate an ellipse, the *twiss ellipse*, of constant area to a constant trace space area. Such constants present in the description of beam propagation leads to the definition of an important figure of merit related to the beam quality, the **beam emittance** [52]. In the  $x - x'$  trace space, beam emittance is defined as  $(1/\pi) \times \text{area of the ellipse}$  which represents the trajectory of the outermost particle in trace space and is denoted as  $\epsilon_x$ . Hence we can rewrite 3.47 in terms of  $\epsilon_x$

$$\hat{\gamma}x^2 + 2\hat{\alpha}xx' + \hat{\beta}x'^2 = \epsilon_x \quad (3.49)$$

In most cases, it is desirable to keep the emittance value of a beam as low as possible. Even though Liouville's theorem predicts emittance conservation, there are many processes which

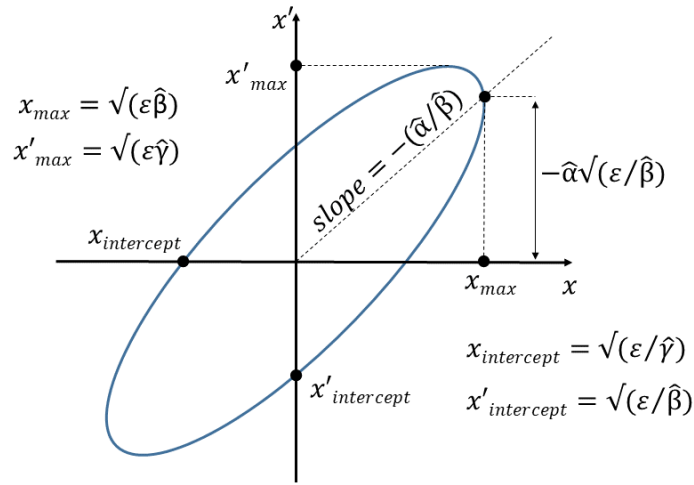


Figure 3.7: Twiss ellipse

act against this in beam propagation. Some of them are synchrotron radiation emission, space charge effects, scattering on residual gas and intra beam scattering [68]. Maintaining the beam emittance under control is one of the challenges in accelerators.

### 3.5 Features of the Twiss ellipse

The equation 3.49 can be rewritten in the following two different forms using the relation  $\hat{\beta}\hat{\gamma} = 1 + \hat{\alpha}^2$ .

$$(\hat{\beta}x' + \hat{\alpha}x)^2 + x^2 = \epsilon_x\hat{\beta} \quad (3.50)$$

$$(\hat{\alpha}x' + \hat{\gamma}x)^2 + x'^2 = \epsilon_x\hat{\gamma} \quad (3.51)$$

Dimensions of the twiss ellipse can be found out from equation 3.49. By setting  $x = 0$  and  $x' = 0$ , it is possible to determine the  $x$  intercept and  $x'$  intercept of the ellipse. The maximum values,  $x_{max}$  and  $x'_{max}$  which denotes the half angle and half width of the beam in trace space, can be determined from equations 3.50 and 3.51 using the differentiation method ( $dx'/dx = 0$  for finding  $x'_{max}$  and  $dx/dx' = 0$  for finding  $x_{max}$ ). The values are shown in Fig. 3.7. These values help to determine the sizes of apertures needed for beam propagation without losses.

### 3.5.1 Ellipse propagation in beam line

Propagation of the ellipse in Fig. 3.7, which represents the beam envelope, through the beam line can be further studied with the help of the *envelope* equation [52],

$$x''_{max} + \kappa_x(s)x_{max} - \frac{\epsilon_x^2}{x_{max}^3} = 0 \quad (3.52)$$

obtained by using the relation  $x_{max} = (\epsilon\beta)^{1/2} = \epsilon^{1/2}\omega$ , in the amplitude function equation 3.43, where  $x_{max}$  is a function of beam line location  $s$ . In the case of a beam line without any focusing ( $\kappa_x(s) = 0$ ), the beam is drifting in free space. With  $x_0$  and  $x'_0$  as the initial conditions at location  $s_0$ , the solution to the above equation for a freely drifting beam is obtained as [51]

$$x_{max}(s) = \sqrt{[(x_0 + x'_0(s - s_0))^2 + \frac{\epsilon_x^2}{x_0^2}(s - s_0)^2]} \quad (3.53)$$

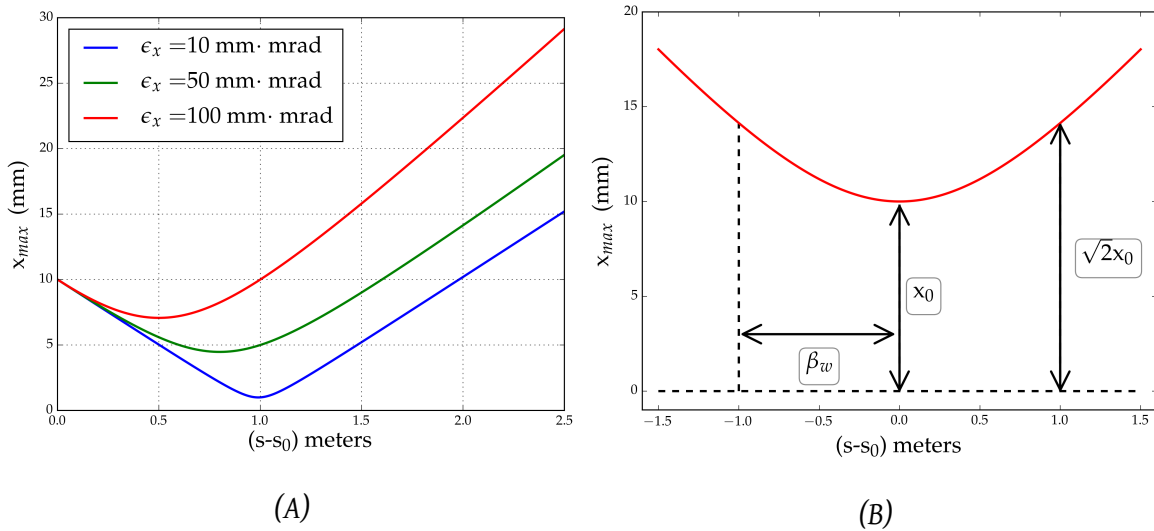


**Figure 3.8:** (A) Variation in the beam radius with distance ( $s$ ) for three different emittance values. (B) Beam radius increases by  $\sqrt{2}$  times at a distance of  $\beta_w$  from beam waist for a beam with zero initial divergence ( $x'_0 = 0$ ).

The solution is plotted in Fig. 3.8(A) for a beam with initial conditions  $x_0 = 10$  mm and  $x'_0 = -10$  mrad at  $s = s_0$ , with different emittance values. Initially, the beam converges to a location with minimum beam radius, the *beam waist* and then starts to diverge. It can be seen that as emittance becomes larger, the width of the beam becomes wider. Fig. 3.8(B) shows a special case of the beam with no divergence at the beam waist,  $x'_0 = 0$ . The equation for this

case can be obtained from equation 3.53 as

$$x_{max}(s) = x_0 \sqrt{1 + \left[ \frac{(s - s_0)}{\beta_w} \right]^2} \quad (3.54)$$

As shown in the figure, the radius of the beam increases by  $\sqrt{2}$  times its width at the beam waist, at a characteristic length  $\beta_w = x_0^2/\epsilon$  for a freely drifting beam. From the figures, it can be understood that the emittance term in the envelope equation (3.52) acts in a manner causing continuous defocusing of the beam [51, 52]. The  $(1/x_{max}^3)$  factor indicates that the defocusing is more when the beam cross sectional area is small and indicates the need for external focusing elements when small beam sizes are required.

### 3.5.2 Orientation of ellipse

Orientation of the ellipse in trace space indicates whether a beam is converging or diverging. This is illustrated in Fig. 3.9, which shows a beam travelling from left to right. The trace space ellipse at 3 locations along the beam direction ( $z$ ) is also shown. The beam is subjected to some focusing inside a solid electrode (indicated by blue color). As the beam converges, the width of the beam ( $2x_{max}$ ) decreases and as seen from the relation,  $x_{max} = (\epsilon_x \beta)^{1/2}$  in Fig. 3.7,  $\hat{\beta}$  has also decreased. Since  $\hat{\alpha}$  is a negative derivative of  $\hat{\beta}$ , an decreasing  $\hat{\beta}$  gives positive value to  $\hat{\alpha}$ . In the case of a diverging beam, beam width increases and this gives a negative value for  $\hat{\alpha}$ . Thus, the slope of the line shown in Fig. 3.7 becomes positive for a diverging beam and ellipse lies in first and third quadrants, as indicated by the 3<sup>rd</sup> ellipse. The slope becomes negative for a converging beam, which means that the ellipse lies in the second and fourth quadrants, as indicated by the 1<sup>st</sup> ellipse. The middle ellipse represents the beam waist location where  $\hat{\alpha} = 0$ .

### 3.5.3 Location of the beam waist

In the case of diverging or converging beams, the beam waist location can be found by direct calculation from a known set of twiss parameters [53]. The twiss ellipse at two different locations ( $z = 0$  &  $z = z$ ) in the beam path is represented by the equations below.

$$\hat{\gamma}_0 x_0^2 + 2\hat{\alpha}_0 x_0 x'_0 + \hat{\beta}_0 x'^2_0 = \epsilon_x \quad (3.55)$$

$$\hat{\gamma}_z x_z^2 + 2\hat{\alpha}_z x_z x'_z + \hat{\beta}_z x'^2_z = \epsilon_x \quad (3.56)$$

After substituting the values of  $x_z$  and  $x'_z$  from equation 3.41 (considering  $s = z$ ) in equation 3.56 and rearranging the terms, we can derive the following relation between the values of

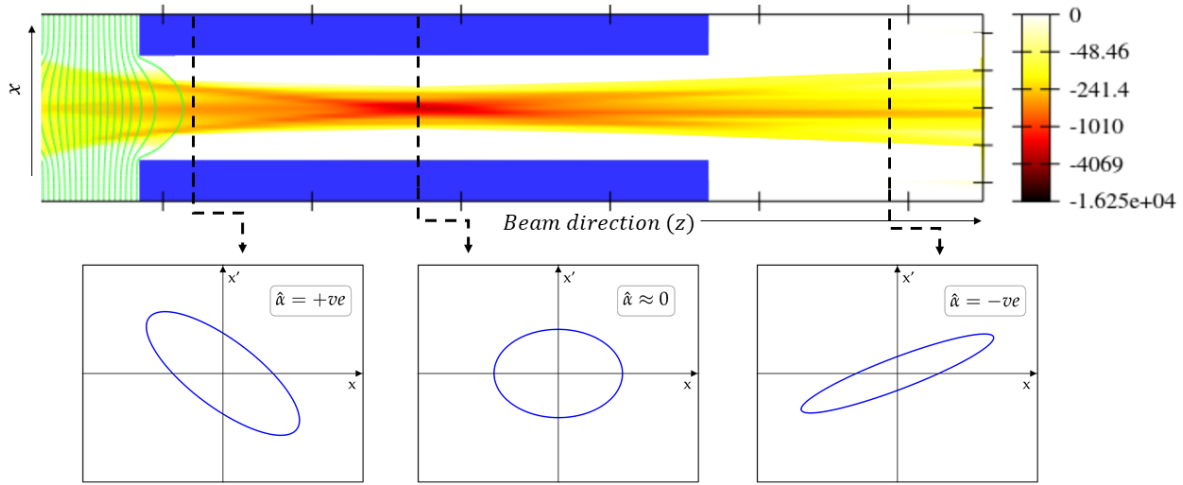


**Figure 3.9:** Differences in the orientation of trace space ellipse at 3 different transverse planes along the path of a beam. The beam undergoes an initial focusing due to potentials on the electrode (blue color). It diverges later in its path. The location of transverse planes are indicated by dashed lines. The color map indicates the current density in the beam.

twiss parameters.

$$\begin{bmatrix} \hat{\beta}_z \\ \hat{\alpha}_z \\ \hat{\gamma}_z \end{bmatrix} = \begin{bmatrix} C^2 & -2CS & S^2 \\ -CC' & CS' + C'S & -SS' \\ C'^2 & -2C'S' & S'^2 \end{bmatrix} \begin{bmatrix} \hat{\beta}_0 \\ \hat{\alpha}_0 \\ \hat{\gamma}_0 \end{bmatrix} \quad (3.57)$$

In the case of transport through a drift space of length  $l$ , the values can be obtained easily as

$$\begin{bmatrix} C(s) & S(s) \\ C'(s) & S'(s) \end{bmatrix} = \begin{bmatrix} 1 & l \\ 0 & 1 \end{bmatrix} \quad (3.58)$$

Substituting these values in equation 3.57, the values of the twiss parameters in the transport through the drift space can be obtained as

$$\begin{bmatrix} \hat{\beta}_z \\ \hat{\alpha}_z \\ \hat{\gamma}_z \end{bmatrix} = \begin{bmatrix} 1 & -2l & l^2 \\ 0 & 1 & -l \\ 0 & 0 & 1 \end{bmatrix} \begin{bmatrix} \hat{\beta}_0 \\ \hat{\alpha}_0 \\ \hat{\gamma}_0 \end{bmatrix} \quad (3.59)$$

The above equation helps to obtain the location of beam waist in a drift space. If  $\hat{\beta}_0$ ,  $\hat{\alpha}_0$  and  $\hat{\gamma}_0$  represent the unknown values of the ellipse at the beam waist location ( $\hat{\alpha}_0 = 0$ ) and  $\hat{\beta}_z$ ,  $\hat{\alpha}_z$  and  $\hat{\gamma}_z$  represent the known parameters at a distance of  $l$  from beam waist, then  $l$  can be obtained as  $l = \hat{\alpha}_z / \hat{\gamma}_z$



### 3.6 RMS Emittance

The definition of emittance in terms of area of the trace space ellipse does not take into account the pattern of distribution of particles in the transverse plane of beam propagation. For example, a beam with particle density higher towards the centre of a beam line and another beam with particle density higher towards the edge of beam line, would result in the same emittance, as long as the outermost particle trajectory remains the same. Also, the information about all the particles will not be available in practical cases and this leads to errors in the calculated area. In order to overcome these drawbacks and define the emittance in terms of beam quality, a statistical method of **RMS emittance** was introduced.

In 1971, Lapostolle [69] introduced rms quantities for calculating the emittance of particle beams, which takes into account the distribution of particles around the mean values. The rms emittance in the  $x - x'$  trace space is defined as follows [32, 52]

$$\epsilon_{x,rms} = [\langle x^2 \rangle \langle x'^2 \rangle - \langle xx' \rangle^2]^{1/2} \quad (3.60)$$

where  $\langle x^2 \rangle = \frac{1}{N} \sum_{i=1}^N x_i^2$ ,  $\langle x'^2 \rangle = \frac{1}{N} \sum_{i=1}^N x_i'^2$ ,  $\langle xx' \rangle = \frac{1}{N} \sum_{i=1}^N x_i x_i'$  represent the rms values of the distribution of N particles. In the case where the particle distribution is available in terms of distribution functions, the terms can be defined as

$$\langle x^2 \rangle = \frac{\iint x^2 I(x, x') dx dx'}{\iint I(x, x') dx dx'} \quad (3.61)$$

$$\langle x'^2 \rangle = \frac{\iint x'^2 I(x, x') dx dx'}{\iint I(x, x') dx dx'} \quad (3.62)$$

$$\langle xx' \rangle = \frac{\iint x x' I(x, x') dx dx'}{\iint I(x, x') dx dx'} \quad (3.63)$$

$I(x, x')$  is equivalent to the distribution function mentioned in section 3.2 and represents the density of particles as a function of the coordinates. In practical situations  $I(x, x') dx dx'$  is the beam current in the elemental area  $dx dx'$ .

The trace space distributions described through the above equations are assumed to be centered at the origin so that the mean values are zeros i.e  $\langle x \rangle = 0$ ,  $\langle x' \rangle = 0$ . If they are not

centered, the equations need to be modified like  $x \Rightarrow [x - \langle x \rangle]$  and  $x' \Rightarrow [x' - \langle x' \rangle]$ . Then we can use the standard deviation notations,

$$\sigma_x^2 = \frac{1}{N} \sum_{i=1}^N (x_i - \langle x \rangle)^2, \sigma_{x'}^2 = \frac{1}{N} \sum_{i=1}^N (x'_i - \langle x' \rangle)^2, \sigma_{xx'} = \frac{1}{N} \sum_{i=1}^N (x_i - \langle x \rangle) (x'_i - \langle x' \rangle) \quad (3.64)$$

and rewrite the rms emittance equation as [70]

$$\epsilon_{x,rms} = \sigma_x \cdot \sigma_{x'} \sqrt{1 - r^2} \quad (3.65)$$

where  $r = \sigma_x \sigma_{x'} / (\sigma_x^2 \sigma_{x'}^2)^{1/2}$  is the correlation factor having values 0 to 1. As seen from this equation the rms emittance defined is associated with 1 standard deviation. If the emittance need to be associated with 2 standard deviations then we can define a  $4 \times$  rms emittance,  $4\epsilon_{x,rms} = 2\sigma_x \cdot 2\sigma_{x'} \sqrt{1 - r^2}$ .

The above definition of rms emittance does not assign any shape to the beam boundary. It is possible to construct an ellipse similar to the twiss ellipse defined in equation 3.49 and Fig. 3.7, to the rms emittance [68]. This is done by assigning the standard deviations of the distribution to the twiss parameters.

$$\hat{\beta} = \frac{\sigma_x^2}{\epsilon_{x,rms}}, \hat{\gamma} = \frac{\sigma_{x'}^2}{\epsilon_{x,rms}}, \hat{\alpha} = -\frac{\sigma_{xx'}}{\epsilon_{x,rms}}; \quad (3.66)$$

The statistical rms emittance is a conserved quantity only when the motion is under linear forces [68].

### 3.7 Normalized emittance

For the derivation of Mathieu-Hill's equation in section 3.4 and emittance studies so far, it was assumed that the beam undergoes no acceleration. But in real accelerators this is not the case. As mentioned in equation 3.19, the beam emittance which represents the 2D transverse area of the trace space, remains a constant of motion only if the longitudinal momentum remains a constant for the beam. Acceleration of the beam changes the longitudinal momentum and couples the longitudinal plane with the transverse planes. The 6D emittance is still conserved during acceleration, but the 2D transverse emittance values are not. As can be seen from equation 3.19, this problem can be resolved if we multiply the trace space area by  $(\gamma\beta)$  and this is used for defining the **normalized emittance** [52].

$$\epsilon_n = \gamma\beta\epsilon \quad (3.67)$$

In particle accelerators, normalized emittance is a more useful quantity since the value remains constant throughout the entire motion. Also, a change in the normalized emittance value is an indication of any non-linear effects affecting the beam quality in the system [52].

### 3.8 Space charge

In section 3.1.2, it was shown that space charge would lead to limitations in ion extraction from the plasma boundary. Also, space charge associated with the ion beam will result in self field forces as seen in equation 3.26. These fields are functions of the charge and current distribution inside the beam [52]. This influence of space charge on beam transport is detailed in this section.

#### 3.8.1 Effect of space charge in beam transport

Let us consider a particle beam of uniform circular cross section of radius  $\sigma_x$  and charge density  $\rho$  propagating through a beam line with constant velocity  $v_z (= \beta c)$ . It carries a current  $I$  with current density  $J$  such that  $J = \rho\beta c$ . It is convenient to study the electric and magnetic fields produced by the beam in polar coordinates  $(r, \phi)$  to take advantage of the symmetry. Since we assume a continuous beam and that the variation of beam radius with longitudinal distance  $z$  is slow, the electric field component  $E_z$  and radial magnetic field component  $B_r$  can be neglected [52, 53]. Using Gauss' law the electric field generated by the charged particles inside a beam pipe of radius  $r_p$  can be derived as [71]

$$E_r^s = \begin{cases} \frac{I}{2\pi\epsilon_0\beta c} \frac{r}{\sigma_x^2} & \text{if } r \leq \sigma_x, \\ \frac{I}{2\pi\epsilon_0\beta c} \ln\left(\frac{r}{r_p}\right) & \text{if } \sigma_x < r \leq r_p. \end{cases} \quad (3.68)$$

The magnetic field generated by the charged particles can be derived from Maxwell's law and Stoke's theorem as

$$B_\phi^s = \frac{I}{2\pi\epsilon_0 c^2} \frac{r}{\sigma_x^2} \quad \text{where } r < \sigma_x \quad (3.69)$$

Hence, the fields vanish at the centre of the beam,  $r = 0$  and increase linearly towards the beam edges. The potential,  $\phi$ , generated inside the beam pipe can be found by integrating equation 3.68. The behavior is shown in Fig. 3.10 for an  $H^-$  beam propagation at different beam energies. As can be seen, the negative ion space charges create a potential well at low energies, whose depth decreases as particle velocity increases.

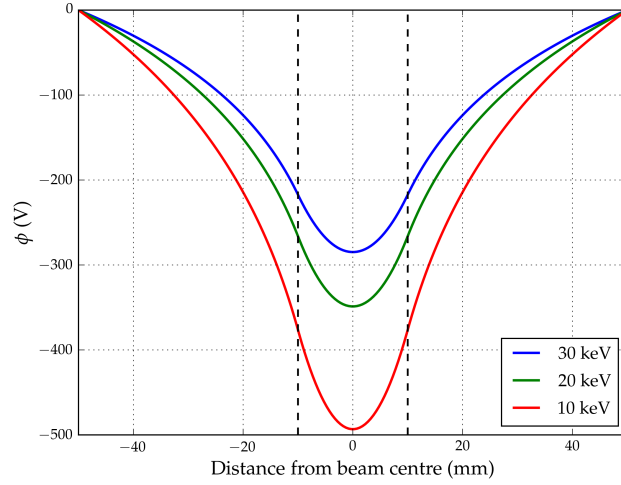


**Figure 3.10:** Variation in the potential, due to space charges, along a plane transverse to beam propagation. An 18 mA  $H^-$  beam with a uniform density and radius of 10 mm, propagating in a beam pipe of radius 50 mm is considered here. The boundary condition  $\phi(r_p) = 0$  is applied. The dashed lines represent the beam edges.

The force due to these self fields by space charge, acting along the transverse  $x$ -direction, can be obtained from Lorentz law,  $F_x^s = q[\vec{E} + (\vec{v} \times \vec{B})]_x^s$ . Since  $B_z^s = 0$  for charged particle motion in  $z$ -direction,  $F_x^s = q[E_x^s - v_z B_y^s]$ . Substituting values from equations 3.68, 3.69 for  $r < \sigma_x$  and using  $E_x^s = E_r^s \cos \phi$ ,  $B_y^s = B_\phi^s \cos \phi$  and  $\cos \phi = x/r$

$$F_x^s = q(E_x^s - v_z B_y^s) = \frac{qI}{2\pi\epsilon_0\beta c} \frac{x}{\sigma_x^2} (1 - \beta^2) = \frac{q}{\gamma^2} E_x^s \quad (3.70)$$

As seen from the above equation, the generated magnetic field acts opposite to the electric field force and they cancel each other at relativistic speeds,  $\beta \approx 1$ . So the space charge effect is mainly a non-relativistic phenomenon. The effect of space charge on particle motion can be seen by substituting the electric field value in equation 3.68 in the equation of motion derived in equation 3.37. Then, ignoring beam acceleration, we obtain

$$x'' + \left[ \kappa_x(z) - \frac{qI}{2\pi\epsilon_0 m \gamma^3 \beta^3 c^3 \sigma_x^2} \right] x = 0 \quad (3.71)$$

$$x'' + \left[ \kappa_x(z) - \frac{K}{\sigma_x^2} \right] x = 0 \quad (3.72)$$

It can be inferred from the above equation that space charges essentially act as a *defocusing lens* leading to an increase of beam size during its propagation through a beam line [52].  $K$  is the dimensionless quantity called *generalized beam perveance* which represents the space

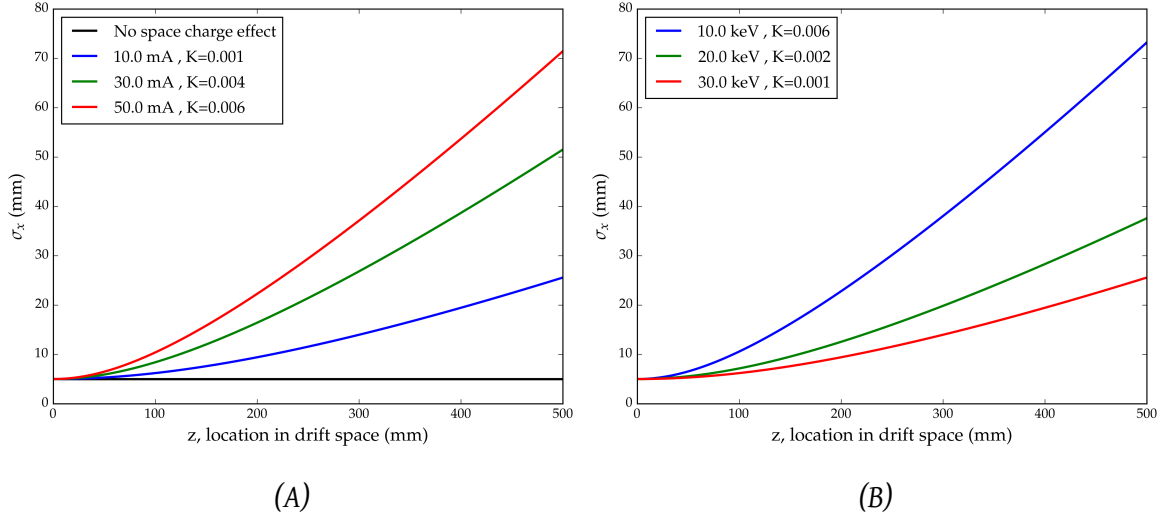


**Figure 3.11:** Space charge effects on beam propagation in drift space (eq.3.73). Variation in beam radius for (A) different beam currents at 30 keV energy and (B) different beam energies for a 10 mA beam.

charge effects in beam propagation. In the case when  $K$  is negative, then this leads to an opposite effect, *focusing* of the beam by space charges.

A particle at the beam boundary experiences a force and an acceleration due to space charge. This can be demonstrated using equation 3.72 by ignoring any external focusing,  $\kappa_x(z) = 0$  and that the particle is located at the beam boundary,  $x = \sigma_x$ . This gives [72]

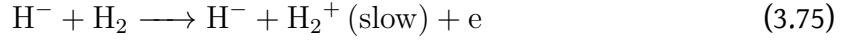
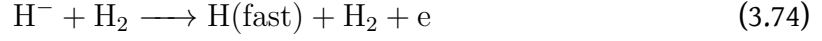
$$\frac{d^2\sigma_x}{dz^2} = \frac{K}{\sigma_x} \quad (3.73)$$

The solution of the above equation for different beam currents and energies, in a drift space, is shown in Fig. 3.11. As can be seen, both higher currents and lower energies will increase the perveance values and the beam spread. Since the current density is uniform, the forces are linear and in theory, the rms emittance will still be conserved. In real beams, the current density will not be uniform as considered here. This will lead to non-linear space charge effects resulting in emittance growth.

### 3.8.2 Space charge compensation

As seen in the previous section, transport of a low energy beam is difficult due to the space charge effects. One of the processes that comes to the rescue is the beam space charge compensation (SCC). During the transport of ion beam through a beam line, depending on the vacuum level of the region, collisions can occur between the particles in the beam and

background gas. This can result in collisional ionization producing other ions, electrons and neutrals. This can lead to *partial neutralization* of the charges in the beam. For example, in the case of  $H^-$  ion transport through a beam line having  $H_2$  background gas, the following reactions can occur [73].



Equation 3.74 is a *stripping* reaction leading to the loss of  $H^-$  ion. Other reactions mentioned above lead to residual gas ionization, producing compensating particles. The electrons are immediately ejected out of the  $H^-$  beam due to the potential well of the space charges as seen in Fig. 3.10. On the other hand, the slow ions oscillate inside the potential well. This will result in SCC and decrease the local charge density in the beam. In the case of a positive ion beam, like a proton beam, positive ions are ejected out of the beam and electrons contribute to compensation [73].

Let  $f_e$  be the ratio of positive ions resulting in compensation to negative ions in the beam, in unit volume.  $f_e = 1$  represents 100 % compensation and  $f_e = 0$  represent no compensation. The resultant electric fields due to space charges, after compensation, are modified by a factor of  $(1 - f_e)$  compared to equation 3.68. The  $K$  value defined in equation 3.72 also gets modified as [52]

$$K \implies K(1 - \gamma^2 f_e) \quad (3.77)$$

When  $f_e < 1/\gamma^2$ ,  $K$  is positive and leads to defocusing. But in the case when  $f_e > 1/\gamma^2$ ,  $K$  is negative and leads to *self focusing*. The self focusing is more important in the case of electron beams, where a small fraction of positive ions lead to focusing [52]. In the case of  $H^-$  ions, the self focusing is not of much use, as it happens at much higher pressures leading to increased stripping of negative ions and hence beam loss [74].

SCC is a crucial mechanism in the transport of intense beams in Low Energy Beam Transport systems (LEBT) [75]. It depends on the residual gas density and cross section of ionization of residual gas, which again is a function of transported ion beam. A characteristic time period,  $\tau$ , is defined for the process, which denotes the time taken for the compensation process to achieve a steady state. In the Linac4  $H^-$  simulation studies, at a pressure of  $1 \times 10^{-5}$  mbar,  $\tau = 50 \mu s$  for an SCC of 90 % [75].

### 3.9 External focusing forces

From the earlier discussions on emittance and space charge, it is understood that external focusing elements need to be used for successful beam transport. Some of the focusing elements commonly used are electric quadrupoles, magnetic quadrupoles and solenoids. The equation of motion in a beam line, involving the action of external forces, are very briefly mentioned here.

The external focusing action in a beam line is introduced through the  $\kappa(z)$  term in equation 3.37. The value of  $\kappa(z)$  depends on the external focusing element in the beam line. From equation 3.36, an expression for transverse acceleration can be obtained as follows. Let us ignore the space charge effects for simplicity, ( $\partial\phi/\partial x \approx 0$ ), but include the acceleration term,

$$x'' + \frac{(\gamma\beta)'}{\gamma\beta}x' = \frac{q}{m\gamma\beta^2c^2} \left[ E_x^a + v_y B_z^a - v_z B_y^a \right] \quad (3.78)$$

$$x'' = -\frac{(\gamma\beta)'}{\gamma\beta}x' + \frac{F_x^a}{m\gamma\beta^2c^2} \quad (3.79)$$

From above, it can be deduced that [51]

$$\langle xx'' \rangle = -\frac{(\gamma\beta)'}{\gamma\beta} \langle xx' \rangle + \frac{\langle xF_x^a \rangle}{\beta c p} \quad (3.80)$$

Thus the effect of external forces on beam propagation can be added into the equation of motion, by finding out the moment of the external force,  $\langle xF_x^a \rangle$ . In the case of linear external forces,  $F_x^a = \pm kx$ . The sign depends on if the force is focusing or defocusing.

### 3.10 Space charge, emittance and focusing forces

In section 3.5.1, it was found from the envelope equation that the emittance term could lead to a beam defocusing effect. Again, in section 3.8.1, it was found that the space charges could also lead to a similar effect. The external forces act to overcome these effects through its focusing action, as mentioned in section 3.9. In this section, these effects are all combined to understand the beam propagation in a beam line. For this, the envelope equation in 3.52 is rewritten in rms terms (equation 3.64) [51].

$$\sigma_x'' - \frac{1}{\sigma_x} \langle xx'' \rangle = \frac{\epsilon_{x,rms}^2}{\sigma_x^3} \quad (3.81)$$

The total transverse acceleration due to space charges and external forces can be found by combining equations 3.79 and 3.73.

$$x'' = -\frac{(\gamma\beta)'}{\gamma\beta}x' + \frac{F_x^a}{m\gamma\beta^2c^2} + K\frac{x}{\sigma_x^2} \quad (3.82)$$

$\langle xx'' \rangle$  can be found similar to 3.80 with  $K \langle xx \rangle / \sigma_x^2 = K$ . Substituting this in equation 3.81 and using normalized emittance, the complete rms envelope equation that describes the variation of the beam envelope slope during the propagation, can be obtained as [75]

$$\sigma_x'' + \frac{(\gamma\beta)'}{\gamma\beta}\sigma_x' - \frac{\langle xF_x^a \rangle}{\gamma\beta^2c^2m\sigma_x} = \frac{\epsilon_{n,x,rms}^2}{(\gamma\beta)^2\sigma_x^3} + \frac{K}{\sigma_x} \quad (3.83)$$

The effects of space charge, emittance, acceleration and external focusing forces, on beam propagation can be summarised in the above equation [51]. As seen from the above sections, both emittance and space charge tries to defocus the beam. Factors like space charge compensation and external focusing thus become important in a successful beam transfer. The longitudinal acceleration term in the above equation acts in a way to dampen the envelope oscillations around the orbit and is hence called ‘adiabatic damping’ [51]. From the above equation it can be seen that there are roughly "two regimes of beam propagation, *space charge dominated* and *emittance dominated*" [52, 76]. A distinction can be made by defining the *laminarity parameter*,  $\rho_l$ , which is the ratio of the space charge term to the emittance term ( $\rho_l = K\gamma^2\beta^2\sigma_x^2/\epsilon_{n,x,rms}^2$ ). When  $\rho_l > 1$  the beam propagation is space charge dominated and quasi-laminar. When  $\rho_l < 1$  it is non-laminar and emittance dominated. The space charge dominated regime is the typical mode for low energy beam transports.



# Chapter 4

---

## Filament ion source experiments

D-Pace has established  $H^-$ ,  $D^-$  and  $C_2^-$  ion beam generation from its TRIUMF [13] licensed multicusp filament ion source. The maximum beam currents achieved from the ion source are 17.4 mA of  $H^-$ , 6.3 mA of  $D^-$  and 0.09 mA of  $C_2^-$  [77]. The negative ions are generated inside the plasma in the ion source mostly through volume production methods, as described in section 2.9.2. Magnetic fields are applied for plasma confinement and for controlling the electron temperatures in the plasma, as described in section 2.6. The basic methods of ion beam formation and propagation in the ion source are described in Chapter 3. As outlined in Chapter 1, improvements in the beam currents are advantageous for broadening the usefulness of the ion source. This requires a deeper understanding of the negative ion production methods in the plasma and the factors contributing to it. Some of the factors that could affect the ion source performance are the magnetic dipole fields in the plasma, surface interactions and electrode properties. The current chapter deals with the details of the experiments conducted in  $H_2$  and  $D_2$  plasmas for studying the influence of these factors in D-Pace's filament ion source.

Initial sections of this chapter detail the studies conducted to understand the influence of the magnetic dipole filter fields in extracting  $H^-$  and  $D^-$  currents. The  $D^-$  beam current obtained from the ion source is about one-third of the  $H^-$  beam current [77]. The same magnetic dipole field configuration is used for the extraction of both  $H^-$  and  $D^-$  ions. Investigations were carried out to understand if different magnetic dipole filter field strengths are required for  $H_2$  and  $D_2$  plasma for maximum negative ion extraction. The response of plasma parameters like electron temperature and electron density to different magnetic dipole filter fields are also studied using a Langmuir probe. The author has published most of the results from the initial sections of this chapter in AIP conference proceedings [78]. The chapter also deals with understanding the role of plasma – wall surface interactions in generating

negative ions in the plasma. Surface temperature dependence of these interactions is also studied. The last section of the chapter considers the role of the plasma electrode aperture sizes in improving the quality of the extracted ion beam.

## 4.1 Filament ion source overview

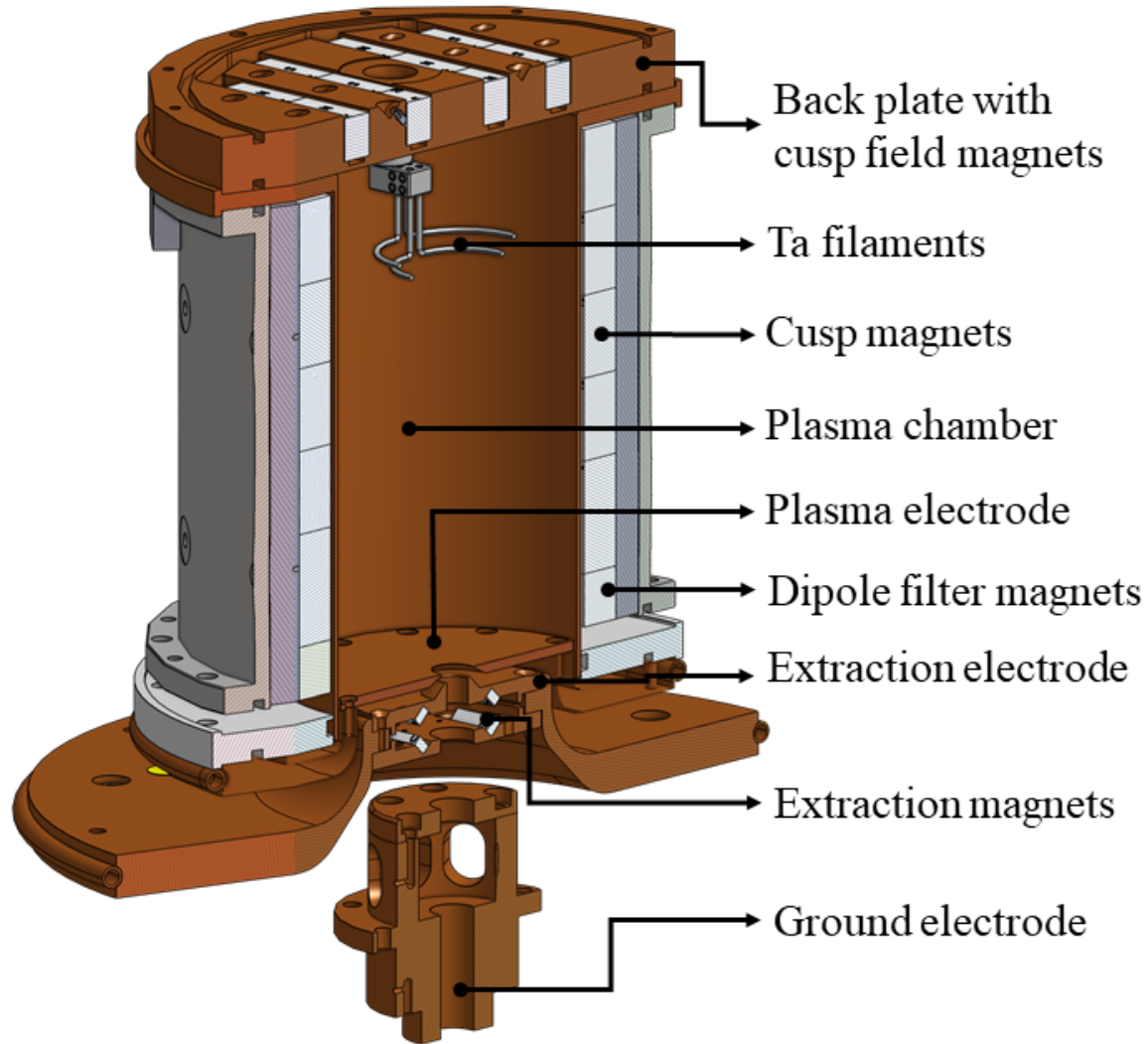


**Figure 4.1:** Section view of D-pace's TRIUMF licensed filament ion source. Water circulation is present around the plasma chamber. The plasma and extraction electrodes are cooled by conductive heat transfer with cooling water tubes. Dipole filter magnets are located close to the plasma electrode. Magnets forming the cusp magnetic fields are present around the plasma chamber and on the back plate.

The section view of D-Pace's TRIUMF licensed filament ion source [13] is presented in Fig. 4.1. The details of the beam extraction system, power supplies, vacuum system, beam

control parameters, beam tuning methods and diagnostics are outlined in Appendix B. The cylindrical copper plasma chamber is 98.4 mm in diameter and 160 mm in length. Plasma is ignited and sustained inside the plasma chamber of the ion source via thermionic emission from the electrically heated filaments. Filaments are made of four half circles of tantalum. The plasma is confined by 20 columns of  $\text{Sm}_2\text{Co}_{17}$  magnets and another 4 columns of magnets on the back plate which holds the filaments. These magnets form cusp fields, which helps in confining the electrons in the plasma, as described in section 2.6.4.

As shown in Fig. 4.1, the ion source uses plasma, extraction and ground electrodes for beam extraction. The plasma electrode and the extraction electrode are biased positive with respect to the plasma chamber. The plasma chamber, plasma electrode and extraction electrode are biased at a negative potential with respect to the ground electrode for the extraction of negative ions. The magnitude of the difference in potential between the ground electrode and plasma chamber determines the energy of the beam (0 – 30 keV) and is controlled by the bias power supply. More details on the power supply arrangement are shown in Fig. B.3.

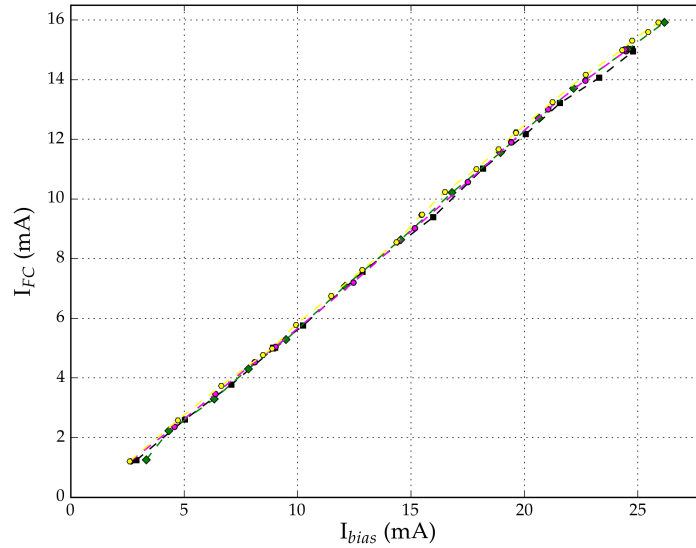


**Figure 4.2:** Relationship between  $I_{FC}$  and  $I_{bias}$  values, obtained from 5 different experiments at 30 keV beam energy.

The current recorded on the bias power supply,  $I_{bias}$ , represents the total current reaching the ground electrode. Even though  $I_{bias}$  consists of some back-streaming positive ions as well as some leakage current, it is approximated as the total amount of negative ions extracted from the plasma to the ground region. The co-extracted electrons from the plasma are deflected onto the extraction electrode by the magnetic field produced by the extraction

magnets. This magnetic field direction is transverse to the beam extraction, as shown in Fig. B.3. Experiments conducted by *Jayamanna et al.* prove that no significant amount of electrons can escape from this magnetic field and reach the ground electrode region [79]. Simulations also indicate the same, as shown in Fig. 6.3. Hence, the co-extracted electrons are considered to be not contributing to the measured  $I_{bias}$  values. The characteristic beam current from the ion source is the current measured at the Faraday cup, located 480 mm downstream from the plasma electrode and is represented as  $I_{FC}$ . The locations of the Faraday cup and emittance scanner are shown in Fig. B.2. The relationship between  $I_{bias}$  and  $I_{FC}$ , for the general experiments is shown in Fig. 4.2. As can be inferred from the graph, the variables change linearly and  $I_{FC}$  values are about 40% to 65 % of the  $I_{bias}$  values. The percentage depends on the degree of space charge compensation and gas flows [80].

## 4.2 Effect of magnetic dipole filters



**Figure 4.3:** Magnet arrangement around the plasma chamber. There are 20 columns of  $\text{Sm}_2\text{Co}_{17}$  permanent magnets. The magnets highlighted in the figure are the main dipole filter magnets, that create a magnetic field perpendicular to beam extraction, close to the plasma electrode. The arrows represent the direction of the north pole of the magnet. The beam direction is out of the page.

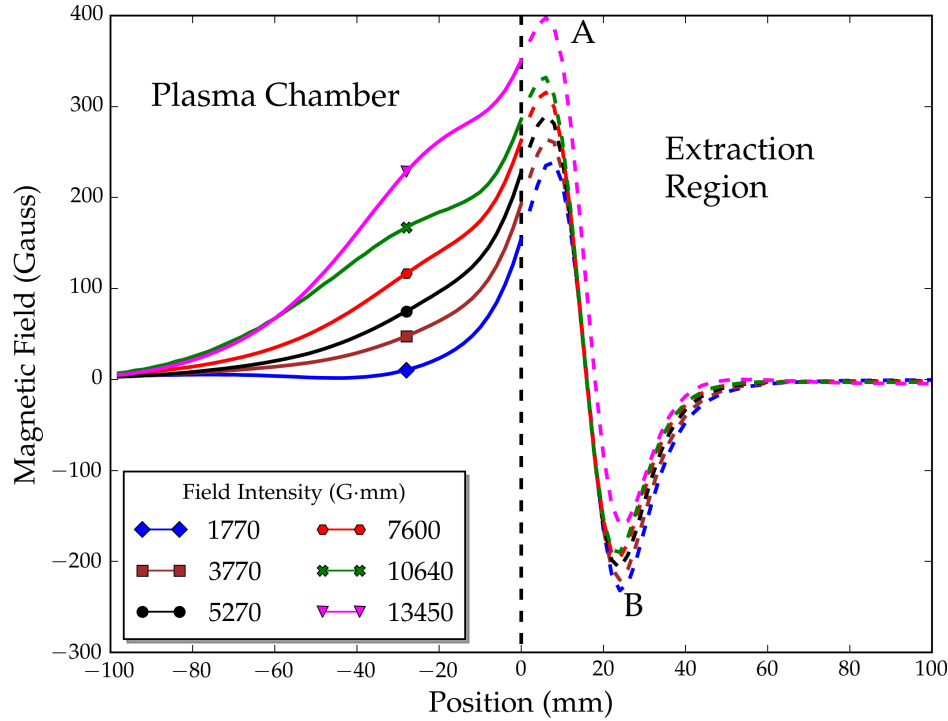


**Figure 4.4:** Variation in the magnetic field strength along the central axis of the ion source for different magnetic dipole filter fields. Field intensity values represent the integrated field value (Gauss·mm) over the 100 mm length in the plasma chamber. The vertical line indicates the location of the plasma electrode. Peaks (A, B) correspond to the field created by the two sets of extraction magnets shown in Fig. 4.1 and Fig. B.3.

The dipole filter magnets, indicated in Fig. 4.1 and Fig. B.3, consists of pairs of  $\text{Sm}_2\text{Co}_{17}$  magnets of opposite polarity placed diagonally opposite to each other. They provide dipole magnetic fields, which play an important role in the formation of negative ions inside the plasma [42, 81]. The magnet arrangement around the plasma chamber is shown in Fig. 4.3. The main set of magnets that contribute to the filter field are highlighted in the figure and they are located close to the plasma electrode side of the plasma chamber. This creates a magnetic field in the plasma, directed perpendicular to the beam extraction as shown in Fig. B.3. Electrons move across this field through collisional diffusion [42, 82]. This reduces the average electron energy near the plasma electrode, as the diffusion across the field is lower for high energy electrons. This is explained in section 2.7.2.

The strength of the filter field can be increased or decreased by changing the number of pairs of magnets in the magnetic filter region. It should be noted that the modification of the filter field requires disassembly of the ion source and rearrangement of the permanent

S	N	N	N	S	S	N	N	N	S	S	S	N	N
S	N	N	N	S	S	N	N	N	S	S	S	N	N
S	N	N	N	S	S	N	N	N	S	S	S	N	N
S	N	N	N	S	S	N	N	N	S	S	S	N	N
S	N	N	N	S	S	N	N	N	S	S	S	N	N
S	N	N	N	S	S	N	N	N	S	S	S	N	N

(A)

S	N	N	N	S	S	N	N	N	S	S	S	N	N
S	N	N	N	S	S	N	N	N	S	S	S	N	N
S	N	N	N	S	S	N	N	N	S	S	S	N	N
S	N	N	N	S	S	N	N	N	S	S	S	N	N
S	N	N	N	S	S	N	N	N	S	S	S	N	N
S	N	N	N	S	S	N	N	N	S	S	S	N	N

(B)

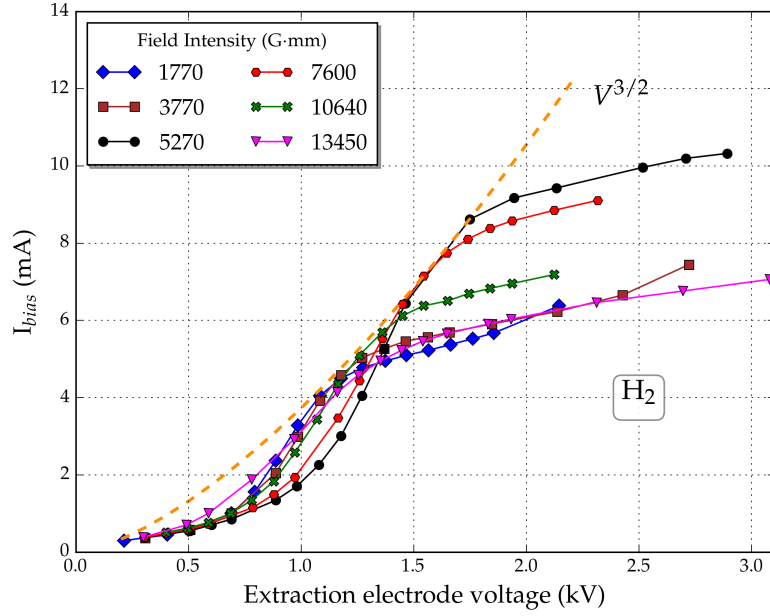
**Figure 4.5:** Details of the magnet arrangement corresponding to Fig. 4.4 for (A) 1770 G·mm and (B) 13450 G·mm integrated magnetic field strength values. Only one half of the arrangement (10 columns) is shown here. The other half is composed of magnets of opposite polarity. Grey shaded cells represent empty locations. The plasma electrode is located close to the last row of magnets.

magnets. The magnetic field intensity variation along the center of the ion source for the different configurations used in the current study is shown in Fig. 4.4. The fields are denoted in the graphs using the integrated magnetic field intensity over a 100 mm length in the plasma chamber. The measurements are made using calibrated Hall probes. The peaks (A, B) in Fig. 4.4 correspond to the field created by the two sets of extraction magnets shown in Fig. 4.1. This field deflects the co-extracted electrons towards the positively biased extraction electrode and thus removes the electrons from the beam line. 1770 G·mm represents the weakest filter field and 13450 G·mm represents the strongest filter field and the corresponding magnet arrangement (one half) for these two fields is shown in Fig. 4.5.

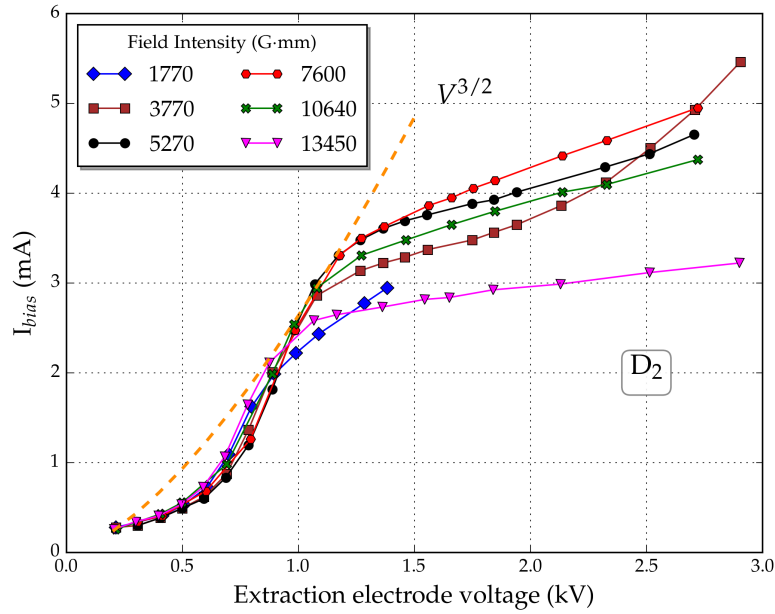
#### 4.2.1 Influence of filter fields on negative ion current

Studies by *Fukumasa et al.* [81] have shown an *isotope effect* in  $H_2$  and  $D_2$  plasmas. This means that there could be differences in the transport and production of species in  $H_2$  and  $D_2$  plasmas, even under the same external magnetic fields. Currently, D-Pace's filament ion source uses the same magnetic dipole filter field for both  $H_2$  and  $D_2$  plasmas. It is important to understand if an increase in  $D^-$  beam current could be obtained if a different magnetic filter field is used. Experiments were performed in  $H_2$  and  $D_2$  plasmas, using the different dipole magnetic field configurations shown in Fig. 4.4. These experiments were performed at 5 kV bias voltage rather than the nominal 30 kV, to prevent the generation of any neutron radiation while extracting  $D^-$  ions. More details on the neutron radiation are mentioned in Appendix C. At 5 keV beam energy, space charge effects are very high and a high fraction of the extracted beam is lost to the ground electrode. The Faraday cup current was too low to measure and hence the current obtained on the bias power supply,  $I_{bias}$ , was used to characterize the influence of the different magnetic dipole filter fields.

Due to space charge effects, an upper limit exists for the maximum negative ion current that can be extracted from the ion source for a particular plasma density. This is predicted by the Child Langmuir law, as mentioned in section 3.1.2. The variation in  $I_{bias}$  for  $H_2$  and  $D_2$  plasmas for the different magnetic filter fields, at 15 A of arc current, is shown in Fig. 4.6. Plasma electrode voltages and gas flows were optimized before each measurement by tuning them to achieve maximum current at the Faraday cup, for the fixed arc current. In general, the  $I_{bias}$  increases at first and flatten out after reaching a particular extraction electrode voltage. This is the typical behaviour in space charge limited regime and plasma density limited (or emission limited) regime, as shown in Fig. 3.3. It can also be seen that  $I_{bias}$  is not perfectly flat in the plasma density limited region, for the D-Pace ion source. The increase in bias current in this region, with higher extraction voltages, could be due to the increase



(A)



(B)

**Figure 4.6:** (A) The variation in bias current for (A)  $H_2$  and (B)  $D_2$  plasmas for different magnetic fields shown in Fig. 4.4. A constant arc current of 15 A, an arc voltage of 120 V and a bias voltage of 5 kV is used. The plasma electrode voltage and gas flow are optimized for each case. The  $V^{3/2}$  dashed line is shown for reference only.



in the concavity of the plasma sheath due to a higher electric field. This is demonstrated later in section 6.7. The increase in voltage can lead to an increase in the effective area of extraction and higher amounts of extracted negative ions from the plasma.

It can also be seen from the graphs that the maximum extracted negative ion currents in the space charge limited regime, decreases for very high and very low filter field strengths. The increase in current in the plasma density limited regime is not considered [36]. In order to find the optimum magnetic field for  $H_2$  and  $D_2$  plasma the maximum  $I_{bias}$  value in the space charge limited regime for each of the magnetic field distribution needs to be determined.

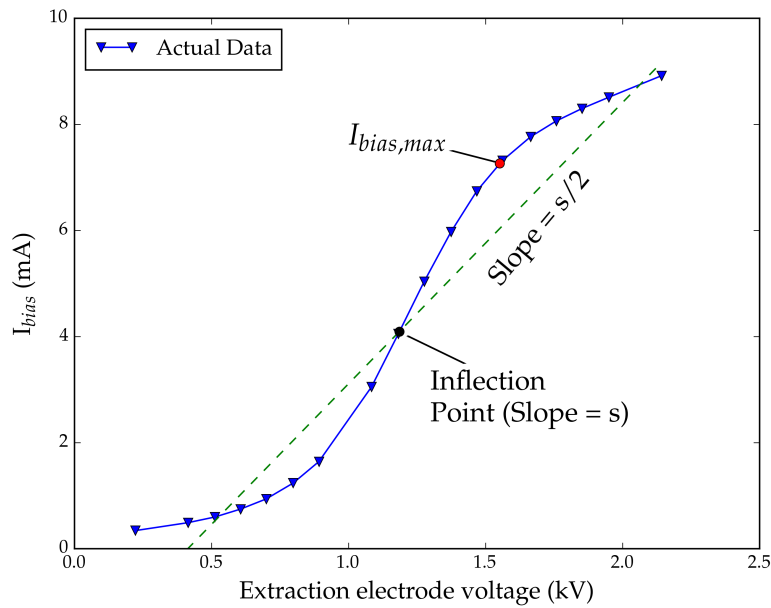


**Figure 4.7:** Method of finding  $I_{bias,max}$ , the characteristic value of  $I_{bias}$  from the data shown in Fig. 4.6. Slope,  $s$ , at the inflection point of the actual data is determined first. A new linear arbitrary line is constructed with slope value  $s/2$ . Using this new line as  $x$ -axis,  $I_{bias,max}$  is found using the derivative method.

The increase in  $I_{bias}$  value in the plasma density limited region makes it difficult to find the maximum  $I_{bias}$  in the space charge limited regime, for each case. A method of finding a characteristic  $I_{bias}$  value,  $I_{bias,max}$ , for a particular magnetic field configuration, is illustrated in Fig. 4.7. The typical shape of the  $I_{bias}$  data curve indicates the presence of an inflection point. At first, the inflection point of the actual data curve is found using the second derivative method. The inflection point is where the second derivative value equals zero and crosses from positive values to negative values. Then, a new arbitrary line is created with a slope value equal to half of the value of the slope at the inflection point. Considering the new line

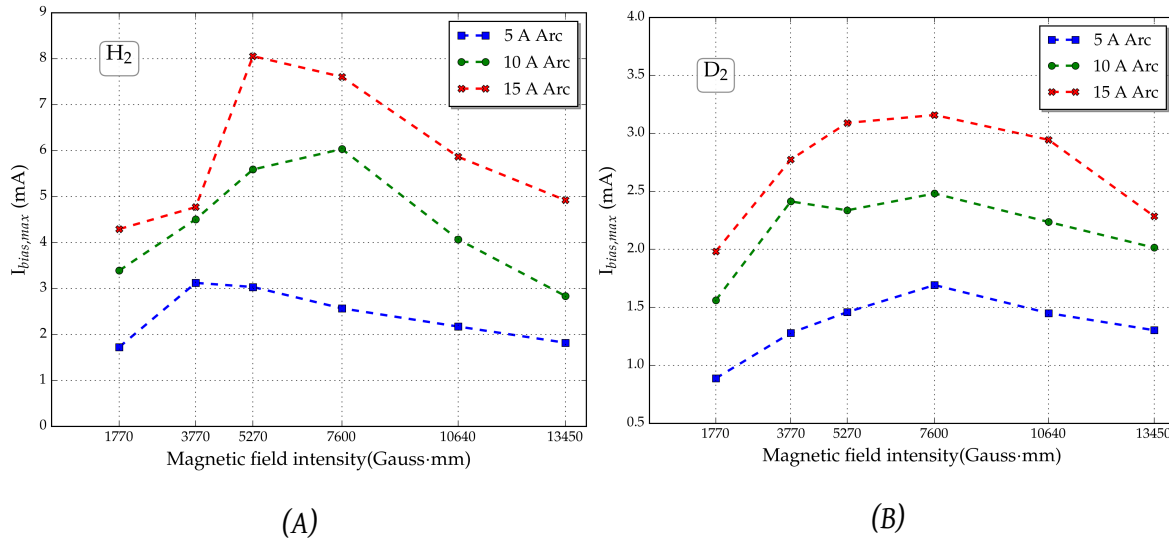


**Figure 4.8:** Variation of  $I_{bias,max}$  for (A)  $H_2$  and (B)  $D_2$  plasma at different magnetic filter field intensities and arc currents, at an arc voltage of 120 V and a bias voltage of 5 kV. Gas flows and plasma electrode voltages are tuned such that the Faraday cup current is maximum.

as  $x$ -axis, the actual data curve will have a maximum and a minimum. The maximum value is then determined using the derivative method by differentiating the actual data curve with respect to the new line. This gives zero values for the maximum points on the data curve and the corresponding data value is assigned to  $I_{bias,max}$ . As seen from the figure, this value corresponds to the maximum current in the space charge limited regime, in a qualitative manner.

The experiment was repeated for 5 A and 10 A of arc currents also and it showed results similar to Fig. 4.6. The  $I_{bias,max}$  values were determined using the method mentioned above, for the different arc currents and magnetic filter field intensities in  $H_2$  and  $D_2$  plasma. The combined results are shown in Fig. 4.8. As observed from the graphs, the magnetic filter field intensity should be optimized for maximising  $I_{bias,max}$ . Low intensity fields ( $< 3500$  G·mm) and very high intensity fields ( $> 10000$  G·mm) will decrease the ion current extracted from the ion source. The graphs also suggest that the optimum magnetic field strength required for  $D_2$  plasma ( $\approx 7000$ - $8000$  G·mm) could be higher compared to  $H_2$  plasma ( $\approx 4000$ - $6000$  G·mm) for maximum negative ion extraction. But, the reactions generating  $D^-$  is same as that for  $H^-$  [81]. Hence, the observed differences in the optimum magnetic fields could indicate some differences in the plasma properties in  $H_2$  and  $D_2$  plasma.

### 4.2.2 Plasma parameters in H<sub>2</sub> and D<sub>2</sub> plasma

The variations in the plasma parameters under different magnetic filter fields were analysed using a movable Langmuir probe [83] in H<sub>2</sub> and D<sub>2</sub> plasmas. The probe was made of tantalum and enclosed in a ceramic sleeve. The probe had a tip length of 5 mm and a diameter of 1.6 mm. It was inserted into the plasma chamber through the plasma electrode aperture of the ion source. The current-voltage characteristics of the probe were determined at different locations inside the plasma chamber. The voltages on the plasma electrode and bias power supply were maintained at zero and no beam was extracted during the Langmuir probe measurements. A gas flow of 7.5 sccm and an arc current of 5 A, at an arc voltage of 120 V, was used for the study.

The plasma potential  $V_p$  was determined by finding the inflection point of the  $V$ - $I$  characteristics through the second derivative method. The electron temperature ( $k_b T_e / e$ ) was found directly from the exponential curve fit for the  $V$ - $I$  characteristics of the probe, based on equation 4.1 [83]. Electron density ( $n_e$ ) was calculated using the electron temperature values using equation 4.2 [83]

$$I = -\frac{1}{2}eAn_iU_B + \frac{1}{4}eAn_e\sqrt{\frac{8k_bT_e}{\pi m_e}}\exp\left(-\frac{e(V_p - V)}{k_bT_e}\right) \quad (4.1)$$

$$I_p = \frac{1}{4}eAn_e\sqrt{\frac{8k_bT_e}{\pi m_e}} \quad (4.2)$$

$I_p$  is the current at the plasma potential  $V_p$ ,  $n_i$  and  $n_e$  are the ion and electron densities,  $m_e$  is the electron mass,  $U_B$  is the Bohm velocity,  $A$  is the probe surface area,  $e$  is the electron charge,  $k_b$  is the Boltzmann constant and  $V$  is the varying voltage on the probe. The results of electron temperature and density calculations at different locations inside the ion source, for the different magnetic fields in Fig. 4.4, are shown in Fig. 4.9. The typical error bars in the Langmuir probe measurements of electron temperature and density is shown separately for one of the magnetic fields in Fig. 4.10.

As evident from the graphs (A) and (B), the electron temperature decreases towards the plasma electrode (0 mm location) for all the magnetic filter field configurations. This is an anticipated result, as it is through this mechanism that the filter fields enhance the formation of negative ions in the plasma, through the volume production mechanism described in section 2.9.2 [42, 79, 81]. This behaviour can also be observed in the Laser Photodetachment experiments mentioned in figures A.4 and A.3. It can also be seen that a decreasing magnetic filter field intensity further increases the electron temperature close to the plasma electrode region. For example, the electron temperature at about 5 mm from the plasma electrode is  $\approx$

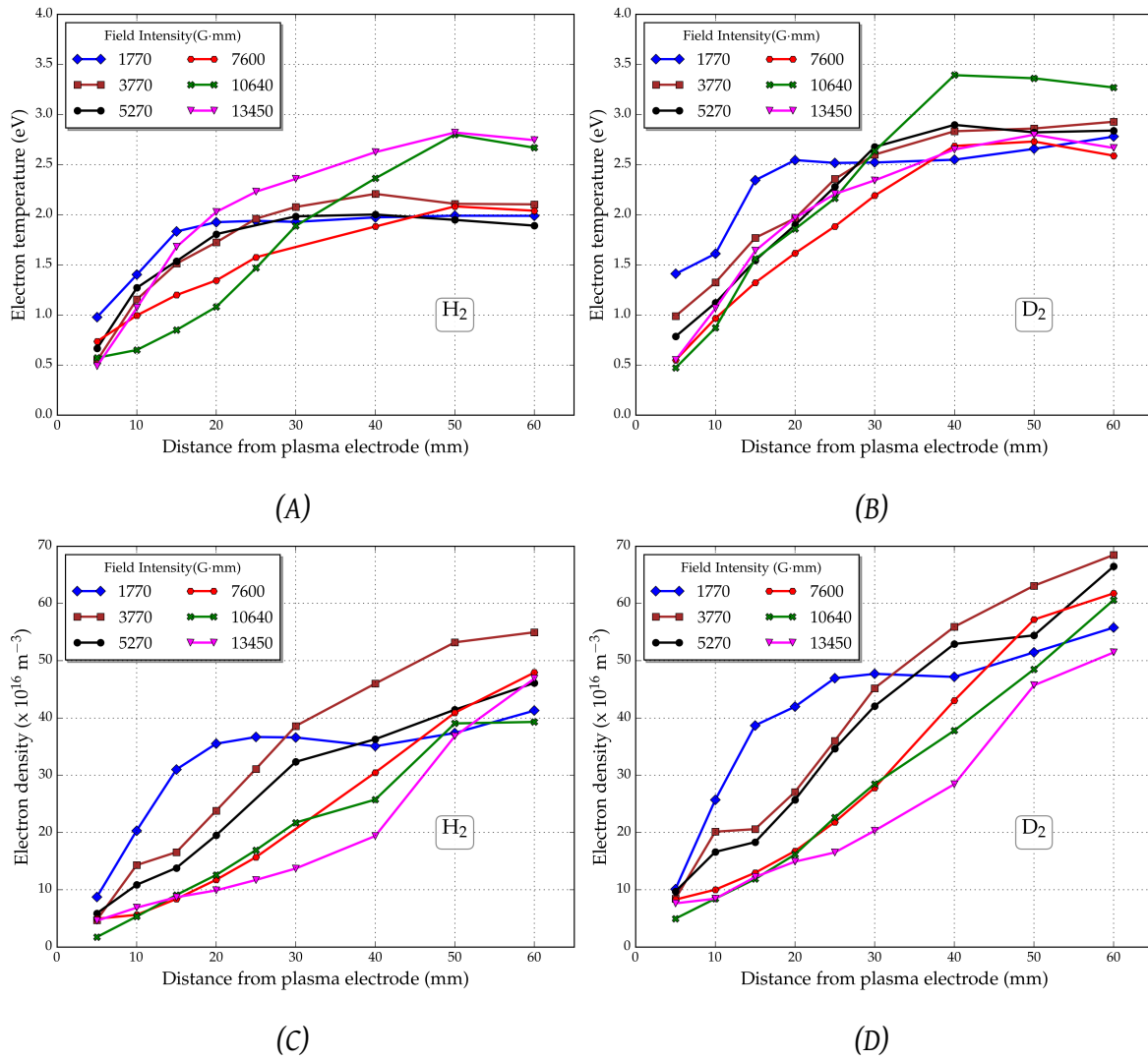


**Figure 4.9:** Variation of electron temperature inside the ion source for different magnetic filter fields for (A)  $H_2$  and (B)  $D_2$ . Variation in electron density inside the source for different magnetic filter fields for (C)  $H_2$  and (D)  $D_2$ . An arc current of 5 A, arc voltage of 120 V and gas flow of 7.5 sccm is used. Plasma electrode is at 0 mm position.

0.5 eV for 7600 G-mm field, whereas it increases to  $\approx 1.4$  eV for 1770 G-mm field, in  $D_2$  plasma. The electron temperature needs to be certainly lower than 1 eV in the plasma electrode region to maximize negative ion generation reactions [42]. Figures (C) and (D) shows that the filter field also reduces the electron density in the regions close to the plasma electrode (0 - 30 mm). In general it indicates that the highest field intensity is resulting in the lowest density in the region and vice versa. It could be that this reduction in electron density in the region, below a threshold value, the reason for the decrease in the bias current for high field intensity, as seen from Fig. 4.8.

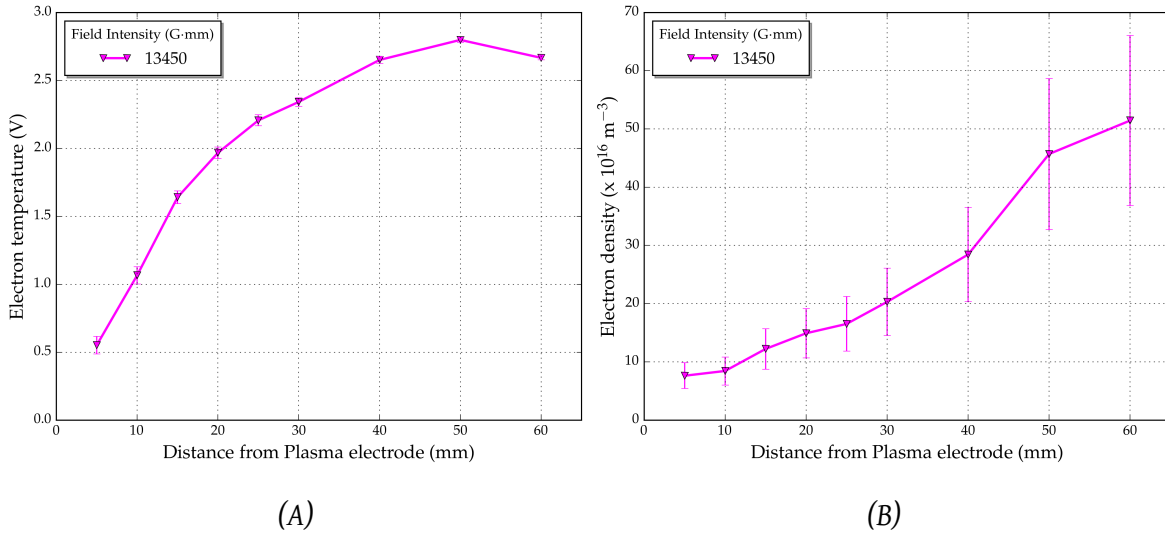


**Figure 4.10:** Typical error bars in Langmuir probe measurements of (A) electron temperature (B) electron density.

Even though the experiments were conducted at the same arc currents and gas flows, it is seen that electron temperature and density are higher for the  $\text{D}_2$  plasma compared to  $\text{H}_2$ . Also, a magnetic field intensity of around 5000 G·mm is required for  $\text{H}_2$  plasma to reduce the electron temperature to low values of 0.5 eV, whereas  $\text{D}_2$  plasma requires fields around 8000 G·mm to achieve this temperature. This could explain the stronger optimum magnetic field required for  $\text{D}_2$  plasma as seen in Fig. 4.8. Another possible factor contributing to this observation is the difference in Larmor radii between the isotopes, as explained by Bacal and Wada [82]. The Larmor radius is higher for ions with higher mass,  $r_L \propto \sqrt{m}$  as in equation 2.46. Thus a higher amount of positive deuterium ions are transported to the extraction region from the main plasma, compared to hydrogen ions for the same magnetic filter field. In order to maintain quasi neutrality of the plasma, the electrons are restored in the extraction region [82]. Hence a higher magnetic filter field intensity is required for  $\text{D}_2$  plasma to decrease the Larmor radius of the deuterium ions.

#### 4.2.3 Experimental results at 30 keV beam energy

Results obtained in Fig. 4.8 were for beam currents with an energy of 5 keV. It is interesting to see if the results are valid for 30 keV beam energy, as it is the typical beam energy used in the filament ion source. Regular tuning experiments were performed for some of the dipole filter fields shown in Fig. 4.4, in  $\text{H}_2$  plasma, for 30 keV beam energy. The electrode voltages and gas flows were optimised for maximum  $\text{H}^-$  current extraction. The bias currents ( $I_{\text{bias}}$ )

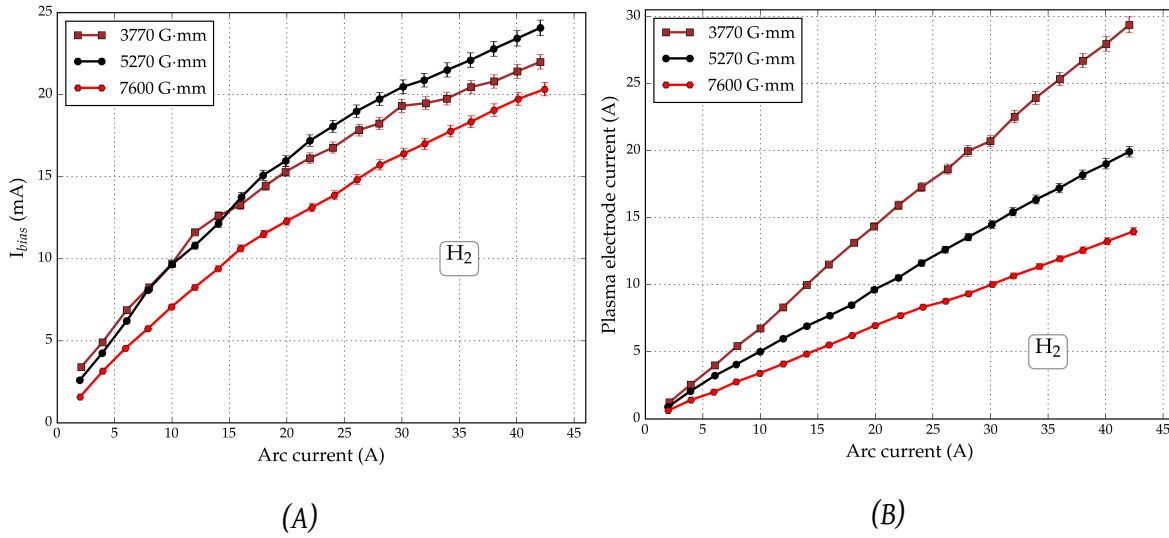


**Figure 4.11:** Variation in (A) bias currents and (B) plasma electrode currents in  $H_2$  plasma, for 3 different magnetic filter fields. The extracted beam energy is 30 keV. The results are from tuning experiments where electrode voltages and gas flows are optimised for maximum beam current.

and plasma electrode currents obtained in these experiments are shown in Fig. 4.11(A) and (B). The highest  $I_{bias}$  is obtained for the 5270 G·mm field and it decreased on further increase or decrease of the magnetic field strength. This is the same result obtained in Fig. 4.8 for the 5 keV beam energy. The general behaviour of the plasma electrode current in 4.11 (B) shows a reduction in the current, as the strength of the magnetic dipole filter field increases. This suggests a reducing electron density for increasing magnetic field strengths. This decrease in electron density was also seen from the results of Langmuir probe measurements in Fig. 4.9.

The 30 keV beam energy experiments were performed in  $D_2$  plasma also. Only 2 different magnetic fields were tested due to the constraints mentioned in Appendix C. The results are shown in Fig. 4.12(A) and (B). It was surprising to see that 7600 G·mm field generated a lower bias current than the 5270 G·mm. This contradicted the result obtained for  $D_2$  plasma in Fig. 4.8 where a higher beam current was predicted for the 7600 G·mm and the reason is not clearly understood. But the plasma electrode current behaviour displayed an expected trend, where its value was lower for the higher magnetic field strength. This can again be attributed to the lower electron density for higher magnetic field strengths as seen in Fig. 4.9.

The general comparisons between  $H_2$  and  $D_2$  plasma, at 30 keV beam energy, for the 5270 G·mm magnetic field is shown in Fig. 4.13(A) and (B). The  $H^-$  bias current from the  $H_2$  plasma is higher than  $D^-$  current from the  $D_2$  plasma by a factor of more than two. Studies

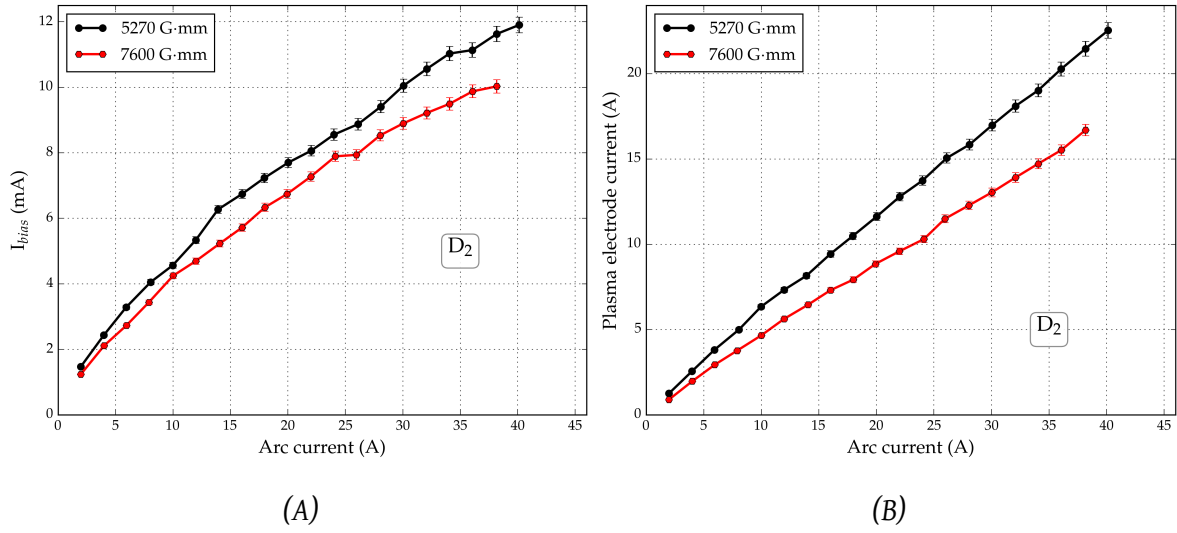


**Figure 4.12:** Influence of two different magnetic dipole filter fields on (A) bias current and (B) plasma electrode current, in D<sub>2</sub> plasma, for different arc currents. The extracted beam energy is 30 keV. Electrode voltages and gas flows are optimised for maximum beam current.

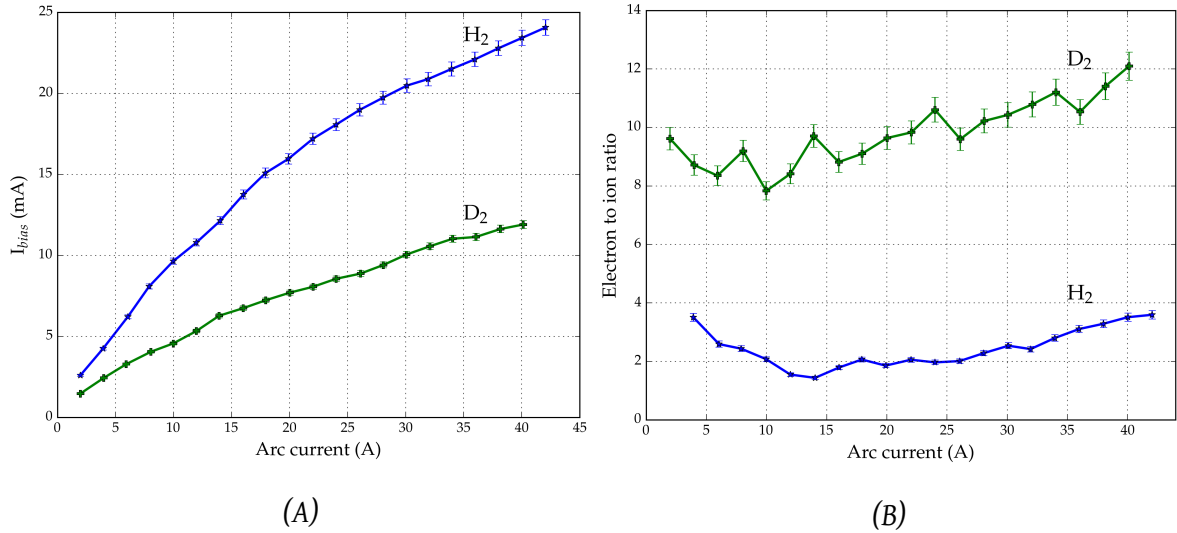


**Figure 4.13:** Variation in the (A) bias current and (B) the electrode to ion ratios in H<sub>2</sub> and D<sub>2</sub> plasma, for different arc currents. The magnetic filter field strength for the above data is the 5270 G-mm in figures 4.11 and 4.12.

have shown that the lower amount of  $D^-$  ions compared to  $H^-$  ions could be attributed to the differences in the diffusion of these ions through the magnetic dipole filter [84]. Another factor that could lead to lower  $D^-$  ions is the lower dissociative attachment cross sections in  $D_2$ , as shown in Fig. 2.10. The electron to ion ratios are also shown in the figure, which shows that the ratios are higher for  $D_2$  plasma by a factor of at least 4. The high ratios from  $D_2$  plasma is a typical behaviour and one of the challenges when high amounts of  $D^-$  need to be extracted, as in the fusion ITER experiment [85]. The higher co-extracted current for  $D^-$  could be attributed to the presence of higher concentration of atoms in  $D_2$  plasma compared to  $H_2$  [82]. This results in the destruction of  $D^-$  ions through reactions similar to the one mentioned in equation 4.4 and leads to higher electron currents in the extraction region.

### 4.3 Role of surface interactions in $H^-$ generation

The experiments presented in this section (4.3) were performed jointly with *Melanson* [80] and published in AIP conference proceedings [86]. As mentioned in section 4.1, the plasma inside the ion source is generated and sustained through thermionic emission from heated tantalum (Ta) filaments. These filaments are biased at a potential of  $-120$  V with respect to the plasma chamber during the operation. This results in positive ion bombardment and sputtering of the filament material. In addition, the filaments are operated at high temperatures, reaching  $\approx 3000^\circ\text{C}$ , causing evaporation. All these lead to Ta being adsorbed on the walls of the plasma chamber and the surface of the plasma electrode.

An experiment was performed to understand the effect of the Ta adsorbates in negative ion production in the filament ion source. All the Ta residues on the plasma chamber and plasma electrode were removed prior to the experiment. The results of the experiment are shown in Fig. 4.14. It shows the variation in the beam current measured at the Faraday cup for 20 A of arc current. The beam current data is captured every  $\approx 10$  sec. As evident from the results there is a clear rise in the beam current with time. Since all the other operation parameters were kept constant, this rise could be attributed to the ongoing Ta deposition on the surfaces of the plasma chamber and the plasma electrodes. It is also interesting to note that the beam current increase is rapid in the first hour but plateaus after about 4 hours. Overall, this could indicate that the Ta adsorbates on surfaces can contribute to  $H^-$  ion generation and also that above a certain Ta film thickness it cannot further improve the  $H^-$  ion density. The influence of such metal adsorbates on wall surfaces was studied by *Bacal et al.* [87] and found that a plasma electrode coated with tantalum adsorbate enhances the  $H^-$  ion production in two ways. One of the ways is that the Ta adsorbate on the surface helps



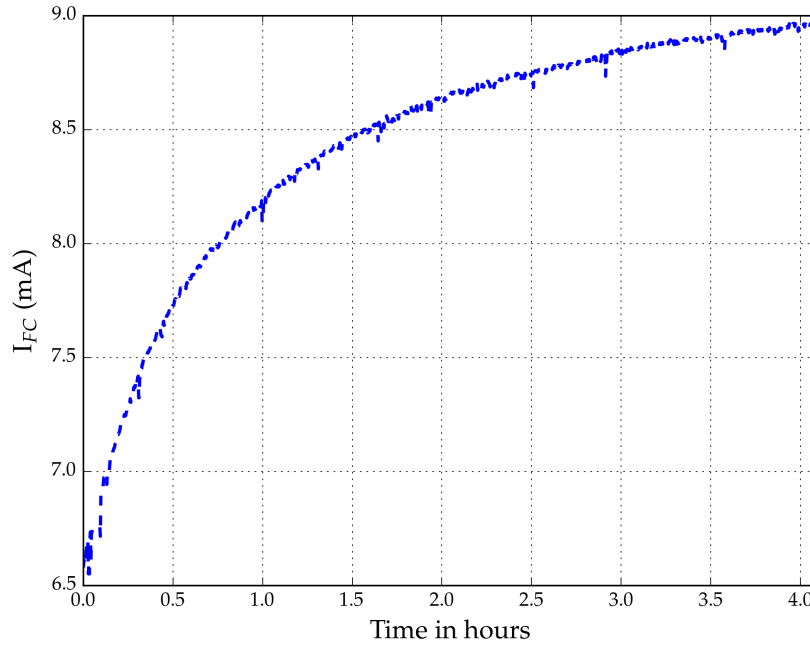
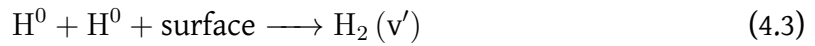


**Figure 4.14:** Variation in beam current with time, measured at the Faraday cup for 20 A of arc current in the filament ion source (beam energy = 30 keV, arc voltage = 120 V, plasma electrode voltage = 3.6 V, extraction electrode voltage = 3.08 kV, gas flow = 15 sccm  $H_2$ ).

in recycling the atomic hydrogen into vibrationally excited hydrogen molecules through recombinative desorption [88].



These vibrationally excited molecules can enhance the volume production process leading to negative ion formation. Another reaction is that the Ta coated plasma electrode can reduce the amount of hydrogen atoms reflected into the  $H^-$  region close to the plasma electrode, for the incident flow of atoms and molecules. The hydrogen atoms can act as a killer for  $H^-$  ions as shown below.



Since the presence of hydrogen atoms can lead to the destruction of  $H^-$  ions [42], a reduction in its concentration can lead to enhancement of  $H^-$  ion concentration.

Further experiments were performed in D-Pace's RF ion source for understanding the effect of Ta deposits on the chamber surface. It should be noted that there are no Ta filaments present in the RF ion source. Details of the RF ion source are mentioned in section 5.1. The results of the regular beam tuning experiments with different configurations in the RF ion source are shown in Fig. 4.15(A). Initially, the filament ion source was run at 20 A of arc

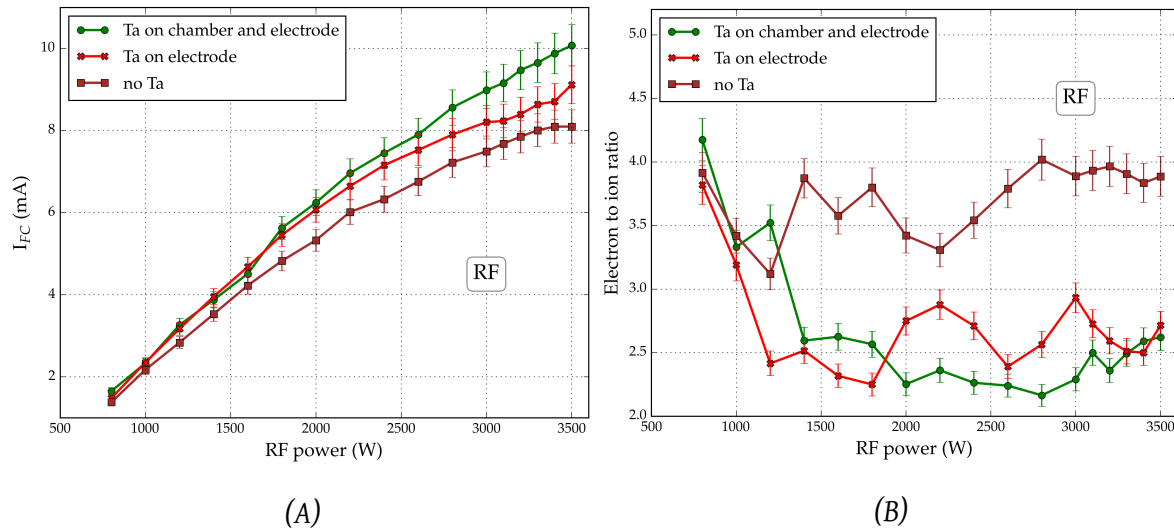


**Figure 4.15:** Variation in (A)  $H^-$  beam currents measured at the Faraday cup and (B) the electrode to ion ratios, in the RF ion source. The beam energy was set at 30 keV. The RF power was applied from the external antenna (section 5.1). Other electrode voltages and gas flows were optimised for obtaining maximum current at the Faraday cup.

current for two hours, at 15 sccm gas flow, for depositing Ta on the plasma chamber and plasma electrode. After that the ion source was opened to replace the back plate with the RF ion source back plate. Later, the regular tuning experiment was conducted in the RF ion source and the obtained results are shown as 'Ta on chamber and electrode' in the figure. After this run, the plasma chamber and electrodes were cleaned again and the Ta coating was reapplied using the filament ion source. Then the Ta deposits on the plasma chamber alone were removed. The RF ion source results of this configuration, with Ta deposit only on the plasma electrode, is shown under the curve 'Ta on electrode'. The last configuration tested in the RF ion source was without any Ta deposits on the chamber and the plasma electrode. This is presented as 'no Ta' in the figure.

As evident from Fig. 4.15(A), Ta deposits lead to an increase in the beam currents in the RF ion source. About 2 mA of beam current increase is obtained when the plasma chamber and the plasma electrode are coated with Ta. This also suggests an increase in the amount of  $H^-$  ions in the plasma. The corresponding co-extracted electron to ion ratios are shown in Fig. 4.15(B). As can be seen, the ratios are comparatively lower when some quantity of Ta is adsorbed on the surfaces. In addition to equation 4.3, this could be attributed to the reaction mentioned in equation 4.4, which describes that a reduction in the atomic hydrogen density near the extraction region can also lead to a decrease in the concentration of electrons. Thus the presence of Ta adsorbates has a beneficial effect in  $H^-$  ion generation in the ion sources.

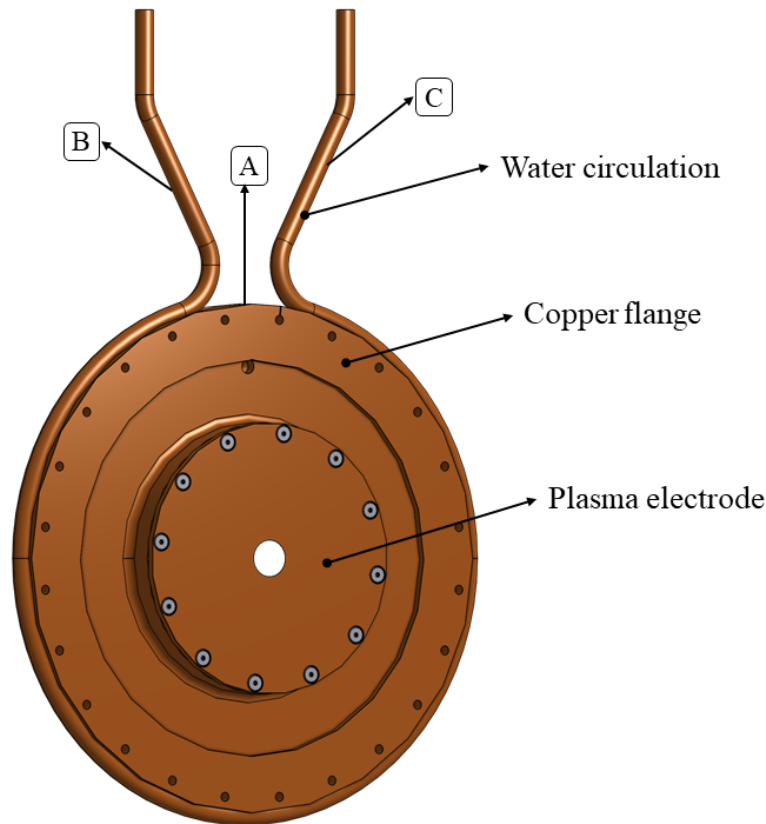


**Figure 4.16:** A model of the copper plasma electrode and flange in the filament ion source. The drawing shows the plasma facing side of the plasma electrode. Copper tubes carrying circulating water is brazed to the copper flange.

## 4.4 Effect of different plasma electrode materials

D-Pace's TRIUMF licensed filament ion source uses a copper plasma electrode for its regular operation. The assembled model of the plasma electrode is shown in Fig. 4.16. The diameter of the electrode is 96 mm and the diameter of the aperture is 13 mm. The electrode is bolted onto a copper flange and the flange forms a brazed joint with cooling water tubes, as shown in the figure. Thus, the plasma electrode is cooled through conductive heat transfer between the parts. The positively biased plasma electrode plays an important role in controlling the co-extracted electrons and in the formation of negative ions. The material composition of the plasma electrode could also influence the performance of the ion source. Section 4.3 indicates an enhancement in negative ion production when Ta coated surfaces are present. This section deals with the details of the experiment conducted for studying the influence of different plasma electrode materials like Cu, Al, Ta and SS (stainless steel) on the extracted  $H^-$  beam current from the ion source.

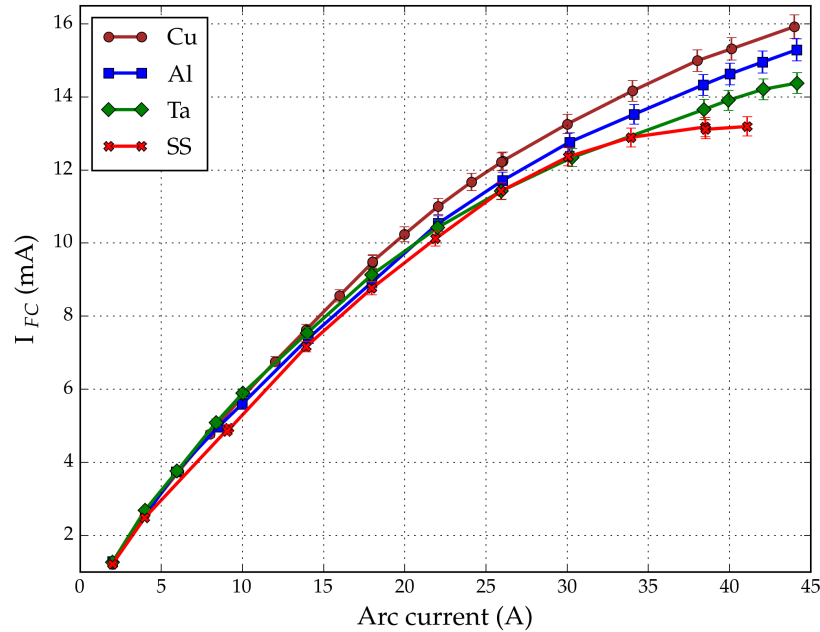


**Figure 4.17:** Variation in  $H^-$  beam currents measured at the Faraday cup, for different plasma electrode materials.

Plasma electrodes of the same dimension as the standard copper plasma electrode were manufactured using Al, Ta and SS. Experiments were performed using these different plasma electrodes in  $H_2$  plasma. The replacement of the plasma electrodes during the experiments involved dismantling and reassembly of the ion source. The ion source was vacuum pumped for at least 12 hours before the beginning of each experiment. The results of the experiments are shown in Fig. 4.17 in terms of the beam currents,  $I_{FC}$ , measured at the Faraday cup.

As evident from the results, the beam currents from the ion source are dependent on the type of plasma electrode material. The difference is much more pronounced at arc currents  $> 30$  A. Cu plasma electrode gives the best result of 16 mA of beam current at about 44 A of arc current. SS plasma electrode configuration produces the lowest beam current of about 13 mA. The corresponding beam current from Al electrode is about 15 mA and Ta electrode is about 14 mA. It is interesting to find that the Ta plasma electrode do not possess any advantage over the copper plasma electrode, whereas in section 4.3, it was shown that fresh Ta adsorbates on the metallic inner walls of the plasma chamber and surface of the plasma electrode could lead to an increase in the extracted  $H^-$  current. It can also be understood from the results that difference observed in the beam currents could be attributed to the material property of the plasma electrodes.

One of the major differences between the plasma electrode materials in the experiment is the thermal conductivity property. The coefficient of thermal conductivity of the different

Material	Thermal conductivity (W/m-K)
Copper (C110)	388
Aluminium (6061 alloy)	170
Tantalum	57.5
Stainless steel (304)	14

**Table 4.1:** Thermal conductivity values for the different plasma electrode materials used.

plasma electrode materials used in the experiments are shown in table 4.1. Since the heat transfer rate is proportional to the thermal conductivity, the plasma electrode with the highest thermal conductivity will be operating at the lowest temperature and vice versa, for a constant heat load. This suggests that the temperature of the copper plasma electrode will be the lowest among the electrodes under consideration here, for a fixed arc current. In the same manner, the SS plasma electrode will be operating at the highest temperature. The temperature on the plasma electrode cannot be measured directly since it is completely enclosed by the ion source, as shown in Fig. 4.1. But, the circumference of the copper flange, containing the water tubes, is accessible from outside the ion source.

A set of simulations were performed for determining the approximate surface temperatures of the plasma electrodes. *Solidworks* simulations [89] were used for determining the temperature on the surface of the plasma electrodes. A *thermal study* simulation in *Solidworks* helps in finding the temperature distribution on different parts of an assembly, for a known amount of heat (temperature, heat flux etc.) applied on a surface in the assembly. *Solidworks* simulations use Finite Element Analysis (FEA) method for solving the geometries, where a model is divided into smaller and simpler elements.

The challenge in creating the thermal simulation was the unknown heat load at the plasma electrode during the operation of the ion source. In order to find this value, the temperature at the exposed locations (A, B and C) of the copper flange, indicated in Fig. 4.16, were measured using a thermocouple during the ion source operation with the Cu plasma electrode. The difference in temperature between locations B and C provided the rise in water temperature during the operation. Temperature measurement at location A provided the copper flange temperature. At about 4560 W of arc power (38 A arc current, 120 V arc voltage), the temperature at location A was about 50.4°C and the rise in water temperature was about 5°C. The approximate heat load on the plasma electrode during the operation can now be determined from the simulations such that the resultant temperatures match with the thermocouple measurements. The simulations also require thermal contact conductance values between surfaces and the values used are shown in table 4.2. The heat load applied on the plasma electrode surface was confined uniformly to a diameter of 83 mm.

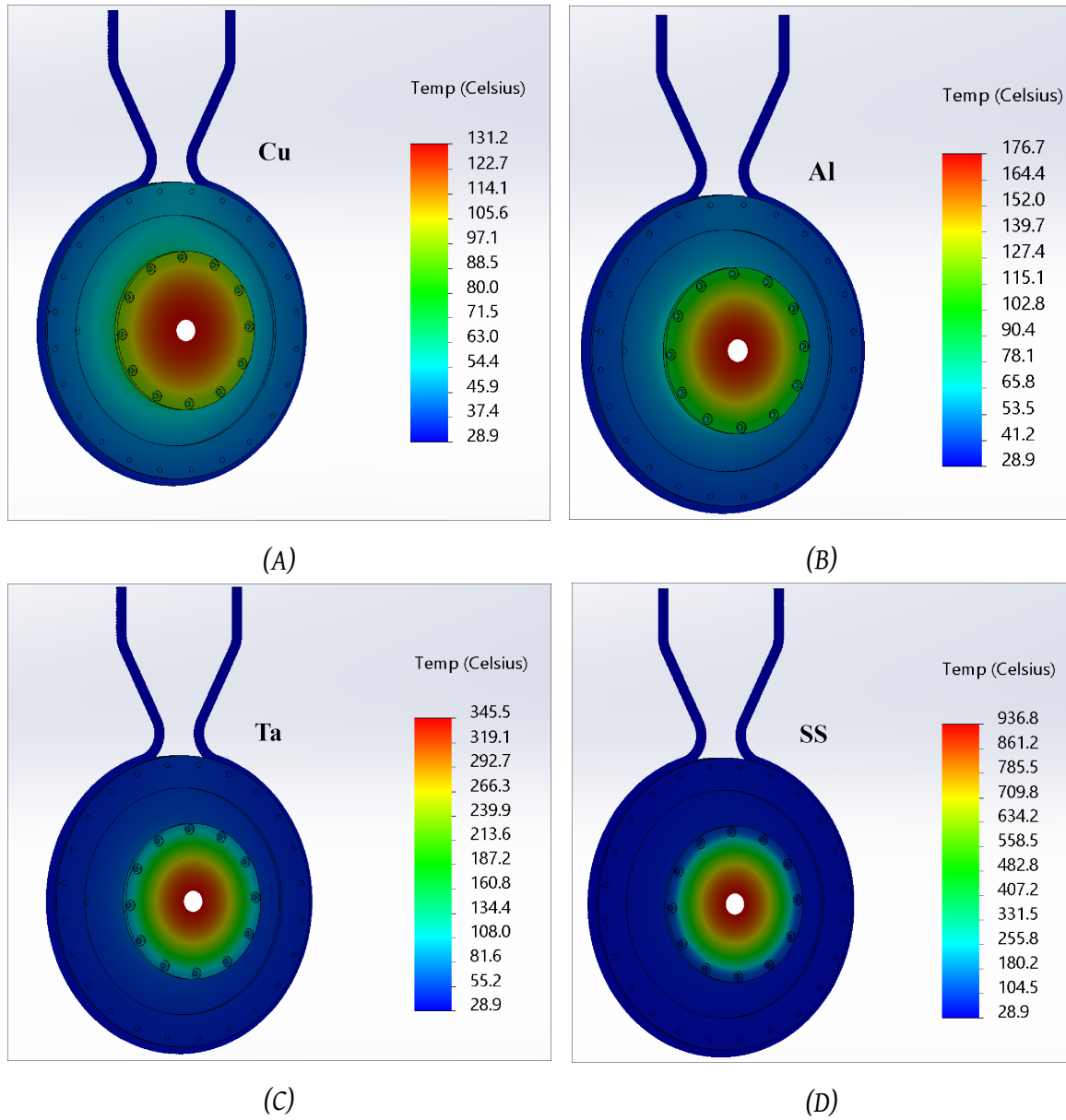


**Figure 4.18:** Solidworks thermal simulation results for the temperature distribution on the plasma electrode - flange assembly, for different plasma electrode materials. A uniform heat load of 475 W is applied on an area of 83 mm diameter on the plasma facing side of the plasma electrode. The simulation parameters are shown in Table 4.1 and 4.2.

Parameter	Contact surfaces	Value
Contact conductance	Cu plasma electrode – Cu flange	10000 W/m <sup>2</sup> K
Contact conductance	Cu flange – water tubes	17500 W/m <sup>2</sup> K
Convective heat transfer	water tube – water	11000 W/m <sup>2</sup> K

**Table 4.2:** The parameters used in copper plasma electrode simulations. The contact resistance values between surfaces are based on [90] and convective heat transfer coefficient values are based on [91] for a water flow of 1.7 L/min.

It was found from the simulations that about 475 W of heat load on the Cu plasma electrodes gave the best match to the experimentally measured temperatures on the plasma flange at 4560 W of arc power. The temperature distribution obtained from the simulations for the Cu plasma electrode is shown in Fig. 4.18(A). As shown in the figure the maximum temperature on the surface can reach up to 131°C. The simulations were also performed by replacing the copper plasma electrodes with the other materials (Al, Ta and SS). Only the thermal conductivity of the plasma electrode material was varied in these simulations, with all other contact conductance values and heat load remaining the same. The results of the simulations are shown in Fig. 4.18(B), (C) and (D). As shown in the results, the maximum temperatures can reach up to 131°C in Cu, 177°C in Al, 345°C in Ta and 936°C in SS. Note that the differences obtained in the surface temperatures is due to the differences in the thermal conductivity of the materials. It is interesting to note that SS plasma electrode temperature is much higher than the other materials. It can also be seen that the flange temperature is much less in the SS electrode configuration, compared to other materials, indicating very low heat transfer from the electrode surface.

The pictures of the SS and Cu plasma electrodes, before (top) and after (bottom) the tests, are shown in Fig. 4.19. As can be seen, there are heavy burn marks at isolated parts on the surface of the SS plasma electrode. This suggests that a high operating temperature on the electrode surface, as found from the simulations, is a possibility. The simulations also assume a uniform heat load distribution on the plasma electrode surface. This could be an oversimplification, as the magnetic field effects on charged particles are not considered here. Hence, the heat distribution could be non-uniform in the real scenario and this could explain the isolated burn marks seen on the SS electrode surface.

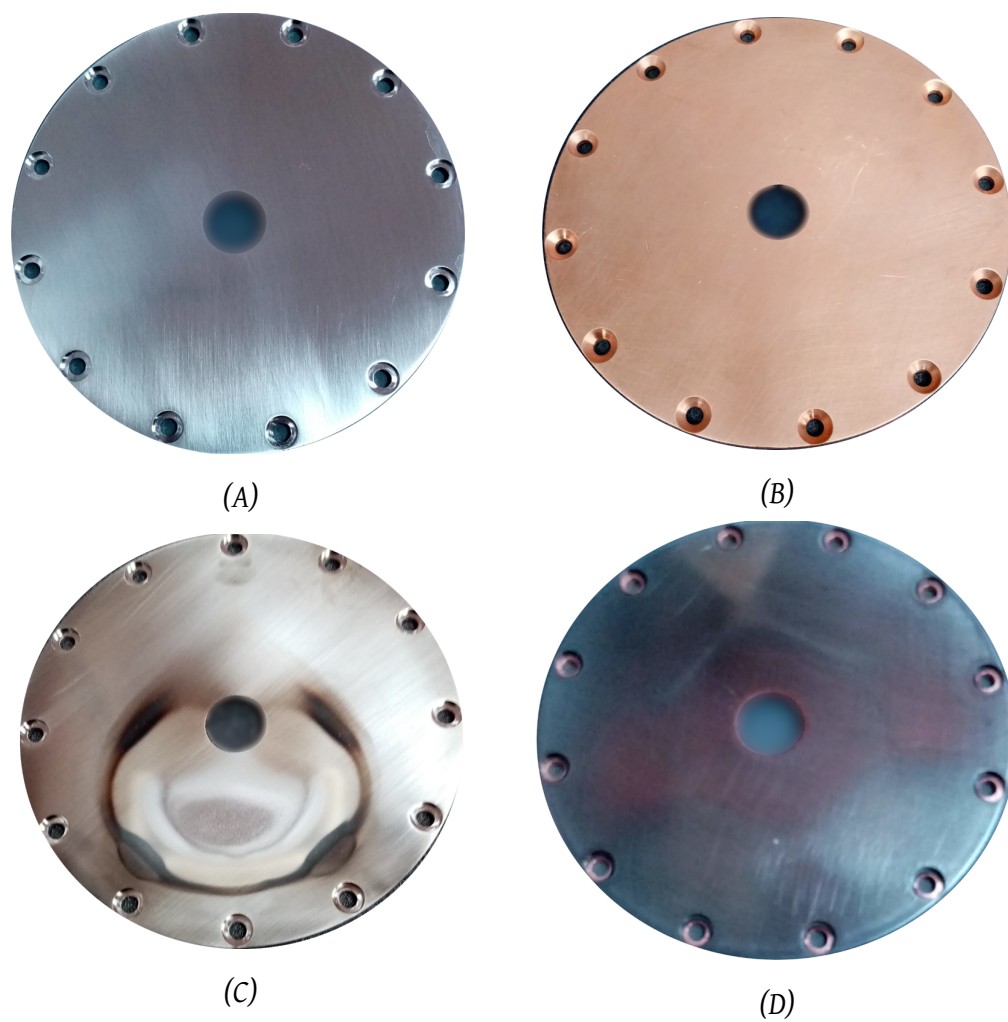


**Figure 4.19:** Pictures of plasma electrodes before and after the tests. (B) and (D) shows copper plasma electrode before and after the tests. (A) and (C) shows stainless steel (SS) plasma electrode before and after the tests. Burn marks can be seen on the surface of the SS electrodes.



One of the other factors overlooked in the simulations is the difference in contact conductance between the different plasma electrode materials and the copper flange. A material of lower thermal conductivity will also lead to lower contact conductance [90]. But the dependence of the temperature distribution results on the contact conductance value is not very significant in the current study. For example, in the case of copper plasma electrode, the maximum temperature reduces to about  $115^{\circ}\text{C}$  when the contact conductance value between the plasma electrode and flange is increased to  $25000\text{ W/m}^2\text{ K}$ . The maximum temperature on the SS plasma electrode reduces to  $912^{\circ}\text{C}$  when the contact conductance is increased to  $15000\text{ W/m}^2\text{ K}$ .

A comparison between the simulation results and Fig. 4.17 suggests that the surface temperature of the plasma electrode, during the ion source operation, could be a contributing factor towards the differences seen in the beam currents. The SS plasma electrode with the highest surface temperature generated the lowest beam current, whereas the copper electrode with the lowest surface temperature generated the highest beam current. Beam currents in Al and Ta configurations also follow the surface temperature trend. Considering a fixed plasma density, this does indicate that a lower plasma electrode surface temperature is favorable in the formation of more negative ions in the plasma. The contribution of ‘surfaces’ in negative ion generation is mainly through the recombinative desorption process mentioned in equation 4.3. As explained in section 4.3, the Ta adsorbates on the surface of the plasma electrodes is the main factor contributing to this effect. Hence the differences in beam currents could indicate a degradation in the ‘Ta effect’. One of the observations that support this inference is the absence of any Ta deposits on the SS plasma electrode after the tests as shown in Fig. 4.19. A visual examination of the plasma electrodes after the tests also indicates that the thickness of Ta deposit on the surface is in the order  $\text{Cu} > \text{Al} > \text{Ta} > \text{SS}$ . All these observations indicate that a lower plasma electrode temperature could be advantageous in Ta deposition on its surface which in turn can increase the negative ion density in the plasma through the recombinative desorption process.

## 4.5 Influence of plasma electrode aperture size

In most cases, the particle beam from the ion source needs to be transferred to the entrance of an accelerator or a magnet for its further applications. For reducing the beam losses, it is desirable to have a minimum beam emittance. One of the ways of modifying the beam emittance from the ion source is by altering the aperture sizes of the electrodes. An experimental study was conducted in  $\text{H}_2$  plasma to study the range of beam emittance values that

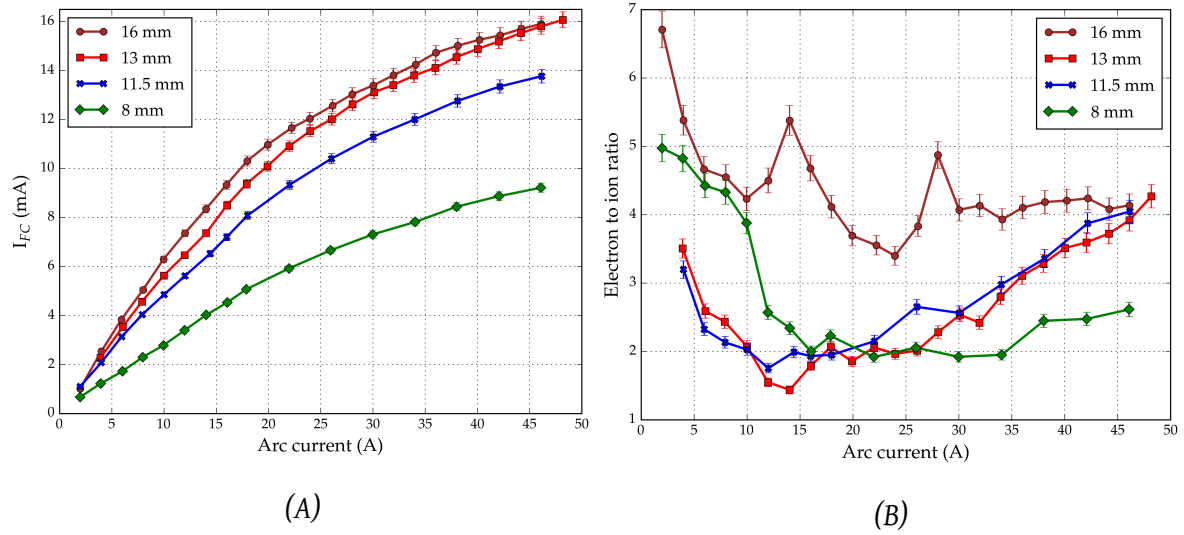


**Figure 4.20:** Results of the experiments in  $H_2$  plasma using different plasma electrode aperture sizes. (A) Variation in beam currents measured at the Faraday cup and (B) variation in electron to ion ratio. The extracted beam energy is 30 keV. Electrode voltages and gas flows are optimised for obtaining the maximum current at the Faraday cup.

could be obtained from D-Pace's filament ion source, using plasma electrodes of different aperture sizes. The diameter of the different apertures considered are 8 mm, 11.5 mm, 13 mm and 16 mm. The 13 mm aperture size is used for the regular experiments.

The results of the experiment are shown in Fig. 4.20. The  $H^-$  beam currents obtained at the Faraday cup for different arc currents in the ion source are shown in (A). As can be seen from the graph, the beam currents decrease as the size of the aperture decreases.  $I_{FC}$  decreases from 16 mA to about 9 mA, when the aperture size changes from 16 mm to 8 mm. This result is expected as the effective plasma sheath emission area reduces as the aperture size decreases, as understood from equation 3.10. This can be better understood with the help of IBSimu simulations [21] results shown in Fig. 4.21. The figure shows the simulation results for an  $I_{FC}$  value of about 8 mA, from 8 mm and 16 mm apertures. More details on IBSimu are mentioned in Chapter 6. The applied voltages on the electrodes are the same as obtained from the experiments. The reduction in the plasma sheath area is evident from the simulations for the 8 mm aperture. The general electron to ion ratio values for the experiment is shown in 4.20(B). The ratios are considerably higher for the 16 mm aperture size and it denotes more co-extracted electrons from the plasma. This was evident during the experiment, as it was difficult to keep the co-extracted current under control without saturating the extraction electrode power supply. The extraction electrode power supply saturates above 140 mA and hence irregular values of electrode voltages and gas flows were

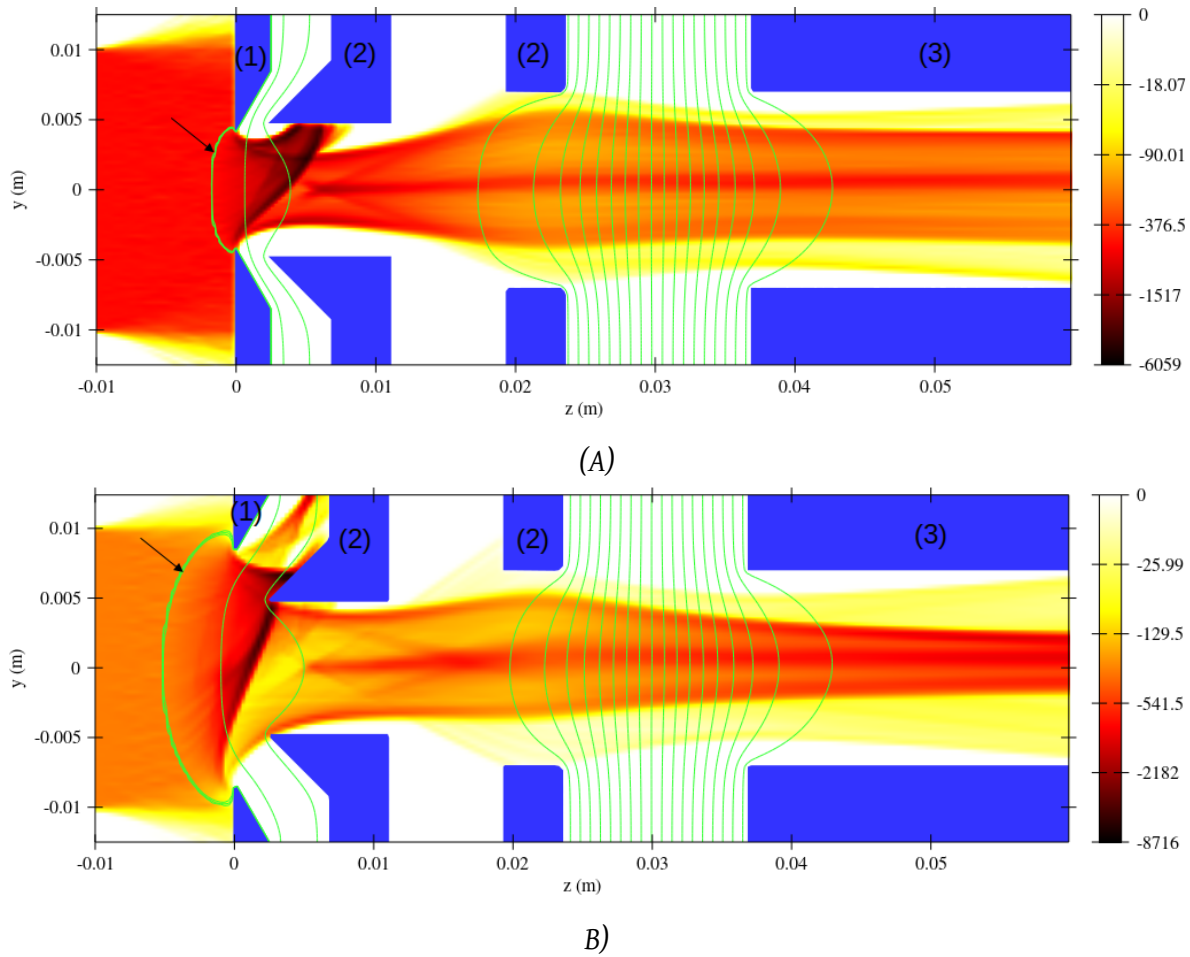


**Figure 4.21:** 2D IBSimu current density simulation results showing the location of the plasma sheath (black arrow) for (A) 8 mm and (B) 16 mm apertures. The simulated conditions correspond to about 8 mA of  $I_{FC}$  for both apertures. The (1) plasma (2) extraction and (3) ground electrodes are shown in blue color. Plasma region is located at values  $z < 0.0$  m. Beam propagation is towards the right. Current flow towards the extraction electrodes can also be seen.

needed to keep the co-extracted current under control. This is the reason for the appearance of peaks in the ratio for the 16 mm aperture size. This also leads to loss of beam currents.

The corresponding 4 RMS normalized beam emittance values obtained from the experiments are shown in Fig. 4.22, for the different  $I_{FC}$  values mentioned in Fig. 4.20(A). As can be inferred from the graph, a smaller beam emittance can be achieved for a beam current  $I_{FC}$ , by using the plasma electrode with a smaller aperture. For example, the 8 mm aperture can generate an 8 mA beam with an emittance value of 0.38 mm·mrad, whereas it is 0.6 mm·mrad for the 16 mm aperture size. But, it should also be noted that the arc currents and hence the plasma densities required for the smaller apertures are much higher than that required for larger apertures, for achieving a fixed value of  $I_{FC}$ , as shown in Fig. 4.20(A).

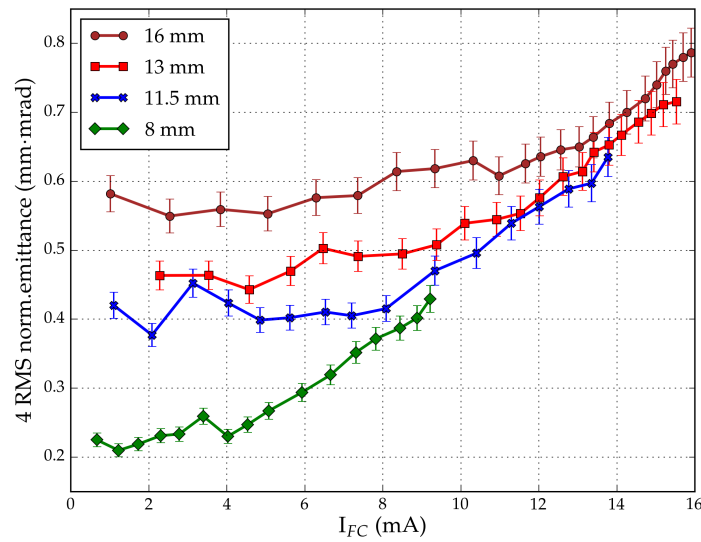


**Figure 4.22:** Beam emittance variation obtained using different plasma electrode apertures.

## 4.6 Conclusions

Some of the factors that affect the negative ion current obtained from D-Pace's TRIUMF licensed ion source were examined in this chapter. The influence of different magnetic filter field configurations, surface interactions, plasma electrode surface temperatures and aperture sizes were considered. The results indicate that an optimum dipole magnetic filter field is required for extracting maximum negative ions from  $H_2$  and  $D_2$  plasma. It was also understood from the 5 keV beam energy studies that the integrated magnetic field strength required by the  $D_2$  plasma ( $\approx 7000$ - $8000$  G-mm) was higher than needed by the  $H_2$  plasma ( $\approx 4000$ - $6000$  G-mm), with the difference in field values contributed only by the strength of the magnetic dipole filter close to the plasma electrode. Differences in plasma parameters in  $H_2$  and  $D_2$  plasma, under the different dipole fields, were analysed with the help of a Langmuir probe. The chapter also examined the surface interactions between Ta coated surfaces and the plasma, and confirmed the beneficial impact of Ta deposition on negative ion generation in the ion source. Further studies indicated that the temperature of the interacting surface also plays an important role in the surface interactions, with very high surface temperature leading to lower negative ion generation in the plasma. Solidworks thermal simulations were used for predicting the surface temperature of the plasma electrode. Experiments were also conducted using different plasma electrode apertures for improving the emittance of the extracted beam. This result is very useful in situations where a more spatially concentrated beam is required from D-Pace's filament ion source.

# Chapter 5

---

## RF ion source upgrades

D-Pace has established a 13.56 MHz Radio Frequency(RF)-powered ion source at the Ion Source Test Facility [77]. This is a hybrid design between TRIUMF licensed filament ion source [13] and RADIS ion source licensed from University of Jyväskylä [92], for generating negative ion beams. The ion source uses a planar antenna, placed external to the plasma chamber, for transferring power to the plasma through inductive coupling. The main advantage of the RF ion source over the filament ion source is that no filaments are needed for plasma generation. Thus, the downtime and consumable cost associated with the replacement of worn-out filaments will not occur. This is intended to allow for a longer maintenance-free operation of the source. The plasma will be also free from evaporated or sputtered filament materials. The D-Pace ion source was able to extract up to 8.3 mA of  $H^-$  and 3.6 mA of  $D^-$  currents, at a maximum of 3500 W of RF power so far [77]. But, there were still some challenges in the stable operation of the ion source. This chapter deals with the details of those challenges and upgrades performed in D-Pace's RF ion source as part of the thesis. The author has published some sections of this chapter in Jacow publications [93].

### 5.1 RF ion source overview

The section view of D-Pace's RF plasma and extraction system is shown in Fig. 5.1. The difference between this and the filament ion source shown in Fig. 4.1 is in the back plate design of the plasma chamber. The filament ion source has a copper back plate and it holds the filaments for the thermionic emission, whereas the back plate of the RF ion source is mainly an aluminium nitride (AlN) ceramic disc of 120 mm diameter and 6 mm thickness. The extraction system and other components are the same for both ion sources and are shown in Fig. B.2 and B.3. A *Comet Cito RF generator* supplies the 13.56 MHz power (0-5000

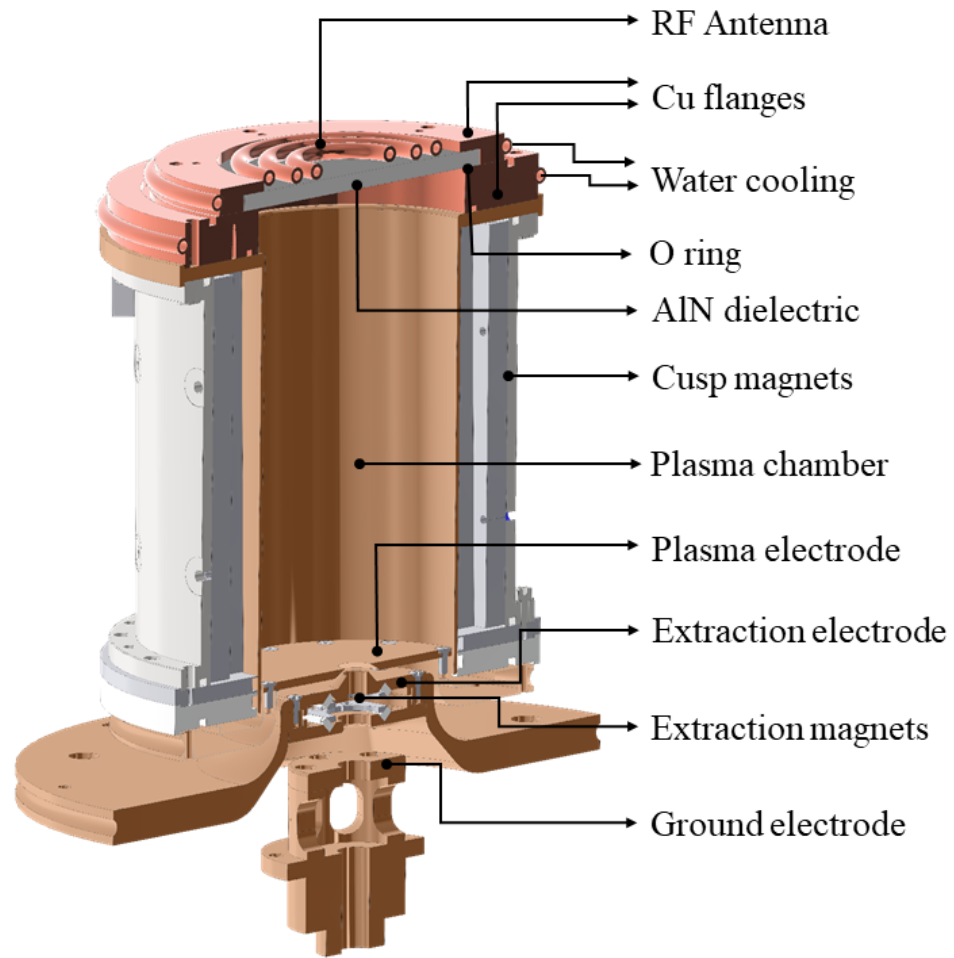


**Figure 5.1:** Section view of RF plasma and extraction system. The RF antenna is made of copper tube and has water circulation through it. The AlN dielectric window couples the RF energy from the RF antenna to the plasma chamber. The copper flanges are cooled by water flowing through copper tubes brazed to the flanges.

W) to the RF antenna. The circuit is shown in Fig. 5.6. The plasma is mainly sustained by inductively coupling the RF energy from the external RF antenna to the plasma chamber and hence is an *inductively coupled plasma* (ICP). The RF antenna is a 3 turn planar spiral copper tube of 5 mm diameter with internal water circulation. The AlN dielectric window couples the RF power from the antenna into the plasma chamber. The RF coil is placed about 3 mm from the window. The AlN window is held in place by copper flanges and is in contact with the plasma directly. The copper flanges are cooled by water flowing through copper tubes brazed to the flanges.

Negative ions are produced inside the low pressure plasma chamber through volume production methods mentioned in section 2.9.2. The extraction electrodes and the associated power supplies, magnetic fields, vacuum system, Faraday cup and emittance scanner

diagnostics are the same as that for the filament ion source and are shown in Fig. B.3 and Fig. B.2.

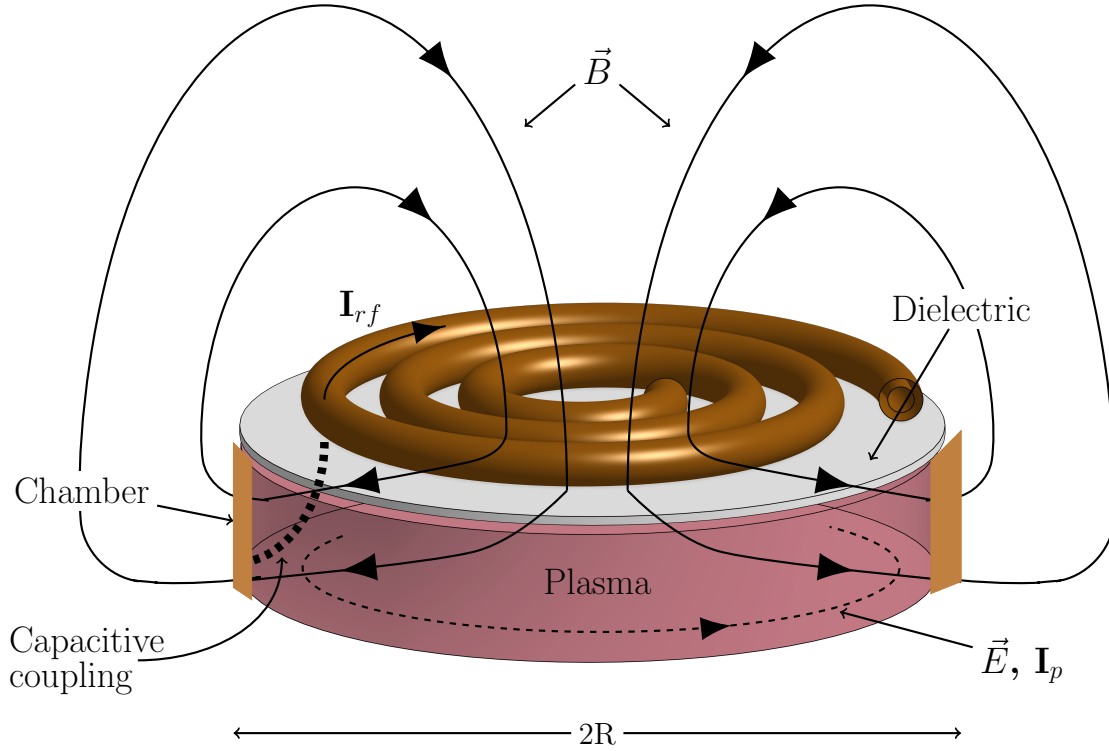


**Figure 5.2:** Schematic representation of the electric and magnetic fields in an inductively coupled plasma (ICP) and the resultant currents ( $I_p$ ) in the plasma. The high voltage on the coils also induces a capacitive coupling to the grounded chamber walls. The figure is based on references [94–96].

The RF voltages applied to the antenna generate time-varying magnetic fields. This induces azimuthal RF electric fields and currents in the plasma. The induced current in the plasma is opposite to the direction of the antenna current. This further induces opposing fields, which limits the magnetic field penetration from the antenna to a skin depth,  $\delta$ . The approximate resultant fields are shown in Fig. 5.2 for the RF current  $I_{rf}$  through the external antenna [94, 96]. In addition to the inductive coupling, the high voltage regions of the RF antenna also generate a capacitive coupling, as shown in the figure. This capacitive coupling is useful in igniting the plasma, but will result in high plasma sheath voltages which is not desirable in the operation of the plasma [95]. This is discussed in detail in the later sections.

### 5.1.1 Power absorption in ICP

The general inductive power absorption behaviour of RF antenna-plasma systems can be described using the *transformer model* as shown in Fig. 5.3 [98, 99]. Here, the antenna is the

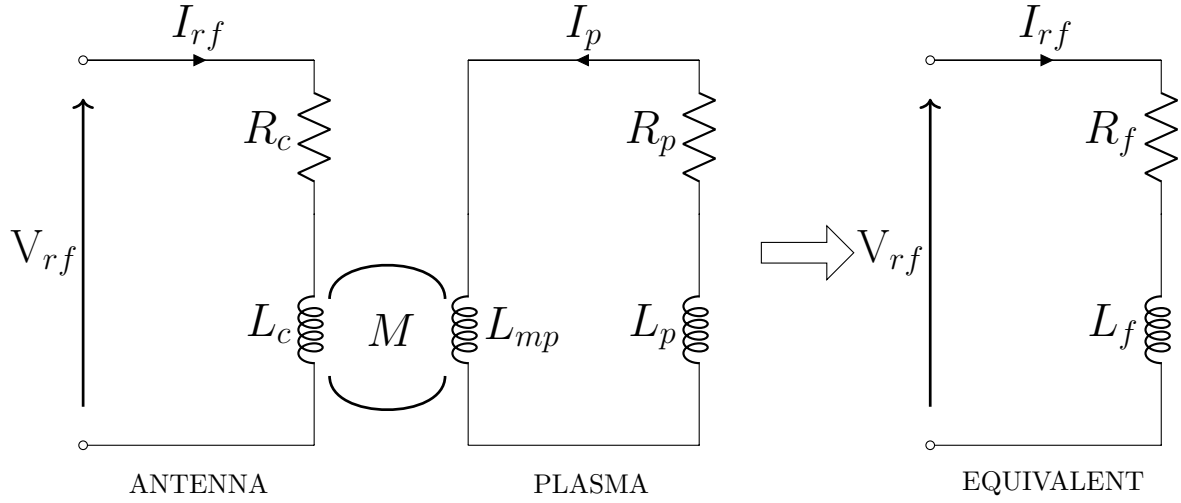


**Figure 5.3:** Transformer model of an ICP plasma. An equivalent circuit is shown on the right side. The model is based on the references [94, 97].

primary coil and plasma is the one turn secondary coil of an air-cored transformer.  $I_{rf}$  is the RF current flowing through the antenna having resistance  $R_c$  and inductance  $L_c$ . The plasma current,  $I_p$ , flows through the secondary coil.  $R_p$  is the plasma resistance,  $L_p$  is the inductance due to electron inertia and  $L_{mp}$  is the inductance related to the flux created by  $I_p$ . The mutual inductance,  $M$ , couples the antenna to the plasma current loop. The combination can also be represented by an equivalent circuit with a resistance  $R_f$  and inductance  $L_p$ . The change in resistance,  $\rho$ , due to plasma can be derived as [99]

$$\rho = R_f - R_c = \frac{\omega^2 M^2 R_p}{R_p^2 + \omega^2 (L_p + L_{mp})^2} \quad (5.1)$$

The change in reactance,  $\chi$ , due to plasma can be derived as

$$\chi = L_f - L_c = -\frac{\omega^2 M^2 (L_p + L_{mp})}{R_p^2 + \omega^2 (L_p + L_{mp})^2} \quad (5.2)$$

The power absorbed by the plasma,  $P_{abs}$  is obtained as

$$P_{abs} = \rho I_{rf}^2 \quad (5.3)$$

The complex geometry of the planar coil geometry makes it difficult to obtain the parameters ( $R_p$ ,  $M$ ,  $L_p$ ,  $L_{mp}$ ) in the equations directly and is estimated numerically [99, 100]. As evident from equation 5.1 as  $R_p \rightarrow 0$ ,  $\rho \rightarrow 0$  and as  $R_p \rightarrow \infty$ ,  $\rho \rightarrow 0$ . Hence the absorbed power in the inductively coupled plasma tends to zero for very low and very high plasma resistance values [99]. The plasma resistance further depends on the plasma density as shown in



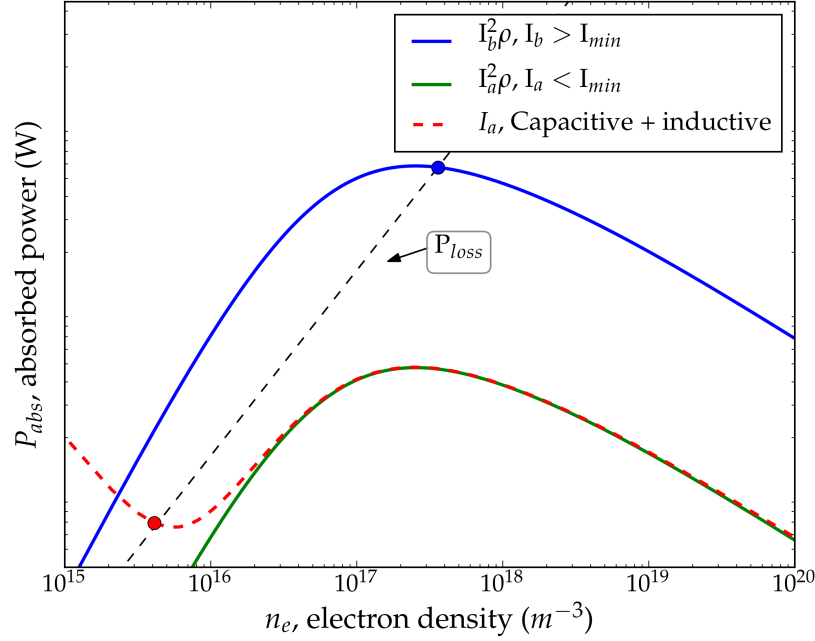


**Figure 5.4:** An illustration of power absorption behaviour in RF powered plasma [94]. The black dashed line represents the power loss curve ( $\propto n_e$ ). The power absorption including the capacitive coupling is shown as dashed red curve ( $\propto 1/n_e$ ) for  $I_a < I_{min}$ . Both axes are in logarithmic scale.

equations 12.2.1 and 12.2.4 of reference [94]. It describes that, at low electron densities,  $P_{abs}$  increases with electron density almost linearly,  $\rho \propto n_e$ . It reaches a maximum and starts to decrease with further density increase as  $\rho \propto n_e^{-1/2}$ . The resultant general behaviour of power absorption in ICP is shown in Fig. 5.4 for different electron densities. The graph is only for illustration of the power absorption properties. In the graph, we assume that a minimum RF coil current,  $I_{min}$ , is needed for a stable inductive plasma. We also consider two different coil currents,  $I_a$  and  $I_b$ , where  $I_a < I_{min}$  and  $I_b > I_{min}$ . The corresponding power absorption behaviour for the two coil currents is shown in green and blue curves.  $P_{loss}$  curve represents the power loss from the plasma and  $P_{loss} \propto n_e$  [97]. The intersection of this curve with the power absorption curve, for a particular current value, indicates the stable point of operation [94]. As shown in the figure, the power absorbed in the inductive coupling reduces towards low and high densities. It is also shown that if the current is less than  $I_{min}$ , no stable operation point exists and an inductive discharge is not possible. But a capacitive coupling can still create a discharge, as explained in the next section.

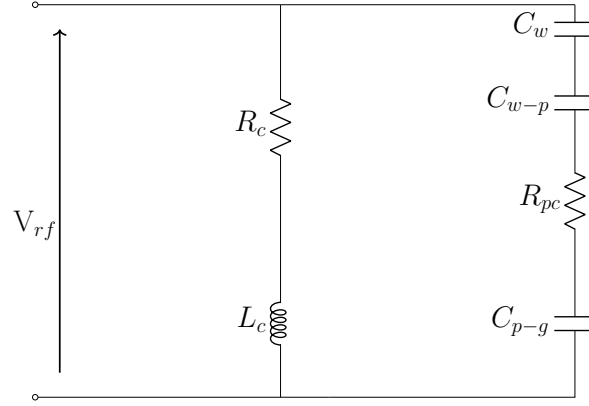


**Figure 5.5:** Circuit model of capacitive coupling from the RF antenna to plasma.  $R_c$  and  $L_c$  are the resistance and inductance of the antenna. This model is based on reference [101].

### 5.1.2 Capacitive coupling

As shown in Fig. 5.2, there exists the capacitive coupling between the RF coils and the plasma. The high RF voltages on the coil can create a capacitive RF current through the AlN window, plasma sheaths, plasma and then to the grounded chamber walls [97]. This can be represented by the circuit model in Fig. 5.5 proposed by *Watanabe et al.* [101]. Here,  $C_w$  represents the RF window capacitance. The capacitance of the two plasma sheaths, RF window–plasma and plasma–chamber(ground potential), are represented by  $C_{w-p}$  and  $C_{p-g}$ . These capacitance values are not easy to determine as they depend heavily on the plasma conditions.  $R_{pc}$  represents the plasma resistance corresponding to capacitive power absorption.  $R_{pc}$  is dependant on the plasma density and is  $\propto 1/n_e$  [97], which suggests that the capacitive power decreases as plasma density increases. The power absorption behaviour of plasma including the capacitive coupling is shown as a dashed red curve in Fig. 5.4 for the current  $I_a$ . The capacitive power absorption is more dominant at lower densities. Even when an inductive mode is not possible,  $I_{rf} < I_{min}$ , a stable operation point exists with the capacitive coupling. In other words, this coupling is essential for igniting the plasma. The D-Pace RF ion source usually exists in the capacitively coupled mode or electrostatic *E-mode* during the ignition. As absorbed RF power increases, the transition to the inductive mode or electromagnetic *H-mode* happens, accompanied by a sudden increase of electron density inside the plasma.

### 5.1.3 Impedance matching

The impedance of the RF antenna–plasma combination should match with the  $50\ \Omega$  load impedance of the RF power supply for efficient power transfer. The resistance of the plasma

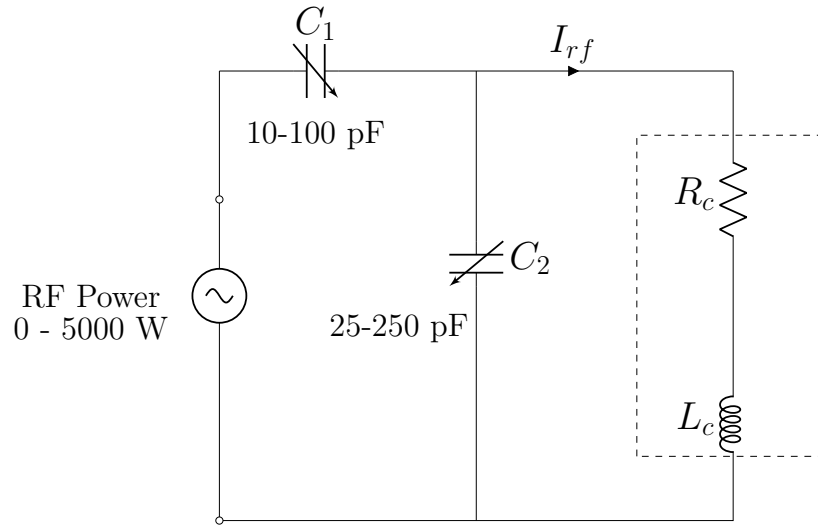


**Figure 5.6:** Schematic of the impedance matching box. The dashed box represents the copper RF antenna coil with a resistance  $R_c$  and inductance  $L_c$ , as in Fig. 5.3.

varies, depending on the plasma properties, as seen in equation 5.1 and hence the circuit impedance should be changed as the experiment progresses. The impedance match is established with the help of an impedance matching circuit as shown in Fig. 5.6. It consists of two motorized tunable capacitors whose capacitance values can be varied to have the lowest reflected power in the circuit. These values are controlled manually during the RF source operation. This is an important part of the operation, as improper tuning can lead to poor energy coupling to the plasma.

## 5.2 Challenges in the RF ion source operation

The RF power from the antenna is transferred to the plasma through the AlN dielectric window. This window offered some challenges in the operation of the ion source. It reached high temperatures during the operation ( $\approx 400^\circ\text{C}$  at 2500 W) of the ion source. The window is sealed to the ion source back plate copper flange using a fluorocarbon O-ring, as shown in Fig. 5.1. The O-ring is not directly exposed to the plasma. However, the high temperatures on the window lead to a partial deformation of the O-ring. The temperature on the window and the regions close to the O-ring location were measured using thermocouples during the ion source operation [80] and is shown in Fig. 5.7(A). The thermocouples were attached to the center of the window and to the edge of the window close to the O-ring. It can be seen that the AlN window temperature is approximately having a linear response to the increasing RF power. The black curve indicates edge temperatures close to the O-ring's location. The

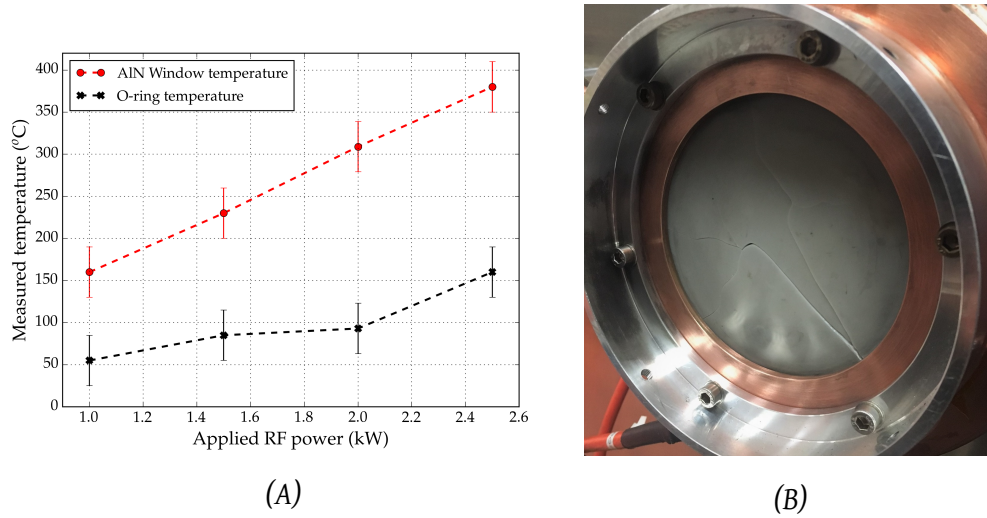


**Figure 5.7:** (A) Temperatures at the centre of the AlN window and edge of the window close to the O-ring, measured using a thermocouple [80]. (B) Fracture of AlN dielectric window during the ion source operation.

heat ‘resistance’ for fluorocarbon O-rings is  $\approx 204^{\circ}\text{C}$  [102]. Due to this, the RF power was limited to about 2500 W during the regular experiments, even though the RF power supply was capable of generating power up to 5000 W.

The situation was further worsened when a fracture occurred on AlN window during one of the experiments. The fracture is shown in Fig. 5.7(B). This led to damages to the vacuum system. It adversely affected the confidence in stable operation of the ion source and its potential to achieve higher negative ion beam currents. One of the goals of the thesis was to find a solution to this problem and operate the ion source at its full potential of 5000 W RF power safely.

### 5.3 Simulation studies of AlN window

The temperature and stress conditions prevailing on the AlN window during the ion source operation, need to be determined for addressing the challenges outlined in the previous sections. These were simulated using *Solidworks* simulations [89]. A *thermal study* simulation helps in finding the temperature distribution on different parts of an assembly, for a known amount of heat (temperature, heat flux, etc.) applied on a surface in the assembly. A *stress study* simulation generates the resultant stress on the assembly for a given set of bonding conditions and temperature distributions. Solidworks simulations use Finite Element Analysis (FEA) method for solving the geometries, where a model is divided into smaller and simpler elements.

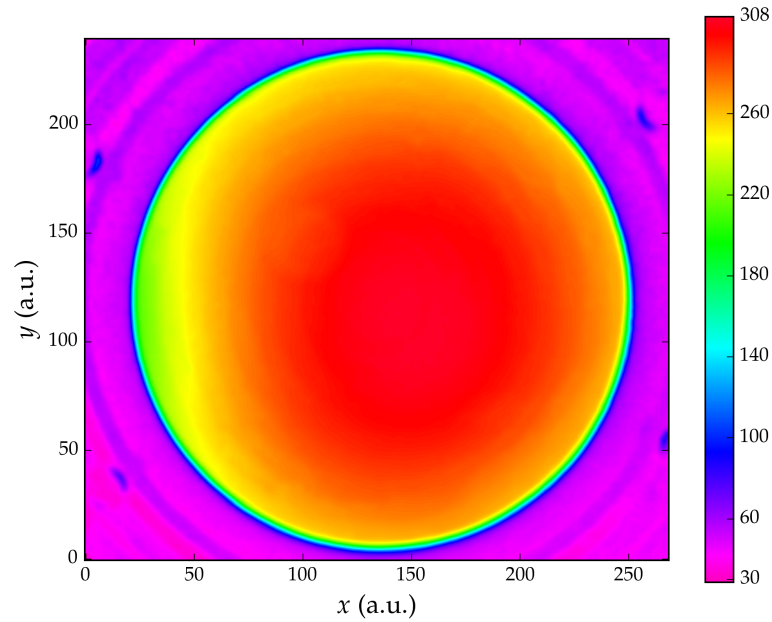


**Figure 5.8:** Contour plot of the temperature distribution on the AlN window and adjacent flanges after removing the input power to the plasma chamber. The data is generated from a thermal image using Fluke thermal imager. The axes units are arbitrary. The outer circular edge is the location of copper flange.

In order to generate a simulation closer to reality, data about the distribution of temperature on the AlN window and adjacent flanges was needed. This was made possible by capturing a thermal image of these parts using a handheld Fluke camera (*TiS55 Thermal Imager*). Such a method was utilized by Melanson [80] for a different set of experiments. It is not possible to capture the image while running the ion source due to the presence of the external antenna and impedance matching box in front of the window. Hence, the image was captured after switching off the RF power and then moving the matching box and antenna from the line of sight of the camera. So, there is a delay of approximately 15 seconds for image capture. A color plot of the thermal image, after operating the ion source at 1800 W of RF input power, is shown in Fig. 5.8. As seen from the figure, the temperature at the centre of the window reached around 310°C in the thermal image. The temperature dropped to around 200°C close to the copper flange and the flange was around 40°C – 50°C. The flange is cooled by water tubes around them, as shown in Fig. 5.1. It is not clear why the heat distribution is not exactly symmetrical in the thermal image.

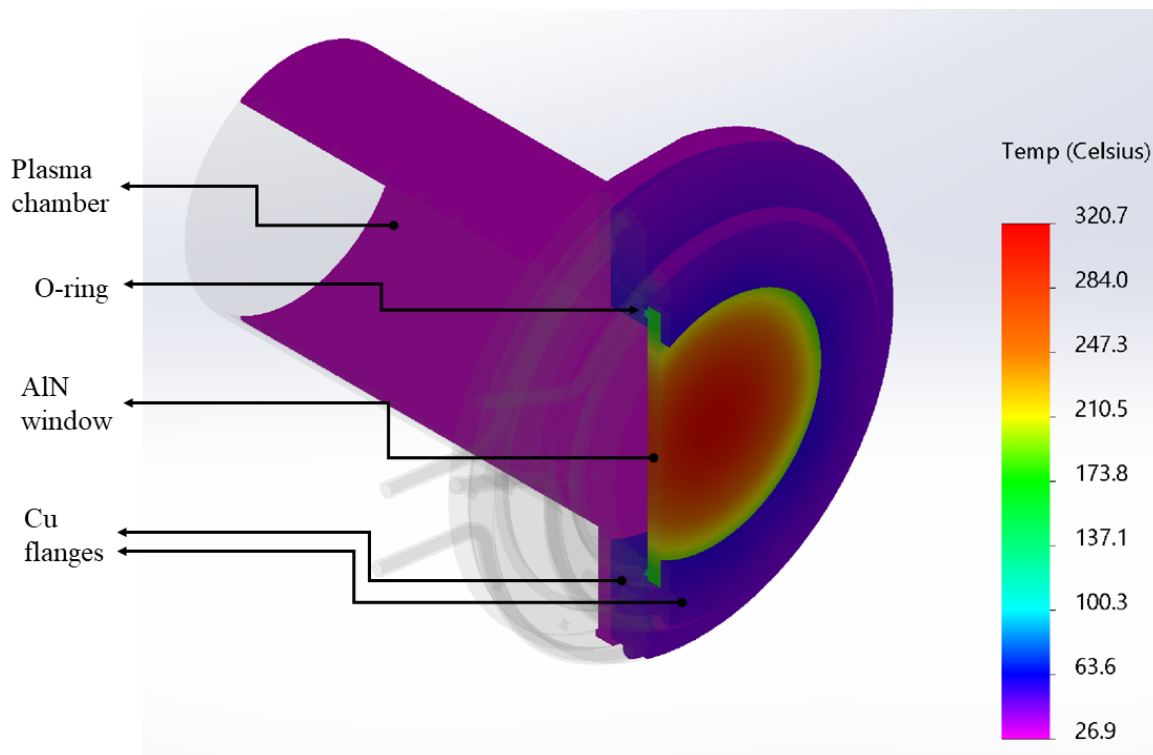


**Figure 5.9:** Section view of the RF ion source model in Solidworks static thermal simulation, receiving 1600 W of RF power on the plasma facing side of AlN window. The RF antenna, electrodes and magnets are not included in the simulation.

Parameter	Contact surfaces	Value
Contact resistance	Cu flange - cooling water tube	15000 W/m <sup>2</sup> K
Contact resistance	AlN window - copper flange	1500 W/m <sup>2</sup> K
Contact resistance	O-ring - copper surface(vacuum)	Bonded-no resistance
Convective heat transfer	Cooling water tube - water	11000 W/m <sup>2</sup> K

**Table 5.1:** The parameters used in Solidworks simulations. The contact resistance values between surfaces [90] and convective heat transfer coefficient values [91] for a water flow of 1.7 L/min are shown.

Based on the results from the thermal image and the thermocouple data in Fig. 5.7(A), a thermal model of the plasma chamber, AlN window and adjacent flanges with water cooling, was created using Solidworks thermal study simulations. The electrodes, magnets and magnet casing were not included in the thermal simulation, as its contribution to the heat transfer from the AlN window is negligible. The heat conduction between any two surfaces in the model can be specified using the *thermal contact resistance* values between them. Continuous heat transfer to the cooling water flow can be modelled by specifying the *convective heat transfer coefficient* on the respective surfaces. These values used for the simulations are

shown in Table 5.1. Simulations were performed to replicate the temperature distributions in the thermal image where the applied RF power was 1800 W. In the simulations, a uniform heat power of 1600 W was needed to be applied on the plasma facing side of the dielectric window for matching the temperature distribution in the thermal image. In reality, this is an oversimplification, as the power loss in the plasma can be due to various other factors like collisions and losses to the plasma chamber walls. Also, the RF window can be heated up due to the bombardment of ions and electrons. Hence the power considerations in the simulations are approximate. Results of the simulation are shown in Fig. 5.9. It can be seen from the results that the centre of the window reached a temperature around 320°C and it dropped to around 200°C towards the copper flange. The temperature on the adjacent copper flanges was around 50°C. The O-ring temperature was found to be varying in the range 130°C – 160°C on the surface bonded to the AlN window. Hence the simulations generated a temperature distribution very similar to that seen in figures 5.7(A) and 5.8.

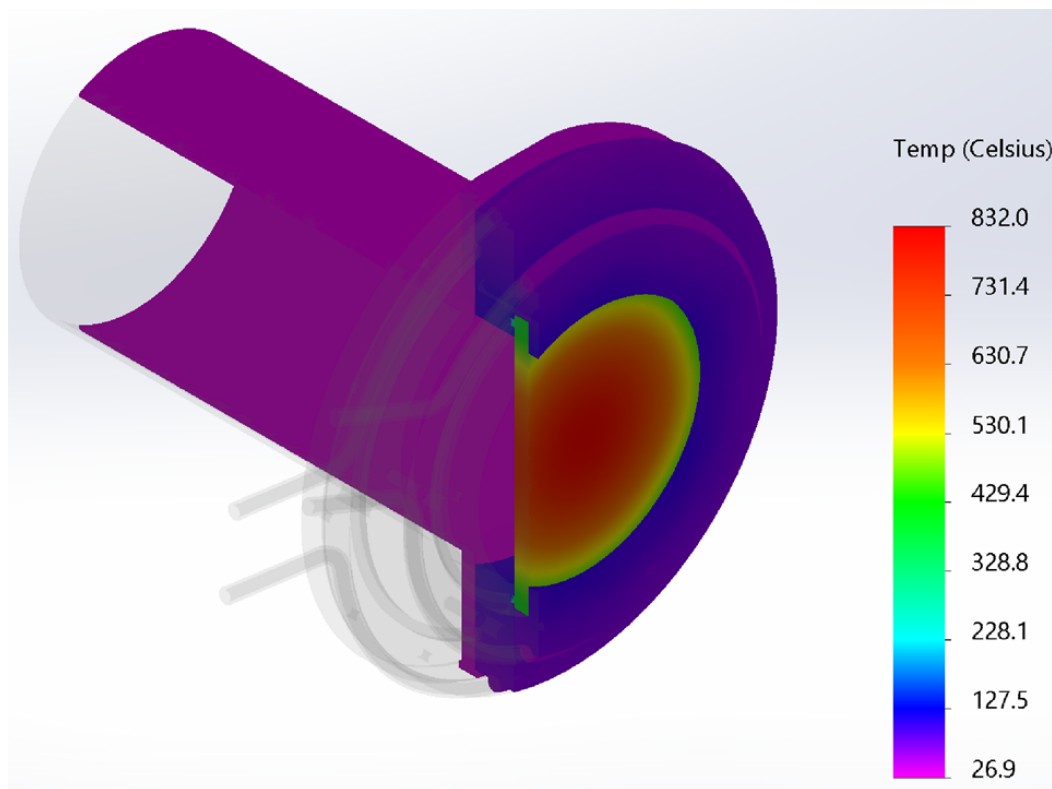


**Figure 5.10:** Section view of RF ion source model in Solidworks static thermal simulation, receiving 4400 W of RF power on the plasma facing side of AlN window. This is the probable temperature distribution when the applied RF power to the ion source is 5000 W.

Using the same set of parameters as in Table 5.1, another simulation was generated to find the probable temperature distribution when the maximum RF power from the power

supply, 5000 W, would be applied. This is about 2.8 times the power used for generating the thermal image in Fig. 5.8. Considering a linear behaviour in power loss, the heat power applied on the plasma facing side of the AlN window was also increased by 2.8 times, to 4400 W, for simulating the 5000 W RF power from the power supply. All other conditions were kept the same as in the previous thermal study simulations. The results of the simulation are shown in Fig. 5.10. As shown in the plot, there is the probability for the AlN window temperature to reach up to 830°C at 5000 W of applied RF power. The temperature obtained on the O-ring surface is in the range of 350°C – 400°C. This would be an alarming situation as this temperature is very much higher than the heat resistance of the O-ring [102] and can lead to vacuum seal failure.

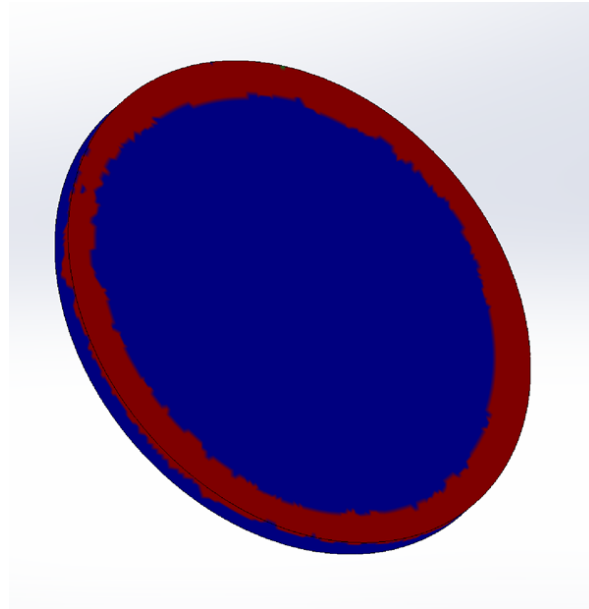


**Figure 5.11:** Results of factor of safety (FOS) evaluation on the AlN window using the temperature distribution results in Fig. 5.10. The plasma chamber and cooling tubes are not used in stress simulations. The copper flanges and O-rings are included in the simulations, but is hidden in the above picture. The regions with  $FOS < 1$  is indicated in red and safe regions are in blue. Results indicate that the failure probability is higher towards the edge of the plasma facing side of the AlN window.

The stress on the AlN window was studied using the Solidworks static stress analysis. Results from the thermal study simulations for 5000 W RF power in Fig. 5.10 were used as the thermal load in the static stress analysis. The plasma chamber was not included in the stress simulations since it is not expected to add any effect on the mechanical stress on the window. A 15 psi pressure was also applied normal to the plasma facing surface of the AlN window surface to simulate vacuum conditions. The AlN window is constrained by vacuum on the plasma facing side and copper flange on the atmosphere side. The Solidworks stress



simulations can perform a *factor of safety* (FOS) [103] calculation of a material based on the value of stress on it. An FOS value of  $< 1$  indicates stress values higher than what the material can withstand. In the case of a brittle material like AlN, the simulations use *Mohr-Coulomb stress* to predict the material failure [104]. This is done by comparing the stress values to the limit of tensile and compressive stress of the AlN material. The resulting FOS distribution on the AlN window, using the simulations, is shown in Fig. 5.11. It indicates that regions towards the edge of the window exceed the stress limit of the material, as per the Mohr-Coulomb failure criterion used in the simulations. Hence it can be seen that there is a probability of failure of AlN window if it is operated at high RF powers.

It should be noted that the results do not indicate that the thermal stress on the window is the absolute reason for the fracture observed during experiments. But it indicates that the high temperature on the RF window is not advantageous in the stable operation of the RF ion source. Failure of brittle ceramics can also occur due to the thermal stress on pre-existing cracks, leading to crack propagation [105]. Other related failure mechanisms are thermal shock (sudden change in temperature) and thermal fatigue (repeated cycling between two temperatures) [106]. Additional contributing factors from the plasma are the ion bombardment on the window, chamber material (copper) deposition on the window etc., which are beyond the scope of the simulations. The quickest way forward for upgrading the RF ion source was by addressing the possibility of fracture occurring due to the thermal load on the window.

In the existing original design, the AlN dielectric window is cooled indirectly by water circulating through brazed copper tubes around the copper flanges as shown in the top picture of Fig. 5.14. But simulations indicate that this cooling is inadequate, as it leads to O-ring failures and high stress values on the AlN window. Different solutions like brazing the window to the copper RF antenna, increasing the thickness of the AlN window and continuous water circulation on the window were simulated. The easiest solution for decreasing the window temperature was adding a water flow channel directly on the top surface of the AlN window. This was again simulated using Solidworks thermal simulations. A spiral water flow was added on the top surface of the AlN window, with all other conditions same as in Fig. 5.10. The results of the added water flow channel is shown in Fig. 5.12. As can be seen, adding the spiral water channel has the potential to reduce the peak temperature on the AlN window by about 80% at 5000 W of applied RF power. But, the water flow rate should be maintained such that the convective heat transfer coefficient of the water flow should be at least  $11000 \text{ W/m}^2\text{K}$  for maintaining the water temperature to less than  $80^\circ\text{C}$  in regions close to the AlN window. In the practical scenario, a new part needed to be added on top of the AlN window, with channels for water circulations. The material for this part should be

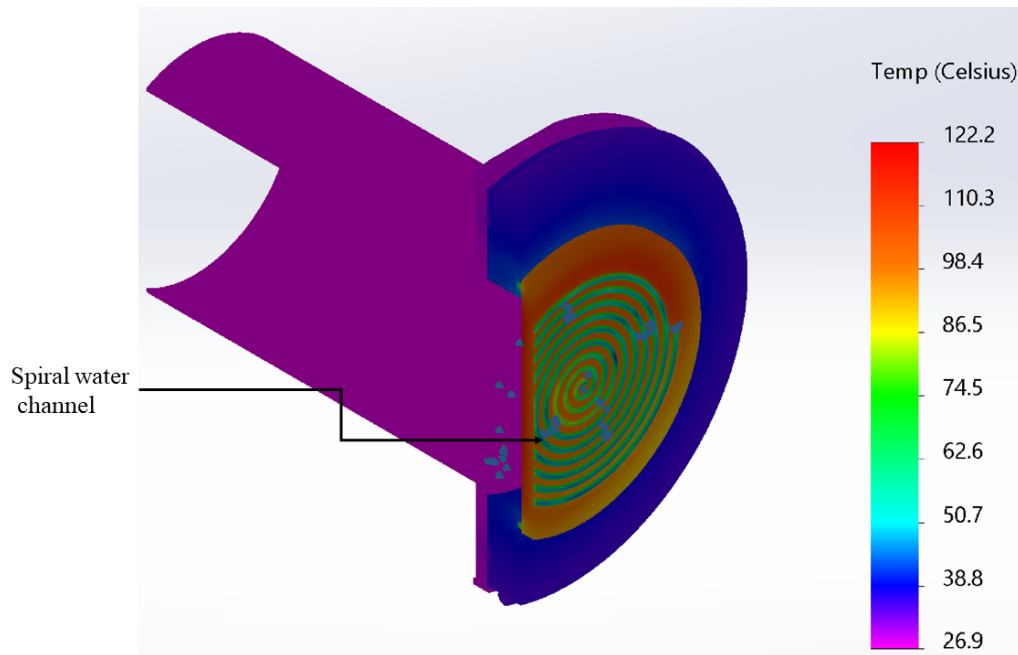


**Figure 5.12:** Thermal simulation results after adding a spiral water flow channel on top of the AlN ceramic window. Compared to Fig. 5.10, the temperature is reduced by about 80%.

a dielectric material with a low loss tangent, such that it does not absorb much of the RF energy. The drawback is that the RF antenna would be further away from RF window, which results in low energy coupling efficiency. But, a higher beam current could be achieved, if 5000 W RF power can be applied successfully.

## 5.4 Design changes - 'PEEK design'

The part designed for adding water channels on the AlN window, to increase the heat transfer, is shown in Fig. 5.13 and the assembly is shown in the bottom picture of Fig. 5.14. Here, the outer copper flange in the existing design was replaced with a jacket made of PEEK (polyether ether ketone) material in the improved design. This has separate water inlet and outlet connections. The cold water entering through the center of the PEEK jacket follows a spiral channel along the surface of the dielectric and exits through the side of the jacket. An additional O-ring created a leak proof seal between the PEEK jacket and AlN dielectric. The water circulation was expected to absorb heat from the AlN window such that the thermal stress could be maintained in the safe limit even at 5000 W of RF power. The new design was also expected to maintain the temperature of the window below the heat resistance limit of the O-ring.

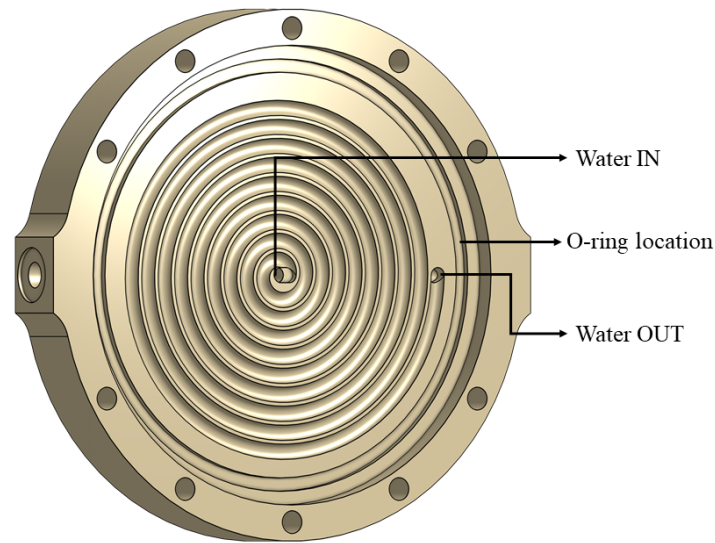


**Figure 5.13:** New part made of PEEK material for providing spiral water flow to the outer surface of the AlN window.

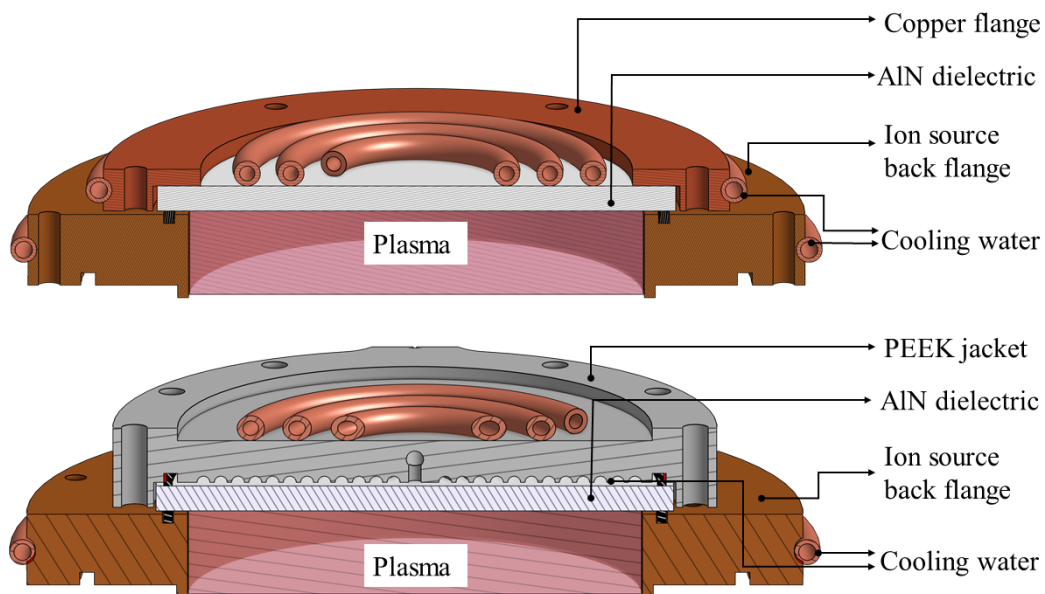


**Figure 5.14:** Section view of the RF ion source back plate region of the 'original design' (top) and new 'PEEK design' (bottom). Plasma chamber and electrodes are not shown. There is cooling water flow through the copper RF antenna also. The RF antenna is further away from the AlN dielectric window by 10 mm in the 'PEEK design'.

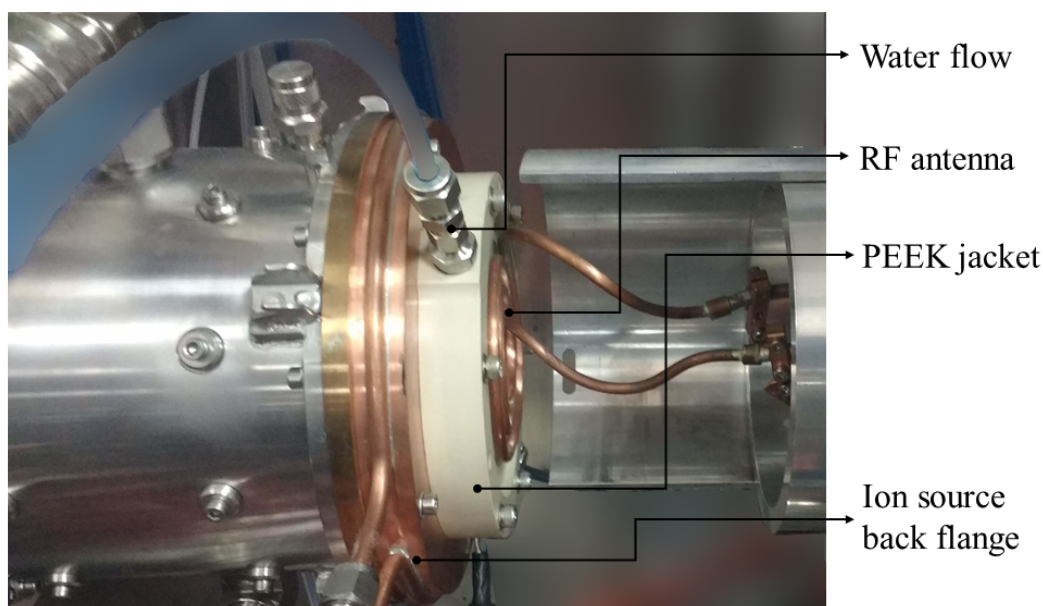
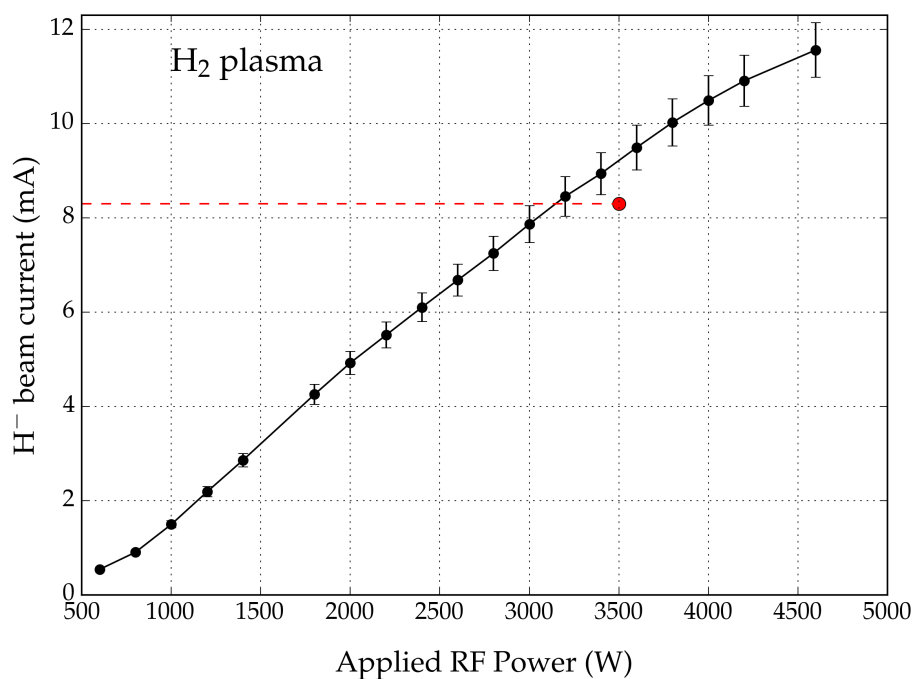


**Figure 5.15:** Picture of the experimental arrangement for PEEK water jacket design.

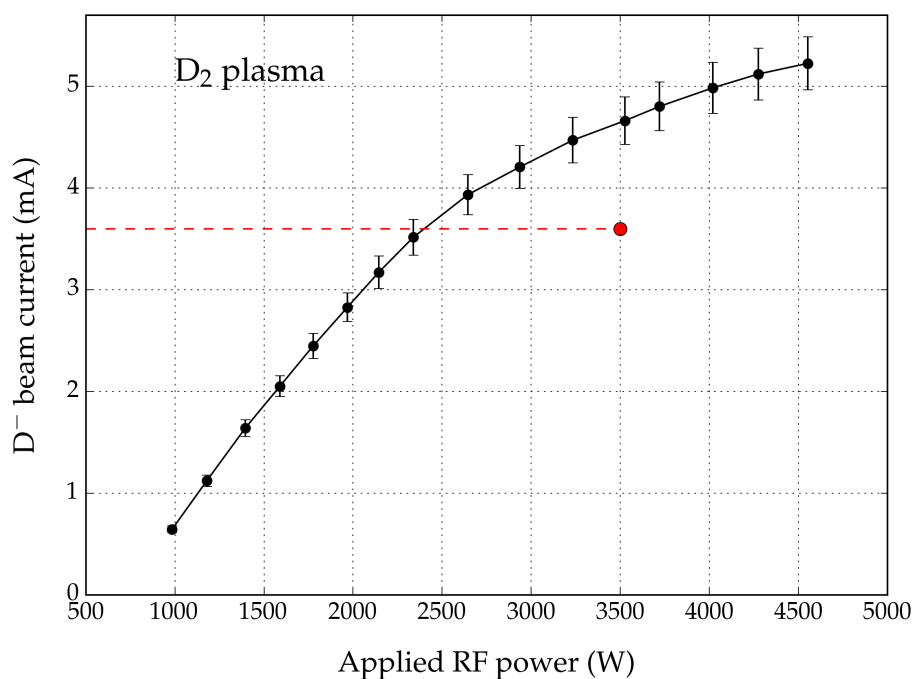
## 5.5 Experimental results

The PEEK water jacket design was manufactured and experiments were carried out in  $H_2$  and  $D_2$  plasmas. The photograph of the arrangement is shown in Fig. 5.15. The new design required higher RF power for initiating the H-mode discharge in the plasma, indicating a lower power coupling from RF antenna to plasma. This is detailed in later sections.

The ion source, with the design upgrade, was successfully operated at 5000 W of RF power and thus attained the full potential of operation with the design change. The water flow through the jacket was about 1.5 L/min, corresponding to a minimum convective heat transfer of  $15000 \text{ W/m}^2 \text{ K}$  [91]. The temperature of inlet and outlet water flowing through the PEEK jacket was continuously monitored using a thermocouple attached to the fittings during the experiment. The difference in temperature between the inlet and outlet water through the PEEK was about  $18^\circ\text{C}$  at 5000 W of applied RF power for  $H_2$  plasma. This corresponds to about 2000 W of power removed from the system. The ion source was able to generate 11.7 mA of  $H^-$  and 5.3 mA of  $D^-$  beam currents at the Faraday cup at about 5000 W of applied RF power. The beam current values for different applied RF powers are shown in Fig. 5.16 and the tuning parameters for the highest beam extraction are shown in Table 5.2. The experiment was repeated several times and the ion source showed stable operation. The attained beam currents are the highest achieved so far in D-Pace's RF ion source.



(A)



(B)

**Figure 5.16:** (A)  $H^-$  beam currents (20 sccm gas flow, 30 keV beam energy) and (B)  $D^-$  beam currents (18 sccm gas flow, 30 keV) achieved using PEEK jacket design. The beam currents are measured using Faraday cup at a distance of 480 mm from plasma electrode. The red circle represents the maximum beam current achieved with the previous RF ion source design [77] and the black circles represent the data with the upgraded PEEK jacket design.

Parameter	Value (H <sup>-</sup> )	Value (D <sup>-</sup> )
Total beam current, $I_{FC}$ (mA)	11.8	5.3
Forward RF power (W)	4800	4900
Reflected RF power (W)	40	154
Bias (mA, kV)	20.1, 30.0	10.9, 30.0
Extraction electrode (mA, kV)	93.4, 3.4	100.3, 3.1
Plasma electrode (A, V)	12.0, 34.6	15.6, 35.8
Gas flow (sccm)	20	18
4 RMS Normalized emittance (mm.mrad)	0.68	0.42

**Table 5.2:** Tuning parameters for the maximum beam current obtained from the RF ion source using PEEK water jacket design.

### 5.5.1 Coupling efficiency and mode transitions

The percentage of RF power coupled to the plasma from the RF antenna cannot be measured precisely, as there will be a loss of energy to the surroundings and the PEEK jacket. The coupling also depends on the capacitance values of the capacitors in the impedance matching box. The RF antenna should be as close as possible to the plasma for maximum coupling efficiency. As the distance between the coil and plasma increases, the mutual inductance decreases [107] and this affects the power transfer efficiency, as shown in equation 5.1 ( $P_{abs} \propto \rho \propto M^2$ ). In such a case, a higher current flow through the antenna,  $I_{rf}$ , is needed for maintaining the same power absorption in the plasma. As seen from Fig. 5.14, compared to the original design, the antenna is away from plasma by about 10 mm (thickness of PEEK water jacket) for the PEEK design. This can contribute to reduced coupling efficiency. The difference in coupling efficiency between the two designs can be seen by studying the E-mode to H-mode transition [97] characteristics of H<sub>2</sub> plasma inside the RF ion source. As seen in Fig. 5.4, the plasma exists in E-mode during ignition. It later moves into H-mode accompanied by a sudden increase of electron density inside the plasma. The threshold power required for E–H mode transition is a good indication of the coupling efficiency. The transition can also be identified visually, when the plasma transforms from a low brightness plasma into a high brightness one. Hence, the spectrum from the plasma can indicate the mode transition. H<sub>2</sub> plasma emission spectrum from the existing design and the PEEK design were captured using an optic fiber. This fiber was placed about 368 mm downstream of the plasma electrode, inside the vacuum box. Light from the fiber is transferred to Ocean Optics optical spectrometer [108] to determine the wavelengths and corresponding intensities. A typical spectrum from the RF plasma, obtained from the spectrometer software, is shown in

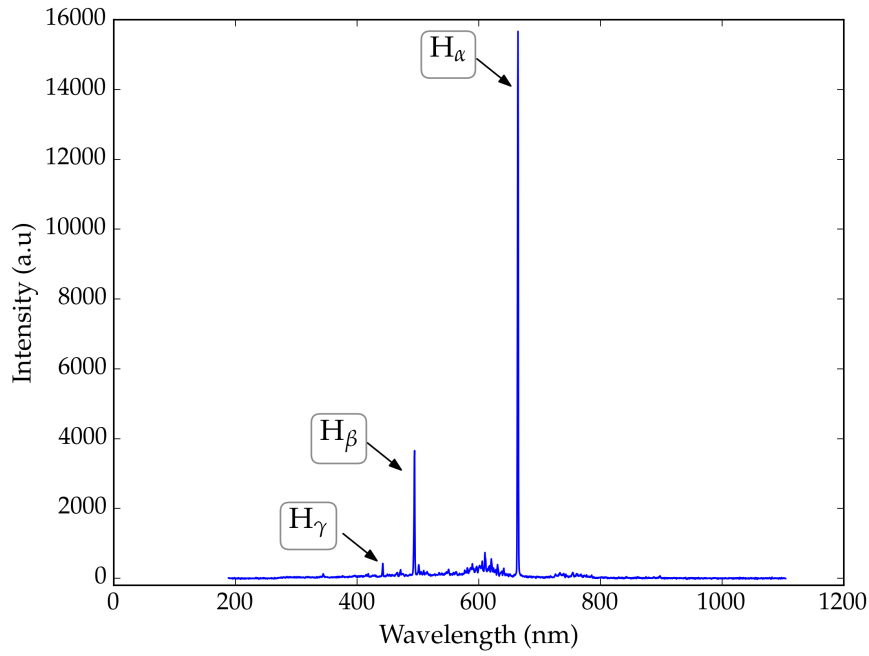


**Figure 5.17:** A typical spectrum of  $H_2$  plasma from the RF ion source. The applied RF power is 600 W and the gas flow is 10 sccm. The Balmer lines are shown.

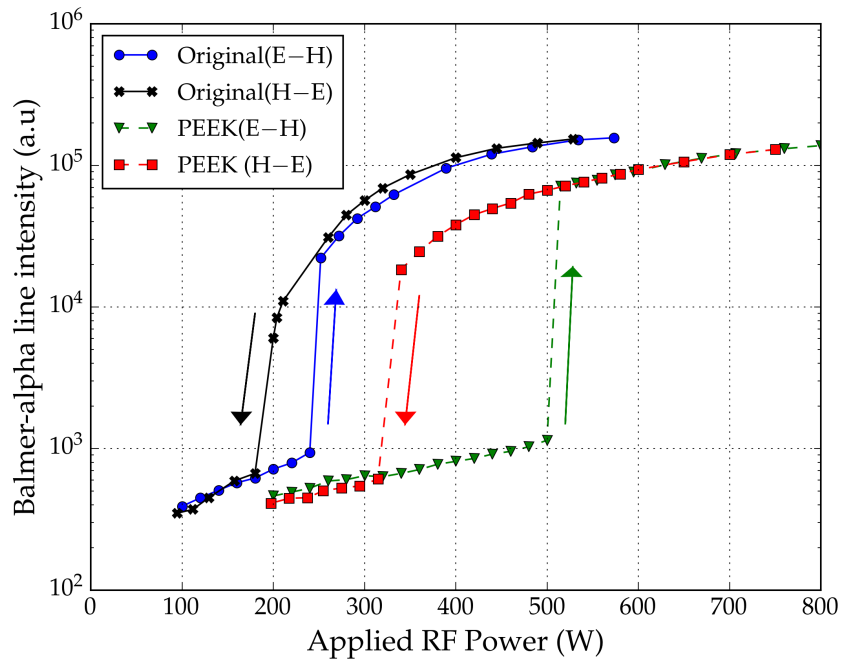


**Figure 5.18:** Mode transitions for the existing design and the improved PEEK design(dotted lines) for hydrogen plasma at a gas flow of 10 sccm. The up arrows (E–H) indicate increasing power and down arrows (H–E) indicate decreasing power.

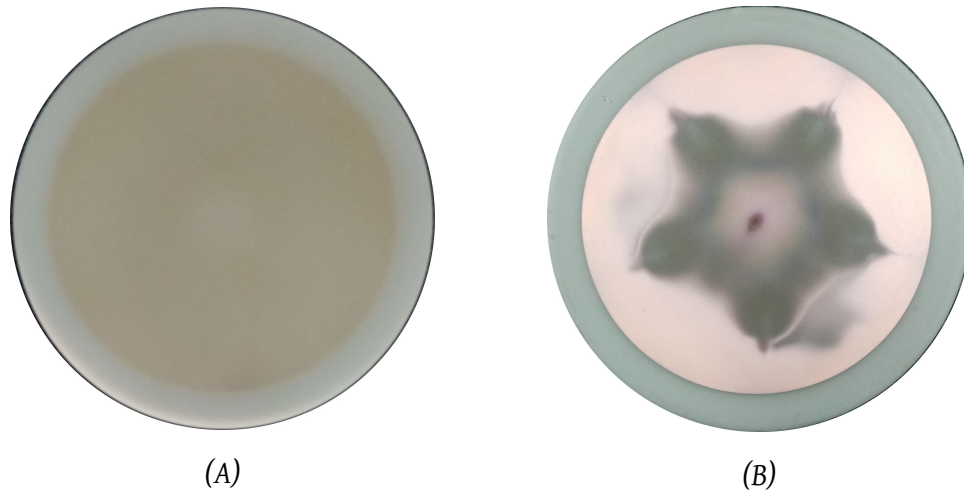


**Figure 5.19:** Picture of AlN ceramic window (A) before and (B) after the operation of the RF ion source with the PEEK water jacket, at 5000 W of RF power, 20 sccm gas flow. A continuous film of copper is deposited on the plasma-facing side of the window, obstructing the RF energy coupling from the RF antenna to the plasma.

Fig. 5.17, in which the Balmer series lines of  $H_\alpha$ ,  $H_\beta$  and  $H_\gamma$  can be identified. The intensity of all the three lines increases by manifolds during the E–H mode transitions.

The intensity of the Balmer alpha line,  $H_\alpha$ , is used in the current study for identifying the E–H mode transitions. The intensity of the  $H_\alpha$  is recorded from the software for different RF powers. The results of the Balmer-alpha line study for the two designs are shown in Fig. 5.18. The E–H mode transition for the existing design occurs at around 220 W and for the improved PEEK design, it occurs at around 520 W. This indicates more loss of power and lower coupling efficiency for the new design due to increased distance between the antenna and plasma. The plots also indicate the typical hysteresis behaviour observed in inductively coupled plasmas, which represent multiple stable operating points in the plasma. This is mainly attributed to the non-linearities in power absorption and dissipation in such plasmas. Various literature is available on this topic [109, 110] and is not pursued further in the current thesis.

### 5.5.2 Copper deposition on AlN window

Another major challenge encountered in the operation of the improved PEEK design was the increased copper deposition on the AlN window during the operation. A continuous film of copper was formed on the surface of the window, leading to a decrease in energy coupling from the external antenna to the plasma. This is due to the sputtering of chamber materials by energetic ions in the plasma. This copper deposition is shown in Fig. 5.19. The



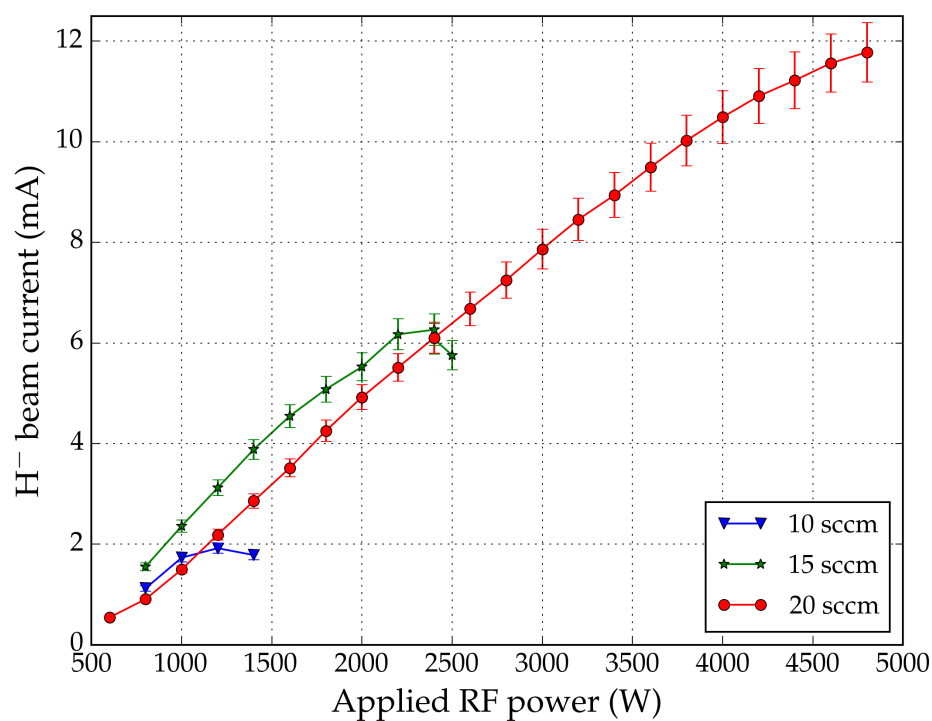
‘star’ shaped pattern seen on the window follows the geometry of cusp magnetic fields shown in 2.7. Ion tracking simulations, in ion sources with similar magnetic cusp fields, generate such a pattern [111]. Experiments were also conducted using an aluminum plasma chamber, but still the copper deposition results were the same as in the picture. This indicates that most of the sputtering is from the copper ion source back flange shown in Fig. 5.14 and Fig. 5.15.

An interesting variable related to the copper deposition is the amount of pressure/gas flow in the source. Experiments were performed using different gas flows. At lower gas flows like 10 sccm, the beam currents started to decrease even at low values of RF power, due to copper deposition on the window. But for higher gas flows of about 20 sccm, no decrease in beam currents was observed during the operation. This is shown in Fig. 5.20(A). As can be inferred, a higher gas flow reduces the rate of copper deposition, enabling to reach higher beam currents. The influence of higher gas flow on copper deposition can be understood by analyzing the plasma sheath potentials. The corresponding values of the optimum plasma electrode voltages for the same experiments are shown in Fig. 5.20(B). It shows that the voltage required for maximum beam extraction is higher for lower gas flows. The potential applied on the plasma electrode helps the negative ions in the plasma overcome the plasma sheath potential well. Hence, the optimum plasma electrode voltage value usually lies close to the plasma sheath potential [112]. Thus it can be inferred that the plasma sheath potential is lower for higher gas flows and vice versa.

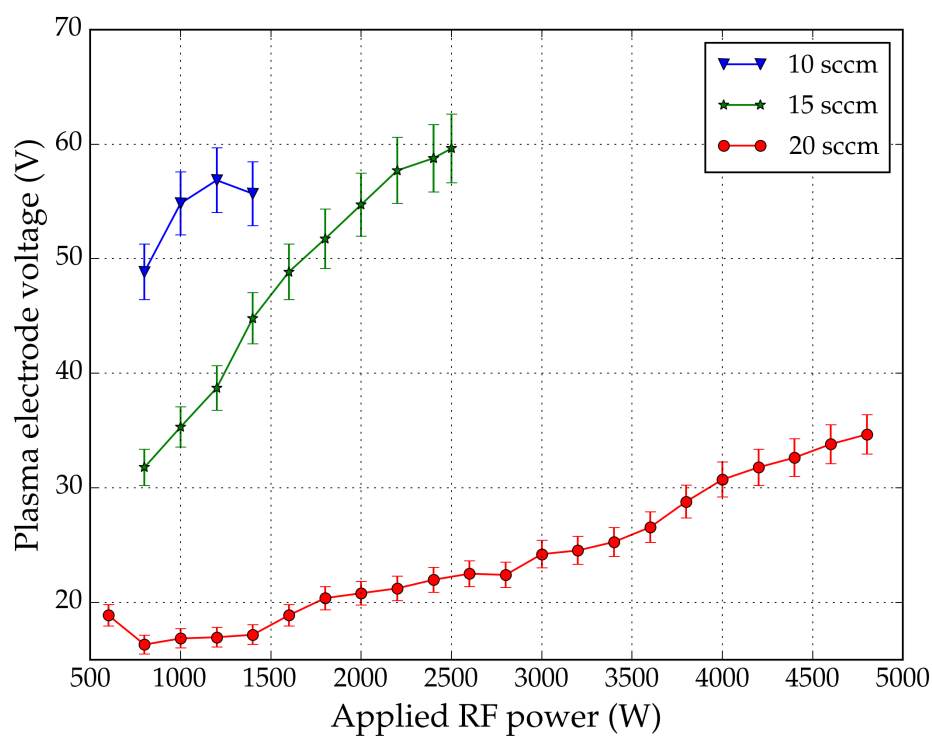
The plasma sheath potential is mainly influenced by the RF currents generated by the capacitive coupling. The circuit model shown in Fig. 5.5 represents the plasma sheath between chamber and plasma as a parallel plate capacitor of  $C_{p-g}$ . Let the voltage drop across this sheath be  $V_{p-g}$ . We can consider the width of this sheath as equivalent to the Debye length [101],  $\lambda_D \propto (1/n_0)^{1/2}$ , as in equation 2.12. Hence for a constant RF power,

$$V_{p-g} \propto \frac{1}{C_{p-g}} \propto \lambda_D \propto \frac{1}{n_0^{1/2}} \quad (5.4)$$

For a fixed power absorbed, an increase in gas flow could lead to an increase in electron density, which further results in a decrease of the plasma sheath voltages. Thus, the copper deposition is dependant on the sheath voltage. The high sheath voltages can cause ion acceleration towards the walls of the plasma chamber and cause sputtering of the chamber materials. This can result in the observed copper deposition [113]. This in turn is caused mainly by the capacitive coupling between the high voltage RF antenna and the plasma, which modulates the RF sheath potential. For low plasma densities, the skin depth is larger and hence most of the RF voltages is dropped across the sheath [94]. Note that for the case



(A)



(B)

**Figure 5.20:** (A) Dependence of  $H^-$  beam currents measured at the Faraday cup, on different gas flows. (B) Variation of optimum plasma electrode voltages for different gas flows. The dip in values for 10 sccm and 15 sccm gas flows are due to copper deposition on the AlN window.

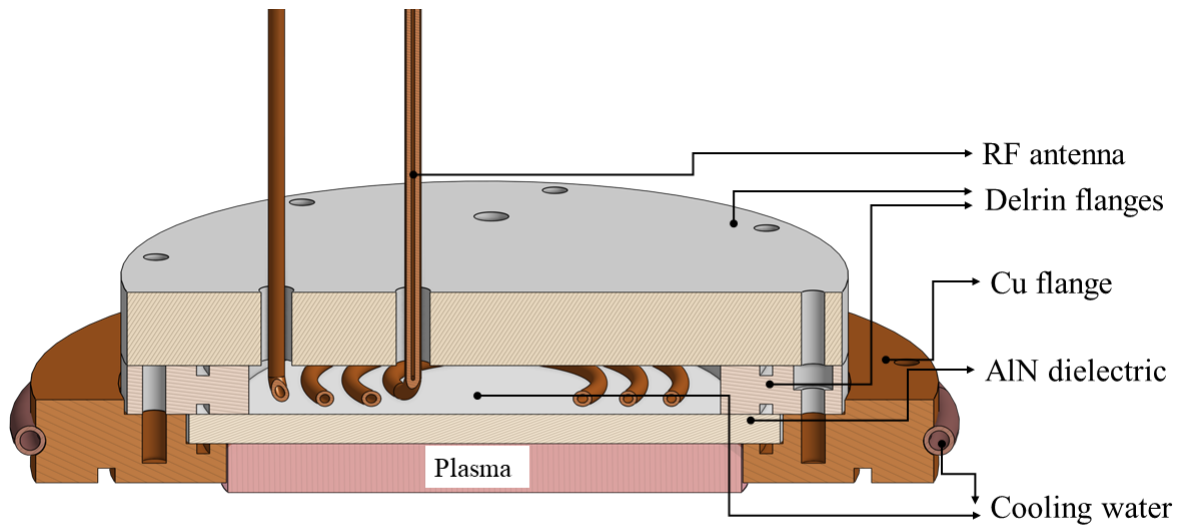


**Figure 5.21:** Cross sectional view of the ‘immersed antenna’ design. The antenna is immersed in deionised water and is positioned close to the AlN ceramic window.

of the filament ion source, the maximum optimum plasma electrode voltage is  $\approx 4$  V, which indicates that high plasma voltages in the RF ion source is in fact due to the RF coupling to the plasma.

## 5.6 Water immersed RF antenna

As seen in section 5.5.1, the PEEK design resulted in a reduced energy coupling efficiency from RF antenna to plasma. In order to improve this, a second design was made by replacing the PEEK jacket. In this design the RF antenna was immersed in circulating deionised water and placed about 3 mm from the AlN window such that there is minimum power coupling loss. Additional delrin flanges were made to seal the water circulation region. This design is shown in Fig. 5.21.

In the PEEK design, the plasma gets ignited in the capacitive E-mode and on further increase of power, it moves into inductive H-mode. The drawback of the immersed antenna design was that the plasma never attained the inductive H-mode. The plasma was getting ignited and it remained in the capacitive E-mode even after increasing the applied RF power to about 1500 W. The transition to the H-mode was not occurring. But, the design attained the H-mode of operation easily when experiments were performed without the water circulation. Hence it can be inferred that the continuous water circulation adversely affects the RF energy

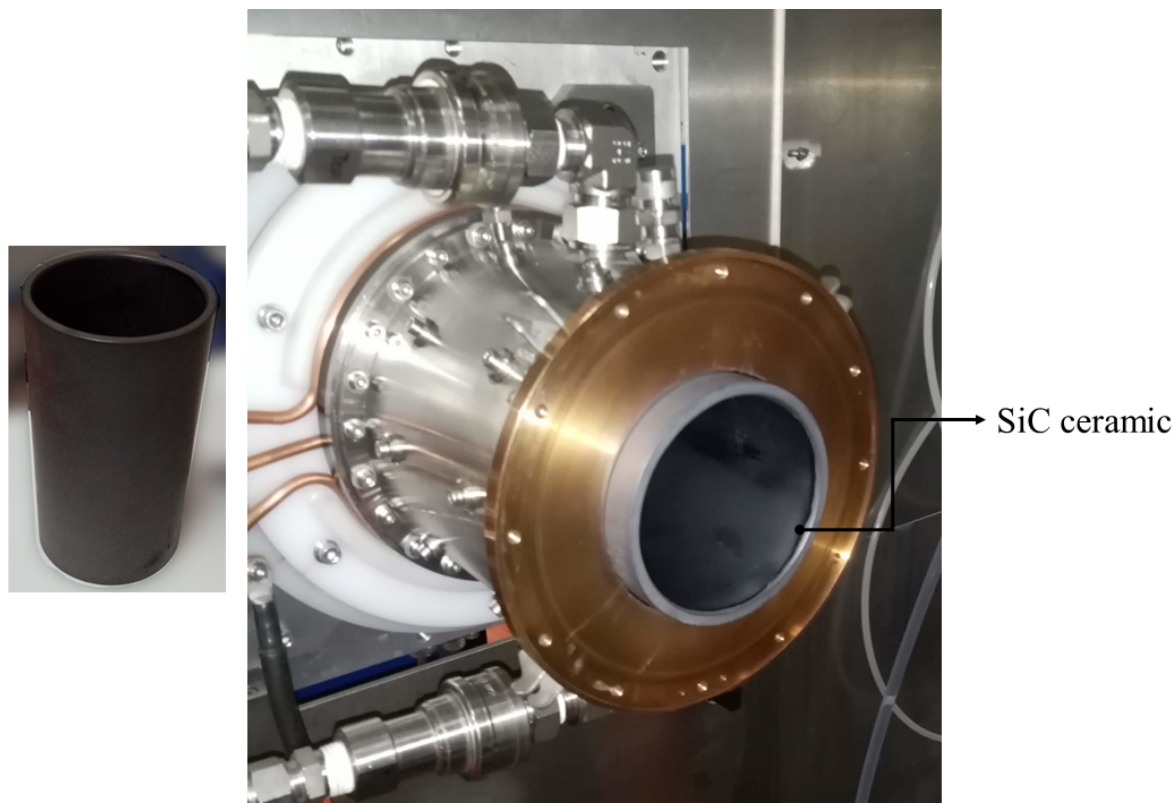


**Figure 5.22:** Picture of silicon carbide ceramic insert and its location inside the copper plasma chamber. The ceramic insert extended up to the plasma electrode.

coupling into the plasma. It should be noted that for the PEEK design shown in Fig. 5.14, water flow was confined to a narrow spiral channel and it attained the H-mode.

## 5.7 Effect of a ceramic plasma chamber

In order to reduce the copper deposition on the AlN window by reducing the chamber sputtering, a ceramic insert made of silicon carbide (SiC) was tested as shown in Fig. 5.22, in the PEEK jacket design. The ceramic formed the boundary of the plasma chamber. The dimensions of the insert were such that there was very little copper surface on the chamber in contact with the plasma.

The experiment was conducted using 15 sccm of gas flow. The plasma ignited and sustained successfully in the H-mode discharge. However, the performance of the ion source was adversely affected, as only about 1 mA of  $H^-$  beam current was recorded at the Faraday cup at 1200 W of RF power. Further tuning of the source was not possible as the plasma electrode current was too low and not increasing, even though the plasma electrode voltage

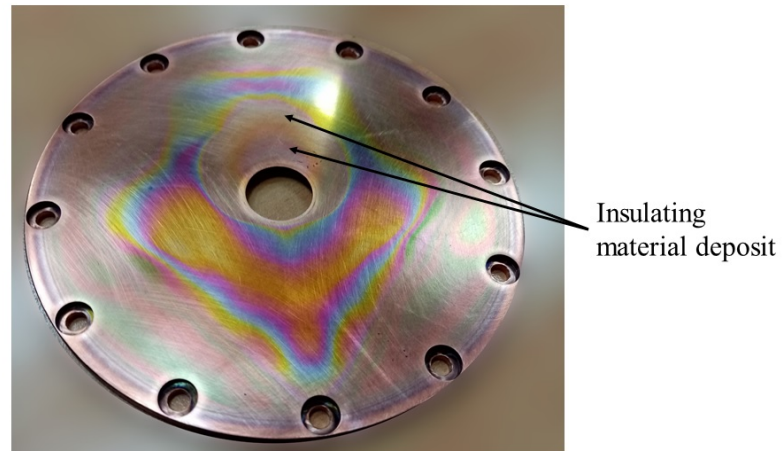


**Figure 5.23:** Picture of plasma electrode after the experiment using SiC insert. There was a deposit of insulating film on the surface leading to low beam currents.

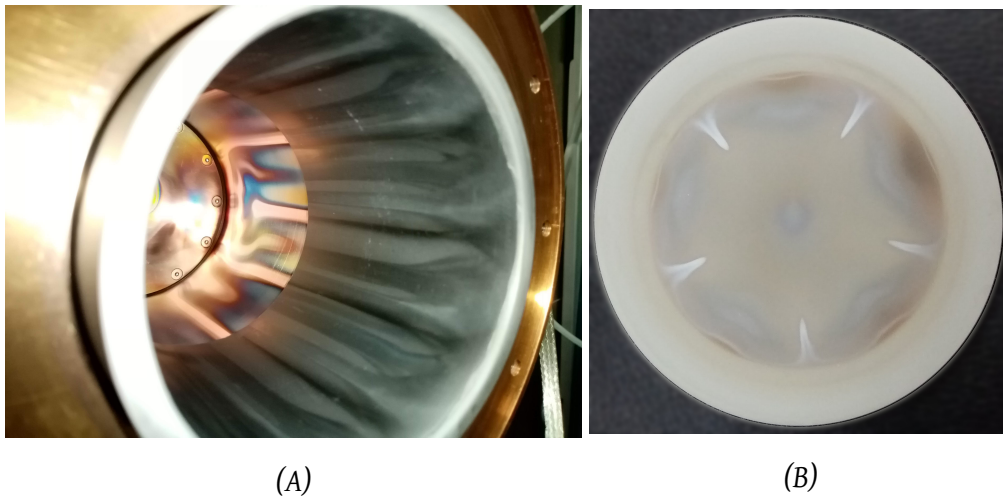


**Figure 5.24:** (A) Picture of plasma chamber after the experiment using half cut SiC ceramic insert. Deposits are seen on the parts of copper plasma chamber exposed to plasma. (B) Picture of AlN window after the experiment. Even though appearing free of any copper deposit, some regions of the window had metal deposition.

was  $\approx 60$  V. Upon examining the source after the experiment, it was surprising to find that the copper plasma electrode had some layers of insulation deposit on its surface as shown in Fig. 5.23. This is believed to be due to the sputtering of material from the SiC ceramic insert itself due to the high plasma potential. This made the surface of the plasma electrode non-conducting, leading to a decrease in ion beam extraction.

Another experiment was conducted by reducing the length of the SiC ceramic insert in half, such that it is much more distant from the plasma electrode. This was conducted to

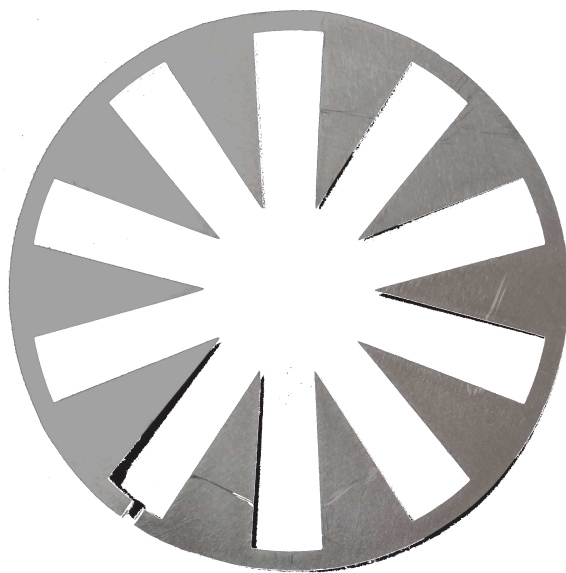


**Figure 5.25:** A picture of the Faraday shield used for initial trials. The sheet was made of SS.

see if it reduced the sputtered material deposit on the plasma electrode. The performance was slightly better compared to the uncut ceramic insert. About 2.6 mA of  $H^-$  beam was recorded at the Faraday cup at 2000 W of RF power at an optimum plasma electrode voltage of 38 V. Thereafter the plasma electrode current began to decrease. The picture of the plasma chamber and AlN window after the experiment, is shown in Fig. 5.24. As seen in the picture, there were some colored deposits seen on parts of the copper plasma chamber exposed to plasma. The exact composition of these deposits is not known. The AlN window was mostly clear visually. But, some parts of the window showed a lower resistance, indicating metal deposition on the surface of the window.

## 5.8 Conclusions

The chapter describes the experimental works undertaken for upgrading the performance of D-pace's RF-powered ion source. The major goals of the upgrades were related to improving the safety of operation and achieving the full operating power of 5000 W. Factors affecting the stable operation of the ion source were simulated and a new design to solve the temperature and stress related issues on the AlN window was made and implemented. This upgrade has successfully attained 5000 W of RF power operation of the ion source and achieved 11.7 mA of  $H^-$  and 5.3 mA of  $D^-$  beam currents. This is the highest ever recorded by D-Pace's RF ion source. Also, no window failures have been observed so far since the implementation of the PEEK design.

One of the important challenges that needs to be solved before the commercialization of this design, is the copper deposition on the AlN window. Attempts to solve this problem with a ceramic plasma chamber and an immersed RF antenna design have not succeeded so far. One of the other established ways for reducing the capacitive coupling is with the help of a Faraday shield [94, 95, 97], which is a metallic grounded shield in between the RF antenna and the AlN window. This provides an alternate path for the capacitive coupling rather than through the plasma. The shield also should not obstruct the magnetic field coupling to the plasma. Initial trials were conducted using one such Faraday shield shown in Fig.5.25. The challenge encountered with this shield was related to the difficulty in igniting the plasma and achieving the inductive coupling from the antenna. As mentioned in the earlier sections, capacitive coupling is essential for plasma ignition and hence should not be reduced completely. Another limiting factor in using the shield is the possibility of electrical breakdown between high voltage antenna coils and the grounded shield. Future works aim at developing an effective Faraday shield, that can reduce the capacitive coupling without affecting the plasma ignition. Also, alternate methods that support the plasma ignition in the ion source need to be determined.

# Chapter 6

---

## Simulations using IBSimu code

Computational tools have a high significance in designing and upgrading ion beam extraction systems and beam lines. Often, the first step in the design of extraction systems is the development of a simulation using the computational tool. IGUN [114], PBGUNS [115], SIMION [116], KOBRA [117] and IBSIMU [21] are some of the codes used for simulations. These codes make stronger approximations of the physical processes inside the plasma, but are much faster than the particle in cell (PIC) codes [118]. The current chapter deals with the studies related to IBSimu code. This plasma extraction code is widely used in creating ion beam simulations at different ion source facilities like CERN, Oak Ridge National Laboratory, Texas A & M institute and University of Jyväskylä. Hence, the studies related to improving the code are greatly beneficial to the ion source community. Disagreements were observed between experimental results and IBSimu simulations in some ion sources [118]. In order to have more clarity on these observations, an experimental campaign was conducted using D-Pace's ion sources, in collaboration with Dr. Taneli Kalvas, the author of IBSimu code. This campaign was mainly aimed at studying the variation in the beam emittance from the ion source under different plasma conditions and comparing the results with IBSimu simulations. The chapter deals with the results of the experimental campaign and a study on the dependence of beam emittance on factors like gas flow and electrode voltages. The author has published some sections of this chapter in the journal, Review of Scientific Instruments [119]. The details of the IBSimu code described in this chapter are based on texts from [32].

### 6.1 Overview of IBSimu code

IBSimu [21],[118],[120] code is released under an open-source license, which makes it more usable for the ion source community. It uses a C++ programming interface that includes



separate modules for solving the electric potential distribution, charged particle trajectory, phase space diagnostics, etc. The program for running the simulation is written by the user and these different modules are included in the particular program, as needed. It can be used for solving problems in 2D and 3D geometries. Complex electrode geometries in the ion source can be imported into the simulation from CAD models. The electric potentials on these electrodes are specified as the boundary conditions in the simulation. The simulation domain is divided into rectangular meshes whose resolution can be specified by the user. The code uses *finite difference method* in *Poisson's equation* for solving the electrostatic potential distribution in the simulation domain. The charged particles are created in the simulation by specifying the uniform current density of different species (negative ions, electrons, etc.) over a fixed area in the plasma region. The charged particles are propagated from this area using ray-tracing techniques and Lorentz force calculations from the solved electric field distributions. These charges further affect the electric field distribution. Hence, several iterations are needed for a self-consistent solution of charge density and electric field. During the first iteration, the beam space charges are not considered and the potentials inside the plasma volume are forced to zero. The resulting potential distribution is found by solving the Laplacian. The effect of space charge is added from the second iteration and electric fields are recalculated. The number of iterations can be specified in the simulation. A good indication of a converged simulation is that the beam emittance value at a particular location stays almost constant between the iterations.

The magnetic field distribution can be included in the simulation from an external file. The magnetic field is suppressed in the bulk plasma and from the plasma sheath towards the extraction region till a potential of  $\approx 10$  V. In reality, there will be collisions and associated collisional drifts in the plasma. The electrons undergo circular motion due to the perpendicular magnetic filter fields at regions close to the plasma sheath. The model used in IBSimu is non-collisional and proper modelling starts only at the sheath. Hence, suppression of the magnetic field in the plasma is needed to provide a uniform ion distribution at the sheath.

The schematic view of the potentials in the plasma model used for negative ion extraction in IBSimu is shown in Fig. 6.1 [120]. The basic assumption is that the negative ions are born at the plasma electrode potential. It also considers the presence of an equipotential surface with  $\phi = 0$  V, between the positive bulk plasma potential  $\phi_p$  and the positively biased extraction region. Negative ions and electrons get accelerated from the plasma potential into the extraction region. Positive ions from the bulk plasma reach this surface with an energy  $e\phi_p$  and proceed to the extraction region till it get reflected back due to the high positive extraction electrode potentials. These constitute the fast positive ion population,

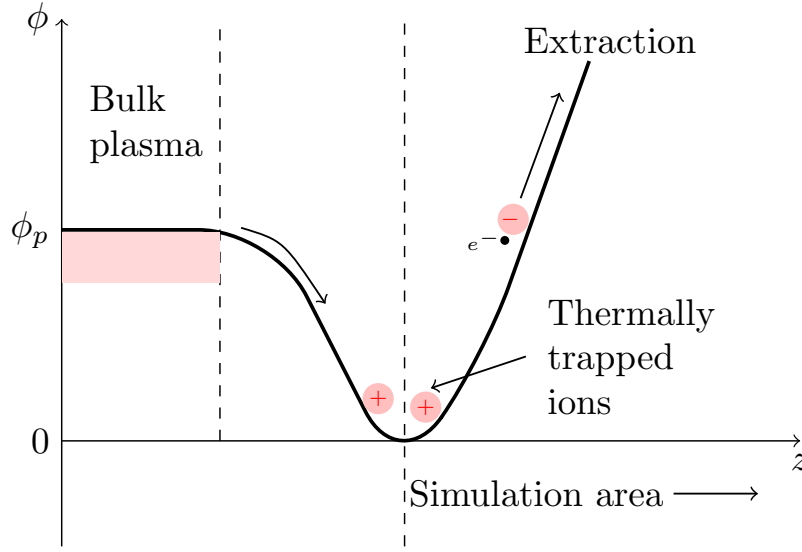


**Figure 6.1:** Schematic of the negative ion extraction plasma model in IBSimu. This model is reproduced from [120].

with density  $\rho_f$ . The space charge density of the fast positive ions can be defined as

$$\rho_f = \rho_{f0} \left( 1 - \frac{e\phi}{E_i} \right) \quad (6.1)$$

where  $\rho_{f0}$  is the fast positive ion density at the plasma electrode wall potential and  $E_i$  is the corresponding kinetic energy of the ions. The above equation is valid only for  $\phi < E_i$  and is zero for  $\phi > E_i$ . Another population of low energy positive ions (thermal),  $\rho_{th}$ , get trapped in the potential well. These ions are associated with a Maxwellian distribution and their space charge density can be defined as

$$\rho_{th} = \rho_{th0} \exp\left( - \frac{e\phi}{k_b T_p} \right) \quad (6.2)$$

where  $\rho_{th0}$  is the trapped thermal ion density at the plasma electrode wall potential and  $T_p$  is ion temperature. The plasma quasi neutrality is maintained at  $\phi = 0$  V potential by maintaining the sum of charge densities of negative and positive particles to be zero,  $\rho_{tot0} = \rho_{rt0} + \rho_{f0} + \rho_{th0} = 0$ .  $\rho_{rt}$  corresponds to the charge density of ray traced electrons and negative ions (suffix 0 represents the location at  $\phi = 0$  V). The amount of compensating fast positive ions is specified in the simulations using the  $R_f$  factor, where  $R_f = \rho_{f0}/\rho_{rt0}$ . Hence, the density of different species, thermal ion temperature and initial energy must be specified in the simulations.

The different plasma parameters mentioned in the above equations cannot be estimated accurately and hence can lead to errors in results. The approximations made in the IBSimu

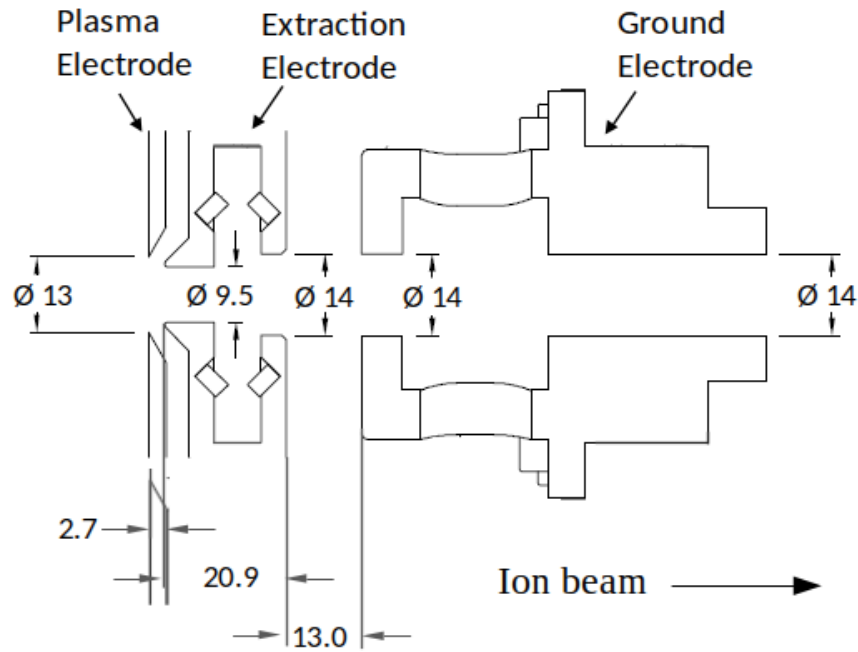


**Figure 6.2:** Section view of the D-Pace ion source extraction system. Dimensions are in mm.

plasma model enables faster calculations, but can be incorrect. Differences in the beam emittance behaviour between IBSimu predictions and experiments were obtained in some ion sources [118]. One of the possible reasons considered for this is the incorrect estimation of charge densities near the plasma sheath in the simulations, leading to an error in beam emittance. The charge densities modelled in the simulations are manually estimated by the user from the co-extracted electron and ion current values obtained in the experiments. Since all the charged particles influencing the plasma sheath will not be extracted, this leads to incorrect estimation of charge densities in the simulations.

## 6.2 Ion source and simulations

D-Pace's filament and RF ion sources were used for the experimental campaign. The general section views of these sources are shown in sections 4.1 and 5.1. As described in these sections, the ion source uses three electrodes in the extraction system consisting of plasma, extraction and ground electrodes. The schematic of the electrode arrangement in the D-Pace ion source extraction (both RF and filament ion sources) is shown in Fig. 6.2. The co-extracted electron current is measured on the extraction electrode power supply. The ion source (plasma chamber, plasma electrode and extraction electrode) is biased at a negative potential ( $-30$

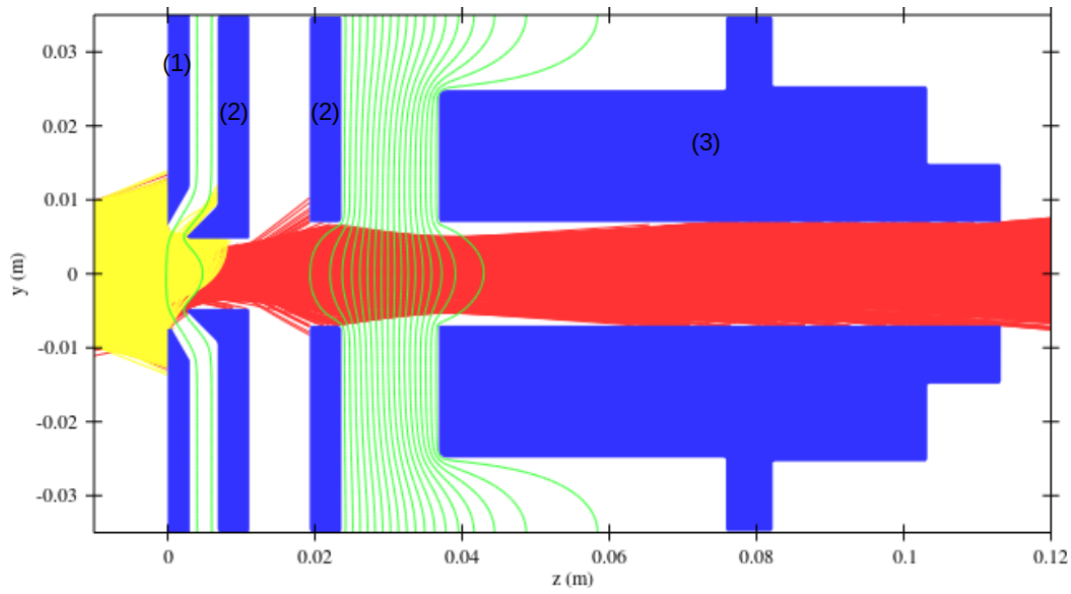


**Figure 6.3:** Typical simulation result using IBSimu. Electrons are shown in yellow and negative ions in red. Beam direction is from left to right. The (1) plasma, (2) extraction and (3) ground electrodes are displayed in blue. Equipotential lines are shown in green.

kV) with respect to the ground electrode by the bias power supply. As described in section 4.1, the current measured on the bias power supply,  $I_{bias}$ , consists of the negative charges reaching the ground region from the ion source and positive charges reaching the ion source from the ground. The latter is difficult to estimate and is approximated as negligible. Hence in this study, the amount of negative ions reaching the ground region is treated as equivalent to  $I_{bias}$ . The ratio between the co-extracted electron current and  $I_{bias}$  is taken as the extracted electron to negative ion ratio in the experiments.

A typical IBSimu simulation result from the D-Pace ion source is shown in Fig. 6.3. Here, a simulation region from -10 mm to 120 mm from the plasma electrode is displayed. The electrons are shown in yellow and negative ions in red. The positive ions are not displayed in the simulation. The potentials on the extraction and ground electrodes in the simulations are the same as obtained in experiments. Charge density population of the particular type of species to be extracted need to be created in the plasma region ( $z < 0$ ) of the simulation. These charge densities are defined on a planar surface of 20 mm diameter in the plasma area, at a location  $z = -10$  mm away from the plasma electrode. The user can modify this surface diameter and location. Positive ion population is created by specifying the  $R_f$ ,  $T_p$  and  $E_i$  values as explained in the previous section. The magnetic field distribution data is also specified in geometry. It can be seen from the simulation that the co-extracted electrons are deflected towards the front plate of the extraction electrode due to this magnetic field

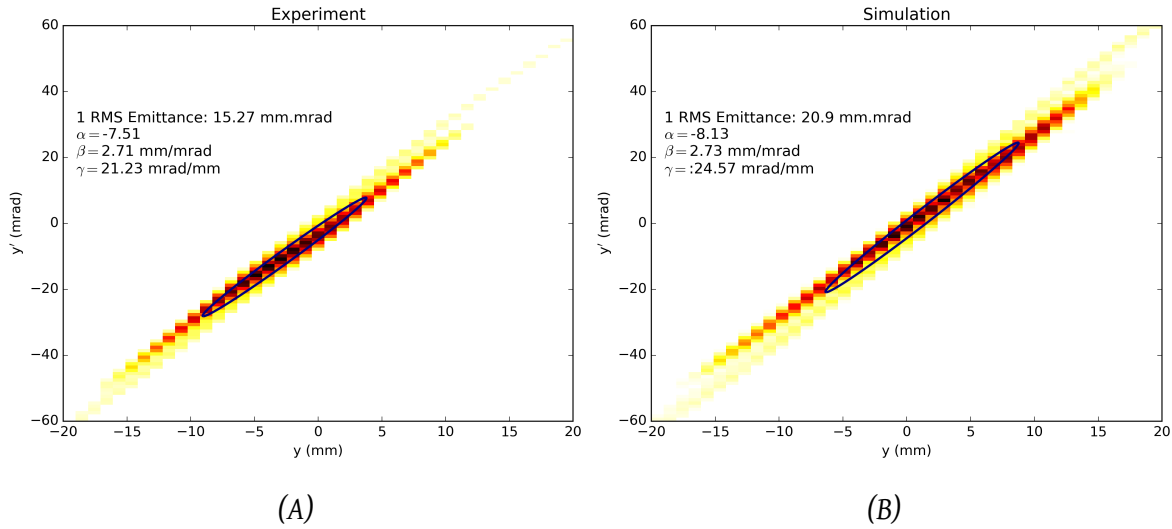


**Figure 6.4:** Phase space density plots for 13.9 mA  $H^-$  bias current from the filament ion source, at 3.5 kV extraction electrode voltage, 5 V plasma electrode voltage and 15 sccm gas flow. (A) Experimental data and (B) Simulated data using IBSimu, are shown. Both are measured at location  $z = 368$  mm from the plasma electrode. The plots are generated using similar python scripts. The emittance ellipse represents the 1 RMS emittance area.

and none of them reach the ground region. IBSimu can also generate particle current density graphs as shown in Fig. 6.6 and 6.13.

Experimental beam emittance is measured at 368 mm downstream from plasma electrode by D-Pace ES4 emittance scanner. The details of the scanner are given in B.3.2. The IBSimu simulation region can also be extended from the plasma to the location of the emittance scanner. The simulation can generate the emittance calculation and phase space plots through one of its diagnostics modules. An example of an emittance plot comparison between experiment and simulation is shown in Fig. 6.4. The plot is generated using similar python scripts using the particle distribution data from experiments and simulations. Background noise in the emittance data is eliminated by discarding the intensity values below 4% of the maximum value.

### 6.3 The optical effect of plasma sheath

The electric field distribution in the vicinity of the ion source extraction is determined by the properties of the plasma, geometry of the electrodes around the plasma and electric potential of the electrodes. Between the quasi-neutral plasma region and the extraction region, where mainly negative charges are present, the plasma sheath boundary layer is formed. In this sheath, the separation of charges takes place due to the extraction field and the beam is

formed. The three-dimensional shape of the sheath is determined by the interplay of the plasma charges, the charged particle beam formed and the electric and magnetic fields in the extraction. The shape of the plasma sheath defines the extraction electric field shape locally and therefore affects its focusing properties in the region where the extracted beam still has a low velocity. Modelling the plasma sheath is a tedious task and cannot be achieved easily. Simplified plasma models need to be used for simulating the sheath and IBSimu is one such tool that reproduces the plasma sheath by modelling both the extracted and non-extracted particle species. The optical effect of the plasma sheath can be considered in a qualitative manner. Under some plasma conditions, the sheath acquires an optimal shape and location. Modification of the plasma density causes the shape of the sheath to become sub-optimal. If the plasma density decreases, the plasma sheath will become concave, focusing the beam too much and if the plasma density increases, the sheath becomes more convex, providing too little focusing to the extracted beam. The dependence of the curvature of the sheath on the plasma densities is described in section 3.1.2. Therefore the sheath can be considered as an optical lens and it can strongly affect the properties of the extracted beam.

The most accessible experimental data dependent on the plasma sheath is the emittance of the beam, which represents the phase space distribution. Emittance of a beam depends on the focusing at the plasma sheath. At optimal shape of the sheath, the produced beam emittance has a minimum value. As the plasma sheath shape becomes sub-optimal, beam emittance increases. The beam emittance can also get affected by the properties of the extraction system. The beam can undergo aberrations leading to emittance growth and collimations leading to beam loss in its propagation. Nevertheless, the presence of an emittance minimum, corresponding to the optimum sheath shape, is expected in a well-designed extraction system.

## 6.4 Simulation methods

A model of the D-pac ion source plasma extraction was made using IBSimu for this experimental campaign. The simulation geometry started from inside the plasma ( $z = -10$  mm from the plasma electrode) and extended till 368 mm from the plasma electrode in the direction of the beam. Beam emittance values in the simulation are measured at the end of this geometry, which represents the location of the emittance scanner in the experiments. The charge density of the negative ions in the plasma region is chosen such that the simulation produces a negative ion current equal to the bias current,  $I_{bias}$ , obtained in the experiment. The electron charge density in the plasma is specified using the experimentally obtained

co-extracted electron to bias current ratio. The simulation was split into two codes. The first code simulated the initial 60 mm geometry with a high resolution mesh size of 0.5 mm, since this region consists of the plasma sheath and extraction. The Debye length for a 2 eV plasma with electron density of the order of  $10^{16} \text{ m}^{-3}$  can be calculated using equation 2.12 and is around 0.1 mm. Hence, the mesh size in the simulation cannot resolve the plasma sheath, but can still predict the plasma sheath shape as verified by higher resolution simulations. Grid sizes shorter than 0.5 mm provided the same phase space results. The second code simulated the remaining geometry (60 – 368 mm) and used a lower resolution mesh size of 0.8 mm. This was done for reducing the running time for simulations. The average time required for one complete simulation set in these experiments is about 15 minutes.

## 6.5 Filament ion source experiments and simulations

Experiments were performed in the filament ion source using  $\text{H}_2$  plasma. In the usual beam tuning methods mentioned in B.4, the electrode voltages and gas flows are varied continuously, for obtaining the optimum beam current, for the different arc currents. Contrary to this, these parameters were kept constant during this experiment to determine the effect of only the arc current or plasma density on the beam emittance. The plasma electrode voltage was fixed at 5 V and gas flow at 15 sccm of  $\text{H}_2$ . This ensures that the resulting change in emittance values are only due to the variation in plasma densities for fixed electrode voltages. The emittance behaviour for three different fixed extraction electrode voltages (3.0 kV, 3.5 kV and 4.0 kV) were also studied. The beam emittance variation obtained as a function of the experimentally obtained  $\text{H}^-$  bias current is shown in Fig. 6.5. The data points correspond to different arc current values or plasma densities. Emittance values are represented as 4 RMS normalized values. Note that the high emittance values at low currents are due to the unusual electrode voltages, that lead to poor focusing and optics.

IBSimu simulations were also performed for each data point. The extraction and ground electrode voltages and electron to ion ratios in the simulations are same as that obtained from experiments. Plasma parameters were chosen from typical values [120] and later slightly modified to achieve phase space distribution close to experiments (plasma potential = 5 V, ratio of fast compensating positive ions to negative charges,  $R_f = 0.2$ , initial drift energy of extracted particles,  $E_i = 5 \text{ eV}$ , transverse negative ion temperature,  $T_t = 0.2 \text{ eV}$ , trapped positive ion temperature  $T_p = 0.1 \text{ eV}$ ). The emittance results from the simulations are also shown in Fig. 6.5.

The results indicate that IBSimu is capable of simulating some of the beam emittance trends in the filament ion source. The simulations are also predicting the emittance minimum

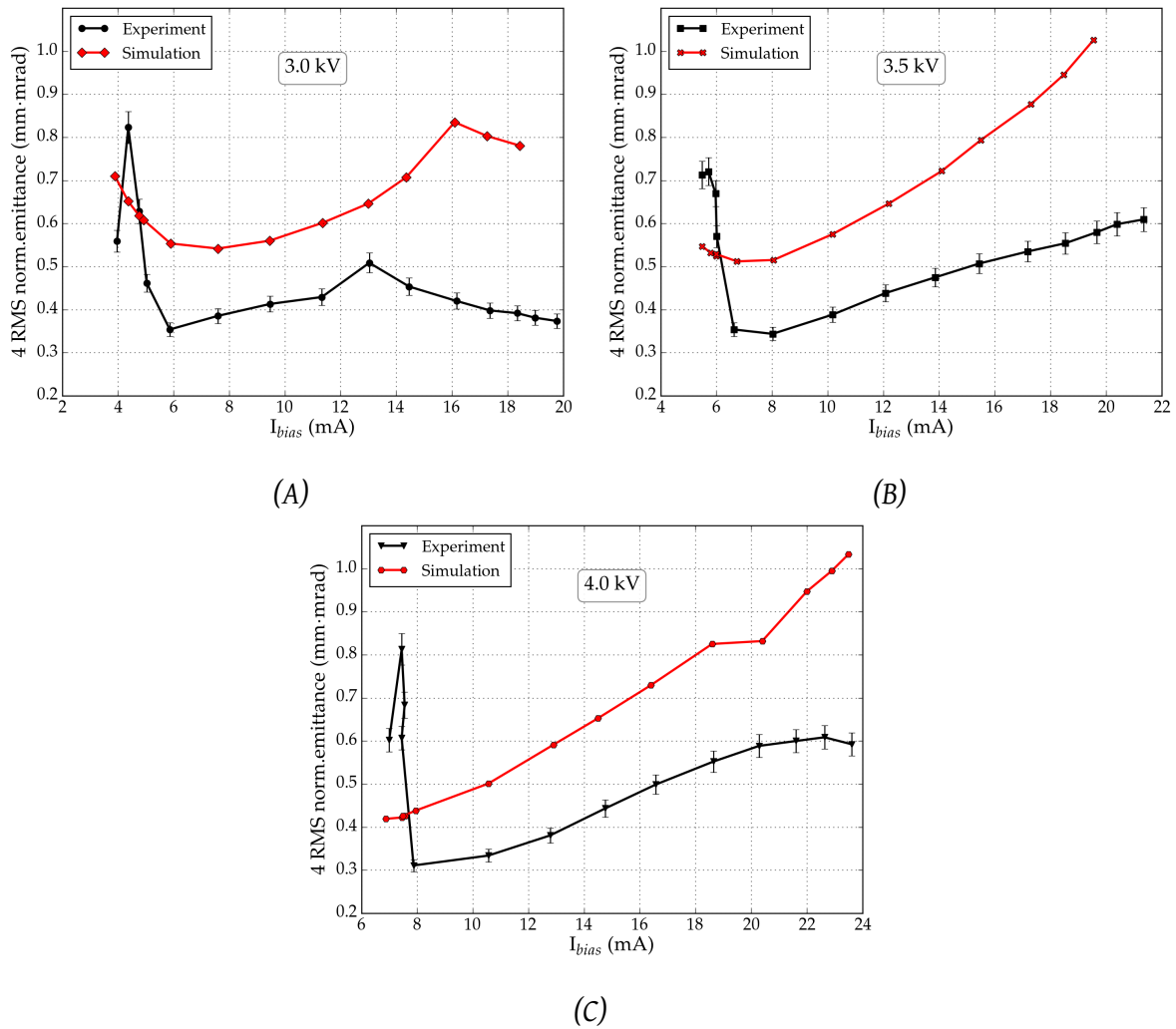


**Figure 6.5:** Beam emittance comparison between experiment and simulation in  $H_2$  plasma for different plasma densities, at 3 different extraction electrode voltages, (A) 3.0 kV (B) 3.5 kV & (C) 4.0 kV. Gas flow (15 sccm), Arc voltage (120 V) and plasma electrode voltage (5 V) are kept constant.

in the trends, which represent the optimum plasma sheath shape. The  $H^-$  current values, for which the emittance minimum occurs, are very close between experiments and simulations. The emittance values increase to either sides of the emittance minimum for both experiments and simulations.

Fig. 6.5(A) also shows a decrease of emittance at higher bias currents ( $> 13$  mA). This is also reproduced in the corresponding simulations in the figure. The emittance scanner scans a region of about 50 mm in length in a direction perpendicular to beam propagation. The geometry considered in the simulations is also of the same area. Simulations reveal that there is more amount of negative ions extracted from the source at higher arc currents. However, the beam is more divergent due to space charge effects, leading to the loss of



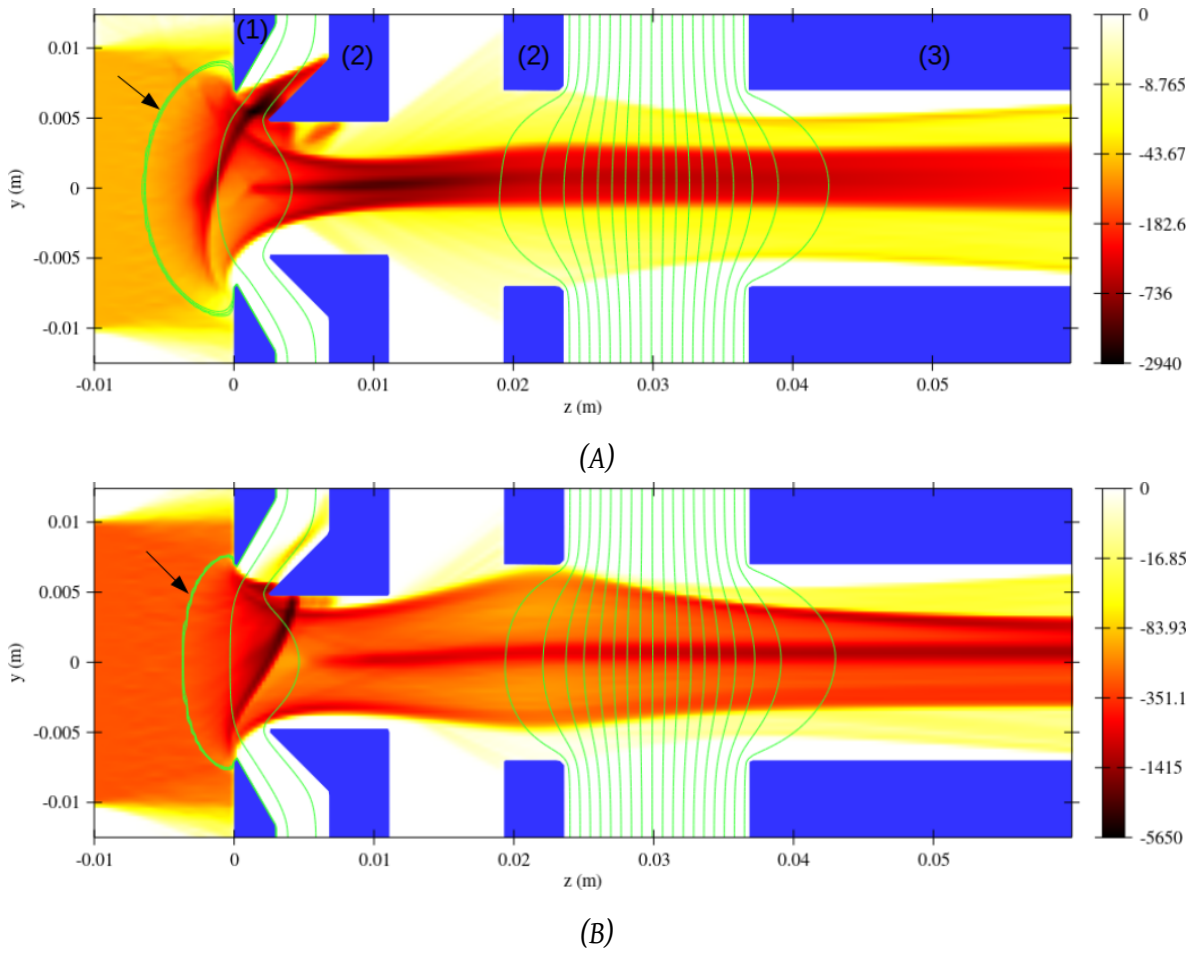


**Figure 6.6:** Results of current density simulation for two different plasma densities at an extraction electrode voltage of 3 kV: (A) Negative ion density of  $26 \text{ A/m}^2$  and electron density of  $28 \text{ A/m}^2$  resulting in a bias current of 5.9 mA. (B) Negative ion density of  $90 \text{ A/m}^2$  and electron density of  $165 \text{ A/m}^2$  resulting in a bias current of 16.2 mA. The 4 RMS normalized emittance values are (A)  $0.09 \text{ mm}\cdot\text{mrad}$  (B)  $0.19 \text{ mm}\cdot\text{mrad}$ . Electrodes (plasma (1), extraction (2) & ground (3)) are shown in blue color. Green lines represent equipotentials. Arrows indicate the location of the plasma sheath ( $\phi = 0$  V).

charged particles to regions outside the emittance measurement and hence a decrease in emittance values. There is also more particles hitting the extraction electrodes, leading to beam collimation. The decreasing trend occurs at a different current value in the simulations compared to experiments, indicating a difference in the effect of plasma sheath shape on beam divergence.

The increase and decrease in emittance values for different plasma densities can be explained by the optical effect of the plasma sheath, as shown in IBSimu simulation in Fig. 6.6. It shows the shape and location of the plasma sheath for 2 different plasma densities, for the same set of electrode voltages. The plasma sheath becomes less concave as plasma

density increases, leading to a larger divergence and therefore increase in emittance in the extraction. The general influence of plasma densities on the radius of the emission surface was described in equation 3.12. The effect of extraction voltage on the observed beam emittance is discussed in section 6.7.

Even though the general emittance trends are matching between IBSimu and experiments, there is still a mismatch between the emittance values, as can be inferred from Fig. 6.5. It was also confirmed through simulations that a further reduction of transverse ion temperature,  $T_t$ , does not have an effect on the simulated emittance level. As mentioned in the earlier sections, the differences in the simulation results could be due to the approximations used in IBSimu, incorrect charge densities simulated in the plasma region or due to differences in the behaviour of the plasma sheath shape between IBSimu and real scenario, for the same plasma densities. Some of these are considered in the following sections.

### 6.5.1 Effect of gas flow on beam emittance

A set of experiments were performed to study the influence of different gas flows or pressures on the beam emittance values from the filament ion source. The experiments were run at constant electrode potential values of 3.5 kV extraction electrode voltage, 5 V plasma electrode voltage and 30 keV beam energy. Gas flows were varied from 8 sccm to 17 sccm for constant arc currents. The corresponding gas pressures are shown in Fig. B.4. The increase in  $H^-$  bias current extracted from the plasma is obtained by increasing the arc current and hence the plasma density.

The variation in the co-extracted electron current obtained at the extraction electrode and  $H^-$  current obtained on the bias power supply, for different arc currents and gas flows is shown in Fig. 6.7 (A),(B). As can be seen from the graphs, both the co-extracted electron current and the bias current decrease as the gas flow increases. The plasma electrode current was also found to decrease in the experiments for increasing gas flows. This could suggest a decrease in electron density as the gas flow increases, in the regions close to the plasma electrode and the plasma sheath. The corresponding co-extracted electron current to negative ion current ( $H^-$  bias current) ratio is shown in 6.7(C) in terms of the bias current. Evidently, the ratio tends to lower values for higher gas flows. The minimum value of the ratio also shifts to higher bias current values as the gas flow increases. Thus, the amount of gas flow significantly influences the charge densities inside the plasma and the extracted currents.

The decrease in the observed extracted currents with higher gas flows suggests a decrease in the electron and negative ion charge densities near the plasma sheath. This could lead to variation in the beam emittance. The beam emittance values for the different conditions

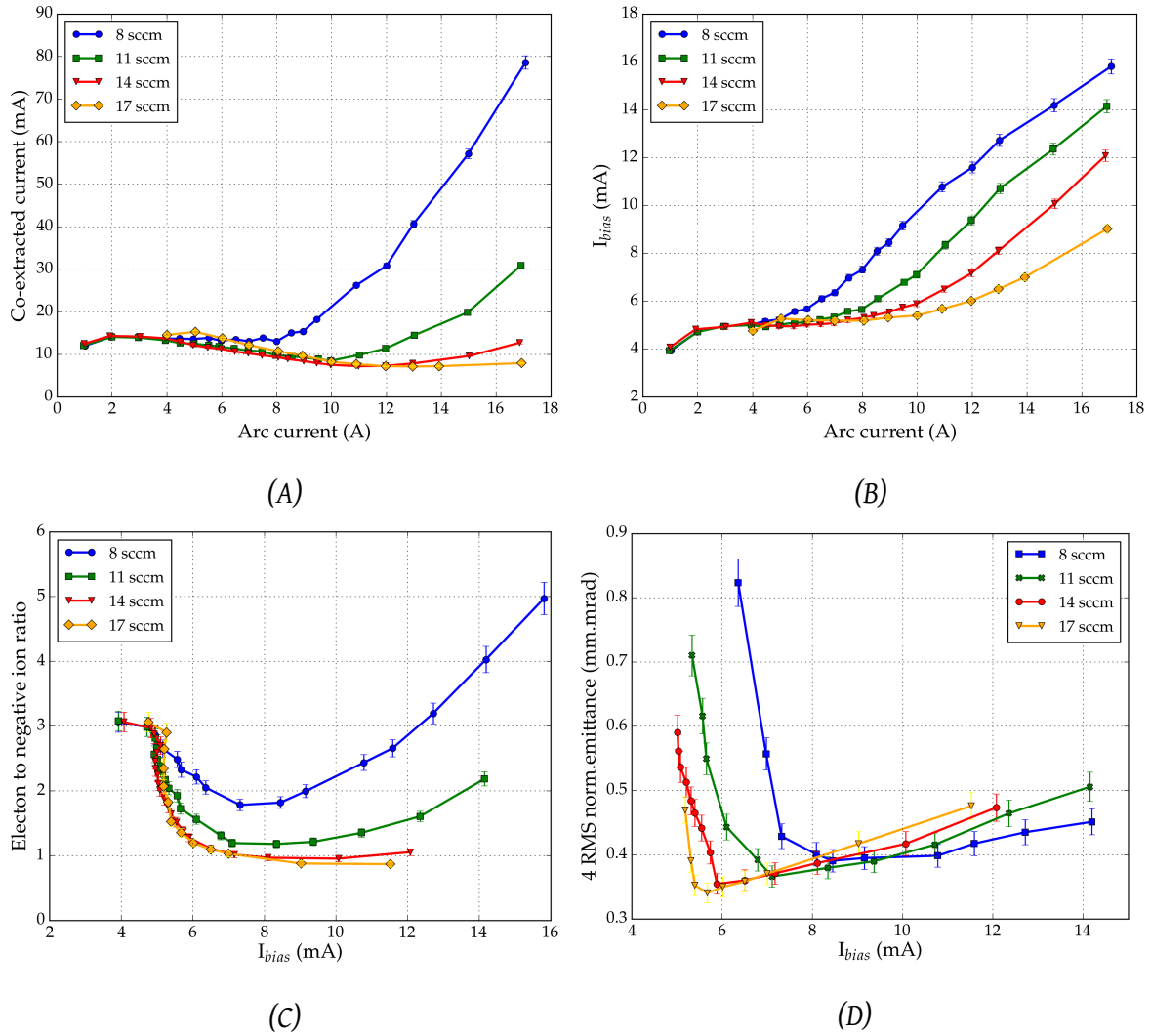


**Figure 6.7:** (A) Variation in co-extracted electron current and (B)  $H^-$  bias current, for different arc currents and gas flows. (C) Variation in the electron to ion ratio and (D) the beam emittance values, for different bias currents and gas flows. Extraction electrode voltage is 3.5 kV and plasma electrode voltage is 5 V.

created in the experiment are shown in Fig. 6.7(D), in terms of the bias current extracted from the source. As can be inferred, the emittance minimum drifts to lower bias current values as the gas flow increases. This is contrary to the behaviour observed in some other filament ion sources as mentioned in [118].

The dependence of emittance values on the gas flows points to the fact that the plasma sheath dynamics are influenced by the electron and negative ion charge densities near the sheath. It is sometimes considered that the type of particle species, ions or electrons, do not influence the plasma sheath behaviour, but it is dependent only on the total charge density [120]. The total negative charge density ( $\rho_{tot-}$ ) inside the plasma, near the sheath, can be

represented as sum of negative ion densities ( $\rho_{H^-}$ ) and electron densities ( $\rho_e$ ) [118].

$$\rho_{tot-} = \rho_{H^-} + \rho_e = \frac{J_{H^-}}{v_{H^-}} + \frac{J_e}{v_e} \quad (6.3)$$

, where  $J_{H^-}$  and  $J_e$  are the negative ion and electron current densities near the sheath and  $v_{H^-}$  and  $v_e$  are the corresponding velocities. Let the observed current densities be denoted by  $J_{H^-}^*$  and  $J_e^*$ , corresponding to the bias current and co-extracted electrode current values obtained in the experiment. The observed densities can be different from the actual current densities near the plasma sheath. The actual current densities can then be estimated by using an ion density correction factor,  $R_{ic}$  and an electron density correction factor,  $R_{ec}$ . Using these correction factors, the actual current densities at the plasma sheath can be written as [118]

$$J_{H^-} = R_{ic} J_{H^-}^* \quad (6.4)$$

$$J_e = R_{ec} J_e^* \quad (6.5)$$

Equation 6.3 can be written in terms of the observed currents, using the above equations.

$$\rho_{tot-} = R_{ic} \frac{J_{H^-}^*}{v_{H^-}} + R_{ec} \frac{J_e^*}{v_e} = \frac{1}{\sqrt{2qU}} \left[ R_{ic} \sqrt{m_{H^-}} + R_{ei} R_{ec} \sqrt{m_e} \right] \quad (6.6)$$

In the above equation,  $U$  is the potential achieved by the negative charges and  $q$  is the magnitude of the charge.  $R_{ei}$  is the observed electron to ion current ratio which equals the ratio of  $J_e^*/J_{H^-}^*$ , when both species uniformly fill the extraction aperture. Assuming no collimation in the extraction region, the total charge density in the equation can be replaced with an effective  $H^-$  current that can be defined from the above equation as [118]

$$I_{eff} = R_{ic} I_{H^-}^* + R_{ec} I_e^* \sqrt{m_e/m_H} \quad (6.7)$$

where  $I_{H^-}^*$  and  $I_e^*$  are the observed bias current and co-extracted electron current in the experiment.

The emittance values in Fig. 6.7(D) can now be plotted in terms of the effective current,  $I_{eff}$ . This is shown in Fig. 6.8(A). The correction factor values used are  $R_{ec} = 1$  and  $R_{ic} = 1$ . It is to be noted that in this set of experiments, the variation in emittance values is due to the change in charge densities in the plasma. Since  $I_{eff}$  is proportional to the total charge density of electrons and negative ions in the plasma sheath region, the emittance minimum is expected to be at the same location in  $x$ -axis for the different gas flows. But, as can be noticed, the behaviour is still similar to Fig. 6.7(D) when  $R_{ec} = 1$  and  $R_{ic} = 1$  is used and the emittance minimum is still drifting to lower bias currents as gas flow increases. The same

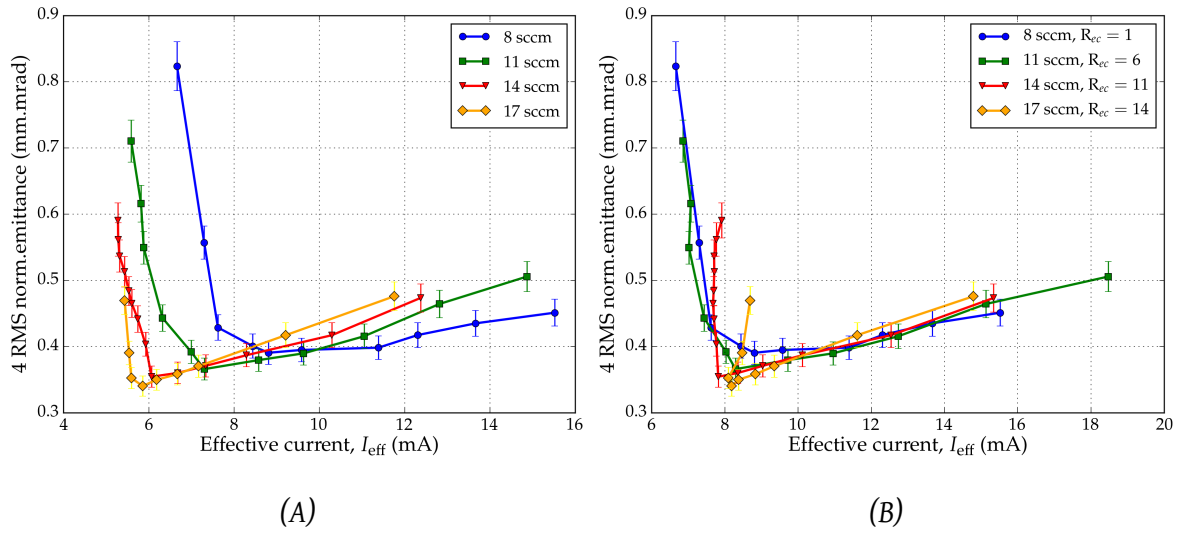


**Figure 6.8:** (A) Variation in beam emittance for effective current,  $I_{eff}$ , with values  $R_{ec} = 1$  and  $R_{ic} = 1$ . (B) Variation in beam emittance for effective current,  $I_{eff}$  with different  $R_{ec}$  factors and  $R_{ic} = 1$ .

emittance values are again shown in Fig. 6.8(B), but with density correction factor values,  $R_{ic} = 1$  and  $R_{ec} = 1, 6, 11$  and  $14$ , for the different gas flows. As can be seen, the emittance minimum is now at the same location in  $x$ -axis for all gas flows with this modified  $R_{ec}$  factors.  $R_{ec} > 1$  values suggest that the electron density in the plasma sheath region is higher than the observed current density corresponding to the co-extracted electron current at the extraction electrode. This is an anticipated result, as part of the electrons near the sheath will never get extracted. These electrons would get accelerated from the sheath, bend due to the magnetic fields and hit the plasma electrode. Hence the real electron to ion ratio at the sheath would be different from the values obtained at the electrodes in the experiments. It can also be seen that the value of  $R_{ec}$  increases with gas flow. This can be understood in terms of effect of pressure on electron transport and collisions in the plasma [118]. But such high  $R_{ec}$  values are difficult to comprehend as it represents very high electron density at the plasma sheath.

Another set of correction factors which can produce similar results is when  $R_{ec} = 1$  and the ion density correction factor  $R_{ic} = 0.65, 0.8, 0.95$  and  $1.0$  for the different gas flows. This indicates that the bias currents recorded at lower gas flows consist of charges other than the negative ions.

In all cases,  $R_{ec} \neq R_{ic}$  for different gas flows indicate that the emittance is also dependent on the density of the type of particle species, ions or electrons, near the plasma sheath and not only on the total charge density. This is in contradiction to the basic assumption in

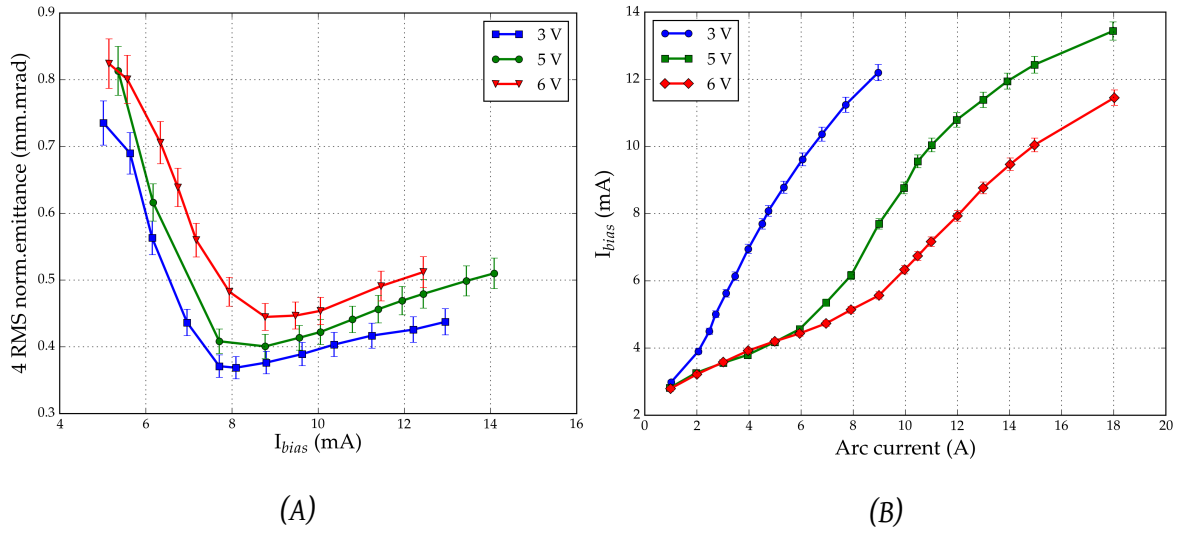


**Figure 6.9:** (A) The variation in beam emittance behaviour at different plasma electrode voltages for 8 sccm gas flow and 3.5 kV extraction electrode voltage. (B) Variation in bias currents obtained for different plasma voltages and arc currents.

IBSimu, where the ions and electrons are not treated differently near the plasma sheath and the sheath is influenced only by the total charge density. In order to overcome this problem, the density of the particular species need to be artificially changed near a fixed region in the plasma sheath in the code. But additional constraints need to be imposed in the code such that the changed density will not alter the existing space charge effects in the beam propagation.

### 6.5.2 Effect of plasma electrode voltage on beam emittance

Experiments were performed to understand the influence of plasma electrode voltage on beam emittance, using a fixed  $H_2$  gas flow of 8 sccm and three different plasma electrode voltages (3 V, 5 V and 6 V). The plasma electrode current increased proportional to the voltage for constant arc currents. This was accompanied by a decrease in the co-extracted electron current and the bias current values. This suggests that the increasing plasma electrode voltages depletes the corresponding charge densities at the plasma sheath, since the gas flow is constant. The effect of plasma electrode voltages on the beam emittance is shown in Fig. 6.9(A) for the three different voltages. As seen in the figure, the beam emittance minimum does not shift appreciably in terms of bias current. But, in general, the beam emittance value increases as the plasma voltage increases, for a fixed bias current. This could be attributed to the higher total charge densities needed for attaining a particular bias current at high plasma electrode voltages as shown in Fig. 6.9(B). For example, 8 mA of bias current is achieved at

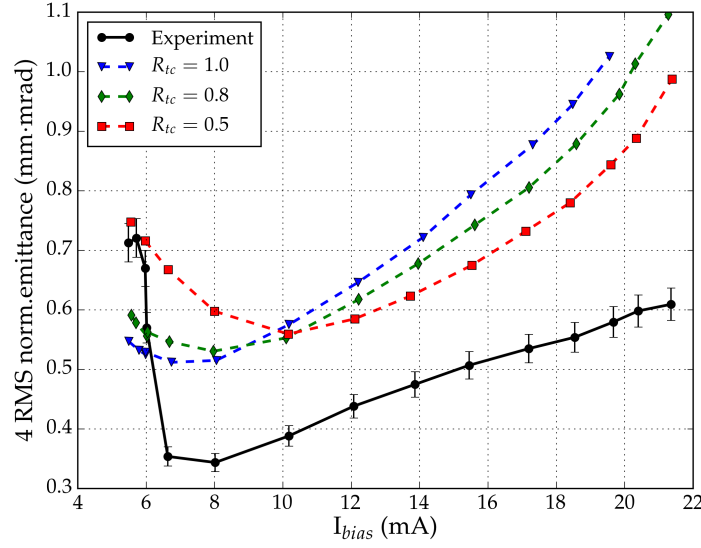


**Figure 6.10:** The effect of correction factor  $R_{tc}$  on beam emittance values. The ‘experiment’ and ‘ $R_{tc} = 1.0$ ’ curves are same as in Fig. 6.5(B).

about 5 A arc current for 3 V plasma electrode. But in the case of 6 V, it requires about 12 A of arc current. In addition to this, the plasma electrode voltage can also affect the electric fields in the plasma sheath leading to the trends in the graph.

### 6.5.3 Charge density correction factor in simulations

As pointed out earlier, there might be errors in the estimation of charge densities in the simulations, leading to the mismatches obtained in Fig. 6.5. As seen in the figure, at low currents there is an abrupt increase in emittance value from the emittance minimum. This is most likely due to some effect that can not be modelled by IBSimu. At higher currents, the simulations produce too high emittance values compared to experiments. Considering this, it can be a possibility that the charge densities near the plasma sheath (sum of negative ion densities and electron densities) are overestimated by the plasma model leading to less concave plasma sheath. It is possible to add a density correction factor,  $R_{tc}$ , to reduce the total charge density near the plasma sheath.  $R_{tc} = \rho_{tot-} / \rho_{tot-}^*$ , where  $\rho_{tot-}$  is the real charge density in plasma and  $\rho_{tot-}^*$  is the observed charge density for  $H^-$  ions and electrons. As in equation 6.6, the total charge density from the observed electron and negative ion beam currents can be obtained as

$$\rho_{tot-}^* = \frac{J_{H-}^*}{v_{H-}} + \frac{J_e^*}{v_e} \quad (6.8)$$

The simulated charge density in the simulation is now obtained by multiplying with the  $R_{tc}$

factor. The total negative charge density from the ray-tracing algorithm, at a defined region (beginning of plasma in the simulation geometry till plasma electrode) is now modified as  $\rho_{tot-} = R_{tc} \rho_{tot-}^*$ . The density of compensating positive ions are also modified in the simulation accordingly to maintain quasi neutrality.

The effect of this factor on beam emittance in the simulations is shown in Fig. 6.10. As shown in the graph, the emittance values show a decrease when the simulated density is half,  $R_{tc} = 0.5$ . But the correction factor moves the location of the emittance minima to higher currents and this does not correspond to the correct experimental result. Thus, the artificial reduction of the simulated total charge densities in the plasma do not provide a better match to the experimental results.

The mismatch seen in Fig. 6.5 could also be due to some effect near the plasma sheath that is not correctly modelled by IBSimu. Modelling should be very accurate in the extraction region as there are no compensating particles. A good reason that can be considered is the approximation in IBSimu that the particles reach the sheath from the plasma in straight trajectories, without any angular spread [32]. This assumption that the particles arrive at the plasma sheath as a planar flux causes an uneven distribution of particles at the sheath in the case of a highly curved sheath, and this can lead to an incorrect prediction of the sheath shape. Such an effect would also explain the deviation in the bias current level where collimation happens in the case presented in Fig. 6.5 (A).

## 6.6 RF ion source experiments and simulations

The experimental campaign was performed in D-Pace's RF ion source also. The study was conducted using a constant gas flow of 20 sccm and a plasma electrode voltage of 30 V. The plasma density and hence the bias current were varied by adjusting the applied RF power from 800 W to 3000 W. Emittance was measured for three different extraction electrode voltages, 3.0 kV, 3.5 kV and 4.0 kV for each of the applied RF powers. The variation in beam emittance for different bias currents is shown in Fig. 6.11. The emittance trends observed in the RF ion source were very similar to the results obtained in the filament ion source. Emittance minimum was observed for each extraction voltage curve. The variation in emittance values for different plasma densities can be explained as in section 6.5. IBSimu simulations were also performed for each data point. The extraction and ground electrode voltages and electron to ion ratios in the simulations were the same as that obtained from experiments. The plasma parameters used in the simulations [120] (plasma potential = 5 V, ratio of fast compensating positive ions to negative charges,  $R_f = 0.2$ , initial drift energy of extracted particles,  $E_i = 5$  eV,



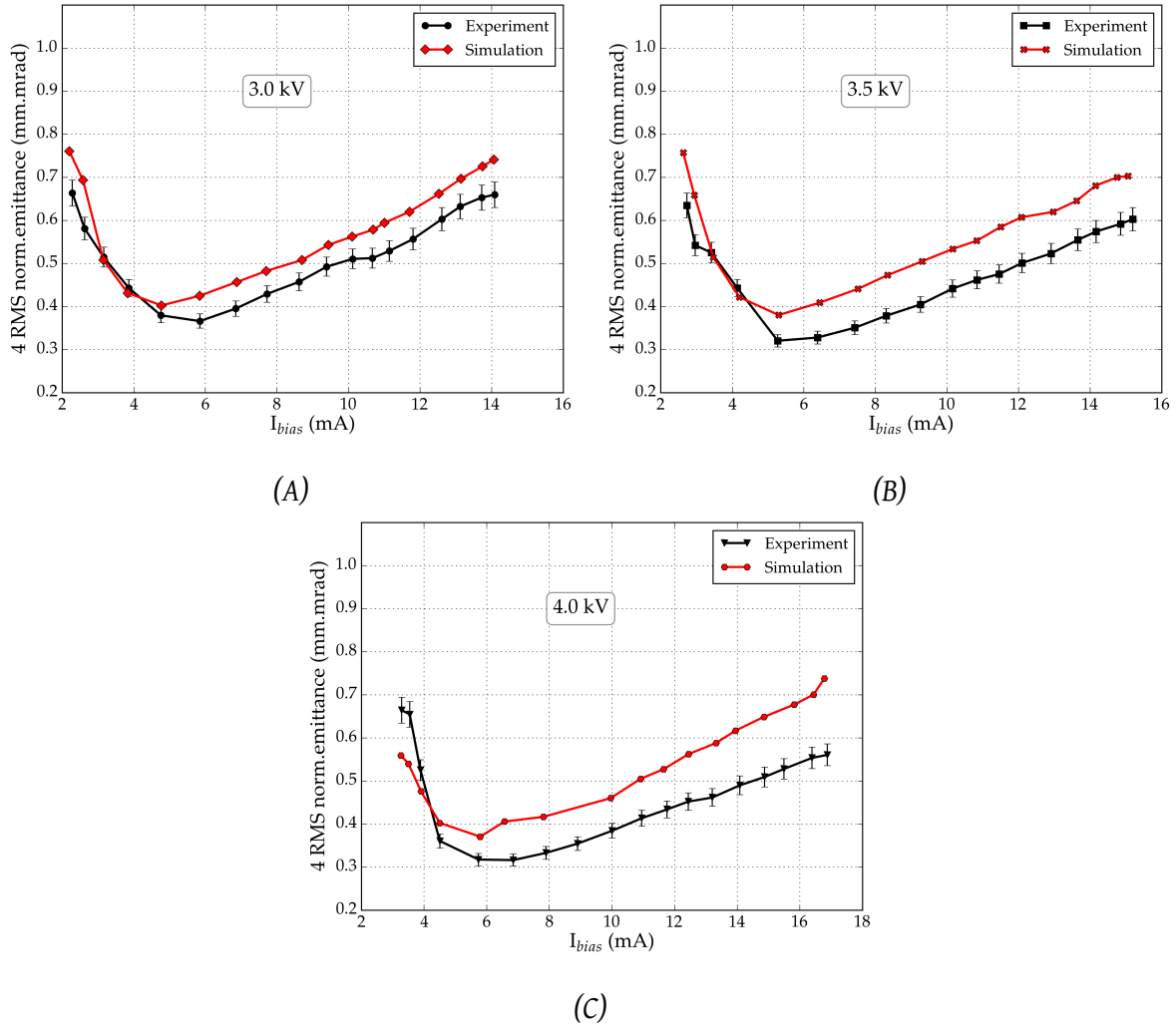


**Figure 6.11:** Beam emittance comparison between experiment and simulation for various applied RF powers at 3 different extraction electrode voltages, (A) 3.0 kV (B) 3.5 kV & (C) 4.0 kV. Gas flow (20 sccm) and plasma electrode voltage (30 V) are kept constant.

transverse negative ion temperature,  $T_t = 0.5$  eV, trapped positive ion temperature  $T_p = 0.1$  eV) were similar to the filament ion source simulation parameters.

As seen in the figure, the simulations are producing results close to the experimental values. The emittance minimum and the general trends are reproduced in the simulations effectively. The emittance values from the simulations are in general higher than obtained from experiments. But, it can also be inferred that the simulation results of the RF ion source seem more fitting to the experimental results compared to the filament source results from Fig. 6.5. However, the reason for the better match obtained in the RF ion source is not clearly understood.

## 6.7 Effect of extraction voltage on beam emittance

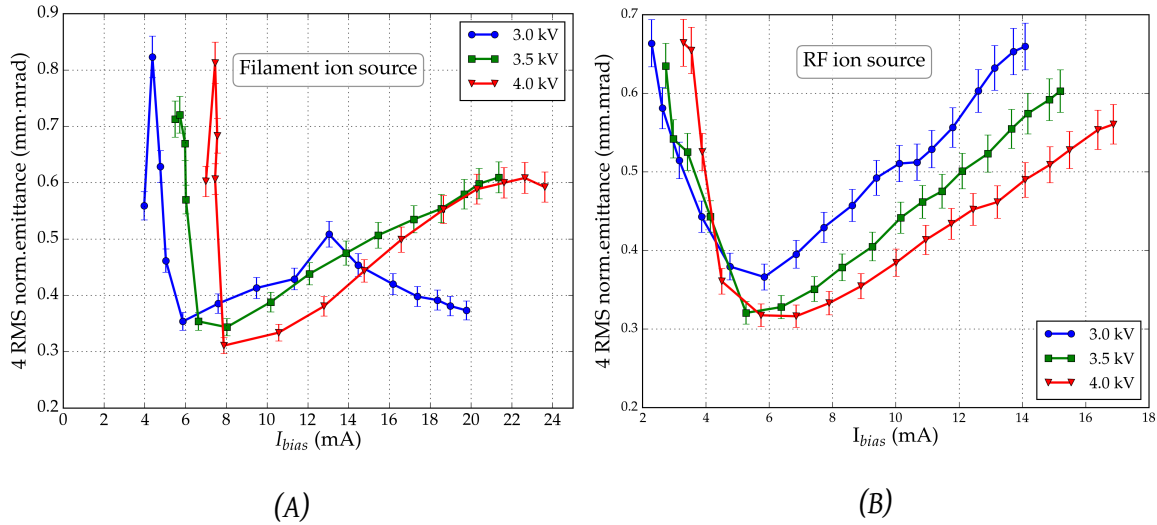


**Figure 6.12:** The combined graphs indicating the variation in beam emittance values for different extraction electrode voltages and bias currents in (A) filament ion source and (B) RF ion source.

The combined experimental data for all the three extraction electrode voltages, for both RF and filament ion sources, is shown in Fig. 6.12. As can be seen in the figure, the value of beam emittance drifts to lower values as the extraction electrode voltage increases in both sources. This is mainly seen when the plasma density increases from the emittance minimum. The curvature of the plasma sheath might play a role in this behaviour. Increase in the extraction voltage causes higher positive electric field near the plasma electrode, pushing the positive ions towards the plasma in the ion source. This causes the boundary of the quasi-neutral plasma also to be shifted further towards the plasma, resulting in a more concave plasma sheath. For a fixed plasma density, the plasma sheath is more concave for higher extraction electrode voltages and this could lead to lower emittance values and an increase in bias currents. This is illustrated using simulation results in Fig. 6.13, where the plasma sheath is more concave for higher extraction electrode voltage, even though the plasma density is the same. Another factor that could contribute to the lower emittance values at high extraction voltages is the reduced space charge effects. As shown in section 3.8.1, higher beam velocities experience reduced space charge forces and this could reduce the beam spread. This can also contribute to the reduction in spherical aberrations experienced by the beam at the electrodes, which could further reduce the beam spread [121].

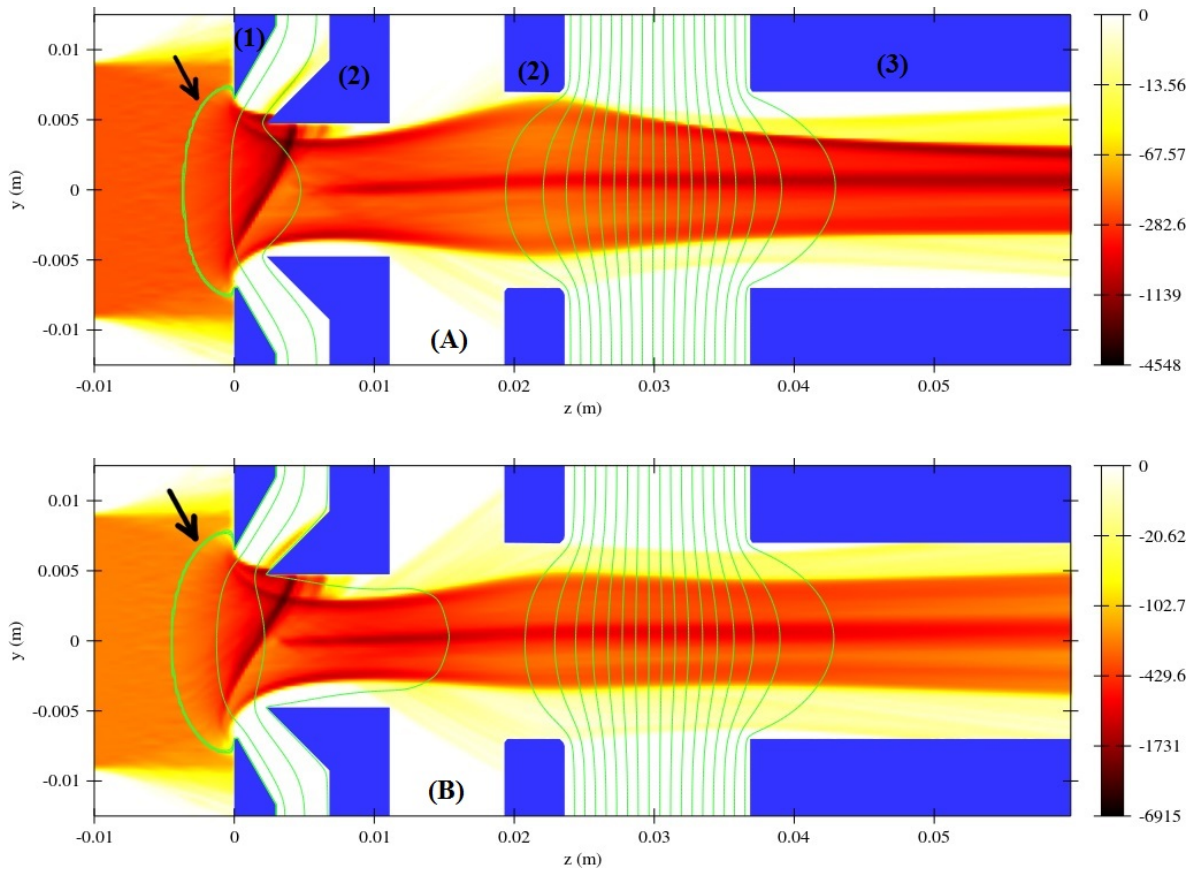


**Figure 6.13:** IBSimu current density simulations showing the variation in the shape and location of the plasma sheath (indicated by black arrow) for 2 different extraction electrode voltages, (A) 3.0 kV and (B) 4.0 kV, using the same plasma current densities (55 A/m<sup>2</sup> negative ion density and 70 A/m<sup>2</sup> electron density). This results in a beam emittance of (A) 0.23 mm·mrad and (B) 0.18 mm·mrad.

## 6.8 Emittance comparisons between the ion sources

The combined experimental emittance data for the RF and filament ion sources is presented in Fig. 6.14. It should be noted that the gas flows and plasma voltages for the RF source experiments (20 sccm, 30 V) were higher than the filament source experiments (15 sccm, 5 V). As is evident from the figure, there appears to be a shift in the general emittance behaviour between the sources. In general, the emittance minimum of the filament source occurs at slightly higher bias currents compared to the RF source. This shift remains the same even if the effective current,  $I_{\text{eff}}$  in equation 6.7, is used in  $x$ -axis with  $R_{ec} = R_{ic} = 1$ . This again points to the result from section 6.5.1 that the observed extracted currents are not a true representation of the charge densities at the plasma sheath.

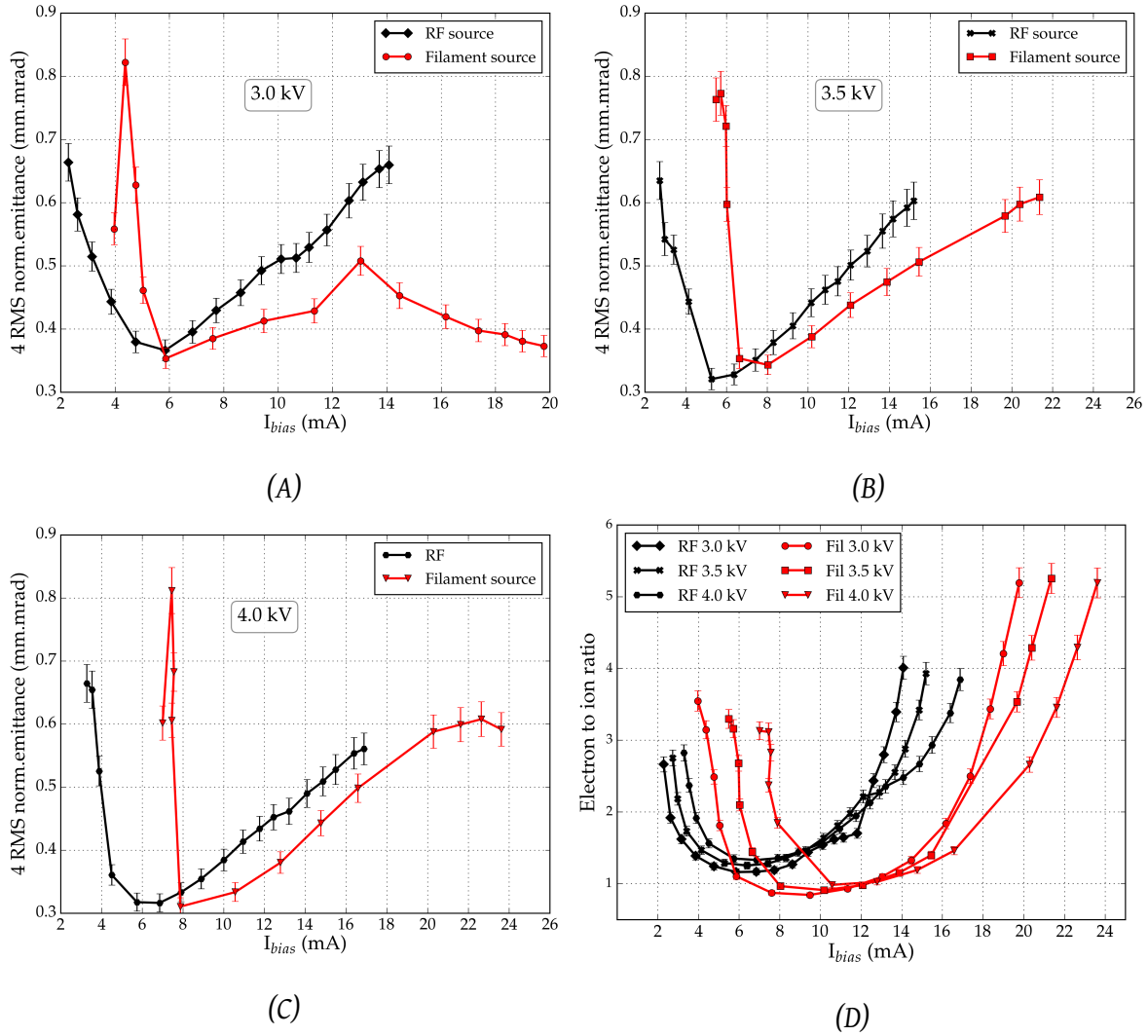


**Figure 6.14:** (A) – (C) Experimental beam emittance comparison between RF ion source and filament ion source for 3 different extraction electrode voltages. (D) Electron to ion ratios for filament and RF ion sources at different extraction electrode voltages.

The graphs also indicate that the emittance values of the RF ion source is higher for bias current values  $> \approx 8$  mA. The variation in the extracted electron to ion ratios for the two ion source configurations is presented in Fig. 6.14(D). In general, the ratios in the RF source are higher compared to the filament source for a fixed bias current, except at very low bias currents ( $< 6$  mA). This suggests the presence of higher electron density at the RF source plasma sheath for achieving a particular bias current. It should also be noted that unlike the filament ion source, the electron energy in the RF ion source is much less. This is due to the fact that there is no thermionic emission from Ta filaments in the RF ion source and no subsequent acceleration of electrons due to the  $-120$  V bias on the filaments with respect

to the plasma chamber. The presence of high energy electrons in the range of  $\approx 50$  eV is essential in generating the vibrationally excited molecular states, which are the predecessors of negative ions in the plasma as explained in section 2.9.2. Also, the lack of Ta deposition on the wall surfaces results in lower negative ions and higher electron density as shown in section 4.3. Hence, the negative ion generation is less efficient in the RF ion source. This could lead to the observed higher ratios in the RF ion source. These differences in the charge densities at the plasma sheath could be the reason for the shift observed in the emittance behaviour between the sources.

## 6.9 Conclusions

Simulation studies were performed on  $H^-$  beam extraction from D-Pace's filament and RF ion sources, using IBSimu plasma extraction code. Differences in the emittance values between IBSimu predictions and experimental results were observed. The exact reasons for these observations could not be determined, but some factors were discussed in the chapter. The experimental results point towards the fact that the plasma sheath behaviour is dependent on the type of particle species and not only on the total charge density. This contradicts the basic assumption in IBSimu. The estimation of plasma densities at the plasma sheath seems to be the most important challenge in the IBSimu code. The code neglects the effect of magnetic field and collisions at the plasma sheath region. This can lead to errors in plasma sheath estimation. The simulations also assume that the particles arrive at the plasma sheath as a planar flux. This can result in an uneven distribution of particles at the sheath in the case of highly curved sheath.

Another possible factor that can contribute to the observed differences is the bias current,  $I_{bias}$ , obtained in the experiments.  $I_{bias}$  represents the total negative charges from the source to the ground region. The simulations also support this assumption as it do not show any electrons crossing the extraction electrode (Fig. 6.3). But there might be additional negative charges in the form of secondary electrons and also positive charges flying from the ground region to the ion source. Hence the actual negative ion current could be slightly different from the experimentally recorded bias current. In simulations, the negative ion charge density at the plasma sheath is defined such that the resulting beam current matches the  $I_{bias}$  value. In short, the differences between simulated negative ion densities and the real densities could contribute to the emittance mismatch.

In spite of the above-mentioned challenges, the results indicate that IBSimu is a very useful tool in simulating the ion extraction. It could predict the general emittance trends

in D-Pace's ion sources under different plasma conditions. The prediction of the location of the emittance minimum in simulations is very close to the experimental result. This is a positive result for IBSimu, as high variations in the emittance minimum locations were present during the simulation of other ion sources like Pelletron ion source, CERN linac 4 and SNS ion source [118].

# Chapter 7

---

## Conclusions

Negative ion beams, extracted from ion sources, are used in a variety of applications in the field of science and technology. The quality of the beam and the amount of beam current depend heavily on the features of the ion source and optimisation of the ion source operation parameters. A deeper understanding of the ion source operation is hence essential for successful applications in particle accelerators. The thesis describes different studies performed by the author in D-Pace's filament and RF-powered negative ion sources, with a view to improving the ion source performance in terms of  $H^-$  and  $D^-$  beam currents. Various goals of the thesis are reiterated in this chapter and the level of success attained by the author in achieving these goals is described.

One of the goals of the thesis was achieving an improvement in the beam currents extracted from the filament ion source, especially increasing the  $D^-$  beam current to a range of 10 mA, which is needed for BNCT applications, as described in Chapter 1. Low beam energy (5 keV) experiments showed that an integrated magnetic field strength of  $\approx 7000$ -8000 G·mm is required for maximum  $D^-$  beam extraction, whereas the requirement reduces to  $\approx 4000$ -6000 G·mm for  $H^-$  beam. However, the optimised magnetic filter field did not produce an increase in  $D^-$  current at high energy (30 keV) experiments. The maximum  $D^-$  current achieved at the Faraday cup was about 5.6 mA. This is only about 56 % of the target value of 10 mA and hence further improvements are needed. The  $D^-$  beam current was limited by the high electron to ion ratios in the  $D_2$  plasma, giving rise to high co-extracted electron current, which saturated the extraction electrode power supply. This led to constraints in tuning the ion source. An extraction electrode power supply with a higher saturation current could be a solution to this problem. Another challenge in conducting experiments using  $D^-$  beams was the generation of neutron radiation, as mentioned in Appendix C. Hence, adequate radiation shielding need to be implemented in future for conducting continuous

experiments. The study of the different factors affecting the beam currents has provided new insights into the operation of the ion source. The contribution of surface reactions to the extracted negative ion current, through the interaction of plasma with Ta adsorbates on the plasma chamber surface, were identified in the study. It was also concluded that for a given set of plasma conditions, a surface with higher thermal conductivity is favorable for  $H^-$  formation through surface reactions. For an applied arc power of about 5000 W, a reduction of about 20 %  $H^-$  beam current was observed when the copper plasma electrode was replaced with an SS plasma electrode.

One of the other goals of the thesis was solving the challenges associated with the stable operation of D-Pace's RF-powered ion source. There were incidents in which the AlN RF window, which coupled RF energy from the external flat spiral antenna into the plasma chamber, was broken during the operation of the ion source. Thermal and stress simulations were performed as part of the thesis and the results indicated the possibility of window failure associated with the temperature distribution on the window. In order to overcome the high temperature a water jacket design was implemented, as described in Chapter 5. This method has proven to be a successful solution so far in terms of the stability of the RF window. More power could also be applied to the ion source without the fear of window breakage, which resulted in attaining about 11.7 mA of  $H^-$  and 5.3 mA of  $D^-$  beam currents. This is about 40 % increase in the beam currents compared to previous results. Even though a solution for the stability issue was found, the design still needs to be further upgraded due to the chamber material erosion during the operation. For the copper plasma chamber, the AlN window gets coated with copper during the operation, degrading the energy coupling to the plasma from the external antenna. Some attempts were made for reducing the copper deposition on the RF window, but a successful solution to this problem has not been achieved so far. Future attempts need to be made to design and implement a Faraday shield for reducing the capacitive coupling as shown in Fig. 5.25. Such shields can reduce the capacitive coupling, but can also lead to plasma ignition problems.

The thesis also aimed at validating the ion extraction simulation code, IBSimu, using D-Pace's filament and RF-powered ion sources. The validity of the code was evaluated by comparing the beam emittance values between IBSimu simulations and experimental results. Beam emittance comparisons were made at different applied powers, gas flows, plasma electrode voltages and extraction electrode voltages. The experiments have given a better understanding of the plasma sheath behaviour under different plasma conditions. One of the drawbacks identified in the study was the difference in emittance values between experiments and IBSimu simulations. This was attributed to the assumption in IBSimu that the particles arriving at the plasma sheath would be having a planar flux profile. Another



drawback identified in IBSimu was the assumption that both ions and electrons behave similarly in the plasma sheath region. Experimental results indicated that the emittance behaviour was dependent on the type of particle species and not only on the total charge density, as considered by IBSimu. Apart from these drawbacks, it was found from the study that IBSimu successfully simulated the general experimental beam emittance trends. One of the characteristic features of the emittance behaviour from the D-Pace ion sources is the existence of an emittance minimum in the trend at different applied powers. The simulation also predicted the occurrence of an emittance minimum very close to the experimentally obtained result. This is an important result, which proves the validity of the IBSimu code.

The studies conducted in the thesis have provided a better understanding of D-Pace's filament and RF ion sources. The influence of factors like magnetic filter fields and surface reactions in the plasma, towards the generation of negative ions were observed in the experiments. The design changes performed in the RF ion source have contributed towards achieving better ion source performance and reliable operation. The experimental campaign for validating IBSimu has provided a data set of different beam emittance values that can be obtained from the ion sources and a simulation tool for future upgrades of the negative ion sources.

# Appendix A

---

## Laser Photodetachment

Laser photodetachment is one of the established tools for the determination of negative ion density inside a plasma. This was used extensively by *Bacal and Hamilton* [122] for measuring the  $\text{H}^-$  density inside  $\text{H}_2$  plasma. These studies made a significant impact in the understanding of the formation of negative ions through volume production methods [42]. This section of the thesis contains the experiments performed by the author at Doshisha University, Japan [123]. The main goal of the experiments was the measurement of negative ion density inside a filament ion source, using the laser photodetachment diagnostic technique.

Laser photodetachment method relies on the low electron affinity of negative ions [124]. In this method, the loosely bound electron in a negative ion is removed by shining a beam of laser of the required energy through the plasma. The negative ions are broken down into free electrons and neutrals. In the case of  $\text{H}^-$  ion, the electron is bound by an energy of only 0.75 eV and the photodetachment reaction can be written as [124]



where  $h$  is the Planck's constant and  $\nu$  is the laser frequency. The release of photoelectrons into the plasma results in a rapid rise in the electron density ( $\Delta n_e$ ). The change in the electron density can be characterized by placing a metallic probe, biased at a higher positive potential compared to the plasma, close to the path of the laser. The photoelectrons released into the plasma get captured by the positively biased probe. The increase in probe current,  $\Delta i_e$ , will be proportional to the increase in electron density due to photodetachment. Considering that the laser beam energy is sufficient for destroying all the negative ions in its path and the generated electrons strike the probe, then  $\Delta n_e = n_-$ , where  $n_-$  is the density of negative ions in the laser path. This gives the following equation [124],

$$\frac{n_-}{n_e} = \frac{\Delta i_e}{i_e} \quad (\text{A.2})$$

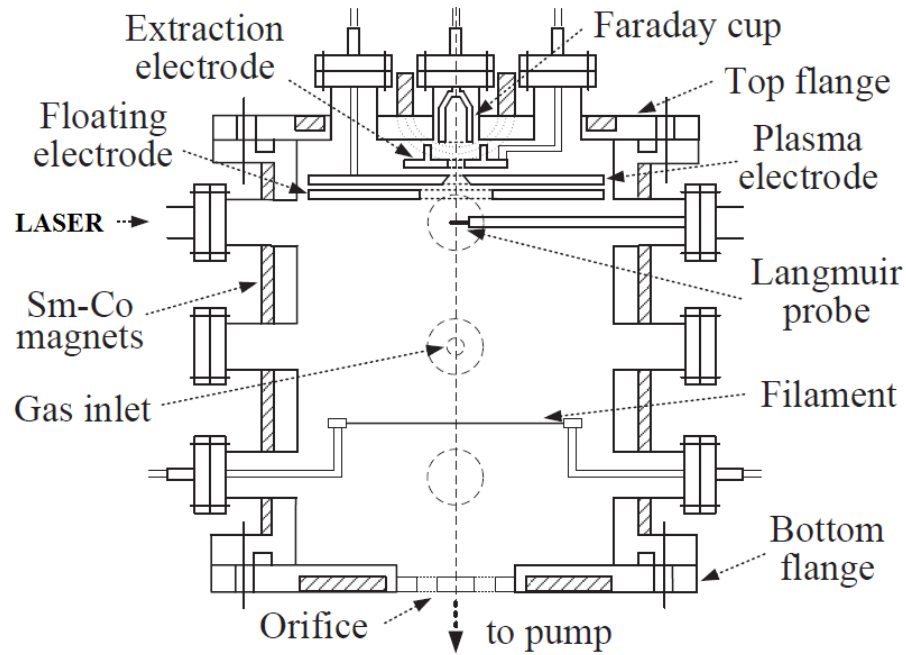


**Figure A.1:** Schematic of the ion source used for photodetachment experiments [125]. Laser is fired through one of the ports and the Langmuir probe is inserted through the opposite port.

where  $n_e$  is the electron density and  $i_e$  is the current through the positively biased probe, in the absence of the laser beam. As evident from the above equation, the negative ion density can be determined when all the other three values are known.

## A.1 Experiments and results

The schematic view of the filament ion source used for the experiments is shown in Fig A.1 [125]. The ion source has a cylindrical plasma chamber 150 mm in diameter and 200 mm in length. Plasma is sustained through thermionic emission from a 0.5 mm diameter tungsten filament of 90 mm length. The Sm-Co magnets provide magnetic multicusp plasma confinement. There is an additional floating electrode for preventing direct exposure of plasma to the plasma electrode. The plasma electrode and the floating electrode are both made of stainless steel. The floating electrode, as the name indicates, does not have any potential on it. The laser used for the photodetachment experiments is an Nd:YAG laser—*Big sky laser ultra* [126] with a wavelength of 1064 nm and pulse energy of 75 mJ. The pulse width of the laser is 3.3 ns and the spot size is 3 mm. The laser beam is passed to the plasma through one of the optical ports, as shown in the figure. A movable Langmuir probe, using 0.5 mm diameter tungsten wire and enclosed in a ceramic sleeve, is inserted into the plasma through

another port, located opposite to the optical port. The probe has a length of 7 mm tungsten wire exposed to the plasma. It is connected to an oscilloscope for current measurements during the experiments.

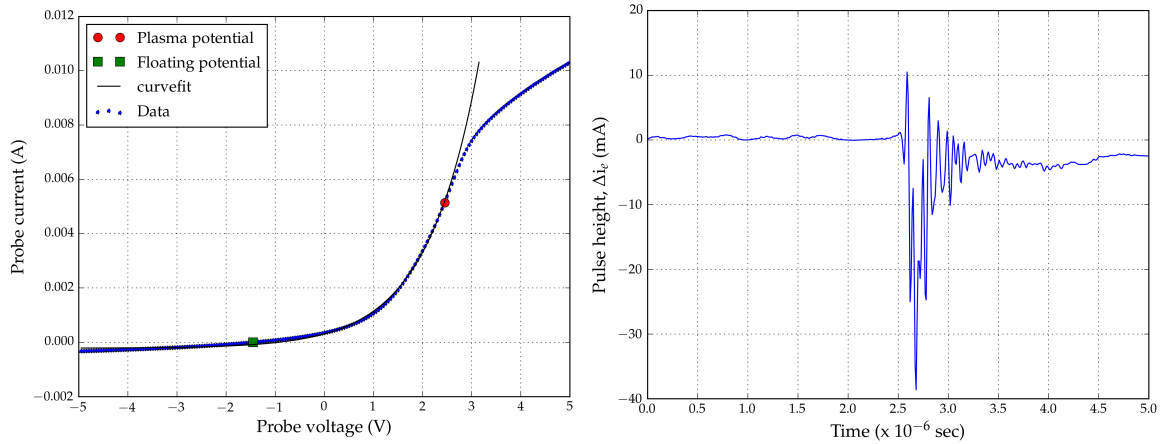


**Figure A.2:** (A) Typical Langmuir probe current-voltage characteristic [83] and curve fitting. The location corresponding to the plasma potential (red circle) and the floating potential (green square) is shown. (B) Typical photodetachment pulse obtained on the oscilloscope connected to the Langmuir probe during a laser pulse.

During the experiments, the background electron current ( $i_e$ ) is determined by the DC current flowing through the Langmuir probe. The probe is biased at a positive DC potential of 12 V during this measurement. The electron density ( $n_e$ ) and other plasma parameters are determined from the Langmuir probe current-voltage characteristics, in which the DC voltage on the probe is swept from negative to positive voltages and the resultant current is measured. The typical behaviour is shown in Fig A.2 (A). The plasma potential is initially found out from the inflection point on the data. A curve fitting is done from the lowest voltage to the plasma potential, using equation 4.1 and the electron temperature is determined. The electron density ( $n_e$ ) is further determined using the electron temperature value and equation 4.2. After these measurements, the laser is fired through the plasma. An increase in the local electron density occurs as mentioned in equation A.1. The resultant increase in the probe current ( $\Delta i_e$ ), corresponding to the capture of the detached electrons, is recorded in the oscilloscope and the typical shape is shown in Fig A.2 (B). The time period for the rise and decay of the pulse is of the order of  $\approx 800$  ns. This depends on the plasma density and is faster for higher densities [122]. Thus, all the parameters required for the determination of the negative ion density, as mentioned in equation A.2, can be found.

Two different experiments were conducted using the laser photodetachment method. One experiment was aimed at the determination of  $H^-$  density distribution in a plane parallel

to the plasma electrode. The other experiment was focused on determining the effect of gas pressure on the  $H^-$  density at a fixed location in the ion source.

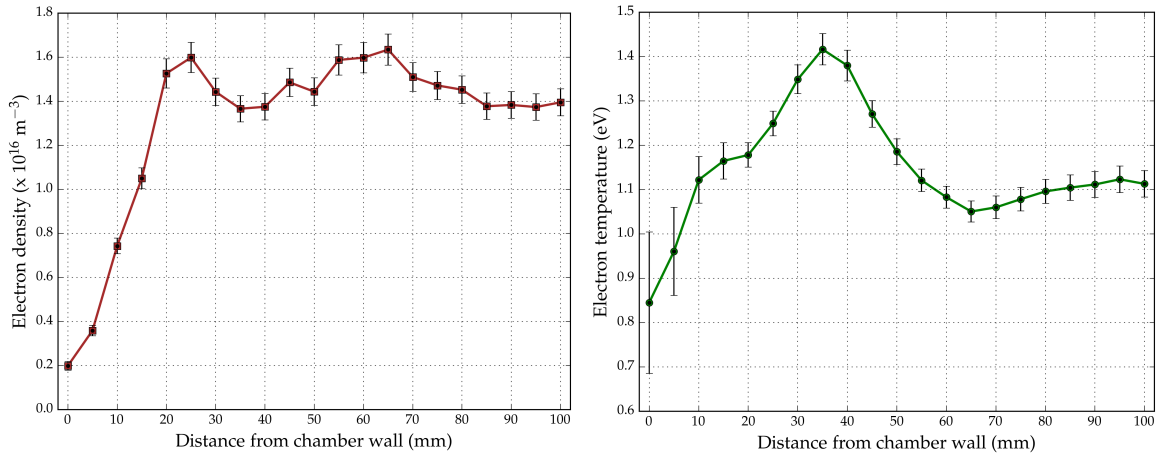


**Figure A.3:** (A) Electron density and (B) electron temperature values obtained from the Langmuir probe measurements at different locations in the plasma, in a plane parallel to the plasma electrode. The  $x$ -axis values are the distance between the wall and the Langmuir probe. The error bar represents values within one standard error. An error of  $\pm 0.5$  mA is assumed for the current measurements.

During the first experiment, the Langmuir probe is moved in a plane parallel to the plasma electrode surface. The probe can be translated up to 100 mm in the experimental set up. Note that the plasma chamber diameter is 150 mm. The electron density and temperature distributions obtained from the Langmuir probe measurements at different locations in the

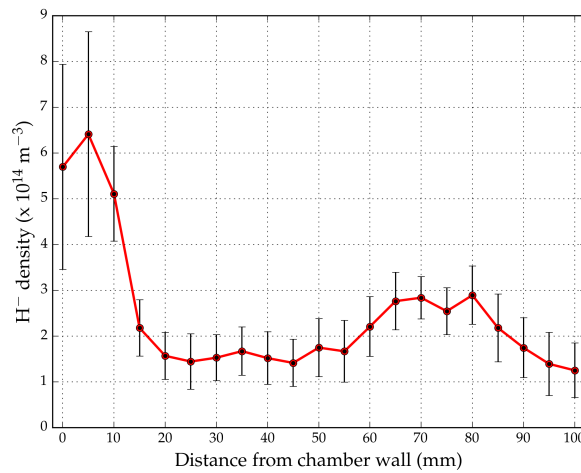


**Figure A.4:** Density of  $H^-$  ions obtained from the laser photodetachment measurements in the ion source, at different locations in a plane parallel to the plasma electrode.

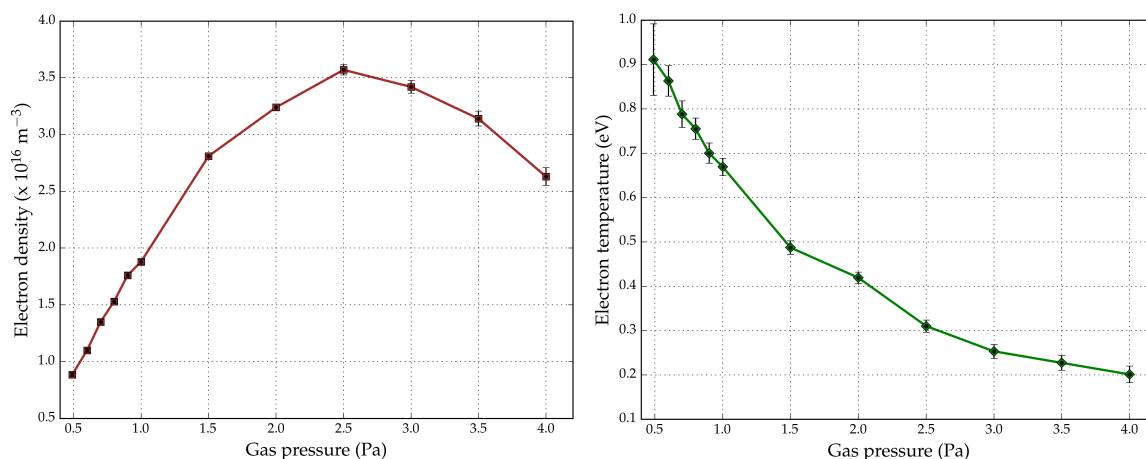


**Figure A.5:** (A) Electron density and (B) electron temperature values obtained from the Langmuir probe measurements at the centre of ion source. The error bar represents values within one standard error. An error of  $\pm 0.5$  mA is assumed for the current measurements.

plasma is shown in Fig A.3. An arc current of 1 A and an  $\text{H}_2$  gas pressure of 0.5 Pa were used. The results indicate a decaying trend for the electron density and electron temperature distributions in regions closer to the chamber wall (0 mm – 20 mm). This could be attributed to the presence of magnetic cusp fields along the chamber wall, as explained in 2.6.4. These cusp fields could be acting as magnetic filters towards the chamber walls, preventing the energetic electrons from reaching the walls. As can be seen, the electron temperature is less than 1 eV in the regions close to the wall. The corresponding  $\text{H}^-$  ion density calculated from the laser photodetachment experiments is shown in Fig A.4. It can be seen from the figure that the  $\text{H}^-$  density increases towards the wall (0 mm – 20 mm). This could again be attributed to the lower electron temperature and density in those regions as seen in Fig A.3. Such low electron temperatures are favorable for the dissociative attachment reactions that lead to negative ion production. Also, the  $\text{H}^-$  ions can reach these regions from the main plasma region due to higher Larmor radius, compared to electrons and have a longer lifetime due to lower local electron temperatures.

Another set of experiments were conducted to see the effect of gas pressure on the density of negative ions. The  $\text{H}_2$  gas pressure was varied between 0.5 Pa to 4.0 Pa during the experiments. The Langmuir probe tip was located at the centre of the chamber during the experiments and an arc current of 1 A was set. The electron density and temperature results from Langmuir probe current-voltage characteristics are shown in Fig A.5. The corresponding  $\text{H}^-$  density measurements from laser photodetachment are shown in Fig A.6. As evident from the graph, there is an optimum pressure for the  $\text{H}^-$  density. As the pressure increases, the

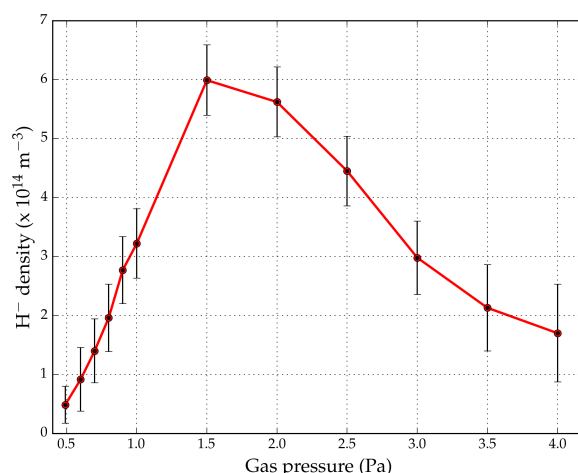


**Figure A.6:** Density of  $\text{H}^-$  ions obtained from the laser photodetachment measurements for different gas pressures in the ion source.

$\text{H}^-$  density increases initially to a maximum value and then decreases on a further increase of gas pressure. It has been understood from studies [36] that the highest  $\text{H}^-$  density occurs when maximum population of the highly excited molecular vibrational state ( $v=10-13$ ) occurs. Further increase of pressure from optimum leads to collisions of the vibrationally excited molecules with other molecules. This results in the decay of the excited states and hence a decrease in the  $\text{H}^-$  density. The presence of an optimum gas pressure is seen in the electron density behaviour also. It can also be seen that the electron temperature decreases with increasing gas pressure. This could be attributed to the loss of energy due to increased collisions as gas pressure increases.

Attempts were made to conduct the laser photodetachment studies in D-Pace's ion sources, as part of the thesis study. However, there were some practical difficulties. The absence of any optical ports around the plasma chamber (Fig. 4.1) proved this to be a difficult mission. Another way for firing the laser was through the extraction end of the ion source. This required powerful lasers since the beam must cover at least 600 mm length through the vacuum box (Fig. B.2). The operation of such lasers needed special safety considerations in the experimental venue. Hence the laser photodetachment studies were not conducted in D-Pace's ion sources. But the results outlined in this section is expected to be applicable to D-Pace's filament ion source also.

# Appendix B

---

## Experiment venue - ISTF

The thesis-related research was performed at the Ion Source Test Facility (ISTF) [127], Buckley Systems Ltd, Auckland. ISTF is a joint venture between D-Pace [18], Canada and Buckley Systems [19], New Zealand and was started in November 2015. This test facility has already displayed its contribution in characterizing different ions, calibration of various instruments for the accelerator industry and verification of computer simulations. This appendix presents an overall picture of the test facility and the various components relevant in the context of the thesis.

A general view of the ISTF is shown in Fig B.1. A Faraday cage encloses the ion source, extraction system and high voltage power supplies, to protect the users from high voltages. The cage doors are equipped with additional safety interlocks. The power supplies that are at high floating voltages are placed in the high voltage rack. All other power supplies are in the low voltage rack. The communication between a dedicated computer and the various power supplies and controllers related to beam extraction, is via Programmable Logic Controller (PLC) modules. Special optic fiber based communication system is used for data transfer to and from the high voltage connections. A mass spectrometer system with 90 degree bending magnet is available for the characterization of extracted species. The beam from the ion source and extraction system can be transported to the mass spectrometer system. It should be noted that experiments related to beam characterization using mass spectrometry were not performed as part of the thesis, as those studies were already performed at the ISTF [80]. Hence the mass spectrometry is not discussed here. The process gas cylinders are placed inside cabinets as shown in the figure. These cabinets are equipped with gas leak detection systems for safety. De-ionized water circulation is present at the facility and is used for cooling the components in the ion source and extraction system.



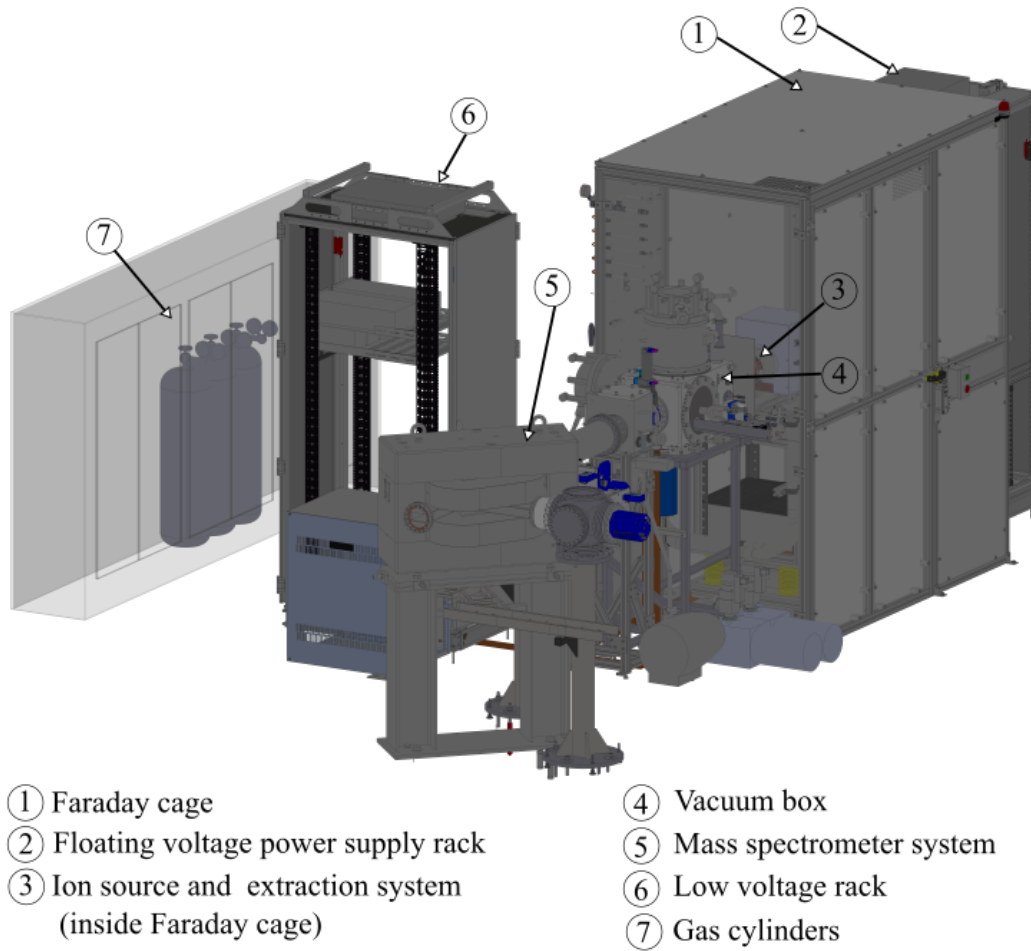


**Figure B.1:** An overall view of the Ion Source Test Facility (ISTF).

The section view of the main experimental set up used for the different beam extraction studies presented in the thesis is shown in the Fig B.2. It consists of the filament ion source, extraction system, vacuum system and diagnostic components. The relevant components and their locations with respect to the plasma electrode (0 mm location) are also shown. Details of the components are explained in the following sections.

## B.1 Ion source and extraction

Two types of ion sources are used in the experiments. One of them is D-Pace's TRIUMF licensed *filament-powered ion source* [13]. The other is D-Pace's *RF-powered ion source*, a hybrid design between the filament ion source and RADIS ion source licensed from the University of Jyväskylä [92]. Both ion sources use the same plasma chamber and extraction system. The main structural difference between the ion sources is the back plate design of the plasma

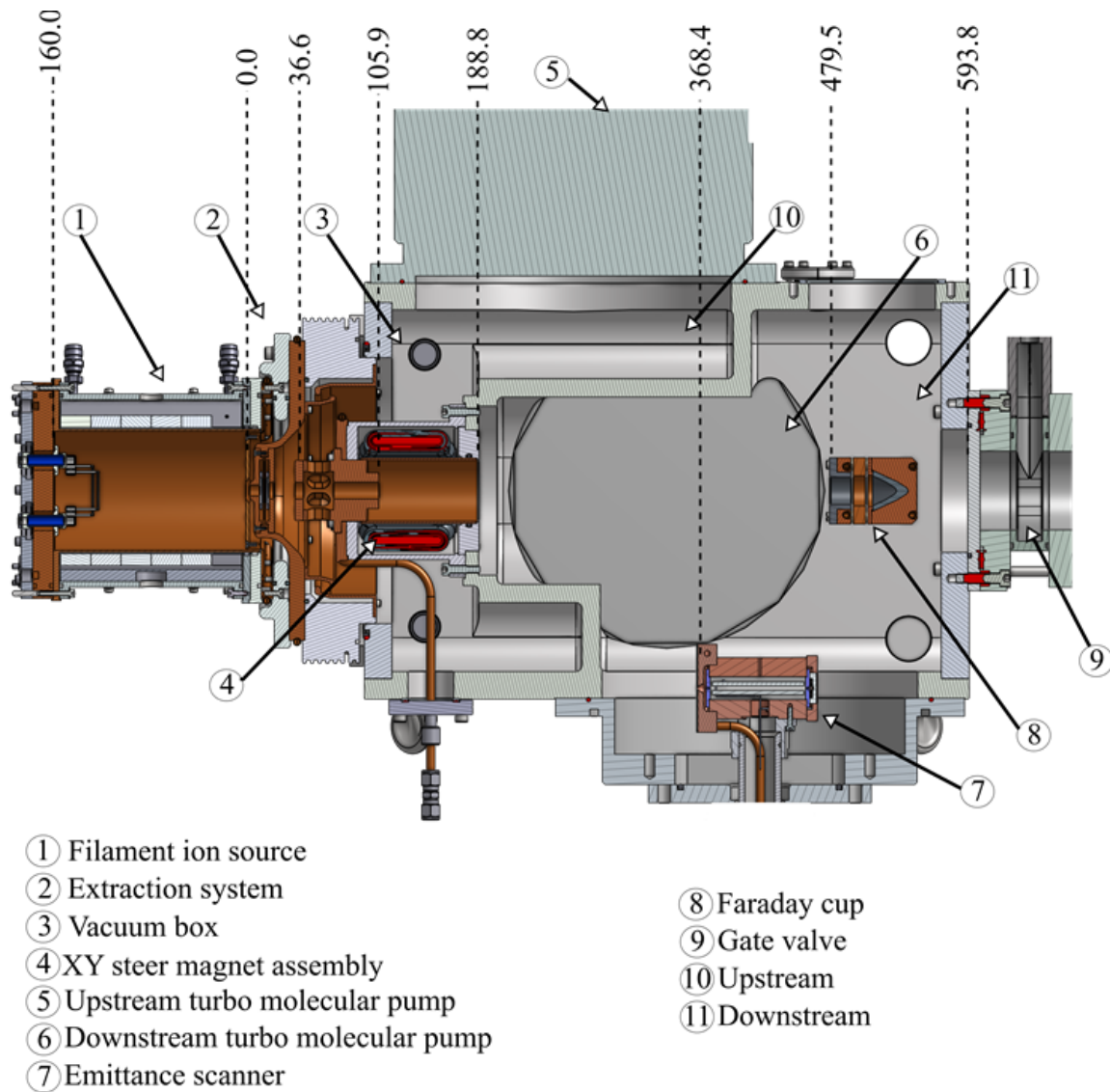


**Figure B.2:** The section view of the filament ion source-extraction-diagnostics assembly used for the experiments in the thesis. The dimensions are in mm. 0 mm corresponds to the location of the plasma electrode.

chamber. The filament ion source has a copper back plate and it holds the filaments for the thermionic emission, whereas the back plate of the RF ion source is an AlN ceramic disc for external RF energy coupling to the plasma. Section views of the ion sources are shown in Fig 4.1 and 5.1.

The schematic of the filament ion source and extraction system is shown in Fig B.3. The ion source has a cylindrical copper plasma chamber of dimensions 98.4 mm X 160 mm. The plasma chamber is cooled by de-ionized water circulation on the outside of the copper wall through the magnet housings. The extraction system consists of the plasma, extraction and

ground electrodes. These electrodes are made of copper and are cooled through conductive heat transfer to brazed water tubes attached to the electrode flanges. The electrode aperture dimensions are also mentioned in the schematic.

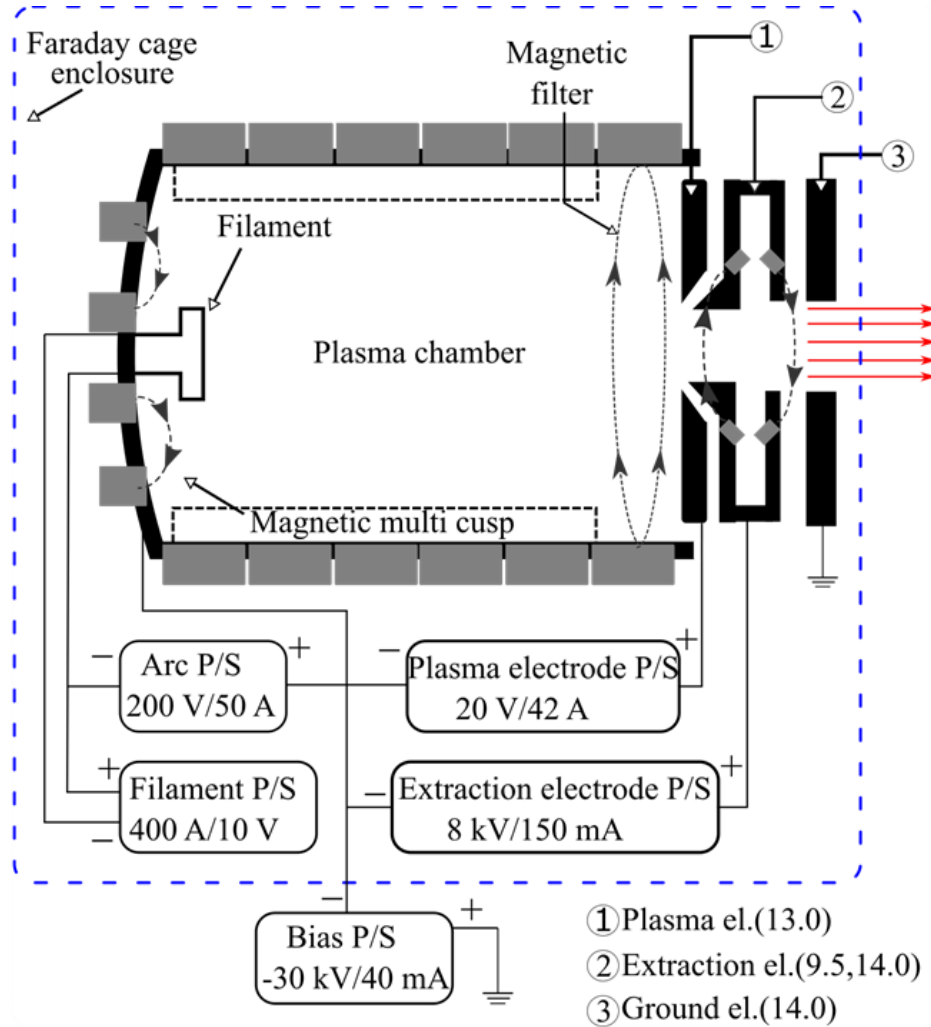


**Figure B.3:** A schematic of the filament ion source and extraction system. The different power supplies used for beam extraction and their ratings are shown. The permanent magnets are shown in grey color. The arrows point from north pole of magnet to the south. The diameter (mm) of the electrode apertures are mentioned in brackets.

### B.1.1 Magnetic fields

Different permanent magnetic fields are present in the system. The magnets present on the outside of the plasma chamber, as shown in the schematic, provide magnetic *multicusp* fields, as presented in section 2.7(B) which aids in plasma confinement. The magnets on the

back plate of the filament ion source also provides a cusp field as shown in the schematic. Note that this plasma confinement is absent in the RF ion source since there are no magnets in the back plate. The cusp configuration is changed to a transverse magnetic filter field towards the plasma electrode location. This transverse field helps in filtering energetic electrons from the plasma electrode region, as mentioned in section 2.7.2. There are two sets of permanent magnets on the extraction electrode that provide transverse magnetic field for the beam extracted from the plasma. The electrons extracted from the plasma encounter this field and get deflected onto the extraction electrode due to Lorentz force. The extracted ions suffer only a slight offset due to higher mass and larger gyro radius. The second set of magnets on the extraction electrode are present to correct this offset of ions, as they provide a magnetic field orientation opposite to the first set of magnets.

### B.1.2 Extraction control parameters

The extraction of stable ion beams from the ion source requires efficient control of the applied power, gas pressure and electric fields. This is achieved via different power supplies and controllers. These are further controlled by the user through a dedicated computer interfaced with PLC modules [128]. The schematic of the power supplies that control the performance of the filament ion source and extraction system is shown in Fig B.3. All power supplies, except the filament power supply, works in the voltage control mode. The filament power supply works in the current control mode. The functions of the power supplies and the main variables associated with it are described below.

- i **Arc power supply:** The amount of power applied to the plasma is determined by the arc power supply. The potential difference between the filament and the plasma chamber, the *arc voltage*, is controlled by this power supply. Different voltages can be applied, but for the experiments presented in the thesis a fixed voltage of 120 V is used. Note that the filament is biased at a negative potential for supporting the thermionic emission from the filaments. The arc voltage accelerates the electrons and causes gas ionization by electron impact processes, as described in section 2.8. The *arc current* measured on the power supply denotes the current flowing between the filaments and plasma chamber. This is dependent mainly on the conductivity of the plasma and hence can be modified by varying the amount of thermionic emission from the filament. This is achieved via a PID feedback loop [129] from the arc current to the filament power supply. The required arc current can be set by the user and the feedback loop resets the filament current from the filament power supply such that the target arc current is achieved. The feedback

from the arc current happens automatically every 10 ms via the PID loop and this ensures a stable arc current ( $\pm 0.76\%$  [129]) in the ion source.

- ii **Filament power supply:** The *filament current* flowing through the Ta filaments is controlled by this power supply. This current flow results in thermionic emission from the filaments and discharge in the plasma. During the experiments, the filament current is controlled manually by the user till the beginning of arc discharge in the plasma. Once the discharge is initiated, the PID control loop [129] is activated, as explained above. This automatically sets the required filament current flow from the power supply, based on the arc current requirements.
- iii **Plasma electrode power supply:** The *plasma electrode voltage* is controlled through this power supply. A positive potential is set on the plasma electrode. This helps in controlling the co-extracted electron current and also enables the negative ions to overcome the plasma potential well. The *plasma current* measured on the power supply corresponds to the amount of charge flow towards the plasma electrode. The voltage value needs to be optimized during the experiments for maximum ion beam extraction and generally needs to be increased as the arc current is raised.
- iv **Extraction electrode power supply:** This power supply enables the *extraction electrode voltage* control by the user. This has an important role, as it provides the required electric fields for charged particle extraction from the plasma. The voltage needs to be optimized for maximum ion extraction. The electrons extracted from the plasma are deflected onto the extraction electrode by permanent magnetic fields around the extraction electrode aperture. Thus, the *extraction current* recorded on the power supply is a measure of the co-extracted electron current from the plasma. The power supply can handle up to 150 mA of current. This limit becomes a challenge in the extraction of  $D^-$  ions as mentioned in section 4.2.3.
- v **Gas pressure control:** The volume of gas flow into the plasma chamber is controlled by mass flow controllers [130]. A gas flow up to 32 sccm of  $H_2$  and  $D_2$  can be maintained. The flow level can be set by the user directly. The gas flow also needs to be optimized for ion beam extraction as seen in Fig. A.6. The gas pressure inside the ion source and extraction system is determined by a combination of gas flow into the system and the action of differential pumping by the vacuum pumps as explained in section B.2.
- vi **Bias power supply:** All the aforesaid power supplies and plasma chamber are floating at a *bias voltage* set by the user, through the bias power supply. The energy of the beam

Parameter	Value
Beam current, $I_{FC}$ (mA)	15.0
Arc P/S (A, V)	38.1, 120
Filament P/S (A,V)	126.0, 2.1
Bias P/S (mA, kV)	24.7, 30.0
Extraction electrode P/S (mA, kV)	115.6, 3.7
Plasma electrode P/S (A, V)	17.2, 3.4
Gas flow (sccm)	20.5
XY steer P/S (X steer (A), Y steer (A))	2.0, 1.5

**Table B.1:** A typical set of control parameters during the extraction of 15 mA of  $H^-$  beam from the filament ion source.

reaching the ground electrode is determined by the bias voltage. The experiments presented in the thesis deal with the extraction of negative ions and hence the applied bias voltage is negative with respect to the ground electrode. The *bias current* recorded on the bias power supply measures the net flow of charges between the plasma and the ground electrode region.

- vii **XY steering power supply:** This power supply controls the current through the XY steering magnet shown in Fig B.2. It is made up of two electromagnet dipoles that are oriented in orthogonal directions. The current flowing through the dipoles generate a magnetic field that can steer the beam in X and Y directions. This steering is needed since the ion beam suffers a slight offset due to the magnetic field in the extraction electrode region.

A typical example set of the above-listed control parameters is shown in table B.1. It represents the conditions for a 15 mA of  $H^-$  beam obtained at the Faraday cup from the filament ion source. It is to be noted that for D-Pace's RF-powered ion source, the arc and filament power supplies are not present. The arc power supply is replaced by a 13.56 MHz RF power supply. The user can set the applied *RF power* to the plasma through this power supply. The output of the RF power supply is attached to an impedance matching box and an external RF antenna. More details on this are presented in section 5.1.

## B.2 Vacuum system

The gas pressure inside the plasma chamber needs to be maintained at a higher pressure relative to other parts of the extraction system for the proper operation of the plasma

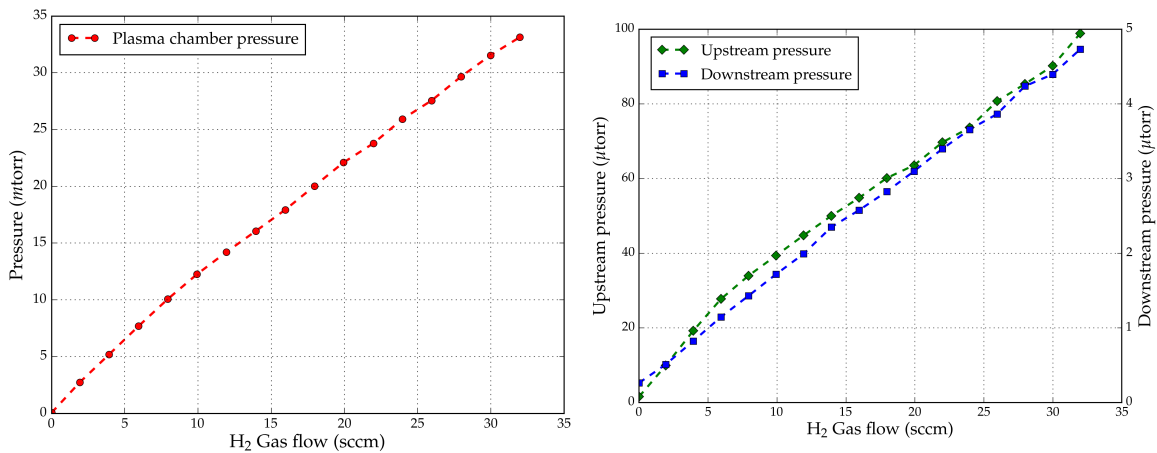


**Figure B.4:**  $N_2$  equivalent pressure recorded for different  $H_2$  gas flows in the (A) plasma chamber, (B) upstream and downstream regions.

discharge. A low pressure level is preferred along the path of the extracted beam to reduce losses due to stripping. The ion source and extraction system is equipped with a differential pumping system which helps in attaining these different gas pressure levels needed for maximum beam extraction. This is done with the help of two turbomolecular pumps, whose locations are shown in Fig B.2. Both pumps have a pumping speed of 1700 L/s in  $H_2$  gas and is supported by two different dry scroll pumps. The geometry of the vacuum box and the location of the turbopumps divide the system into an *upstream region* and a *downstream region* as shown in Fig B.2. The pressure on these regions is monitored by vacuum gauges. The pressure recorded in the upstream region is higher than the downstream region. The downstream is connected to the ion source-extraction region only through the ground electrode tube of 14 mm diameter. Hence the gas in the ion source region is conducted mostly through the upstream region into the upstream turbopump.

The pressure in the plasma chamber cannot be directly monitored during the ion source operation. Hence, the back plate of the ion source was replaced with a Pirani gauge connected flange and pressure was recorded at different  $H_2$  gas flows, without plasma. The results are shown in Fig B.4(A). The corresponding pressures in the upstream and downstream regions is shown in Fig. B.4(B). Note that the values correspond to  $N_2$  equivalent gas pressures. Most of the experiments in the thesis used a plasma chamber gas pressure range of 5 mtorr to 25 mtorr.

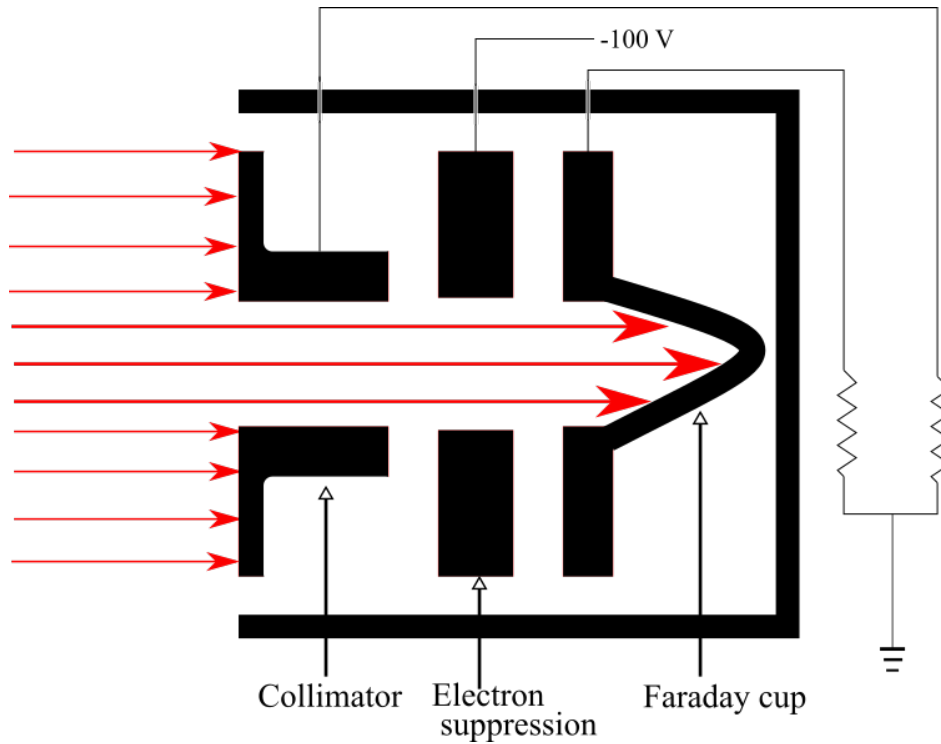


**Figure B.5:** Schematic of the D-Pace Faraday cup beam current measurement. The ion trajectory is represented by the red lines.

## B.3 Beam diagnostics

### B.3.1 Faraday cup

The amount of negative ion currents extracted from the ion source is quantified by the Faraday cup as shown in Fig B.2. The entrance of the Faraday cup is 480 mm from the plasma electrode. The experiments presented in the thesis used D-Pace's 1 kW Faraday cup [18]. This can measure up to 55 mm beam diameter. The cup is retractable and can be moved in and out of the beam path as needed. The basic working can be explained by the schematic shown in Fig B.5. It consists of a collimator, electron suppression plate and the Faraday cup. The red lines represent the beam propagation. The electron suppression plate is biased at -100 V to prevent the emission of secondary electrons from the cup. A graphite Faraday cup is used in the experiments. As evident from the schematic, both the cup and the collimator are grounded through fixed value resistors. The voltage measured across these resistors corresponds to the beam current striking the Faraday cup. The beam current values mentioned in the thesis,  $I_{FC}$ , is the sum of currents obtained on the collimator and the cup.



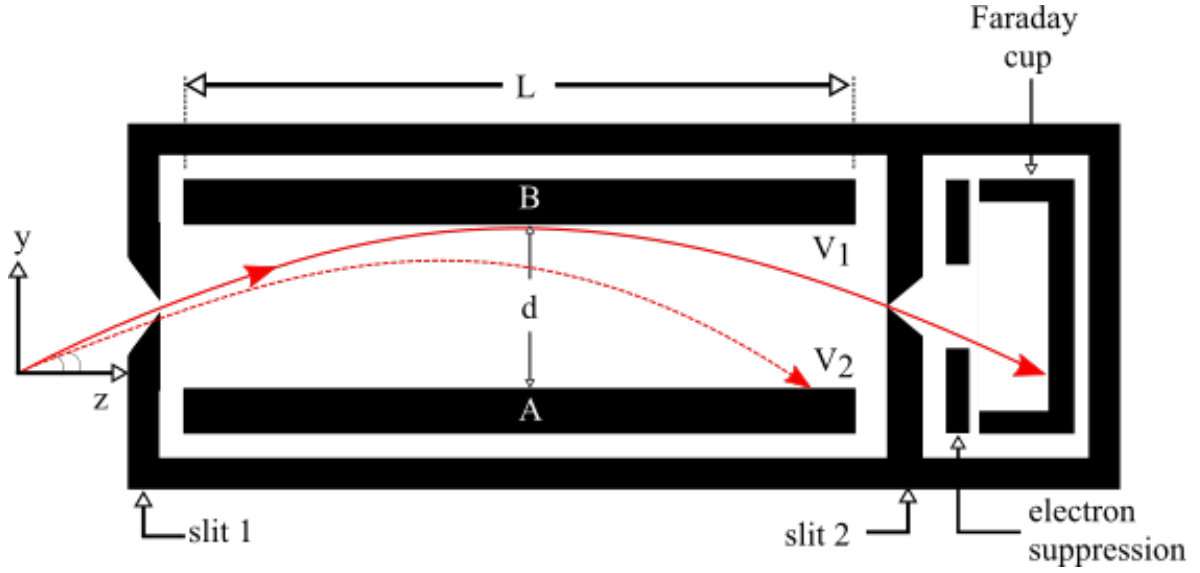


**Figure B.6:** Schematic of the D-Pace emittance scanner. The ion trajectory is represented by the red curve.

### B.3.2 Emittance scanner

The transverse emittance of the ion beam is measured using D-Pace's TRIUMF licensed Allison type [131] emittance scanner [132], shown in Fig B.2. This emittance scanner can record the density of ions in the beam as a function of position ( $x$  or  $y$ ) and angle ( $x'$  or  $y'$ ) simultaneously and determine the distribution,  $I(x, x')$  or  $I(y, y')$ , presented in section 3.6.

The basic working of the emittance scanner is illustrated in Fig B.6. In this case, the beam is propagating in the  $z$ -direction and the scanner is moved in the  $y$ -direction. It consists of two slits, slit 1 and slit 2, two deflecting plates (A and B) biased at varying potentials  $V_1$  and  $V_2$ , an electron suppression plate biased at -100 V and a Faraday cup for measuring the beam current. Slit 1 admits only a slice of the beam to the scanner. The ion beam entering slit 1 encounters the electric field between the plates and gets deflected as represented by the red curves. The ion beam needs to pass through slit 2 to be detected at the Faraday cup. Only those ions entering slit 1 at a particular  $y'$  angle can get past the slit 2, for a set of fixed voltage values on the plates A and B. This is shown by the solid red curve. Other ions with a different angle will encounter the electric field and miss the slit 2, in a manner shown by the dashed red curve. The condition for the beam to reach the Faraday cup can be derived as [131]

$$y' = -\frac{qL}{4d} \frac{\Delta V}{E_k} \quad (\text{B.1})$$

where  $\Delta V$  is the difference in voltage between plates A and B,  $E_k$  is the kinetic energy of the beam entering the emittance scanner,  $L$  is the length of the deflecting plates and  $d$  is the

gap between the plates. As seen from the equation,  $\Delta V$  acts like a selector of a particular beam angle, when the other parameters are fixed. For example, when  $\Delta V = -378.9$  V, for a 30 keV beam energy and the scanner dimensions of  $L = 76$  mm and  $d = 4$  mm, the current recorded on the Faraday cup would correspond to the portion of the beam slice with an angle of 60 mrad. In this manner, a sweep through different voltages on the deflection plates enables the determination of current at different angular values in the beam slice. This voltage sweep is repeated at different  $y$  locations. At the end of the scan, a 2D array of intensity values,  $I(y, y')$ , is obtained, which is used for determining the beam emittance and twiss parameters.

A sweep of  $-60$  mrad to  $60$  mrad, with a resolution of  $1$  mrad, is used commonly for the experiments in the thesis. The scanner is moved from  $y = -20$  mm to  $20$  mm with a step size of  $1$  mm for the scans. The maximum beam angle that can be detected by the Allison scanner depends upon the dimensions of the scanner [131]. The emittance scanner used for the experiments can measure up to a maximum of  $97$  mrad of beam angle. Emission of secondary electrons from the Faraday cup is prevented by an electron suppression ring biased at a voltage of  $-100$  V in front of the Faraday cup. The Faraday cup current is read with a pico-ammeter. The slit 1 of the emittance scanner is located at about  $368$  mm from the plasma electrode. The scanner can be mounted such that the scans are in  $x - z$  plane or  $y - z$  plane. The  $y - z$  scanning plane was chosen for all the experiments in the thesis.

## B.4 Beam tuning methods

The performance or the effectiveness of a modified configuration in the ion source and extraction system is evaluated by way of the general beam tuning experiments. The target of these experiments is to maximize the beam current obtained on the Faraday cup ( $I_{FC}$ ), by varying the different parameters outlined in section B.1.2. The arc current is the main guiding variable in the experiments with the filament ion source. The parameters like arc voltage and bias voltage are mostly fixed throughout the experiment. At first, the arc current is set at a particular value, about  $2$  A, after setting the arc voltage and bias voltage. Then the extraction voltage is increased in steps till the maximum  $I_{FC}$  is obtained. The plasma electrode voltage is now increased to a value which further increases the beam current. Then the gas flow is also adjusted to attain the best beam current. The XY steerer current values are modified to steer the beam onto the Faraday cup. This entire cycle is repeated many times to attain the maximum  $I_{FC}$ , for a fixed arc current. The maximum value achieved after all these optimizations is recorded as the achieved beam current at the particular arc

current. The beam emittance scan is also recorded after these steps. After data collection, the arc current is further increased to the next value and the entire cycle is repeated. Note that in the case of D-Pace's RF ion source the applied RF power is the guiding variable for the beam tuning.

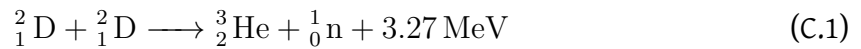
# Appendix C

---

## Neutron radiation

One of the challenges encountered during the  $D^-$  beam extraction from the ion source was the generation of neutron radiation during the experiments. Neutron radiation belongs to the class of ionizing radiation and has adverse biological effects [133]. This led to constraints in performing deuterium experiments at the experimental venue. This section presents a brief description of the extent of radiation observed during the experiments.

The neutron radiation was observed only during  $D^-$  extraction and no radiation was observed in  $H^-$  extraction. One of the possible reactions that could lead to the observed neutron radiation can be the D–D fusion reaction mentioned below [134, 135].



The extracted ion beam current from the ion source is measured using a Faraday cup, as shown in Fig. B.2. The Faraday cup is made of graphite and acts as a beam stopper for the energetic ion beam. It is believed that the accelerated deuterium gets implanted on the cup and this further reacts with the energetic deuterium in the ion beam, giving rise to the reaction mentioned in the above equation [82].

A regular tuning experiment was conducted in  $D_2$  plasma to measure the amount of neutron radiation obtained during  $D^-$  beam extraction. The radiation was measured using a neutron detector that utilized a  ${}^3\text{He}$  gas filled proportional detector [136]. The detector was placed about 0.5 m away from the Faraday cup, outside the vacuum box, as shown in Fig. C.1. A beam energy of 30 keV was used. The experiment was run remotely with no personnel within 20 m from the source.

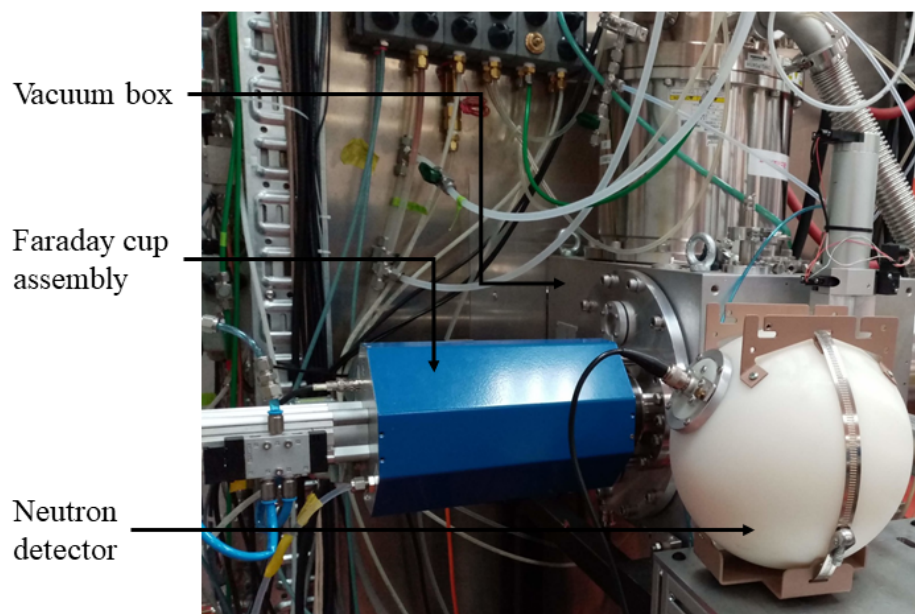


**Figure C.1:** A picture showing the location of the neutron detector used for  $D^-$  beam experiments. The detector is placed close to the diagnostics box.

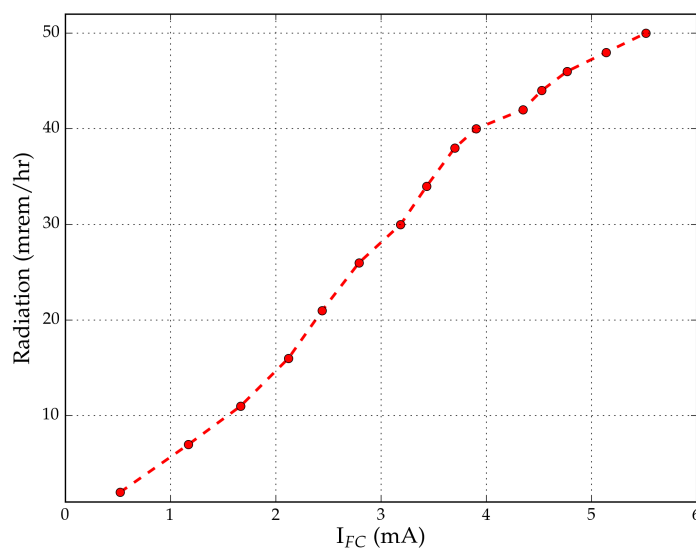


**Figure C.2:** Radiation levels recorded by the detector for different  $D^-$  beam currents at the Faraday cup. A beam energy of 30 keV was used for the experiment. The detector is placed at about 0.5 m away from the Faraday cup.

The radiation levels detected for the different  $D^-$  beam currents measured on the Faraday cup are shown in Fig C.2. The dose rate reached up to 50 mrem/hr for about 5.5 mA of  $D^-$  beam measured at the Faraday cup. Due to this neutron radiation, the  $D_2$  experiments were run only under strict safety conditions. No workers were allowed to be present within a 20 metre distance from the ion source and the experiment was run remotely. This limited the frequency of  $D_2$  experiments, with 30 keV beam energy, during the thesis. Since no radiation was observed for beam energies less than 5 keV, some of the experiments were performed at low energies. But this severely limited the amount of extracted  $D^-$  current from the ion source due to space charge effects, as demonstrated in Fig3.11(B).

# Bibliography

- [1] Ernest O Lawrence and M Stanley Livingston. “The production of high speed light ions without the use of high voltages”. In: *Physical Review* 40.1 (1932), p. 19 (page 1).
- [2] ATLAS Collaboration. “Observation of a new particle in the search for the Standard Model Higgs boson with the ATLAS detector at the LHC”. In: *Physics Letters B* 716.1 (2012), pp. 1–29. DOI: <https://doi.org/10.1016/j.physletb.2012.08.020> (page 1).
- [3] CERN. *Facts and figures about the LHC*. URL: <https://home.cern/resources/faqs/facts-and-figures-about-lhc> (visited on 03/17/2021) (page 1).
- [4] U.S.Department of energy. *Accelerators for America’s Future*. URL: <https://www.odu.edu/content/dam/odu/col-dept/physics/docs/report-future-cas.pdf> (visited on 03/17/2021) (page 1).
- [5] EuCARD. *Application os particle accelerators in Europe*. URL: [http://apae.ific.uv.es/apae/wp-content/uploads/2015/04/EuCARD\\_Applications-of-Accelerators-2017.pdf](http://apae.ific.uv.es/apae/wp-content/uploads/2015/04/EuCARD_Applications-of-Accelerators-2017.pdf) (visited on 03/17/2021) (page 1).
- [6] M E Capoulat and A J Kreiner. “A  $^{13}\text{C}$  (d, n)-based epithermal neutron source for Boron Neutron Capture Therapy”. In: *Physica Medica: European Journal of Medical Physics* 33 (2017), pp. 106–113 (pages 1, 2, 3).
- [7] Valeriia N. Starovoitova, Lali Tchelidze, and Douglas P. Wells. “Production of medical radioisotopes with linear accelerators”. In: *Applied Radiation and Isotopes* 85 (2014), pp. 39–44. ISSN: 0969-8043. DOI: <https://doi.org/10.1016/j.apradiso.2013.11.122> (page 1).

- [8] R. Mehnert. "Review of industrial applications of electron accelerators". In: *Nuclear Instruments and Methods in Physics Research Section B: Beam Interactions with Materials and Atoms* 113.1 (1996). Accelerators in Applied Research and Technology, pp. 81–87. ISSN: 0168-583X. DOI: [https://doi.org/10.1016/0168-583X\(95\)01344-X](https://doi.org/10.1016/0168-583X(95)01344-X) (page 1).
- [9] S B Felch, M I Current, and M C Taylor. "Ion implantation for semiconductor devices: The largest use of industrial accelerators". In: *Proceedings of the North American Particle Accelerator Conference*. 2013, p. 740 (page 1).
- [10] Ian G Brown. *The physics and technology of ion sources*. John Wiley & Sons, 2004 (pages 1, 5, 16, 20, 24, 27, 28, 29, 32, 33).
- [11] Vadim Dudnikov. *Development and applications of negative ion sources*. Springer, 2019 (pages 1, 32).
- [12] G D Alton. *Negative ion formation processes: A general review*. Tech. rep. Oak Ridge National Lab., 1990 (pages 1, 27, 29).
- [13] T Kuo et al. "On the development of a 15 mA direct current H<sup>-</sup> multicusp source". In: *Review of scientific instruments* 67.3 (1996), pp. 1314–1316 (pages 2, 3, 59, 60, 87, 147).
- [14] Ragnar Hellborg. *Electrostatic accelerators*. Springer, 2005 (page 2).
- [15] P. Schaffer and F. Bénard et al. "Direct Production of <sup>99m</sup>Tc via <sup>100</sup>Mo(p,2n) on Small Medical Cyclotrons". In: *Physics Procedia* 66 (2015). The 23rd International Conference on the Application of Accelerators in Research and Industry - CAARI 2014, pp. 383–395. ISSN: 1875-3892. DOI: <https://doi.org/10.1016/j.phpro.2015.05.048> (page 2).
- [16] C. Ankenbrandt et al. *11th International Conference on High-Energy Accelerators: Geneva, Switzerland*. 1980, pp. 260–271. DOI: 10.1007/978-3-0348-5540-2\_28 (page 2).
- [17] Gordon W Hamilton and John E Osher. *Design study of a 14,000-ampere injection system for a fusion reactor*. Tech. rep. California Univ., Livermore. Lawrence Livermore Lab., 1972 (pages 2, 29).
- [18] D-Pace. *Dehnel particle accelerator components and engineering*. URL: <http://www.dpace.com> (visited on 03/17/2021) (pages 2, 146, 154).
- [19] *Buckley systems limited*. URL: <https://www.buckleysystems.com> (visited on 03/17/2021) (pages 2, 146).
- [20] ME Capoulat, DM Minsky, and AJ Kreiner. "Computational assessment of deep-seated tumor treatment capability of the <sup>9</sup>Be (d, n) <sup>10</sup>B reaction for accelerator-based Boron Neutron Capture Therapy (AB-BNCT)". In: *Physica Medica: European Journal of Medical Physics* 30.2 (2014), pp. 133–146 (page 3).



- [21] Taneli Kalvas et al. “IBSIMU: A three-dimensional simulation software for charged particle optics”. In: *Review of Scientific Instruments* 81.2 (2010), 02B703 (pages 3, 34, 84, 114).
- [22] José A Bittencourt. *Fundamentals of plasma physics*. Springer Science & Business Media, 2013 (pages 5, 6, 8, 9, 10, 13, 15, 16, 17, 18, 21, 22, 24, 25, 26, 39).
- [23] Lewi Tonks. “The birth of “plasma””. In: *American Journal of Physics* 35.9 (1967), pp. 857–858 (page 5).
- [24] Francis F Chen et al. *Introduction to plasma physics and controlled fusion*. Vol. 1. Springer, 1984 (pages 5, 7, 8, 10, 14, 17, 18, 21, 24).
- [25] Arthur Beiser. *Concepts of modern physics*. Tata McGraw-Hill Education, 2003 (pages 5, 6).
- [26] Robert J Goldston and Paul Harding Rutherford. *Introduction to plasma physics*. CRC Press, 1995 (pages 5, 6, 7, 11, 16, 17, 25, 26).
- [27] V A Godyak, R B Piejak, and B M Alexandrovich. “Measurement of electron energy distribution in low-pressure RF discharges”. In: *Plasma sources science and technology* 1.1 (1992), p. 36 (page 7).
- [28] K-U Riemann. “The Bohm criterion and sheath formation”. In: *Journal of Physics D: Applied Physics* 24.4 (1991), p. 493 (pages 12, 13, 14).
- [29] Scott Robertson. “Sheaths in laboratory and space plasmas”. In: *Plasma Physics and Controlled Fusion* 55.9 (2013), p. 093001 (page 13).
- [30] James D Callen. “Fundamentals of plasma physics”. In: *Online Book* (2006) (pages 14, 18, 22).
- [31] FEMM. *Finite Element Method Magnetostatics*. URL: <https://www.femm.info/wiki/HomePage> (visited on 03/17/2021) (page 23).
- [32] Taneli Kalvas. “Development and use of computational tools for modelling negative hydrogen ion source extraction systems”. In: *Research report/Department of Physics, University of Jyväskylä* 10/2013 (2013) (pages 23, 35, 51, 114, 130).
- [33] V V Alikaev, V M Glagolev, and S A Morozov. “Anisotropic instability in a hot electron plasma, contained in an adiabatic trap”. In: *Plasma Physics* 10.8 (1968), p. 753 (page 24).
- [34] A P H Goede and T S Green. “Operation limits of multipole ion sources”. In: *The Physics of Fluids* 25.10 (1982), pp. 1797–1810 (page 24).

- [35] W L Stirling, C C Tsai, and P M Ryan. “15 cm duoPIGatron ion source”. In: *Review of Scientific Instruments* 48.5 (1977), pp. 533–536 (page 24).
- [36] M Bacal. “Physics aspects of negative ion sources”. In: *Nuclear Fusion* 46.6 (2006), S250 (pages 27, 67, 145).
- [37] J P Boeuf et al. “Physics of a magnetic filter for negative ion sources. II.  $E \times B$  drift through the filter in a real geometry”. In: *Physics of Plasmas* 19.11 (2012), p. 113510 (page 27).
- [38] W C Martin et al. “Ground Levels and Ionization Energies for the Neutral Atoms (version 1.3)”. In: *National Institute of Standards and Technology, Gaithersburg, MD.[Online]* Available: <http://physics.nist.gov/IonEnergy> (2011) (page 27).
- [39] R Celiberto et al. “Cross section data for electron-impact inelastic processes of vibrationally excited molecules of hydrogen and its isotopes”. In: *Atomic Data and Nuclear Data Tables* 77.2 (2001), pp. 161–213 (pages 28, 30, 31).
- [40] D Hitz et al. “Production of highly charged ion beams with the Grenoble test electron cyclotron resonance ion source (plenary)”. In: *Review of scientific instruments* 75.5 (2004), pp. 1403–1406 (page 28).
- [41] E B Hooper Jr et al. “High current source of He<sup>-</sup> ions”. In: *Review of Scientific Instruments* 51.8 (1980), pp. 1066–1070 (page 29).
- [42] Marthe Bacal and M Wada. “Negative hydrogen ion production mechanisms”. In: *Applied physics reviews* 2.2 (2015), p. 021305 (pages 30, 31, 32, 63, 69, 70, 75, 140).
- [43] K Prelec and T Sluyters. “Formation of negative hydrogen ions in direct extraction sources”. In: *Review of Scientific Instruments* 44.10 (1973), pp. 1451–1463 (pages 30, 32).
- [44] M. Allan and S. F. Wong. “Effect of Vibrational and Rotational Excitation on Dissociative Attachment in Hydrogen”. In: *Phys. Rev. Lett.* 41 (26 1978), pp. 1791–1794. DOI: 10.1103/PhysRevLett.41.1791 (page 30).
- [45] J M Wadehra and J N Bardsley. “Vibrational-and rotational-state dependence of dissociative attachment in e-H<sub>2</sub> collisions”. In: *Physical Review Letters* 41.26 (1978), p. 1795 (page 30).
- [46] Mario Capitelli, Domenico Bruno, and Annarita Laricchiuta. “Fundamental aspects of plasma chemical physics”. In: *Thermodynamics* 66 (2012) (page 31).
- [47] E Nicolopoulou, M Bacal, and HJ Doucet. “Equilibrium density of h-in a low pressure hydrogen plasma”. In: *Journal de Physique* 38.11 (1977), pp. 1399–1404 (page 32).

- [48] K. S. Woodcock. “The Emission of Negative Ions under the Bombardment of Positive Ions”. In: *Phys. Rev.* 38 (9 1931), pp. 1696–1703. DOI: 10.1103/PhysRev.38.1696 (page 32).
- [49] Axel Groß. “Theoretical surface science”. In: *A Microscopic Perspective. Originally published in the series: Advanced Texts in Physics*, 132 (2003) (page 32).
- [50] Steven M Lund. *Lectures on beam physics with intense space charge* (2015). URL: [https://people.nsl.mscl.msu.edu/~lund/uspas/bpisc\\_2015/](https://people.nsl.mscl.msu.edu/~lund/uspas/bpisc_2015/) (visited on 03/17/2021) (pages 33, 41, 42, 43, 44).
- [51] M Ferrario. “Injection, Extraction and Matching”. In: *arXiv preprint arXiv:1705.10564* (2017) (pages 33, 48, 49, 57, 58).
- [52] Martin Reiser and Patrick O’Shea. *Theory and design of charged particle beams*. Vol. 312. Wiley Online Library, 1994 (pages 33, 37, 39, 40, 41, 44, 45, 46, 48, 49, 51, 52, 53, 54, 56, 58).
- [53] Helmut Wiedemann. *Particle accelerator physics*. Springer Nature, 2015 (pages 33, 40, 49, 53).
- [54] EV Stenson et al. “Debye length and plasma skin depth: two length scales of interest in the creation and diagnosis of laboratory pair plasmas”. In: *Journal of Plasma Physics* 83.1 (2017) (page 34).
- [55] O D Alton. “Sources of low-charge-state positive-ion beams”. In: *Experimental Methods in the Physical Sciences* 29 (1995), pp. 69–163 (page 34).
- [56] Q Ji, A Sy, and J W Kwan. “Radio frequency-driven proton source with a back-streaming electron dump”. In: *Review of Scientific Instruments* 81.2 (2010), 02B312 (page 34).
- [57] S Mochalsky et al. “On the meniscus formation and the negative hydrogen ion extraction from ITER neutral beam injection relevant ion source”. In: *Plasma Physics and Controlled Fusion* 56.10 (2014), p. 105001 (page 35).
- [58] J R Coupland et al. “A study of the ion beam intensity and divergence obtained from a single aperture three electrode extraction system”. In: *Review of Scientific Instruments* 44.9 (1973), pp. 1258–1270 (pages 36, 38, 39).
- [59] C D Child. “Discharge from hot CaO”. In: *Physical Review (Series I)* 32.5 (1911), p. 492 (page 37).
- [60] Irving Langmuir. “The effect of space charge and residual gases on thermionic currents in high vacuum”. In: *Physical Review* 2.6 (1913), p. 450 (page 37).

- [61] J A N Gonçalves, J J Barroso, and G M Sandonato. “Experimental study of vacuum diodes under partial space-charge regime”. In: *Diamond and related materials* 13.1 (2004), pp. 60–63 (page 37).
- [62] Henry F Ivey. “Cathode field in diodes under partial space-charge conditions”. In: *Physical Review* 76.4 (1949), p. 554 (page 37).
- [63] Dan Faircloth. “Ion sources for high-power hadron accelerators”. In: *arXiv preprint arXiv:1302.3745* (2013) (page 38).
- [64] M Hosseinzadeh and H Afarideh. “Optimization and numerical simulation for the extraction system of the H- multicusp ion source”. In: *Chinese Physics C* 38.5 (2014), p. 057003 (page 38).
- [65] Katharine B Blodgett. “Currents limited by space charge between concentric spheres”. In: *Thermionic Phenomena*. Elsevier, 1961, pp. 125–135 (page 38).
- [66] Ernest D Courant and Hartland S Snyder. “Theory of the alternating-gradient synchrotron”. In: *Annals of physics* 281.1-2 (2000), pp. 360–408 (page 44).
- [67] J Rossbach and Peter Schmueser. “Basic course on accelerator optics”. In: *Conf. Proc.* Vol. 9209071. 1992, pp. 17–88 (page 45).
- [68] Jean Buon. *Beam phase space and emittance*. Tech. rep. Paris-11 Univ., 1992 (pages 47, 52).
- [69] P. M. Lapostolle. “Possible Emittance Increase through Filamentation Due to Space Charge in Continuous Beams”. In: *IEEE Transactions on Nuclear Science* 18.3 (1971), pp. 1101–1104 (page 51).
- [70] Peter Strehl. *Beam instrumentation and diagnostics*. Vol. 120. Springer, 2006 (page 52).
- [71] Karlheinz Schindl. “Space charge”. In: *Beam Measurement*. World Scientific, 1999, pp. 127–151 (page 53).
- [72] N Chauvin. “Space-charge effect”. In: *arXiv preprint arXiv:1410.7991* (2014) (page 55).
- [73] Moses Chung, V Shiltsev, and L Prost. *Space-charge compensation for high-intensity linear and circular accelerators at Fermilab*. Tech. rep. Fermi National Accelerator Lab.(FNAL), Batavia, IL (United States), 2013 (page 56).
- [74] R Baartman and D Yuan. *Space charge neutralization studies in the H-beam*. Tech. rep. Triumf, 1988 (page 56).
- [75] Cristhian A Valerio-Lizarraga, Ildefonso Leon-Monzon, and Richard Scrivens. “Negative ion beam space charge compensation by residual gas”. In: *Physical Review Special Topics-Accelerators and Beams* 18.8 (2015), p. 080101 (pages 56, 58).

- [76] Leonida Antonio Gizzi. “Laser-Driven Sources of High Energy Particles and Radiation”. In: *Laser-Driven Sources of High Energy Particles and Radiation*. Springer, 2019, pp. 1–24 (page 58).
- [77] Stephane Melanson et al. “H-, D-, C2-: A Comparison of RF and Filament Powered Volume-Cusp Ion Sources”. In: (2017) (pages 59, 87, 103).
- [78] Anand George et al. “Effect of magnetic filter in a volume production multicusp ion source”. In: *AIP Conference Proceedings*. Vol. 2052. 1. AIP Publishing LLC. 2018, p. 050015 (page 59).
- [79] K Jayamanna et al. “A 60 mA DC H- multi cusp ion source developed at TRIUMF”. In: *Nuclear Instruments and Methods in Physics Research Section A: Accelerators, Spectrometers, Detectors and Associated Equipment* 895 (2018), pp. 150–157 (pages 62, 69).
- [80] Stephane Melanson. “The production of negative carbon ions from volume-cusp ion sources”. PhD thesis. University of British Columbia, 2020 (pages 62, 74, 93, 94, 95, 146).
- [81] Osamu Fukumasa and Shigefumi Mori. “Volume production of D- negative ions in low-pressure D2 plasmas—negative ion densities versus plasma parameters”. In: *Nuclear fusion* 46.6 (2006), S287 (pages 63, 65, 68, 69).
- [82] M Bacal and M Wada. “Negative ion source operation with deuterium”. In: *Plasma Sources Science and Technology* 29.3 (2020), p. 033001 (pages 63, 71, 74, 158).
- [83] Robert L Merlino. “Understanding Langmuir probe current-voltage characteristics”. In: *American Journal of Physics* 75.12 (2007), pp. 1078–1085 (pages 69, 142).
- [84] J Komppula et al. “A study of VUV emission and the extracted electron-ion ratio in hydrogen and deuterium plasmas of a filament-driven H-/D- ion source”. In: *Physics of Plasmas* 26.7 (2019), p. 073517 (page 74).
- [85] B Heinemann et al. “Towards large and powerful radio frequency driven negative ion sources for fusion”. In: *New Journal of Physics* 19.1 (2017), p. 015001 (page 74).
- [86] Stephane Melanson et al. “Improvements to a 13.56 MHz RF powered H- ion source”. In: *AIP Conference Proceedings*. Vol. 2011. 1. AIP Publishing LLC. 2018, p. 050030 (page 74).
- [87] Marthe Bacal and M Wada. “Effect due to plasma electrode adsorbates upon the negative ion current and electron current extracted from a negative ion source”. In: *AIP Conference Proceedings*. Vol. 1869. 1. AIP Publishing LLC. 2017, p. 030025 (page 74).

- [88] R I Hall et al. “Vibrational excitation of hydrogen via recombinative desorption of atomic hydrogen gas on a metal surface”. In: *Physical review letters* 60.4 (1988), p. 337 (page 75).
- [89] Solidworks. *Simulation study types*. URL: [https://help.solidworks.com/2021/english/SolidWorks/cworks/c\\_Study\\_Types.htm?verRedirect=1](https://help.solidworks.com/2021/english/SolidWorks/cworks/c_Study_Types.htm?verRedirect=1) (visited on 03/17/2021) (pages 79, 94).
- [90] A F Mills. *Basic heat and mass transfer; 2nd ed.* Upper Saddle River, NJ: Prentice Hall, 1999. URL: <https://cds.cern.ch/record/2291687> (pages 81, 83, 96).
- [91] Dr. Harlan H. Bengtson. *Convection Heat Transfer Coefficient Estimation*. URL: <https://s3.amazonaws.com/suncam/docs/119.pdf> (visited on 03/17/2021) (pages 81, 96, 102).
- [92] T Kalvas et al. “Recent negative ion source activity at JYFL”. In: *AIP Conference Proceedings*. Vol. 1515. 1. American Institute of Physics. 2013, pp. 349–358 (pages 87, 147).
- [93] A.M. George et al. “Improvements in Rf Multi Cusp Negative Ion Source”. In: *Proc. 10th International Particle Accelerator Conference (IPAC’19), Melbourne, Australia, 19-24 May 2019*. International Particle Accelerator Conference, pp. 1928–1931. DOI: doi:10.18429/JACoW-IPAC2019-TUPTS001 (page 87).
- [94] Michael A Lieberman and Alan J Lichtenberg. *Principles of plasma discharges and materials processing*. John Wiley & Sons, 2005 (pages 89, 90, 91, 107, 113).
- [95] I P Ganachev et al. “Faraday shielding of one-turn planar ICP antennas”. In: *2016 Progress in Electromagnetic Research Symposium (PIERS)*. IEEE. 2016, pp. 3257–3260 (pages 89, 113).
- [96] Amy E Wendt. “The physics of inductively coupled plasma sources”. In: *AIP Conference Proceedings*. Vol. 403. 1. American Institute of Physics. 1997, pp. 435–442 (page 89).
- [97] Pascal Chebert and Nicholast Braithwaite. *Physics of radio-frequency plasmas* (Cambridge. 2011 (pages 90, 91, 92, 104, 113).
- [98] J T Gudmundsson and M A Lieberman. “Model and measurements for a planar inductive oxygen discharge”. In: *Plasma Sources Science and Technology* 7.1 (1998), p. 1 (page 89).
- [99] JT Gudmundsson and MA Lieberman. “Magnetic induction and plasma impedance in a planar inductive discharge”. In: *Plasma Sources Science and Technology* 7.2 (1998), p. 83 (pages 89, 90).

- [100] V Vahedi et al. "Analytic model of power deposition in inductively coupled plasma sources". In: *Journal of applied physics* 78.3 (1995), pp. 1446–1458 (page 90).
- [101] M Watanabe et al. "Radio-frequency plasma potential variations originating from capacitive coupling from the coil antenna in inductively coupled plasmas". In: *Journal of applied physics* 85.7 (1999), pp. 3428–3434 (pages 92, 107).
- [102] Parker. *Parker O-Ring Handbook*. URL: <https://www.parker.com/Literature/O-Ring%5C%20Division%5C%20Literature/ORD%5C%205700.pdf> (visited on 03/17/2021) (pages 94, 98).
- [103] Solidworks. *Performing a Factor of Safety Check*. URL: [https://help.solidworks.com/2019/english/SolidWorks/cworks/t\\_Performing\\_Factor\\_of\\_Safety\\_Check.htm](https://help.solidworks.com/2019/english/SolidWorks/cworks/t_Performing_Factor_of_Safety_Check.htm) (visited on 03/17/2021) (page 99).
- [104] Solidworks. *Mohr-Coulomb Stress Criterion*. URL: [https://help.solidworks.com/2019/english/SolidWorks/cworks/r\\_Mohr-Coulomb\\_Stress\\_Criterion.htm](https://help.solidworks.com/2019/english/SolidWorks/cworks/r_Mohr-Coulomb_Stress_Criterion.htm) (visited on 03/17/2021) (page 99).
- [105] D P H Hasselman. "Thermal stress resistance of engineering ceramics". In: *Materials science and engineering* 71 (1985), pp. 251–264 (page 99).
- [106] P K Panda et al. "Thermal shock and thermal fatigue study of ceramic materials on a newly developed ascending thermal shock test equipment". In: *Science and technology of advanced materials* 3.4 (2002), p. 327 (page 99).
- [107] J Hopwood. "Planar RF induction plasma coupling efficiency". In: *Plasma Sources Science and Technology* 3.4 (1994), p. 460 (page 104).
- [108] Ocean Insight. *HR 2000+ spectrometer*. URL: <https://www.oceaninsight.com/products/spectrometers/high-resolution/hr2000es/?qty=1> (visited on 03/17/2021) (page 104).
- [109] MM Turner and MA Lieberman. "Hysteresis and the E-to-H transition in radiofrequency inductive discharges". In: *Plasma Sources Science and Technology* 8.2 (1999), p. 313 (page 106).
- [110] S Xu et al. "Hysteresis and mode transitions in a low-frequency inductively coupled plasma". In: *Journal of Vacuum Science & Technology A: Vacuum, Surfaces, and Films* 18.5 (2000), pp. 2185–2197 (page 106).
- [111] O Tarvainen and S Kurennoy. "Conceptual design of a sputter - type negative ion source based on electron cyclotron resonance plasma heating". In: *Proceedings of ECRIS08, Chicago, IL USA*, pp. 64–67 (page 107).

- [112] Marthe Bacal, Akiyoshi Hatayama, and Jens Peters. "Volume production negative hydrogen ion sources". In: *IEEE Transactions on Plasma Science* 33.6 (2005), pp. 1845–1871 (page 107).
- [113] Stephen Edward Savas, Chen-an Chen, and Shawming Ma. *Electrostatic Shield for Inductive Plasma Sources*. US Patent App. 16/245,973. 2020 (page 107).
- [114] Reinard Becker and WB Herrmannsfeldt. "igun- A program for the simulation of positive ion extraction including magnetic fields". In: *Review of scientific instruments* 63.4 (1992), pp. 2756–2758 (page 114).
- [115] J. E. Boers. "PBGUNS: A digital computer program for the simulation of electron and ion beams on a PC". In: *International Conference on Plasma Sciences (ICOPS)*. 1993. DOI: 10.1109/PLASMA.1993.593577 (page 114).
- [116] SIMION. *The field and particle trajectory simulator*. URL: <https://simion.com/> (visited on 03/17/2021) (page 114).
- [117] Peter Spädtke and S Wipf. *KOBRA 3: a code for the calculation of space-charge-influenced trajectories in 3-dimensions*. Tech. rep. CM-P00069645, 1989 (page 114).
- [118] Taneli Kalvas and J Lettry. "Deviation of H- beam extraction simulation model". In: *AIP Conference Proceedings*. Vol. 2052. 1. AIP Publishing. 2018, p. 050007 (pages 114, 117, 125, 126, 127, 136).
- [119] Anand George et al. "A study of the optical effect of plasma sheath in a negative ion source using IBSIMU code". In: *Review of Scientific Instruments* 91.1 (2020), p. 013306 (page 114).
- [120] T Kalvas et al. "Application of 3D code IBSimu for designing an H-/ D- extraction system for the Texas A&M facility upgrade". In: *AIP Conference Proceedings*. Vol. 1390. 1. AIP. 2011, pp. 439–448 (pages 114, 115, 116, 121, 125, 130).
- [121] K Miyamoto, S Wada, and Akiyoshi Hatayama. "Aberration of a negative ion beam caused by space charge effect". In: *Review of Scientific Instruments* 81.2 (2010), 02A724 (page 132).
- [122] M Bacal et al. "Measurement of H- density in plasma by photodetachment". In: *Review of Scientific Instruments* 50.6 (1979), pp. 719–721 (pages 140, 142).
- [123] Doshisha University. *Plasma physics laboratory*. URL: [https://istc.doshisha.ac.jp/en/course/electrical/laboratories/lab0\\_21.html](https://istc.doshisha.ac.jp/en/course/electrical/laboratories/lab0_21.html) (visited on 03/17/2021) (page 140).



- [124] M Bacal. “Photodetachment diagnostic techniques for measuring negative ion densities and temperatures in plasmas”. In: *Review of Scientific Instruments* 71.11 (2000), pp. 3981–4006 (page 140).
- [125] S Masaki et al. “Study of the materials on plasma electrode surface for negative ion extraction in hydrogen and deuterium operation”. In: *AIP Conference Proceedings*. Vol. 2052. 1. AIP Publishing LLC. 2018, p. 020002 (page 141).
- [126] Quantel laser. *Compact pulsed Nd:Yag lasers*. URL: <https://www.quantel-laser.com/en/products/item/ultra-50-100-mj--134.html> (visited on 03/17/2021) (page 141).
- [127] S Melanson et al. “A negative ion source test facility”. In: *Review of Scientific Instruments* 87.2 (2016), 02B109 (page 146).
- [128] Pheonix contact. URL: <https://www.phoenixcontact.com> (visited on 03/17/2021) (page 150).
- [129] Stephane Melanson et al. “A PID Control Algorithm for Filament-Powered Volume-Cusp Ion Sources”. In: *7th Int. Particle Accelerator Conf.(IPAC’16), Busan, Korea, May 8-13, 2016*. JACOW, Geneva, Switzerland. 2016, pp. 2623–2624 (pages 150, 151).
- [130] Brooks instrument. *Mass flow controllers*. URL: <https://www.brooksinstrument.com/en/products/mass-flow-controllers> (visited on 03/17/2021) (page 151).
- [131] Paul W Allison, Joseph D Sherman, and David B Holtkamp. “An emittance scanner for intense low-energy ion beams”. In: *IEEE Transactions on Nuclear Science* 30.4 (1983), pp. 2204–2206 (pages 155, 156).
- [132] D-Pace. *Emittance scanner ES-4*. URL: <https://www.d-pace.com/images/products/Diagnostic%5C%20Devices/ES-4/spec/2120008-r4-es-4-specification.pdf> (visited on 03/17/2021) (page 155).
- [133] Arthur A. Bless. “Biological effects of neutron radiation”. In: *Proceedings of the Florida Academy of Sciences* 6.1 (1943), pp. 25–28. ISSN: 00970581. URL: <http://www.jstor.org/stable/24313028> (page 158).
- [134] K Bergaoui et al. “Development of a new deuterium–deuterium (D–D) neutron generator for prompt gamma-ray neutron activation analysis”. In: *Applied Radiation and Isotopes* 94 (2014), pp. 319–327 (page 158).
- [135] Mitsuru Kikuchi, Karl Lackner, and Minh Quang Tran. “Fusion physics”. In: (2012) (page 158).
- [136] Ludlum Measurements Inc. *He-3 Neutron detector*. URL: [https://ludlums.com/images/product\\_manuals/M12-4.pdf](https://ludlums.com/images/product_manuals/M12-4.pdf) (visited on 03/17/2021) (page 158).